

**Development of materials and methods for the  
next generation electronic, electrochemical and  
opto-electronic device systems**

**A Thesis Submitted to the AcSIR for the Award  
the Degree of**

**DOCTOR OF PHILOSOPHY  
In  
CHEMICAL SCIENCES**



**By  
Aniruddha Basu  
Registration Number: 10CC14A26027**

**Under the guidance of  
Dr. Chandrasekhar V Rode  
(Research Guide)  
and  
Dr. Satishchandra B Ogale  
(Research co-guide)**

**CSIR-NATIONAL CHEMICAL LABORATORY  
PUNE – 411 008, INDIA**

## Certificate

This is to certify that the work incorporated in this Ph.D. thesis entitled “**Development of materials and methods for the next generation electronic, electrochemical and optoelectronic device systems**” submitted by **Mr. Aniruddha Basu** to Academy of Scientific and Innovative Research (AcSIR) in fulfillment of the requirements for the award of the Degree of **Doctor of Philosophy in Chemical Sciences**, embodies original research work under my supervision. I further certify that this work has not been submitted to any other University or Institution in part or full for the award of any degree or diploma. Research material obtained from other sources has been duly acknowledged in the thesis. Any text, illustration, table etc. used in the thesis from other sources, have been duly cited and acknowledged.

  
**Research Student**

Aniruddha Basu

  
**Research Guide**

Dr. Chandrasekhar Rode


  
**Research Co-guide**

Dr. Satishchandra Ogale

## Declaration

I hereby declare that the thesis entitled “**Development of materials and methods for the next generation electronic, electrochemical and opto-electronic device systems**” submitted for the degree **Doctor of Philosophy** in Chemical Sciences to the Academy of Scientific & Innovative Research (AcSIR), has been carried out by me at the Physical and Materials Chemistry Division of National Chemical Laboratory, Pune under the guidance of **Dr. C. V. Rode and co-guidance of Dr. S. B. Ogale**. Such material which has been obtained by other sources has been duly acknowledged in this thesis. The work is original and has not been submitted in part or full by me for any other degree or diploma to other University.

Date: 29<sup>th</sup> September 2016

  
Aniruddha Basu

National Chemical Laboratory,

(Research Student)

Pune - 411008

*Dedicated to my Family*

## ***Acknowledgements***

*This stage in my life would not have been possible without support and blessings of so many people. At this moment, I express my deep sense of gratitude towards everyone who made this memorable for me.*

*First, I wish to express my deepest sense of gratitude to Dr. Chandrasekhar Rode, my research guide, for accepting to guide my research and helping me along the way through all my difficulties with his insightful academic and technical guidance. His excellent human qualities and friendly approach were important for my development as an individual. He is always a very cheerful and highly efficient person from whom I have been able to learn a lot.*

*I would also like to sincerely thank my friend, philosopher and guide Prof. Satishchandra Ogale for giving me an opportunity to work in his dynamic lab environment. He has always been a constant source of motivation for me during my PhD tenure. His dynamic presence and ability to think beyond conventional thinking has always surprised me as a science student. He always encouraged me to explore the new scientific ideas and critically evaluated the significance of such ideas. Through the coffee sessions and our Saturday group meetings, I have nurtured my scientific and professional skills. His constant support with endless patience has helped me during my whole PhD tenure. His personal excitement about science is a viral feeling, which will stay with me throughout my life.*

*I would like to acknowledge two funding agencies, namely the Department Science and Technology (DST), and Council of Scientific & Industrial Research (CSIR) for research fellowships.*

*Further, I wish to thank Dr. Saurav Pal, (former Director CSIR-NCL), Dr. Ashwini kumar Nangia (Director, NCL) and Dr. Anil Kumar, HOD, Physical and Materials Chemistry Division for the opportunity to work at CSIR-NCL and providing the infrastructure and research facilities. I sincerely thank my Doctoral Advisory Committee (DAC) members, Dr. P. P. Wadgaonkar, Dr. S. K. Bhat and Dr. C. S. Gopinath for their timely discussions, guidance, and evaluations during my course work.*

*The technical and non-technical staff of the Physical and Materials Chemistry division has also been very helpful.*

*I am also thankful to Dr. Rohan Fernandes and Dr. D. C. Kothari of Mumbai University for helping me in XPS characterizations.*

*I wish to further express my thanks to the student academic office staff for their constant help and guidance throughout my course work at AcSIR. My very sincere thanks are also due to Dr. C. G. Suresh (former DAC chairman), Dr. C. J. Gadgil (DAC chairman), Mrs. Puranik, Mrs. Kolhe and Ms. Vaishali for the help and co-operation throughout this period. I also greatly admire the efficiency of the Deans of AcSIR (headquarters) and their staff.*

*I would like to acknowledge my coworkers and friends Dr. Abhimanyu Rana, Dr. Vivek Dhas, Dr. Subas Muduli, Dr. Prasad Yadav Dr. Parvez, Dr. Arif, Dr. Mandakini, Dr. Lily, Dr. Datta, Dr. Meenal, Dr. Shruti, Dr. Abhik, Dr. Rohan, Dr. Onkar, Dr. Debanjan, Dr, Vivek, Dr. Sarika Phadke, Dr. Shraddha, Dr. Anil, Dr. Monika, Dr. Dhanya, Dr. Pradeep, Dr. Satish, Dr. Vishal, Dr. Surender, Dr. Dipti, Raunak, Satywan, Yogesh, Wahid, Umesh, Mukta, Divya, Pooja, Srashti, Ishita, Swati, Poonam, Sheetal, Kingshuk, Rajesh, John, Neha, Varun, Nisha, Sambhabi, Aditi, Shrreya, Apurva, Padmini, Prachi, Sambhaji, Nilima, Supriya, Upendra, Kush, Ajay, Golu, Kartiki, Deepmala, Rahul, Roma, Kaustuv, Agnish, Vinita, Aniruddha, Chinmayee and Danish for their support and for creating a wonderful laboratory environment. They all have been very helpful and friendly.*

*I would also like to thank my current and ex. roommates, Sankha, Monoj, Saikat, Ujjwal and Alam for their constant cheerful support and making the out-of-lab environment pleasant.*

*Further I am very thankful to my friends in NCL, Abhik, Himadri, Mrinmoy, Anup and Arpan for their close friendship and constant encouragement throughout these years.*

*I further like thank my friends Aritra, Bhaskar, Chandra, Bhanja, Suman, Banti, Sanjib, Prithviraj, Deblina, Chandradhish, Chinmoy, Kaustuv, Abishek, Neha and Kanika for their friendly help.*

*I take this opportunity to thank all my teachers from my primary school till my Master's degree for imbibing good values and knowledge in me.*

*I wholeheartedly thank my family Baba, Ma, Dada, Debjani di, boro mama, mejo mama, choto mama, boro masi, choto masi, boro meso, choto meso, dadabhai, didibhai and ittu for their unconditional love, constant support, and sacrifices since my childhood and for allowing me to pursue my ambitions. Without their positive support pursuing PhD would have been very difficult for me.*

*In the end a big thanks to my soul mate, Sudipta. Without her patience and encouragement this would never have been possible. In all these years she stood next to me and helped me overcome tough situations. During this process, she has been a real strength for me.*

*Finally a big thank you to almighty god for taking me and teaching me all the way through this.*

*Aniruddha Basu*

## List of Abbreviations

1D	One Dimensional
2D	Two Dimensional
AM	Air Mass
AFM	Atomic Force Microscopy
BHJ	Bulk Heterojunction
CB	Conduction band
DRS	Diffuse Reflectance Spectroscopy
DSSCs	Dye sensitized solar cells
EIS	Electrochemical Impedance Spectroscopy
FE SEM	Field emission scanning electron microscopy
FTO	Fluorine doped tin oxide
FWHM	Full width half maximum
ITO	Indium doped Tin Oxide
$J_{sc}$	Short Circuit Current Density
J	Current Density
HR TEM	High resolution transmission electron microscopy
HOMO	Highest Occupied Molecular Orbital
HTM	Hole transporting material
IPCE	Incident photon-to-current conversion efficiency
ITO	Indium doped Tin Oxide



LH	Light harvesting
LHE ( $\lambda$ )	Light harvesting efficiency at wavelength $\lambda$
LUMO	Lowest Unoccupied Molecular Orbital
LED	Light Emitting Diodes
MSC	Micro supercapacitor
NF	Nanofibers
PL	Photoluminescence
PEC	Photo-electrochemical
PV	Photovoltaic
$P_{\max}$	Maximum power
SAED	Selected Area Electron Diffraction
SEM	Scanning electron microscopy
TCO	Transparent Conducting Oxide
TEM	Transmission electron microscopy
TTIP	Titanium tetraisopropoxide
UV	Ultraviolet
VB	Valence band
$V_{\text{in}}$	Input voltage
$V_{\text{out}}$	Output voltage
$V_{\text{th}}$	Threshold voltage
XPS	X-ray photoelectron spectroscopy
XRD	X-ray diffraction

# Content

<b>Abstract</b>	<b>I-III</b>
<b>Chapter 1: Introduction</b>	<b>1-55</b>
1.1 The modern world and next generation device systems: .....	2
1.1.1 Transistor based devices: .....	4
I. Field Effect Transistors (FET):.....	4
II. Bipolar Junction Transistors (BJT):.....	5
1.1.2 Opto-electronic devices: .....	6
I. Photovoltaic devices: .....	7
II. Photoconductive devices: .....	8
III. Devices with simulated emissions: .....	9
IV. Devices with radiative recombination:.....	10
1.1.3 Charge storage devices: .....	12
I. Capacitors: .....	12
II. Battery: .....	15
1.2 Specific device systems and materials involved in the present work: .....	17
1.2.1 Flexible Micro Supercapacitors: .....	17
I. Materials in micro-supercapacitors: .....	18
II. Device Fabrication:.....	22
1.2.2 Flexible Organic Field Effect Transistor (OFET):.....	26
I. Materials in OFET: .....	27
II. Device Architecture: .....	29
III. Working Principle: .....	30
1.2.3 Flexible Light Emitting Diode (LED):.....	31
I. Materials in LEDs:.....	31

II.	Device Architecture: .....	33
1.3	Outline of the thesis:.....	35
1.4	References: .....	37

**Chapter 2: Experimental Methods, Characterization Techniques and Device Fabrication 56-76**

2.1	Introduction: .....	57
2.2	Synthesis of materials:.....	57
2.2.1	Hot injection method:.....	57
2.3	Device fabrication: .....	58
2.3.1	CO <sub>2</sub> Laser based micro patterning: .....	58
I.	Laser writing:.....	59
II.	Laser scribing: .....	59
2.3.2	Spin Coating.....	60
2.3.3	Thermal Evaporation.....	60
2.4	Characterization of materials and devices:.....	62
2.4.1	X-ray Diffraction (XRD): .....	62
2.4.3	BET surface area analysis .....	65
2.4.4	X-ray Photoelectron Spectroscopy (XPS).....	67
2.4.5	Photoluminescence (PL) Spectroscopy.....	68
2.4.6	Field Emission Scanning Electron Microscopy (FESEM) .....	69
2.4.7	Transmission Electron Microscopy (TEM) .....	70
2.4.8	Electrochemical Measurements .....	71
I.	Cyclic Voltammetry.....	71
II.	Galvanostatic Charge-Discharge .....	71
III.	Electrochemical impedance spectroscopy (EIS) .....	72
2.4.9	Current-Voltage (I-V) study: .....	73
2.4.10	Chromameter:.....	74

2.5References: .....	75
----------------------	----

**Chapter 3: CO<sub>2</sub> laser direct written MOF-based metal-decorated and hetero-atom doped porous graphene for flexible micro-supercapacitor with extremely high cycling stability 77-93**

3.1	Introduction: .....	78
3.2	Experimental Section: .....	80
3.2.1	Device fabrication: .....	80
3.2.2	Formation of Gel Electrolyte: .....	81
3.2.3	Characterization technique:.....	81
3.3	Result and Discussion: .....	81
3.4	Conclusions:.....	90
3.5	References:.....	91

**Chapter 4A: Highly stable laser-scribed flexible planar micro supercapacitor using mushroom derived carbon electrodes 94-112**

4A.1	Introduction.....	95
4A.2	Experimental Section.....	97
4A.2.1	Synthesis of mushroom derived carbon (MDC).....	97
4A.2.2	Fabrication of micro supercapacitor electrodes.....	98
4A.2.3	Formation of gel electrolyte .....	98
4A.2.4	Characterization techniques .....	98

4A.2	Results and discussion .....	99
4A.3	Conclusion .....	108
4A.4	References: .....	109

**Chapter 4B: A robust highly flexible all-solid-state micro pseudocapacitor based on ternary oxide  $\text{CuCo}_2\text{O}_4$  having ultrathin porous nanowall type morphology blended with CNT** **113-131**

4B.1	Introduction.....	114
4B.2	Experimental Section.....	116
4B.2.1	Materials .....	116
4B.2.2	Preparation of CCO nanosheets .....	116
4B.2.3	Fabrication of flexible micro-supercapacitor .....	116
4B.2.4	Preparation of gel electrolyte .....	117
4B.2.5	Characterization technique .....	117
4B.3	Results and Discussion .....	117
4B.3.1	X-ray Diffraction .....	117
4B.3.2	Electron Microscopy: .....	119
4B.3.3	Device Fabrication: .....	121
4B.3.4	Electrochemical Measurements:.....	121
4B.4	Conclusions.....	128
4B.5	References: .....	128

**Chapter 5: PVA-Pentacene based high performance all organic flexible field effect transistor for inverter application 132-149**

5.1	Introduction: .....	133
5.2	Experimental: .....	134
5.2.1	PVA solution preparation: .....	134
5.2.2	Device fabrication: .....	134
5.3	Characterization: .....	136
5.4	Result and Discussion: .....	136
5.5	Conclusion:.....	144
5.6	References: .....	144

**Chapter 6: CdSe-ZnS core-shell quantum dot based solution processed flexible light emitting diodes for flat-panel display application 150-166**

6.1	Introduction: .....	151
6.2	Experimental: .....	153
6.2.1	Single-Step Synthesis of Quantum Dots:.....	153
6.2.2	Fabrication of QD-LED device fabrication: .....	154
6.3	Characterization: .....	155
6.4	Result and Discussion: .....	155
6.4.1	Synthesis of core-shell quantum dot: .....	155
I.	Mechanism of core-shell QD formation: .....	155
II.	Tuning of QD emission by varying Cd:Zn ratio:.....	156

III.	Tuning of QD emission by varying injection method: .....	157
6.4.2	Fabrication of QD-LED device:.....	158
I.	Fabrication of Device on the hard substrate: .....	158
II.	Fabrication of Device on the flexible substrate: .....	161
6.5	Conclusion:.....	162
6.6	References: .....	163

<b>Chapter 6:</b>	<b>Summary and Future work</b>	<b>167-171</b>
-------------------	--------------------------------	----------------

<b>List of Publications</b>	<b>172-173</b>
-----------------------------	----------------

## Abstract

Over the past few decades the electronic gadgets have developed quite rapidly in terms of their intricacy and performance features. According to the users' need the electronic gadgets are getting smaller, thinner and wearable. The major components of an electronic gadget are its electronic circuitry, display and power source. The electronic circuitry consists of millions of transistors. Hence to make a high performance smaller device, the chips should possess high density of transistors. In 1980, Dr. Gordon Moore, the co-founder of Intel Corp. had predicted that the transistor density in a chip will be doubled every 2 years. This trend has been followed by the developments in the field till now. From Intel 4004 processor (1971) to Ivy Bridge processor (2016) the transistor density in a chip has increased from  $10^3$  to  $10^8$ . While keeping this trend of increment in transistor density, the electronic chips are also getting flexible. In so far as the electronic gadgets are concerned, low powered light emitting diode (LED) displays are becoming more popular. These LED displays can easily be made thin and flexible with ultra-high resolution. Recently, LG has launched flexible organic LED (OLED) TV with ultra-HD resolution. One of the most important components of an electronic gadget is its power source. For flexible gadget, this also has to be flexible. Li-ion batteries are widely used as power source in common electronic devices. But flexible Li-ion batteries are quite difficult to fabricate though work on the same is in progress as well. Recently flexible supercapacitors have come into the picture to provide high power density to small scale devices. These devices are quite easy to fabricate and can be fabricated in different shapes according to the need of the concerned electronic gadget. The present thesis deals with topics in this domain of interesting research.

A brief explanation of the methodologies used is given below in each chapter.

**In the first working chapter (Chapter-3)**, we have discussed the fabrication of laser induced porous graphene from Co-MOF (ZIF-67). The MOF consists of repetitive organic framework having metal atoms embedded throughout the matrix. On application of CO<sub>2</sub> laser, the organic part converted into carbon with metal particulates dispersed in it. These metal constituents are removed from the



carbon matrix to get homogeneous porosity. The nature of the carbon was confirmed from XRD and Raman spectroscopy. Both showed the signs of highly defective nature of the carbon which is desirable for the supercapacitor application for various reasons. The FESEM images also showed high porosity. This carbon was then used to fabricate a flexible micro supercapacitor electrode having feature lines with 100 $\mu$ m width and 5mm length. The device performance was observed using polyvinyl alcohol (PVA)-H<sub>2</sub>SO<sub>4</sub> gel electrolyte. The device showed power density of 580 mW cm<sup>-2</sup>, ultra-high cyclic stability of 100,000 cycles and flexibility of over 150° bending radius.

**In the second working chapter (Chapter-4)**, we have demonstrated an ultra-fast protocol for fabrication of micro supercapacitor using pre-synthesized materials. In this work, we have coated high capacitive carbon and metal oxide on flexible ITO/PET conducting substrate and etched out the material by using CO<sub>2</sub> laser to form interdigitated micro electrode (figure 2) having 300 $\mu$ m width and 5mm length. The laser scribing technique required 20-30 secs for fabrication of 1 cm<sup>2</sup> device. We could also successfully fabricate a flexible micro supercapacitor using carbon and CuCo<sub>2</sub>O<sub>4</sub> (CCO) pre-synthesized material. Both the devices showed high capacitance, and long term cyclic stability. Both these devices showed high flexibility in both bending and flexing conditions.

**In the third working chapter (Chapter-5)**, we have discussed the optimization of gate dielectric layer in p-type organic field effect (OFET) transistor for the fabrication of flexible device. The device contained PVA as the gate dielectric and pentacene as the channel layer. We reduced the dielectric thickness from 500 nm to 300 nm. On reduction of the thickness the on/off ratio of the device was seen to improve from 10<sup>2</sup> to 10<sup>4</sup>. The threshold voltage improved from -47.8 V to -4.3 V and the mobility of the channel layer improved dramatically from 0.016 to 0.45 cm<sup>2</sup> v<sup>-1</sup> s<sup>-1</sup>. We have fabricated flexible OFET using 300nm dielectric layer, which showed high on/off ratio of 10<sup>3</sup> turn-on voltage of -3.2 V. The channel mobility (0.57 cm<sup>2</sup> v<sup>-1</sup> s<sup>-1</sup>) of the device was also fairly impressive. In this case we successfully demonstrated an inverter using the fabricated p-type OFETs.

**In the final working chapter (Chapter-6)**, we have discussed the fabrication of a flexible quantum dot light emitting diode (QLED) device using CdSe/ZnS

core/shell quantum dots (QDs). We have synthesized the core/shell quantum dots using a simple one-pot synthesis protocol. The quantum dots thus synthesized had graded core-shell architecture of either CdSe-CdS-ZnS or CdSe-ZnSe-ZnS depending upon the concentration of the reagents. The photoluminescence of the QDs could be tuned by tuning the core diameter. We have also fabricated a multi-layered QLED device. In this work we have optimized each layer thickness to get the highest performance. We achieved highest luminescence of  $341 \text{ cd m}^{-2}$  with a turn-on voltage of 1.8 V.

# Chapter1

## Introduction

**This chapter highlights the recent advancement in the modern electronic gadgets as well as the current state of art devices. Different types of modern flexible devices are also discussed here in-detail. The three main components of an electronic gadget: transistors, display devices and charge storage devices are explained in detail in this chapter. Further a brief description of specific device systems related to this thesis like flexible micro supercapacitor, flexible organic field effect transistor and flexible quantum dot based light emitting diode, is also included. Finally the chapter is concluded with the outline of the thesis.**

## 1.1 The modern world and next generation device systems:

The revolution in the electronic device systems started since the development of first transistor back in 1948.<sup>1</sup> This discovery matured the field to quite an extent. Devices such as radio, television, phonographs, radar, long distance telephony *etc.* underwent various technological upgrades leading to modernization, which upturned our way of thinking towards technology. The early transistors were made of vacuum tubes. The first transistor without vacuum tube was manufactured by IBM in April 1955. IBM manufactured the world's first all transistorized calculator with product name IBM608. The IBM608 consisted of 3000 germanium transistors.<sup>2,3</sup> Since then the rate of the development of the electronic device systems is increasing with time and requirement. Recent trend in the electronic industry is to have electronic gadgets which are small as well as wearable thus increasing their adaptability and reach to various fields. In order to cope up with this trend the electronic circuitry used in these devices also has to be miniaturized and made flexible without compromising its performance. This requires the device circuitry to be highly dense along with additional flexibility so as to maintain the performance. In 1965, Gordon E. Moore, the director of research and development at Fairchild Semiconductor at that time, predicted that the complexity of the electronic circuitry will be doubled in every two years.<sup>4-6</sup> In other words the density of the transistors in the circuitry will be doubled. At that time it was predicted that electronic circuitry will follow this trend for next ten years, however this trend is observed even today in the development of the modern electronic circuitry (figure 1.1a). The modern day processors such as core i7, Ivy bridge *etc.* consist of more than  $10^8$  no of transistors per chip.

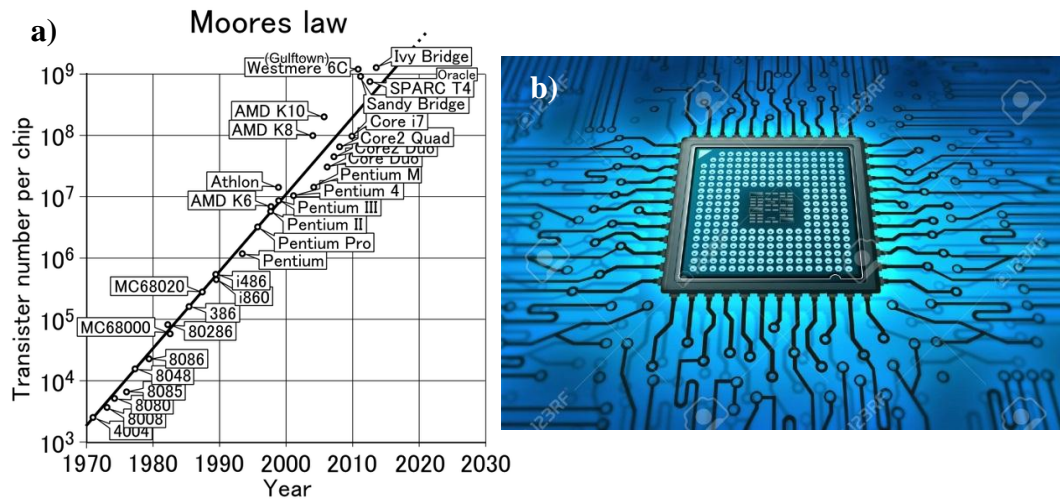


*Figure 1.1: a) Moore's law and development of processors over the years. Ref: <http://betanews.com/2013/10/15/breaking-moores-law/> and b) a typical processor chip with transistors. (Ref: <http://www.123rf.com/stock-photo/microprocessorchip.html>)*

Along with the miniaturized electronic circuits, the concept of flexible electronics or flex circuits developed in early twentieth century.<sup>7</sup> The first work on flexible circuit was published in 1947 by Clelio Brunetti and Roger W. Curtis.<sup>8,9</sup> This publication discussed a method for printing flexible electronic circuits. In 1950 the first flex circuit was developed and patented by the Sanders Associates' inventors (Nashua, NH) Victor Dahlgren and company founder Royden Sanders.<sup>8</sup> This work successfully integrated the flat conductors into the flexible base by printing and etching method. Following this development, the advancement in the flexible printed electronics technology has been rapid. Although today this field is extremely popular world-wide at the time of its inception the Japanese engineers took the lead for its advancement. Flexible electronic circuits as well as displays are currently used in several flexible gadgets such as sensors, televisions, bio-medical applications etc. The flex circuits are not only used in flexible devices but also used in regular non flexible devices just to minimize the space of the circuitry. In the following segments we will discuss about different flexible devices.



*Figure 1.2: Flexible electronic circuitry, a) The integrated flexible circuit in Olympus stylus camera (ref: [https://en.wikipedia.org/wiki/Flexible\\_electronics](https://en.wikipedia.org/wiki/Flexible_electronics)), and b) ETH Zurich researchers fabricated ultra-thin highly flexible circuit (ref: <http://newatlas.com/eth-zurich-ultra-thin-flexible-circuit/30371/>).*

### 1.1.1 Transistor based devices:

Transistors are the fundamental components of the electronic devices and absolutely necessary for the modern electronic systems. Transistors are the semiconductor devices which are basically used either to switch or to amplify the electronic signals and electrical power. Generally, these are three terminal devices. The voltage or current applied at one terminal of the transistor can be manipulated by the voltage or current applied at the other terminal of the same transistor. Hence in this semiconductor device the output can be higher than the input i.e. amplification of the electronic signal.<sup>10</sup> Different types of transistors are used in modern day electronic devices. Depending upon the device architecture the transistors can broadly be categorized in following way,

#### I. Field Effect Transistors (FET):

A FET is a unipolar transistor. It consists of a channel layer, which is either electron or hole conducting and a dielectric or insulating layer. It comprises of three terminals namely gate, source and drain (figure 1.3a). On application of voltage at the gate electrode the dielectric polarization occurs which influences the current between the source-drain electrode across the channel layer. The first successful demonstration of the FET device was done in 1925 by J.E. Lilienfeld and O. Heil. It was later patented in 1930.<sup>11,12</sup>

## II. Bipolar Junction Transistors (BJT):

As the name suggests, it is a bipolar transistor unlike the FET. It forms two junctions with two types of semiconductors, p-type and n-type. Two types of BJTs are generally constructed “p-n-p” and “n-p-n”. There are three regions in the device namely, emitter, collector and base (figure 1.3b). The emitter is generally heavily doped either with p-type or with n-type. In a typical n-p-n BJT device, forward bias is applied at the emitter-base interface and reverse bias is applied in the base-collector interface. On application of forward bias the thermally generated electrons at the emitter is repelled by the electric field. Hence the electrons are diffuse from the emitter to collector through base. As the base is p-type, the majority carriers are hole, so the chances of recombination of these electrons are very high. Hence to avoid the recombination process the thickness of the base is set to be lesser than the diffusion length of the electrons.<sup>13</sup> This type of transistor was invented by William Shockley in 1948.<sup>14</sup> However this type of devices are losing their importance recently in comparison with the MOSFET devices.<sup>13</sup>

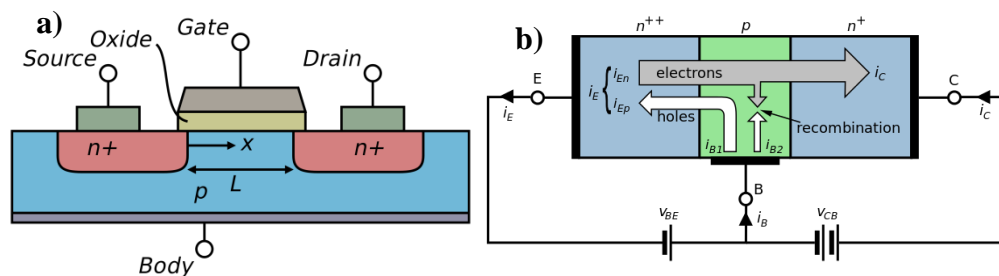


**Figure 1.3:** Device architecture of a) Field effect transistor (Ref: [https://en.wikipedia.org/wiki/Field-effect\\_transistor](https://en.wikipedia.org/wiki/Field-effect_transistor)) and b) Bipolar junction transistor (Ref: [https://en.wikipedia.org/wiki/Bipolar\\_junction\\_transistor](https://en.wikipedia.org/wiki/Bipolar_junction_transistor)).

As stated earlier, transistors are the primary components of the device circuitry, hence to make flexible circuit; fabrication of flexible transistors is the main focus. Currently almost all the device circuits are made using FET type devices. For flexible circuit, predominantly organic field effect transistor (OFET) is being used. Both the channel and the dielectric are organic material in OFET and also the substrate is made of plastic as well. In case of channel, conducting polymers, small molecules etc. are used, and for the dielectric material, mostly insulating

polymers with high dielectric constant are employed. The first work on the OFET was reported by Koezuka and co-workers in 1987.<sup>15</sup> In this FET device, polythiophene based conjugated polymer was used as channel material. The whole device was not organic as SiO<sub>2</sub> was used as dielectric material. In 1990, Peng *et.al.* reported a detailed study on the effect of different organic dielectric materials on the field effect mobility of the organic semiconductor.<sup>16,17</sup> Since then a lot of research work is focused on all organic OEFT devices.<sup>17-19</sup> In May 2007, Sony reported for the first time all organic, flexible true colour display where both the display as well as the device circuitry was flexible (figure 1.4b).<sup>20</sup> Recent focus is on nano-materials based flexible FETs. Mostly carbon based nano materials such as carbon nanotube (CNT),<sup>21</sup> graphene<sup>22,23</sup> etc. and semiconducting metal oxides nano particles<sup>24,25</sup> and quantum dots<sup>26,27</sup> are popular as non-organic flexible channel material.

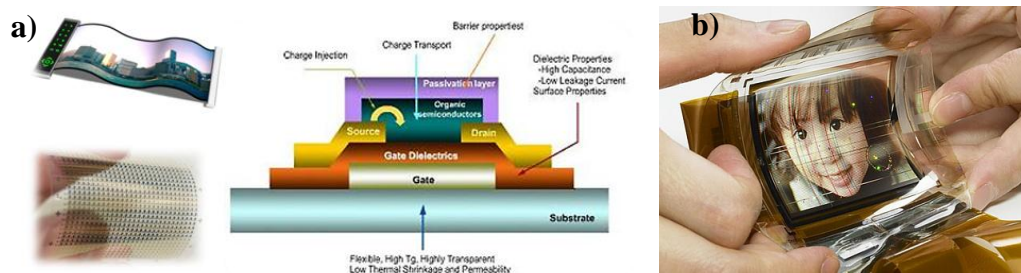


**Figure 1.4:** a) a typical flexible OFET (ref: <http://yang.unist.ac.kr/main/sub24.htm>) and b) first full colour flexible OLED display with fully flexible electronic circuit by Sony (ref: <http://pinktentacle.com/2007/05/flexible-full-color-organic-el-display/>).

### 1.1.2 Opto-electronic devices:

Optoelectronics is a technology where the physics of electronics combines with the physics of light. The opto-electronic devices convert the light into electricity and vice versa. Depending upon the nature of their work these devices are classified.<sup>28</sup>



## I. Photovoltaic devices:

These type of devices generate electricity upon light irradiation. A typical example of photovoltaic device is solar cell, where the active material or light absorbing material absorbs light and generates electricity. This phenomenon is called photovoltaic effect. Upon irradiation of photon, the electron at the low energy valance band (VB) of the active material is excited and transferred to the high energy conduction band (CB) and can act as a charge carrier for electricity (figure 1.5a).<sup>29</sup> The photovoltaic effect was first observed by the French physicist Alexandre-Edmond Becquerel in 1839.<sup>30,31</sup> Since the inception of this concept lot of research effort is directed towards this field. Solar cell is the best possible product of this concept which is apt for the present energy scenario as the solar cells produce electricity by absorbing solar light. Thus it is the best renewable source of energy which is environmental friendly as well. In the late nineteenth century the first photovoltaic device was made using semiconducting selenium by Charles Fritts.<sup>32</sup> Although the efficiency of the device was very low. In 1905 Albert Einstein proposed the famous quantum theory on photoelectric effect for which he received the Noble prize. This theory helped the researchers understand in detail about the photovoltaic effect which eventually led to remarkable progress in the field of Solar cells. Several approaches are initiated to improve the performance of the solar cell.<sup>32</sup> Till date highest efficiency of 46% is achieved using multi junction approach. Flexible solar cells have also been made for convenient large scale processability (figure 1.5b) as well as for integrating it on in all flexible devices. Mostly organic light absorbing semiconductors are used in flexible solar cells.<sup>33,34</sup> Recently, optical nano materials such as quantum dots are gaining importance in the field of flexible solar cell because of their flexibility, ease of processability and stability in solid state and also due to their high photon to current conversion rate.<sup>35-37</sup>

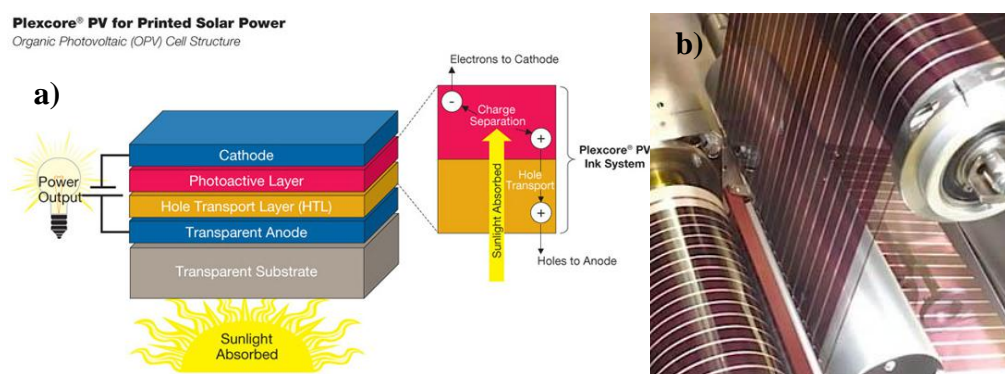


**Figure 1.5:** a) Solar cell device architecture and mechanism (ref: <http://www.sigmaaldrich.com/content/dam/sigma-aldrich/materials-science/organic-electronics/pv-inks/opv-standard-cell-structure.jpg>) and b) Large scale roll to roll processing of flexible solar cell (ref: <http://www.siliconsolar.com/wp-content/themes/woostore/images/flexible-solar-panels-custom.jpg>).

## II. Photoconductive devices:

Photoconductivity is another opto-electronic phenomenon where in presence of light the conductivity of the photoactive material is increased. The basic difference between this and the photovoltaic device is that, photoconductive device is unable produce photo voltage. It requires an external bias for its operation.<sup>38</sup> This type of device is used to detect the light. Photodetectors and photo-FETs are the examples of the photoconductive devices. Several photoactive semiconducting materials such as metal oxides,<sup>39–41</sup> polymers,<sup>42–47</sup> quantum dots<sup>26,27,48–52</sup> etc. are effectively used in photodetectors and photo-FETs. Flexible prototypes of these devices have also been fabricated using polymers and nano materials.<sup>42,43,45–47,49</sup>

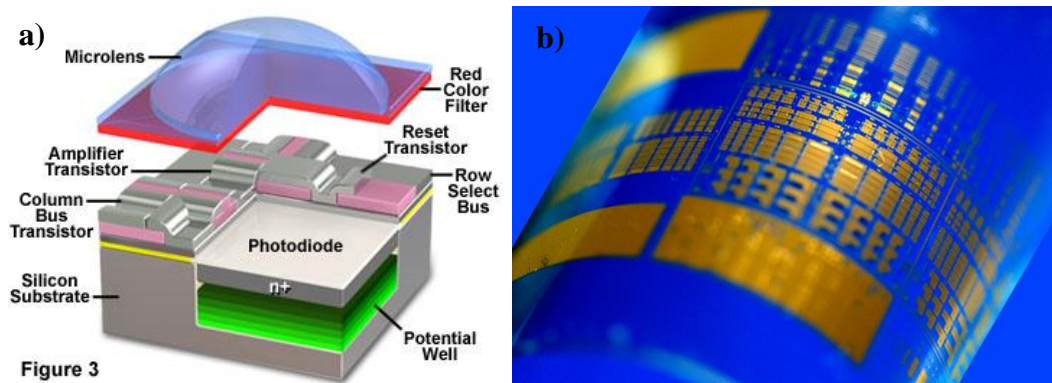


*Figure 1.6: a) Typical architecture of a photodetector (Ref: <https://micro.magnet.fsu.edu/primer/digitalimaging/cmosimagesensors.html>) and b) Flexible prototype of a commercially available photodetector (Ref: <http://phys.org/news/2009-01-flexible-photodetectors-sharpen-photos.html>).*

### III. Devices with simulated emissions:

In simulated emission, excited electrons of a molecule interact with a photon having specific frequency and relax back to a lower energy level by liberating energy. This energy is transferred to an electromagnetic field to create a new photon with phase, direction, frequency and polarization.<sup>53</sup> For simulated emission, molecules with inverted electronic population are used as it requires the higher life time of the excited electrons. This phenomenon was first discovered by Einstein in 1916.<sup>54,55</sup> Based on this principle, LASER (Light amplification by stimulated emission of radiation) device was made by Theodore H. Maiman at Hughes Research Laboratories in 1960.<sup>56-59</sup> In modern life style LASER is one of the most important device. It is associated with many ordinary yet important appliances such as laser printer, bar code scanner, camera, optical disk drivers etc. Lasers also used extensively in highly sophisticated instruments such as DNA sequencer, finger print scanner, surgery equipment, fibre optics, modern military equipment and weapons etc.<sup>60</sup> Recently different lasers are also used for synthesis of functional materials. Depending upon the source, lasers can be of different types such as gas laser, solid state laser, semiconductor laser, fibre laser, dye laser etc. Among them, gas lasers like CO<sub>2</sub> laser, He-Ne laser, HF laser, excimer molecule based laser etc. are quite popular.

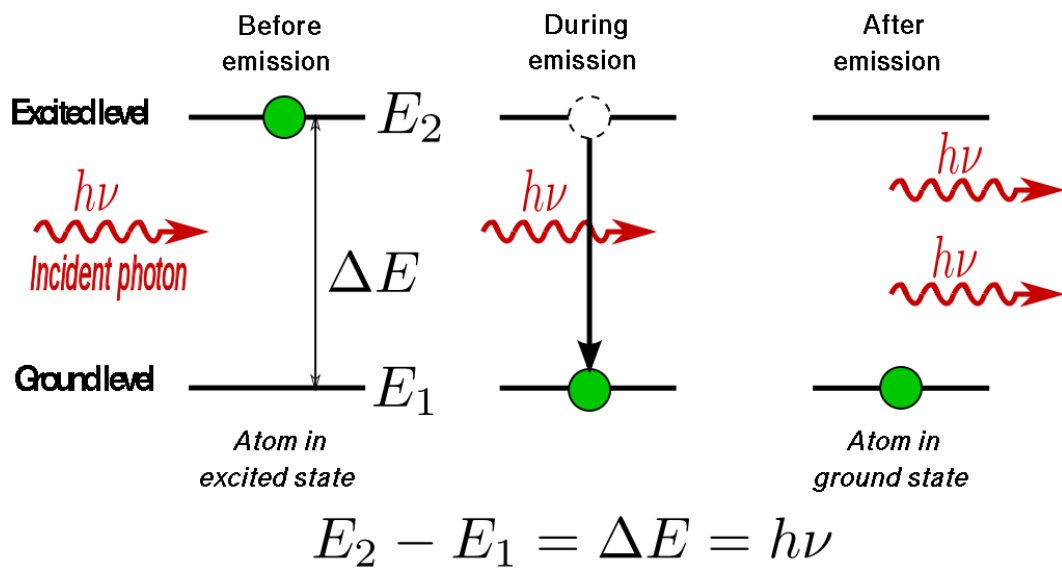


*Figure 1.7: Working principle of LASER*

#### IV. Devices with radiative recombination:

In this process, in solid state semiconductor, charge carriers are generated by means of external energy such as electricity, which are subsequently eliminated radiatively to get the energy in form of radiation.<sup>61</sup> Light emitting diode (LED) is an example of a device. In LEDs, the electrons and holes are incorporated externally by means of electricity at the conduction band (CB) and valence band (VB) of single material (in case of organic LEDs) or two different materials (n-type and p-type here) respectively. Further, the electrons and the hole are allowed to recombine radiatively. The energy released in this process depends upon the energy difference between the VB and CB i.e. the band gap of the material. Hence by selecting the material with proper band gap radiation with different energy can be achieved. In LEDs the band gap of the material falls into the visible region hence it emits visible light. By selecting the material with proper band gap, desired coloured LED can be made. The LED technology has evolved from electroluminescence which was discovered in 1907 at the H. J. Round of Marconi Labs.<sup>62</sup> Later in 1927, a soviet inventor, Oleg Losev reported the first LED.<sup>63</sup> Since then several efforts are directed for the improvement of the technology as well as the efficiency of LEDs. In comparison with the other lighting technologies, LEDs are highly efficient and cost effective. Owing to these properties, LEDs have become primary technology used for illumination in

household and commercial places recently.<sup>63</sup> It is not only used for lighting but also for display purpose. In display technology solid state LEDs or solid state lighting (SSL) are used which includes organic LED (OLED), quantum dot LED (QDLED) etc.<sup>64,65</sup> Recently, flexible LEDs are been made using both OLED and QDLED devices. Flexible OLED device was incorporated in any commercial device for the first time by Samsung in October 2013. Samsung launched a smartphone, “Galaxy round” with 5.7” full HD flexible OLED panels.<sup>66,67</sup> Soon after, on 20th October, 2013, LG launched a smartphone “G flex” with 6” flexible OLED panel.<sup>68</sup> Since then several companies have launched flexible OLED display panel for small applications.

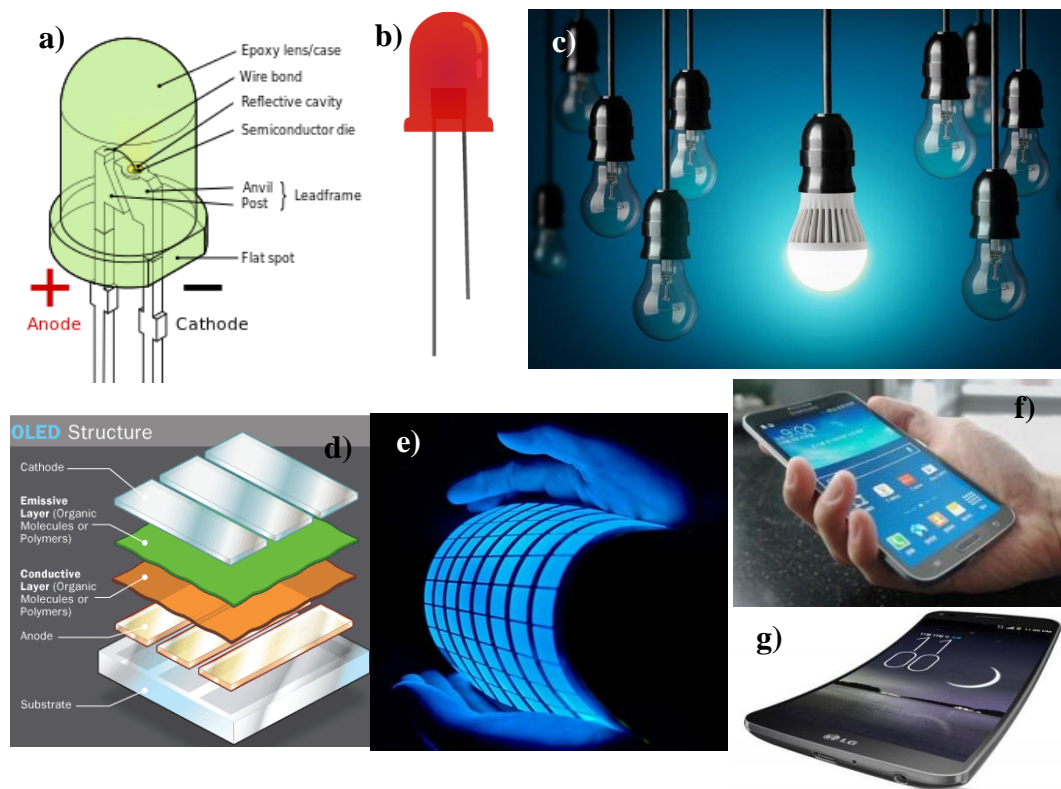


**Figure 1.8:** a) Device architecture of LED bulb (ref: [https://en.wikipedia.org/wiki/Light-emitting\\_diode](https://en.wikipedia.org/wiki/Light-emitting_diode)), b) and c) represents atypical LED bulb (ref: <https://www.raspberrypi.org/learning/introduction-to-processing/components/led/>; <http://www.digitaltrends.com/home/researchers-want-to-use-led-light-bulbs-to-connect-to-the-internet/>), d) device architecture of OLED display device (ref: <http://electronics.howstuffworks.com/oled1.htm>), e) a typical flexible OLED (ref: <http://www.courts.com.sg/promotions/oled.html>), f) “Galaxy round” smartphone by Samsung (ref: 66) and g) “G-flex” smartphone by LG (ref: 68)

### 1.1.3 Charge storage devices:

Any electronic gadget requires electrical input to be functional. Generation of electricity can be done from different sources, such as fossil fuel, solar, wind, nuclear etc. using different techniques. But only electricity generation is not enough, storing of it is also equally important. Hence charge storage devices have evolved greatly in recent years. Capacitors and batteries are most popular among the charge storage devices.

#### I. Capacitors:

In 1745 Ewald Georg von Kleist, from Germany, first invented capacitor.<sup>69,70</sup> Since then the main focus in the field of capacitor is to increase its storage capacity. Supercapacitors are the newest inclusion in the field. About the basics of these devices, capacitors are basically two terminal devices which store electricity temporarily in an electric field.<sup>70</sup> Typically, a capacitor consists of two electrodes separated by a dielectric. A dielectric is basically electrically insulating. On application of voltage, the dielectric gets polarized and stores energy electrostatically. The capacitance of a capacitor,  $C$ , can be defined as the ratio of the total charge stored on each electrode ( $Q$ ) to the voltage difference between the two electrodes ( $V$ ) (equation 1).

$$C = Q/V \quad (1)$$

As it is evident from the above equation that capacitance of a capacitor depends upon the amount of charge stored, the dielectric material which in the capacitor plays a crucial role. A dielectric material should have high permittivity as well as high breakdown voltage. In early stages of development of capacitor, vacuum was used as a spacer as well as the dielectric material. But due to its low dielectric properties and in order to make compact devices, solid state dielectric materials such as plastic, paper, glass, mica *etc.* acquired more importance. However, they suffered from various limitations. For example, paper is prone to absorb moisture, plastic cannot tolerate high temperature and glass as well as mica are both quite expensive although they are suitable as dielectric material.<sup>70</sup>

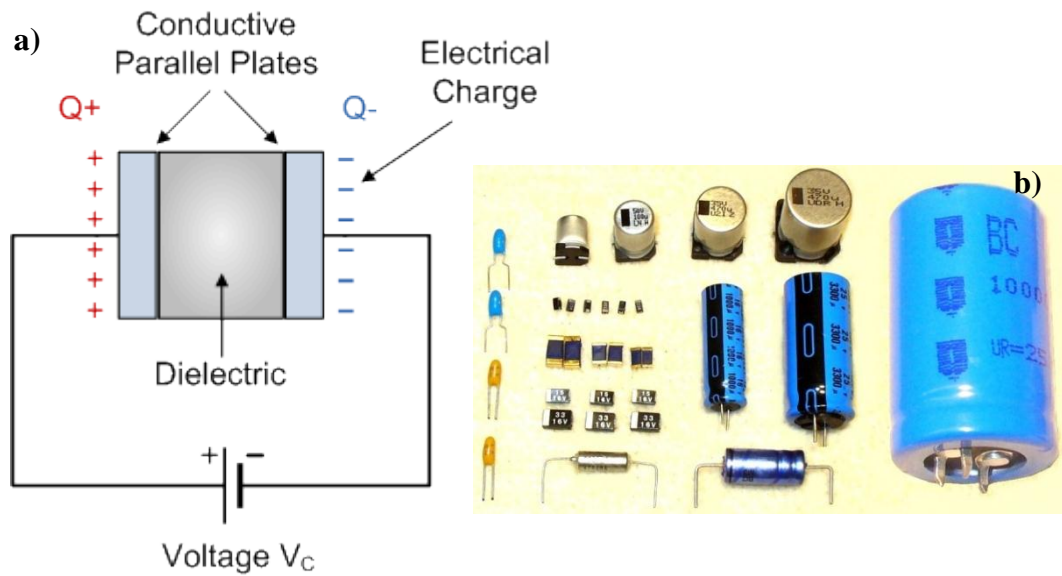


**Figure 1.9:** a) Pictorial representation of the mechanism of capacitors (ref: [http://www.electronics-tutorials.ws/capacitor/cap\\_1.html](http://www.electronics-tutorials.ws/capacitor/cap_1.html)) and b) commercially available most common types of aluminium and tantalum electrolytic capacitors (Ref: [https://en.wikipedia.org/wiki/Electrolytic\\_capacitor](https://en.wikipedia.org/wiki/Electrolytic_capacitor)).

In order to overcome the limitations, electrolytic capacitors, which are known as supercapacitors, came into existence. In 1957, H. Becker developed an electrolytic capacitor using porous carbon for the first time.<sup>71,72</sup> The supercapacitors are basically of two types, 1) electrical double-layer capacitor (EDLC) and 2) electrochemical double layer capacitor or pseudocapacitor.<sup>73</sup> Both types of supercapacitors require electrodes with high surface area. Like the conventional capacitors; the charges are stored at the surface of the electrodes. In electrolytic supercapacitors micro-porous high conducting electrodes mostly porous carbon, CNT, graphene *etc.* (for EDLC) and conducting polymers, metal oxides *etc.* (for pseudocapacitor) are used which have very high surface area. On dipping of the electrodes into the liquid electrolytes, it percolates into the electrode and makes maximum electrode-electrolyte interface. In case of EDLC, on application of voltage at the electrodes, the ions of the electrolyte separate and stored at the surface of the electrode which in turn stores the charge. In pseudocapacitor, the electrolyte ions react reversibly with the surface of the electrode material to store charges. Because of their high capacity, these types of capacitors are called

supercapacitors. Formerly they were known as electrical double layer capacitor (EDLC).<sup>74</sup>

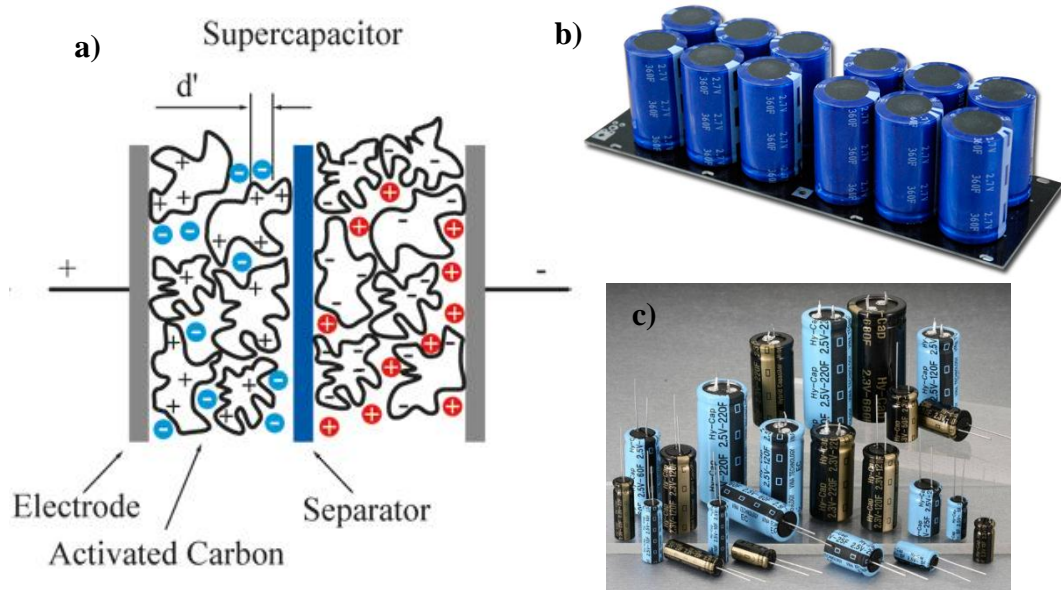


**Figure 1.10:** a) Pictorial representation of the working Principle of supercapacitor (Ref: [https://commons.wikimedia.org/wiki/File:Supercapacitor\\_diagram.svg](https://commons.wikimedia.org/wiki/File:Supercapacitor_diagram.svg)), b) commercially available supercapacitor array in a circuit board (Ref: [http://en.kamcap.com/products\\_list/&pmcId=dc2e1b70-9d46-48ab-9540-705e42d328f9&FrontColumns\\_navigation01-1330069659513FirstColumnId=9dd204f1-0c63-4623-95ad-9e3476f757a9.html](http://en.kamcap.com/products_list/&pmcId=dc2e1b70-9d46-48ab-9540-705e42d328f9&FrontColumns_navigation01-1330069659513FirstColumnId=9dd204f1-0c63-4623-95ad-9e3476f757a9.html)) and c) commercially available different types of supercapacitor (Ref: <http://www.southafricab2b.co.za/default.cgi/action/viewproducts/productid/137220/productname/Supercapacitor/>).

Small capacity capacitors are generally integrated in the electronic circuit board which gives power to the different components of the gadget. As discussed earlier, the devices are getting miniaturized and flexible so is its circuitry. In order to integrate the supercapacitors in this circuitry, these have to be flexible, miniaturized and planer. Recently several approaches are underway to fabricate flexible and planar micro supercapacitor (MSC).<sup>75–79</sup> Initially flip-chip type devices were fabricated as flexible supercapacitors.<sup>80–83</sup> In this type of device solid



state electrolyte is sandwiched between two flexible electrodes. But this type of device is not suitable in the planar geometry of the electronic circuitry. However, with development of in-plane interdigitated MSCs having gel based solid state electrolyte resolved this issue as they fit well in this circuitry.<sup>84-90</sup> In most of the cases the interdigitated electrodes are fabricated using lithographic technique.<sup>21,76,84,88</sup> Although involvement of multiple steps in technique limit its large scale applicability. Recently IR-laser based electrode fabrication techniques are getting popular in this field due to their easy processability and scalability.<sup>90-95</sup>

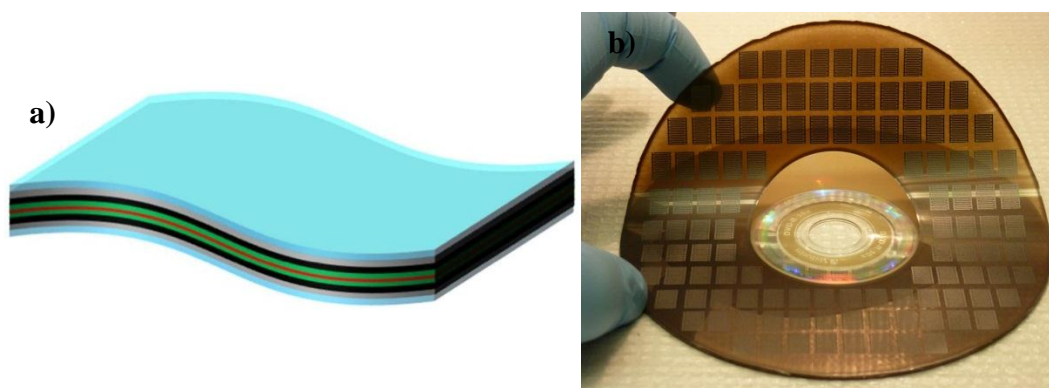


**Figure 1.11:** a) Flexible and wearable flip-chip supercapacitor (Ref: <https://energyvulture.com/2014/10/19/wearable-supercapacitors-making-devices-more-flexible/>) and b) Interdigitated MSC printed on a DVD disk (Ref: <http://www.kurzweilai.net/graphene-micro-supercapacitors-to-replace-batteries-for-microelectronics-devices>).

## II. Battery:

The first electrochemical battery was introduced by Alessandro Volta in 1800. It was simple stack of copper and zinc plates separated by brine soaked paper pile.<sup>96,97</sup> Interestingly, it was able to produce steady source of current although the proper mechanism of the battery was not known at that time.<sup>96</sup> Later in 1813 Sir Humphry Davy introduced the concept of electrolysis which was a major breakthrough in this field. In 1834, Michael Faraday developed the ionic mobility principle and finally explained the chemical reaction involved in the electrochemical battery.<sup>98</sup> Since then this field has developed rapidly. In 1896, the first commercial battery was manufactured by National Carbon Company using carbon-zinc. Although the battery is invented more than 200 years ago,

advancement in this field is still continues. The basic principle of the batteries is simple. Like capacitors, here also to electrodes are separated by electrolyte. On application of voltage to the electrodes, unlike capacitors, chemical reaction happens. While charging the cations are reduced and the anions are oxidized at the electrodes, reverse case happens in case of discharging. Recently lithium ion batteries (LIB) are gaining importance in this field along with sodium ion battery. A typical LIB constructed with four major components, cathode, anode, electrolyte and separator. The schematic of the LIB is shown in the figure 1.12 a.

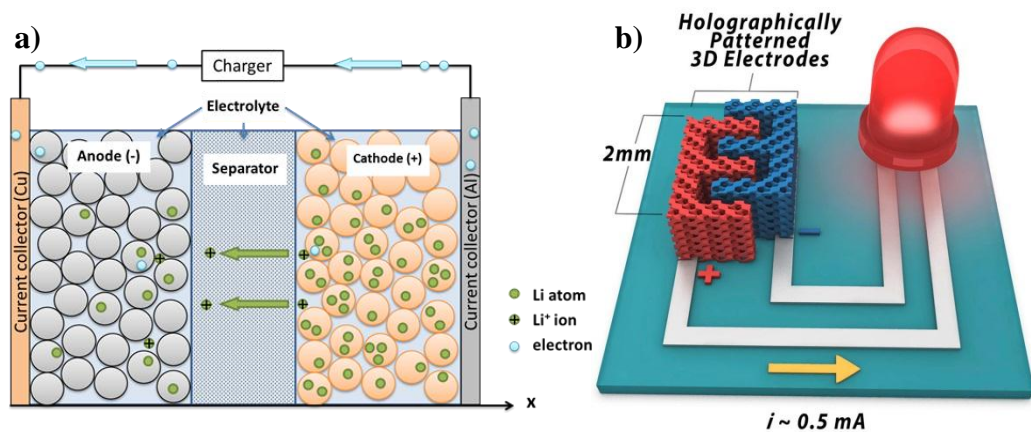
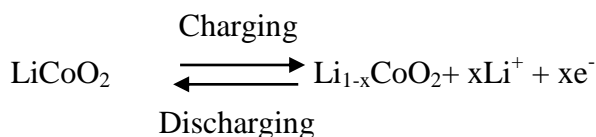


**Figure 1.12:** a) Working principle of Li-ion Battery (Ref: <http://epg.eng.ox.ac.uk/content/energy-storage>) and b) A typical Li-ion micro battery developed by the researcher from university of Illinois, USA (Ref: <http://engineering.illinois.edu/news/article/11092>)

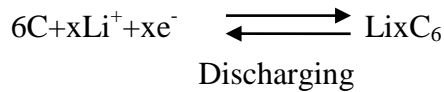
The commercial LIBs are constructed with  $\text{LiCoO}_2$  as cathode and Graphite as anode material.<sup>99</sup> The reactions taking place at the cathode and anode are given below.

At cathode:

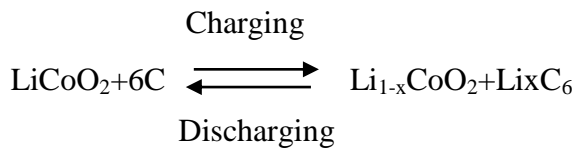


At anode

Charging



The overall net reaction:



Integration of the battery in the flexible devices is extremely challenging as the fabrication methods of flexible planer battery are highly difficult as well as complicated as compared to the micro-supercapacitors. Even with several years of research in this field very less success achieved till date.<sup>100–105</sup>

## 1.2 Specific device systems and materials involved in the present work:

This section mainly focuses on three different types of next generation flexible devices, flexible MSC, flexible field effect transistors and flexible quantum dot light emitting diode. The following sections briefly describe these devices including their development in materials and fabrication techniques.

### 1.2.1 Flexible Micro Supercapacitors:

Recently flexible or wearable microelectronics have become one of the most emerging fields of research. To cope up with this current trend, flexible and wearable charge storage devices are also being developed with continuous miniaturization and efficient processing protocols. However, integration of flexible microscale charge storage devices with electronic circuitry is still challenging because these flexible devices are not well suited with the planar geometry of most electronic devices. Hence planar interdigitated microscale charge storage devices are gaining importance over conventional flip-chip devices.<sup>85,106,107</sup> Advantages of these planar interdigitated devices is that, the planar device structure can provide ultrathin devices with very less chances of electrical short-circuit and the dense interdigitated patterns offer very short ion diffusion

length which in turn increases the power density.<sup>107</sup> Selection of the materials as well as the fabrication techniques, both are important for the construction of a successful device.

### **I. Materials in micro-supercapacitors:**

The materials required for the fabrication of MSC is similar to the conventional supercapacitors. Depending upon the materials, supercapacitors can be of two types, electrical double layer capacitor (EDLC) and pseudo capacitor (faradic capacitor). In case of EDLC type supercapacitors charge is stored by adsorption of ions at the surface of the electrodes. On the other hand the pseudocapacitors involve reversible reaction between the electrode and the electrolyte. The reaction occurs at the surface of the electrodes, unlike batteries where it happens at the bulk. In case of EDLC type supercapacitors mostly porous carbon having high surface area is used<sup>108–111</sup> whereas for pseudo capacitors, binary and ternary metal oxides and chalcogenites<sup>112–114</sup> and conducting polymers<sup>115–117</sup> are quite popular because of their reversible electrochemical reactivity with bases and salts.

#### **A. Electrode materials for EDLC:**

As we have discussed earlier in case of EDLC type supercapacitors a double layer is formed at the interface of the electrode and electrolyte. Hence as the number of interface increase the capacitance also increases. So for high number of interfaces surface area of the material should be high. Porous carbon materials are generally considered to be the best candidate for EDLC type capacitors not only because of their high surface area but also because of very low resistivity, high chemical stability and wide range of operating temperature.<sup>108–111,113,114,118</sup> For industrial application also carbon materials are very popular because of their high abundance, low cost, easy processing and non-toxic nature.<sup>113,118</sup> Carbon materials are very compatible for EDLC type supercapacitors. The cyclic voltammetry graph for most of the carbon based supercapacitors is rectangular in nature which allows maximum storage capacity (figure 1.13).<sup>113,119</sup> Also the galvanostatic charge-discharge curve shows triangular nature which reflects the very high coulombic efficiency.

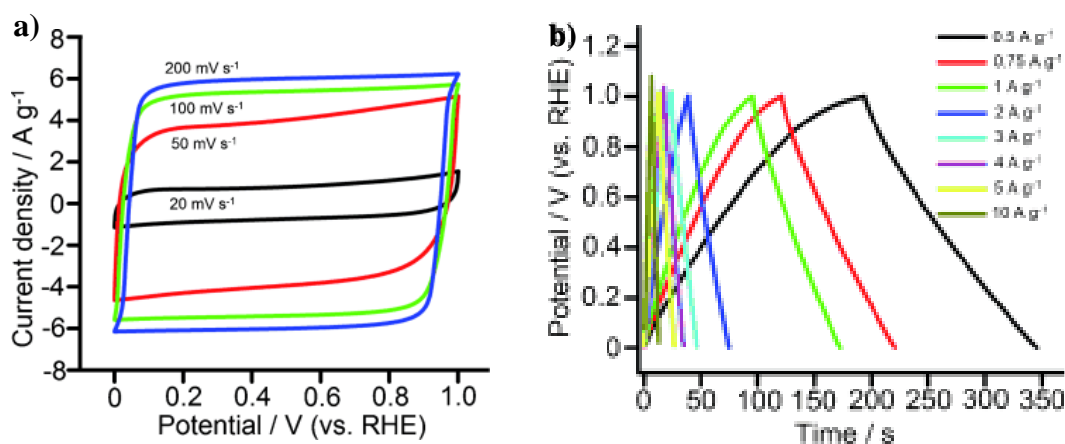


**Figure 1.13:** a) Cyclic voltammetry diagram and b) galvanostatic charge discharge curve of supercapacitor based on hexaporous graphene electrode (reprinted with the permission from ref. 114)

As discussed earlier, surface area is the key for the high performance of the supercapacitors. But increase in the surface area of the electrode material alone cannot improve the performance; proper accessibility of the electrolytic ions in the porous network is also essential. In other words the capacitance predominantly depends upon the surface area of the material accessible to the electrolyte.<sup>113</sup> Hence the specific surface area, pore size distribution and pore shape of the electrode material used mainly governs the performance of supercapacitor. The properties of a good supercapacitor grade material are, 1) high specific surface area; 2) sufficient accessibility of the electrolytic ions in the pores of the material and 3) good inter particle connectivity for better electrical conductivity.<sup>113</sup>

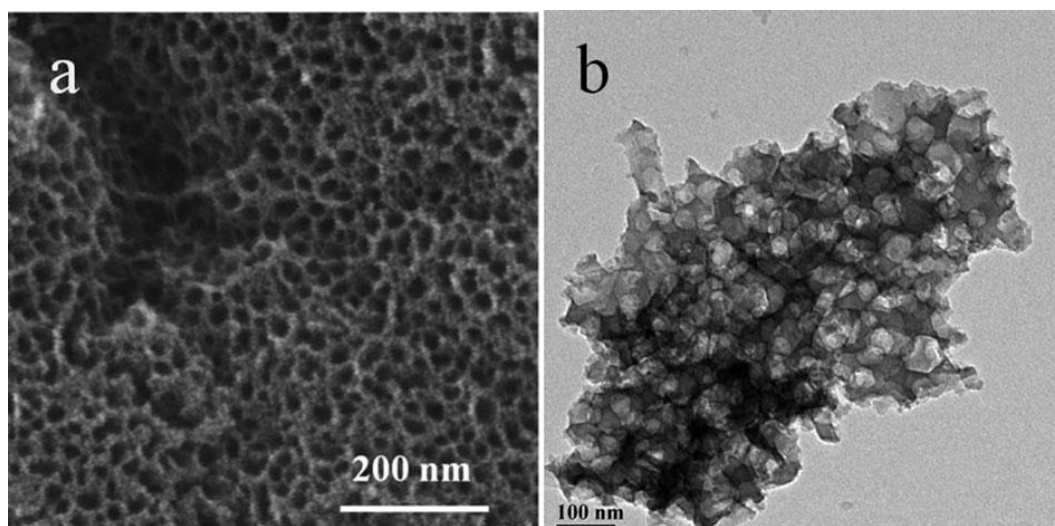


*Figure 1.14: a) Scanning electron microscopy (SEM) and b) Transmission electron microscopy (TEM) images of porous graphene (reprinted with permission from ref. 114)*

The examples of high surface area carbon materials are activated carbon,<sup>120–125</sup> carbon nanotube (CNT),<sup>126–130</sup> carbon aerogel,<sup>131–135</sup> templated porous carbon,<sup>136–140</sup> carbon nano fibres<sup>141–143</sup> etc. Although in most of the cases the capacitance obtained is less than the literature value.<sup>144</sup> Generally the values obtained from carbon based supercapacitors are in the range of 75-175 F g<sup>-1</sup> for aqueous electrolytes and 40-100 F g<sup>-1</sup> for non-aqueous electrolytes.

### **B. Electrode materials for pseudocapacitors:**

In pseudocapacitors (PCs), electrode materials undergo reversible electrochemical reaction (redox reactions) with electrolytes. The process of charge storage in this case is quite similar to batteries except that in battery the redox reaction occurs in entire material whereas in PC it happens only at the surface and the bulk near the surface of the material. There are three types of reactions that occur during charging/discharging in PCs: reversible adsorption type (for example, adsorption of hydrogen at the metal surface such as palladium, platinum etc.), redox reactions involving transition metals and electrochemical doping-dedoping of conducting polymers.<sup>113,117</sup> The PCs generally exhibit very high capacitance and energy density compared to the EDLC type capacitors but suffer from low power density

as the charging and discharging process involved in this case is slower than the EDLC.<sup>113,145</sup> As discussed earlier two types of materials are generally used in PCs, metal oxide and conducting polymers, which can undergo reversible redox reactions.

Metal oxide based PCs exhibit higher energy density than conventional carbon based supercapacitors and also offer very high stability than conducting polymer based PCs. The main criteria for a metal oxide to be the good electrode material for PC are: 1) good electrical conductivity, 2) more than two oxidation states that coexist over a continuous range without any change in original phase and structure of the material and 3) free intercalation of proton into the oxide matrix during reduction. Ruthenium dioxide ( $\text{RuO}_2$ ) is highly favoured electrode material in both the usual and micro PCs. The high performance of  $\text{RuO}_2$  is attributed to its wide potential window, three oxidation state within 1.2 V voltage window, highly reversible redox reaction, high proton conductivity, low material resistance, long cyclic stability and good rate capability.<sup>146–149</sup> The highest capacitance obtained using  $\text{RuO}_2$  is  $720 \text{ F g}^{-1}$ .<sup>146</sup> Apart from  $\text{RuO}_2$ ,  $\text{MnO}_2$  is also widely used as electrode material in PCs.  $\text{MnO}_2$  has some important advantages like low cost, low toxicity, high stability and high theoretical capacitance of 1100 to  $1300 \text{ F g}^{-1}$ .<sup>150–153</sup> Other transition metal oxides like  $\text{NiO}$ ,  $\text{Ni(OH)}_2$ ,  $\text{Co}_2\text{O}_3$ ,  $\text{SnO}_2$ ,  $\text{V}_2\text{O}_5$ ,  $\text{MoO}_2$ ,  $\text{Bi}_2\text{O}_3$  etc. are also interesting candidates for electrode material for PCs.<sup>113</sup> Recently efforts are directed to explore ternary metal oxides as electrode material in this field. These type of ternary metal oxides possess multiple oxidation states which indices the high supercapacitive performance than single component materials. For example,  $\text{Ni}_2\text{CoO}_4$ ,  $\text{ZnCo}_2\text{O}_4$ ,  $\text{Zn}_2\text{SnO}_4$  etc. are widely studied in this field because of their high surface area and high electrical conductivity.<sup>154–157</sup> The highest capacitance of  $2210 \text{ F g}^{-1}$  is recorded for  $\text{Ni}_2\text{CoO}_4$  based supercapacitor.<sup>157,158</sup>

Conducting polymers (CPs) are also very important class of material for this application. Several advantages are associated with CPs such as low cost, environment friendly, high storage capacity, high conductivity in doped state and adjustable redox reactivity by minor chemical modification.<sup>113,159–162</sup> In CPs the redox reaction occurs at the backbone of the polymer. During oxidation ions are

attached to the backbone of the polymer and in reduction the ions are released from it. Hence no major change in the morphology is observed. Also the redox reaction happens not only at the surface but also at the entire bulk of the CPs.<sup>163</sup> The redox reaction was termed as doping in early years. “Doping” is the introduction of positive charge at the polymer during oxidation while “de-doping” is the formation of negative charge at the polymer.<sup>113</sup> Different types of CPs have already been used in supercapacitor application. Among them polyaniline (PANI),<sup>115</sup> polypyrrol (PPY),<sup>164</sup> polythiophene (PTh)<sup>165</sup> and their derivatives<sup>166</sup> have proved to be quite efficient in this application. The basic conductivity of these polymers is not very high which limits their performance. Thus the composites with conducting materials like CNTs improve their performance drastically. PANI-CNT composite can show up to 1030 F g<sup>-1</sup> capacitance in three electrode system.<sup>167</sup> Although more improvement is needed in the optimization of the properties of the composite based PCs.

## II. Device Fabrication:

Fabrication of micro-scale electronic devices is a major challenge because the methods used have to be facile, efficient and compatible with those used in the other flexible device fabrication protocols. Various techniques such as lithography, physical vapour deposition using shadow mask, sputtering, laser writing etc. have been used to fabricate planar interdigitated MSCs till date.<sup>79,88-90,94,168</sup>

### A. Lithography based micro supercapacitor:

Lithography is the highly explored technology in interdigitated MSC devices as it is the well-established method for micro electrode fabrication. The electrodes fabricated using this technique are highly robust which allows the device to sustain in long run.<sup>79</sup> Earlier research demonstrated the electrodeposition of the supercapacitor electrodes onto the lithographically patterned gold electrode on Si/SiO<sub>2</sub> substrate. Mostly polymers like PPY(full form please) and poly(phenylthiophene)(PPT) are used for this type of supercapacitors.<sup>169,170</sup> Although the performance is low for these devices. However several reports in subsequent years have shown improved device performance using this technique. Gogotsi and



co-workers developed a strategy to fabricate monolithic carbide derived carbon (CDC) based micro electrode using lithography.<sup>171</sup> Later on this technique was used in the fabrication of MSC device (figure 1.15) which produces highly efficient device having  $160 \text{ F cm}^{-3}$  capacitance value in aqueous electrolyte.<sup>106</sup>

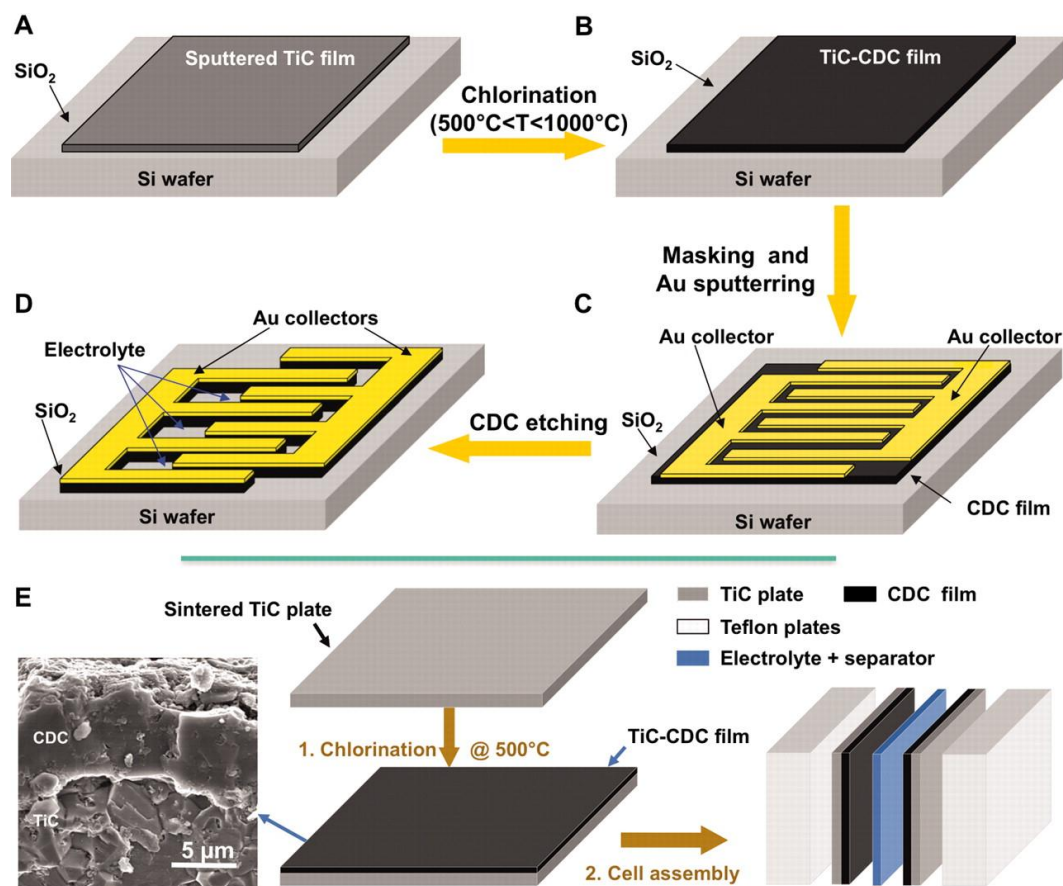


**Figure 1.15:** (A to D) Schematic of the fabrication of a bulk CDC based interdigitated MSC integrated onto a silicon chip using standard photolithography technique. (E) Synthesis of CDC and the preparation of electrochemical test cell. (Reprinted with the permission from ref. 104).

Carbonization of photoresists used in lithography is also a useful technique in this application. This fabrication technique is called carbon-microelectromechanical systems (C-MEMS). In this method the surface area and the porosity of the carbon material can be controlled by either incorporation of activating agents before carbonization or altering the synthetic conditions.<sup>172-174</sup>

There are few reports on the fabrication of pseudocapacitors using metal oxide as electrodes. In most of the cases the metal oxides are electrodeposited onto the lithographically patterned electrode. Wang *et al.* reported electrodeposition of  $\text{MnO}_2$  on the microelectrode developed using e-beam lithography (figure 1.16).<sup>175</sup> This work reports a capacitance of  $53.5 \text{ mF cm}^{-2}$  and also advice stability of up to 1000 cycles. In another work Liu *et al* reported the fabrication of  $\text{MnO}_2$  based MSC where t the  $\text{MnO}_2$  is deposited onto the lithographically patterned interdigitated microelectrodes by CVD method.<sup>176</sup>

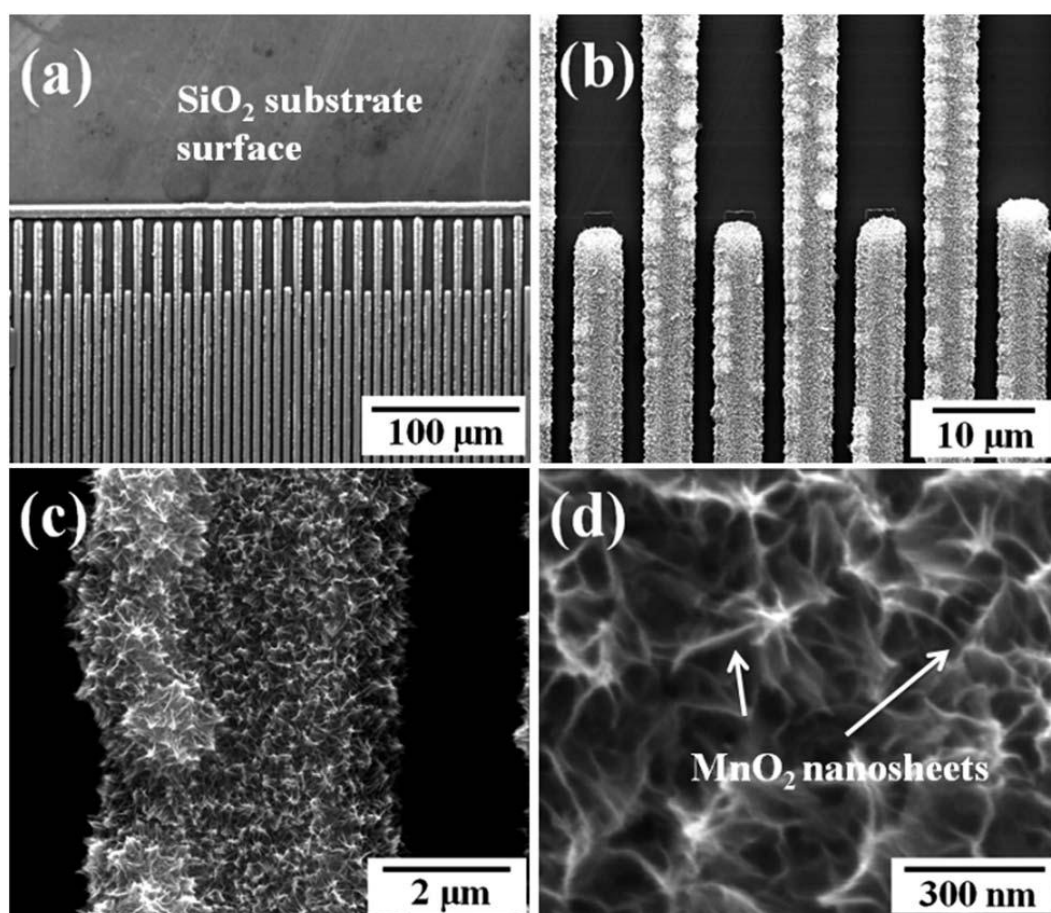


*Figure 1.16: SEM images of manganese oxide electrodeposited onto the microelectrodes array on Si/SiO<sub>2</sub> substrate under different magnifications (reprinted with the permission from ref. 173).*

The basic advantage of the lithography technique is the well-defined patterned electrode. But this method involves multiple steps for a complete MSC device

fabrication. Also this technique requires sophisticated instruments which limit its future large scale application.

### **B. Laser processing based Micro supercapacitor fabrication:**

Laser based MSC fabrication technique is relatively new in this field. Not much work is done on the laser based method yet. Generally reduction of graphene oxide (GO) is done using CO<sub>2</sub> laser scribing method. Gao *et al* developed for the first time a method to fabricate flexible interdigitated MSC using reduced graphene from GO by application of CO<sub>2</sub> laser.<sup>95</sup> Later El-Kady *et. al.* reported the synthesis of graphene from GO and application of the same in flexible flip-chip supercapacitor<sup>93</sup> and the similar method was utilised to fabricate interdigitated MSC on the commercially available CD/DVD by the same group.<sup>88</sup> Recently Lin *et al.* showed fabrication of flexible interdigitated MSC on commercial polymer substrate by direct laser writing method using laser induced graphene (LIG) as electrode (figure 1.17).<sup>94</sup> In this work the authors have used CO<sub>2</sub> laser to synthesize LIG from commercially available polyimide substrate. This method yields highly graphitized carbon with high porosity which is favourable for supercapacitor application. The highest capacitance obtained by this method is more than 4 mF cm<sup>-2</sup>. The device fabrication method is quite simple and highly facile hence large scale application of this method can be done quite easily. The same group later fabricated micro pseudocapacitor (MPC) by electrodeposition of PANI or MnO<sub>2</sub> on the LIG.<sup>177</sup>

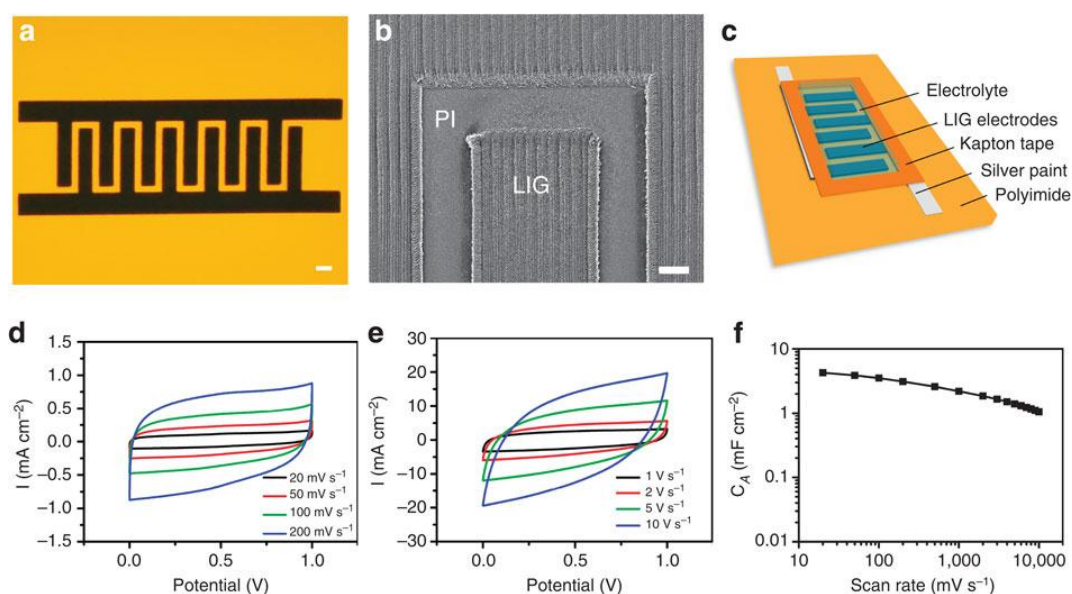


**Figure 1.17:** (a) Digital photograph of LIG-MSCs with 12 interdigitated electrodes (b) SEM image of LIG electrodes. (c) Device architecture of the LIG-MSCs; schematic diagram. (d and e), Cyclic voltammetry curves of LIG-MSCs at scan rates from 20 to 10,000  $\text{mV s}^{-1}$ . (f), Specific areal capacitance ( $C_A$ ) calculated from CV curves as a function of scan rates (reprinted with the permission from ref. 93).

### C. Other fabrication techniques:

Apart from these two techniques there are some other types of techniques utilized for the fabrication of interdigitated MSCs. Plasma etching is common method used in this field. Wu et al have used the oxygen plasma etching technique for MSC device fabrication.<sup>107</sup> In this work GO film is initially spin-coated, it is then subsequently reduced by treating with  $\text{CH}_4$ . The interdigitated gold electrodes are deposited on the RGO by sputtering and then the uncovered RGO is etched out using oxygen plasma etching. The device showed areal capacitance of  $80.7 \mu\text{F cm}^{-2}$  whereas the stack capacitance was  $17.9 \text{ F cm}^{-3}$ . Although the other techniques like CVD, thermal evaporation etc. are used as auxiliary techniques they are generally associated with other techniques.

#### 1.2.2 Flexible Organic Field Effect Transistor (OFET):

Since the invention of OFET in 1986 by Tsumura and coworkers,<sup>178</sup> these type of devices have received substantial attention in the electronic research community

due to their great potential application in modern flexible electronic circuitry. As the electronic properties of organic semiconductors can be tuned by designing the core molecules involved these molecules are very important for the performance of the OFET. The dielectric layer in FET device is equally important for the performance of the device. In OFET, this layer consists of organic dielectric materials. Fabrication of the device is done using both dry process and solution process. As the device consists of micro electrodes, lithography is mostly used for defining these electrodes. In the following part we will discuss about the materials required for OFET as well as the device fabrication technique.

## **I. Materials in OFET:**

### **A. Channel Material:**

Generally  $\pi$ -conjugated organic semiconductors are used as channel material in OFETs. Among the conjugated organic semiconductors poly thiophenes are quite common, especially poly(3-hexylthiophene) (P3HT).<sup>179-182</sup> Also polyfluorene, polydiacetylene, poly(2,5-thienylene vinylene), poly(p-phenylenevinylene) (PPV) etc. are widely used as channel materials for OFET.<sup>183-185</sup> Recently conjugated small molecules have also proved their high potential in this field.<sup>186</sup> Small molecules like pentacene, tetracyanoquinodimethane (TCNQ), rubrene, diindenoperylene, tetracene, perylene diimides etc. are already used in this field. Among them pentacene is the most studied one.<sup>187,188</sup> The highest mobility of  $3 \text{ cm}^2 \text{ V}^{-1} \text{ s}^{-1}$  having  $10^5$  on-off ratio was achieved using pentacene in OFET.<sup>189</sup> Pentacene has an issue of stability in air. It is moderately stable in air. But major advantage of this material is the processability. Highly crystalline uniform thin film of pentacene can be fabricated using thermal evaporation technique.

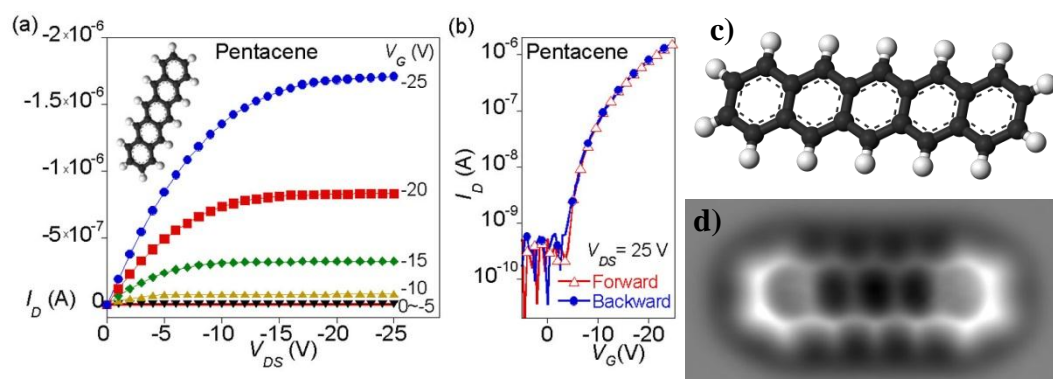


**Figure 1.18:** a)  $I_{ds}$  vs.  $V_{ds}$  graph and b)  $I_{ds}$  vs.  $V_{gs}$  graph for pentacene (ref: <http://spie.org/newsroom/4149-egg-white-in-organic-electronics>), c) ball and stick model of pentacene molecule (ref: <https://upload.wikimedia.org/wikipedia/commons/1/11/Pentacene-3D-balls.png>) and d) AFM image of pentacene (ref: [https://www.zurich.ibm.com/st/atomic\\_manipulation/pentacene.html](https://www.zurich.ibm.com/st/atomic_manipulation/pentacene.html)).

Several n-type semiconductors are also developed as channel layer material for OFET. The organic molecules with high electronegative atoms such as fluorine are best candidate for this kind of application. Recently, a fluoroalkyl-substituted naphthalenetetracarboxylicdiimide film was used as channel layer in OFET.<sup>190</sup> The field effect mobility observed is  $0.01 \text{ cm}^2\text{V}^{-1} \text{ s}^{-1}$  with bottom gate configuration. Substituted fullerenes like, phenyl  $\text{C}_{61}$ -butyric acid methyl ester (PCBM) are quite exploited material in OFET. The field-effect mobility of  $3\text{--}4 \times 10^{-3} \text{ cm}^2\text{V}^{-1} \text{ s}^{-1}$  was achieved using the PCBM in bottom gated device.<sup>191</sup> Due to the low mobility values p-type organic semiconductors are more popular in this field than the n-type.

### B. Dielectric Material:

The performance of the FET devices critically depends upon the dielectric materials used. The dielectric material forms interface with both the gate electrode and the channel layer. The dielectrics having active interfaces with less defect densities generally deliver the best performance.<sup>192</sup> In OFET metal oxide dielectrics are also used along with the organic ones.  $\text{Al}_2\text{O}_3$  and  $\text{TiO}_2$  are one of the widely used metal oxide dielectric for OFET due to high dielectric constants.<sup>193,194</sup> Polymer dielectrics with high dielectric constant are also

extensively used in OFETs.<sup>19</sup> First successful demonstration of polymer dielectric in OFET was by Peng et.al. in 1990.<sup>16</sup> In this work poly vinylchloride (PVC) was used as dielectric. The results of this work indicate the strong correlation between dielectric constant of the dielectric and the field effect mobility of the semiconductors. . The polymers with low dielectric constants like polymethylmethacrylate (PMMA;  $k \approx 3.5$ ), Polystyrene (PS;  $k \approx 2.6$ ) etc. show very low field enhanced current enhancement, while the polymers having high dielectric constants such as poly vinylalcohol (PVA;  $k \approx 7.8$ ), cyanoethylpullulan(CYEPL;  $k \approx 18.5$ ) etc. give very good result.<sup>19</sup> Several other polymer dielectrics such as polyvinylphenol (PVP), poly(ethylene terephthalate) (PET), cross-linked poly-4-vinylphenol (cross-linked PVP), polyvinylacetate (PVAc) etc. have also shown promising results in OFETs.

## II. Device Architecture:

OFETs are basically three terminal devices. The conduction of the majority carriers are modulated by the field applied across the dielectric. Basically two types of device architectures are observed while fabricating the device, top gated and bottom gated. In all cases the dielectric is sandwiched between the gate electrode and the channel layer. For top gated device the gate electrode is at the top and for bottom gated it is at the bottom (Figure 1.19). In the bottom gated device two types of device architectures are observed depending upon the position of the source drain electrode, top contact and bottom contact.<sup>195</sup>

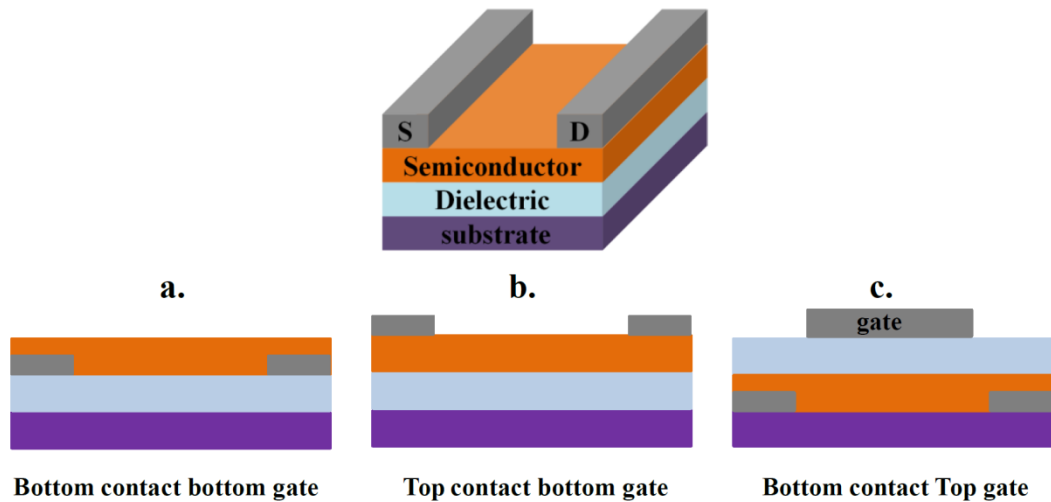


**Figure 1.19:** Device architectures of OFETs: a) bottom contact bottom gate, b) top contact bottom gate and c) bottom contact top gate (reprinted with permission from ref. 195).

### III. Working Principle:

The FET devices are constructed to enhance the channel conductivity by applying gate voltage ( $V_g$ ). For p-type channel negative gate voltage is applied at the gate electrode while for n-type it is positive. On application of  $V_g$  the dielectric polarizes. In case of p-type semiconductor, negative  $V_g$  induces negative polarity at the dielectric-semiconductor interface, which accumulates the holes in the semiconductor. As we increase the negative  $V_g$  the polarization increases which in a way increases the hole accumulation. Hence the conductivity of the channel increases. In case of n-type semiconductor the polarity of the dielectric will be reverse hence accumulation of electron will be there. In this case as well, the channel conductivity increases. When a gate voltage is applied charge carriers are induced at the dielectric-channel interface. The number of charge carriers accumulated depends on the applied gate voltage and insulator capacitance. Below a certain voltage, called threshold voltage ( $V_{th}$ ), all induced charges fill the trap states and hence only for  $|V_g| > V_{th}$  mobile charges are induced in the semiconductor and contribute to the current in a field-effect transistor. Hence the effective gate voltage is  $V_g - V_{th}$ . In the transistor channel the concentration of the charge carrier is uniform without the presence of any source-drain voltage. When a small drain voltage is applied, the current will start flowing between the source and drain electrodes. At low drain voltage ( $V_{ds}$ ) the semiconductor behaves like a



resistance with source drain current ( $I_{ds}$ ) proportional to  $V_{ds}$ . When the  $V_{ds}$  is increased gradually (with source grounded) till  $V_g - V_{th}$  the channel depth near the drain becomes zero. This is called pinch-off point. Beyond this the drain current remains the same with increasing  $V_{ds}$  as the depletion layer near the drain has formed.

### 1.2.3 Flexible Light Emitting Diode (LED):

For flat panel light emitting diode applications electroluminescent materials are the main component. Depending upon the emitting layers the LED devices are named, for example in OLEDs this layer is of organic material while in QLED it is quantum dots. The first electroluminescence in organic materials was observed by André Bernanose and co-workers at the Nancy-Université in France in 1950s.<sup>196</sup> Since then various research is emphasized on the electroluminescence of the organic materials. The basic working principle of flat panel LEDs is the recombination of the electron and hole at the electroluminescent material to emit light. The colour of light is decided on the band gap of the emitting material. Although not only the emitting layer but also the hole and electron conducting layers as well as the device architecture are equally important for an LED device to be function properly. The flexible LEDs are generally made of organic or quantum dots.

#### I. Materials in LEDs:

A basic LED devices are composed of two electrodes (+ve and -ve electrode), two transport layers (hole and electron transport layer) and an emitting layer. In most cases except for the electrodes all other components are organic. This section illustrates the recent progress of the organic materials associated with the OLED device.

As discussed earlier the basic component of the LED device is the emitting layer. In LEDs, different types of emitting layers are used. The basic criteria for selecting the emitting material are very narrow emission and high internal quantum yield.<sup>197</sup> Initially the flexible LEDs were made of organic materials. Both the polymers and small molecules were used in the device as emitting layer. Generally organic rare earth metal complexes show very narrow emission as well

as high quantum yield. Several such complexes like anthracene crystals, 1,10-phenanthroline chelates, europium complexes (Eu(III)tris( $\beta$ -diketonates)), Iridium complexes (bis[2,3-diphenyl-4-methyl-quinolinato-C2,N] iridium(III) acetylacetonate) etc. complexes were used in OLEDs.<sup>197,198</sup> Europium and iridium complexes among these showed very promising results for OLED applications but their main problem is availability and cost. Also their fabrication technique involves complex methods like vapour deposition. Later in order to overcome the processability issue these organic complexes were doped in the polymeric materials such as polymethylmetacrylate (PMMA), polyvinylalcohol (PVA), polycarbonates, polyvinyl carbazole (PVK), polystyrene etc. which enabled these complexes to be deposited by solution processing method. A strategy of blending the electron and hole transport material together as emissive layer was also attempted but it suffered from low device life.

Apart from the organic materials nano materials are also relevant for flexible device architectures. Recently colloidal quantum dots (CQDs) are gaining importance in the flexible LED application as emissive layer due to their high quantum yield and nano morphologies. The CQDs possess unique size dependent optical properties along with the advantage of solution processing.<sup>65</sup> With decrease in the size of the CQDs the photoluminescence (PL) of the material gets blue shifted as the band gap of material increases. As we have discussed earlier for LED applications the emitter should possess very narrow emission in other words the emitted colour should be pure. The CQDs can offer very pure colour along with high quantum yield. Several approaches have been done on the fabrication of CQD based LEDs till date.<sup>199-203</sup> Among them the core-shell based quantum dots proved to be highly efficient for this application. In core-shell quantum dots the core possess lower band gap than the shell. This enables the trapping of the excited electron and hole pair, denoted as excitons. Hence the rate of recombination of the excitons is increased in comparison to the regular CQDs.<sup>65</sup> In LED application also the injected electron and hole pair can easily go into the core and get recombined radiatively but cannot come out due to this energy barrier. Recent report shows application of CdSe-ZnS core-shell quantum dots for fabrication of highly efficient flexible LEDs.<sup>204,205</sup>

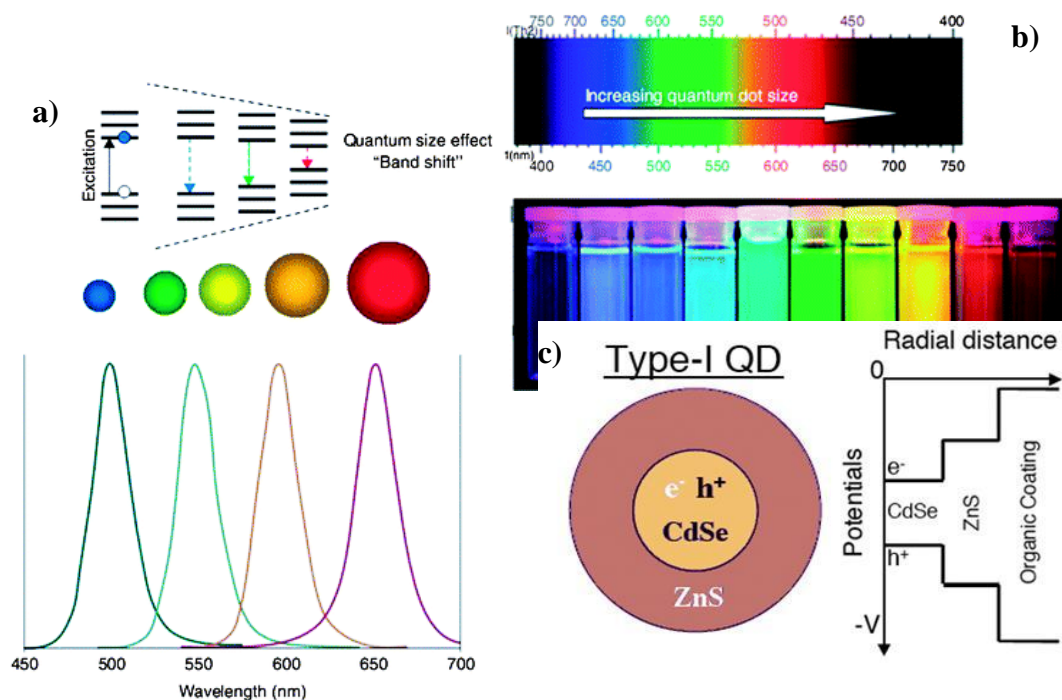


**Figure 1.20:** a) Electronic structure of CQDs correlated with its size and corresponding PL spectra, b) Size dependent colour (reprinted with the permission from Ref. 201) and c) CdSe-ZnS core-shell quantum dot and its band structure (Ref. <http://nanocluster.mit.edu/research.php>).

## II. Device Architecture:

The planer LEDs have basic device architecture where the emitting layer (EL) is sandwiched between hole transport layer (HTL) and electron transport layer (ETL) which are subsequently connected to +ve and -ve electrodes respectively. The HTL and ETL are selected according to the band alignment of the EL. The valance band (VB) of the HTL should be below the VB of EL while the conduction band (CB) of ETL should be above of the CB of EL at the energy level diagram for efficient charge transport. The electrodes are also selected accordingly. In every device one of the electrodes is transparent, mostly tin doped indiumoxide (ITO) or fluorine doped tin oxide (FTO) is used. The other electrode is selected depending upon the band alignment of the adjacent layer.<sup>65</sup>

In OLED all the layers, except for the electrodes, are organic. As HTL poly vinyl carbazole (PVK), Poly[(9,9-dioctylfluorenyl-2,7-diyl)-co-(4,4'-(N-(4-sec-butylphenyl)diphenylamine))] (TFB) etc. are used and as ETL, fullerenes like PC<sub>61</sub>BM, PC<sub>71</sub>BM, benzimidazole derivatives such as TPBi etc. and other small

molecules like bathocuproine (BCP) *etc.* are used. In these devices one additional layer was inserted as hole injection layer (HIL) to improve the hole insertion into the emissive layer. This layer generally has high conductivity. Predominantly poly(ethylenedioxythiophene):polystyrenesulfonate (PEDOT: PSS) is used as the layer. In QLEDs the HTLs are generally organic, same as OLEDs. But the ETLs are mostly inorganic semiconductor nano particle like ZnO. This is due to the fact that the charge transport property of ZnO nano particle is much higher than its organic analogue. QLEDs also possess the HIL. The overall thickness of these layers is quite less. Typically the EL thickness is around 20-30 nm. This is due to the fact that most of the ELs are semiconducting in nature, hence the transportation of the charges in the layers is very low. Hence for a thicker EL the electrons and holes have to travel more distance to recombine, which is highly unfavourable. This can cause trapping of charges which leads to the degradation of the EL.

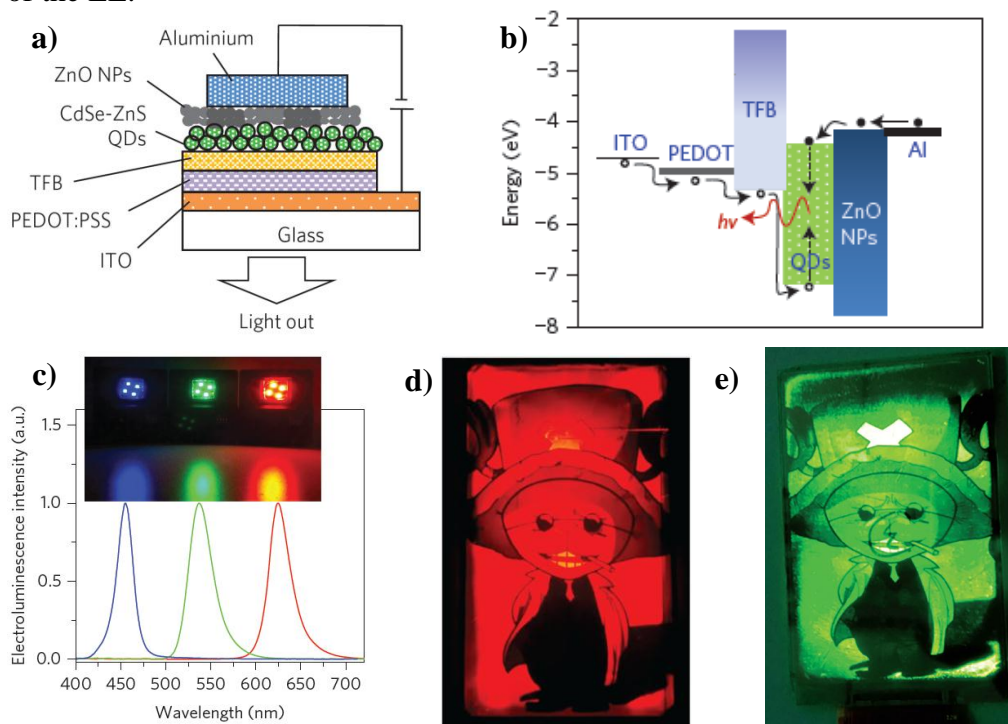


**Figure 1.21:** a) A typical device architecture of QLED, b) band alignment of the layers involved, c) QLED devices and corresponding electroluminescence, d) and e) QLED display prototype. (Reprinted with permission from ref. 202)

### 1.3 Outline of the thesis:

On the basis of the above discussion, the outline of the thesis is given below,

#### A. Chapter 1:

The first chapter represents the brief introduction about the advancement as well as the present state of electronic gadgets. Here the different key devices associated these devices are also discussed.

#### B. Chapter 2:

In the second chapter, synthetic procedures and device fabrication techniques are illustrated along with the discussion of the characterization techniques associated with the materials and the devices.

#### C. Chapter 3:

This chapter discusses the fabrication of few layer graphene based flexible interdigitated micro supercapacitor. The graphene here is synthesised from cobalt based metal organic framework using CO<sub>2</sub> laser pyrolysis and the interdigitated patterning is also created using laser writing of the carbon on flexible substrate.

#### D. Chapter 4:

This chapter illustrates the novel device fabrication technique for in-plane flexible micro supercapacitor using pre-synthesized materials. Here, the interdigitated electrodes are fabricated using laser scribing technique which is highly scalable method. Both EDLC (carbon based) and faradic (ternary metal oxide based) micro supercapacitor are fabricated using the method.

#### E. Chapter 5:

This chapter elaborates the device fabrication technique of the flexible OFET device using organic channel and dielectric material. Devices with different dielectric material thickness are optimized in this work. Finally a working inverter is demonstrated using the OFET devices.

**F. Chapter 6:**

This chapter demonstrates the optimization of the synthesis of CdSe-ZnS core-shell colloidal quantum dots (CQD) using hot injection method. Towards the end of this chapter the use of these CQDs to fabricate QLED device both in hard and flexible substrate is also illustrated.

**G. Chapter 7:**

This is the last chapter of the thesis where the key results of this thesis are highlighted and also describes in brief. The chapter ends with the discussion on the future scope and prospects of this work.

#### 1.4 References:

1. History of the transistor. *Wikipedia* [https://en.wikipedia.org/wiki/History\\_of\\_the\\_transistor#cite\\_note-9](https://en.wikipedia.org/wiki/History_of_the_transistor#cite_note-9) (2016).
2. Pugh, E. W., Johnson, L. R. & Palmer, J. H. *IBM's 360 and early 370 systems*. (MIT Press, 1991).
3. Bashe, C. J. *IBM's Early Computers*. (MIT, 1986).
4. Mollick, E. Establishing Moore's law. *IEEE Ann. Hist. Comput.* **28**, 62–75 (2006).
5. Lundstrom, M. Moore's Law Forever? *Science* (80-. ). **773**, 210–211 (2003).
6. Evans, D. Moore's Law: how long will it last? <http://www.techradar.com> (2014).
7. Gilleo, K. The Circuit Centennial.
8. A Brief History of Flexible Circuits, from saving space to Electronics Tattoos - EKG Machines Blog Articles.
9. Cleddo, B. & Curtis, R. W. Printed Circuit Techniques. *Natl. Bur. Stand.* (1947).
10. Transistor. *Wikipedia* <https://en.wikipedia.org/wiki/Transistor> (2016).
11. Fortunato, E., Barquinha, P. & Martins, R. Oxide Semiconductor Thin-Film Transistors: A Review of Recent Advances. *Adv. Mater.* **24**, 2945–2986 (2012).
12. Edgar, L. J. Method and apparatus for controlling electric currents. (1930).
13. Bipolar Junction Transistors. *wikipedia* [https://en.wikipedia.org/wiki/Bipolar\\_junction\\_transistor](https://en.wikipedia.org/wiki/Bipolar_junction_transistor) (2016).
14. 1948: Conception of the Junction Transistor | The Silicon Engine |

Computer History Museum.

15. Koezuka, H., Tsumura, A. & Ando, T. Field-effect transistor with polythiophene thin film. *Synth. Met.* **18**, 699–704 (1987).
16. Peng, X., Horowitz, G., Fichou, D. & Garnier, F. All-organic thin-film transistors made of alpha-sexithienyl semiconducting and various polymeric insulating layers. *Appl. Phys. Lett.* **57**, (1990).
17. Facchetti, A., Yoon, M.-H. & Marks, T. J. Gate Dielectrics for Organic Field-Effect Transistors: New Opportunities for Organic Electronics. *Adv. Mater.* **17**, 1705–1725 (2005).
18. Veres, J., Ogier, S., Lloyd, G. & de Leeuw, D. Gate Insulators in Organic Field-Effect Transistors. *Chem. Mater.* **16**, 4543–4555 (2004).
19. Ortiz, R. P., Facchetti, A. & Marks, T. J. High-k Organic, Inorganic, and Hybrid Dielectrics for Low-Voltage Organic Field-Effect Transistors. *Chem. Rev.* **110**, 205–239 (2010).
20. Flexible, full-color OLED display ~ Pink Tentacle.
21. Park, S., Vosguerichian, M. & Bao, Z. A review of fabrication and applications of carbon nanotube film-based flexible electronics. *Nanoscale* **5**, 1727 (2013).
22. Park, S. J. *et al.* Ultrasensitive Flexible Graphene Based Field-Effect Transistor (FET)-Type Bioelectronic Nose. *Nano Lett.* **12**, 5082–5090 (2012).
23. Kwon, O. S. *et al.* Flexible FET-Type VEGF Aptasensor Based on Nitrogen-Doped Graphene Converted from Conducting Polymer. *ACS Nano* **6**, 1486–1493 (2012).
24. Wong, W. S. & Salleo, A. *Flexible Electronics\_ Materials and Applications* - Google Books. (Springer, 2009). doi:10.1007/978-0-387-74363-9



25. Nam, S., Jiang, X., Xiong, Q., Ham, D. & Lieber, C. M. Vertically integrated, three-dimensional nanowire complementary metal-oxide-semiconductor circuits. *Proc. Natl. Acad. Sci.* **106**, 21035–21038 (2009).
26. Koh, W., Saudari, S. R., Fafarman, A. T., Kagan, C. R. & Murray, C. B. Thiocyanate-Capped PbS Nanocubes: Ambipolar Transport Enables Quantum Dot Based Circuits on a Flexible Substrate. *Nano Lett.* **11**, 4764–4767 (2011).
27. Hetsch, F., Zhao, N., Kershaw, S. V. & Rogach, A. L. Quantum dot field effect transistors. *Mater. Today* **16**, 312–325 (2013).
28. Optoelectronics - Wikipedia, the free encyclopedia. *Wikipedia* <https://en.wikipedia.org/wiki/Optoelectronics> (2015).
29. Photovoltaics. *Wikipedia* [https://en.wikipedia.org/wiki/Photovoltaics#cite\\_note-13](https://en.wikipedia.org/wiki/Photovoltaics#cite_note-13) (2016).
30. Williams, R. Becquerel Photovoltaic Effect in Binary Compounds. *J. Chem. Phys.* **32**, 1505 (1960).
31. Becquerel. *1911 Encyclopædia Britannica* [https://en.wikisource.org/wiki/1911\\_Encyclop%C3%A6dia\\_Britannica/Becquerel](https://en.wikisource.org/wiki/1911_Encyclop%C3%A6dia_Britannica/Becquerel) (1911).
32. Solar Cell. *Wikipedia* [https://en.wikipedia.org/wiki/Solar\\_cell](https://en.wikipedia.org/wiki/Solar_cell) (2016).
33. Pagliaro, M., Ciriminna, R. & Palmisano, G. Flexible Solar Cells. *ChemSusChem* **1**, 880–891 (2008).
34. Krebs, F. C. Fabrication and processing of polymer solar cells: A review of printing and coating techniques. *Sol. Energy Mater. Sol. Cells* **93**, 394–412 (2009).
35. Kamat, P. V. Quantum Dot Solar Cells. Semiconductor Nanocrystals as Light Harvesters. *J. Phys. Chem. C* **112**, 18737–18753 (2008).
36. Kamat, P. V. Quantum Dot Solar Cells. ‘The Next Big Thing’ in

- Photovoltaics. *J. Phys. Chem. Lett.* **4**, 908–918 (2013).
37. Robel, I., Subramanian, V., Kuno, M. & Kamat, P. V. Quantum Dot Solar Cells. Harvesting Light Energy with CdSe Nanocrystals Molecularly Linked to Mesoscopic TiO<sub>2</sub> Films. *J. Am. Chem. Soc.* **128**, 2385–2393 (2006).
  38. Perkowitz, S. photoconductivity | physics | Britannica.com. *Encyclopædia Britannica* 1 (2009).
  39. Zhai, T.; Fang, X.; Liao, M.; Xu, X.; Zeng, H.; Yoshio, B.; Golberg, D. A Comprehensive Review of One-Dimensional Metal-Oxide Nanostructure Photodetectors. *Sensors* **9**, 6504–6529 (2009).
  40. Zhou, H.; Fang, G.; Liu, N.; Zhao, X.; Huang, M.; Mao, S.; Feick, H.; Yan, H.; Wu, Y.; Kind, H. Ultraviolet photodetectors based on ZnO nanorods—seed layer effect and metal oxide modifying layer effect. *Nanoscale Res. Lett.* **6**, 147 (2011).
  41. J. D. Prades, R. Jimenez-Diaz, F. Hernandez-Ramirez, L. Fernandez-Romero, T. Andreu, A. Cirera, A. Romano-Rodriguez, A. Cornet, J. R. Morante, S. Barth, and S. Mathur, Toward a Systematic Understanding of Photodetectors Based on Individual Metal Oxide Nanowires. *J. Phys. Chem. C* **112**, 14639–14644 (2008).
  42. H. Sirringhaus, N. Tessler, and R. H. Friend, Integrated optoelectronic devices based on conjugated polymers. *Science* **280**, 1741–4 (1998).
  43. Y. Yan, L.-B. Huang, Y. Zhou, S.-T. Han, L. Zhou, J. Zhuang, Z.-X. Xu, and V. A. L. Roy, Self-aligned, full solution process polymer field-effect transistor on flexible substrates. *Sci. Rep.* **5**, 15770 (2015).
  44. Ma, H., Jen, A. K.-Y. & Dalton, L. R. Polymer-Based Optical Waveguides: Materials, Processing, and Devices. *Adv. Mater.* **14**, 1339–1365 (2002).
  45. Narayan, K. S., Kabra, D. & Dutta, S. Polymer Based Photodetectors. *MRS Proc.* **814**, I13.5 (2004).

46. Narayan, K. S. & Kumar, N. Light responsive polymer field-effect transistor. *Appl. Phys. Lett.* **79**, 1891 (2001).
47. M. H. Sayyad, Z. Ahmad, K. S. Karimov, M. Yaseen, and M. Ali, Photo-organic field effect transistor based on a metalloporphyrin. *J. Phys. D. Appl. Phys.* **42**, 105112 (2009).
48. Martyniuk, P. & Rogalski, A. Quantum-dot infrared photodetectors: Status and outlook. *Prog. Quantum Electron.* **32**, 89–120 (2008).
49. G. Konstantatos, I. Howard, A. Fischer, S. Hoogland, J. Clifford, E. Klem, L. Levina, and E. H. Sargent, Ultrasensitive solution-cast quantum dot photodetectors. *Nature* **442**, 180–183 (2006).
50. K. Qiao, H. Deng, X. Yang, D. Dong, M. Li, L. Hu, H. Liu, H. Song, and J. Tang, Spectra-selective PbS quantum dot infrared photodetectors. *Nanoscale* **8**, 7137–7143 (2016).
51. Ghosh, S., Hoogland, S., Sukhovatkin, V., Levina, L. & Sargent, E. H. A tunable colloidal quantum dot photo field-effect transistor. *Appl. Phys. Lett.* **99**, 101102 (2011).
52. G. Konstantatos, M. Badioli, L. Gaudreau, J. Osmond, M. Bernechea, F. P. G. de Arquer, F. Gatti, and F. H. L. Koppens, Hybrid graphene–quantum dot phototransistors with ultrahigh gain. *Nat. Nanotechnol.* **7**, 363–368 (2012).
53. Stimulated emission. *Wikipedia* [https://en.wikipedia.org/wiki/Stimulated\\_emission](https://en.wikipedia.org/wiki/Stimulated_emission) (2016).
54. Einstein, A. Zur Quantentheorie der Strahlung. *Phys. Zeitschrift, Band 18, Seite 121-128.* **18**, (1917).
55. Einstein, A. Strahlungs-Emission und -Absorption nach der Quantentheorie. *Dtsch. Phys. Gesellschaft, Verhandlungen 18, Seite 318-323.* **18**, (1916).

56. Milestones:First Working Laser, 1960 - Engineering and Technology History Wiki. (2010).
57. Bromberg, J. L. & Bromberg, J. L. *The Laser in America, 1950-1970*. (MIT Press, 1991).
58. Townes, C. H. & Townes, C. H. The First Laser. *A Century Nat. Twenty-One Discov. that Chang. Sci. World* 107–112 (2003).
59. Maiman Builds First Working Laser. *Phys. Hist. May 16, 1960* (2010).
60. Theodore H. Maiman at Hughes Research Laboratories. *Wikipedia* <https://en.wikipedia.org/wiki/Laser> (2016).
61. Carrier generation and recombination. *Wikipedia* [https://en.wikipedia.org/wiki/Carrier\\_generation\\_and\\_recombination](https://en.wikipedia.org/wiki/Carrier_generation_and_recombination) (2016).
62. Margolin, J. Road to the Transistor.
63. Zheludev, N. The life and times of the LED — a 100-year history. *Nat. Photonics* **1**, 189–192 (2007).
64. Geffroy, B., le Roy, P. & Prat, C. Organic light-emitting diode (OLED) technology: materials, devices and display technologies. *Polym. Int.* **55**, 572–582 (2006).
65. Shirasaki, Y., Supran, G. J., Bawendi, M. G. & Bulović, V. Emergence of colloidal quantum-dot light-emitting technologies. *Nat. Photonics* **7**, 933–933 (2013).
66. Samsung launches the world's first flexible OLED device, the curved Galaxy Round | OLED-Info. 2013
67. OLED history: A 'guided tour' of OLED highlights from invention to application | OLED-Info.
68. LG officially launches the G Flex, with a 6" 720p plastic curved OLED |

- OLED-Info. Available at: <http://www.oled-info.com/lg-officially-launches-g-flex-6-720p-plastic-curved-oled>.
69. Williams, H. S. A History of Science Volume II - Part VI. Available at: <http://www.worldwideschool.org/library/books/sci/history/AHistoryofScienceVolumeII/chap49.html>.
70. Capacitor. *Wikipedia* (2016). Available at: <https://en.wikipedia.org/wiki/Capacitor>.
71. Howard, B. Low voltage electrolytic capacitor US19540423042 19540414. (1957).
72. Ho, J., Jow, T. R. & Boggs, S. Historical introduction to capacitor technology. *IEEE Electr. Insul. Mag.* **26**, 20–25 (2010).
73. Jayalakshmi, M. & Balasubramanian, K. Simple Capacitors to Supercapacitors - An Overview. **3**, 1196–1217 (2008).
74. Supercapacitor. *Wikipedia* (2016). Available at: <https://en.wikipedia.org/wiki/Supercapacitor><https://en.wikipedia.org/wiki/Supercapacitor>.
75. Yang, P. & Mai, W. Flexible solid-state electrochemical supercapacitors. *Nano Energy* **8**, 274–290 (2014).
76. Wu, Z. S., Feng, X. & Cheng, H. M. Recent advances in graphene-based planar micro-supercapacitors for on-chip energy storage. *Natl. Sci. Rev.* **1**, 277–292 (2014).
77. Sung, J.-H., Kim, S.-J., Jeong, S.-H., Kim, E.-H. & Lee, K.-H. Flexible micro-supercapacitors. *J. Power Sources* **162**, 1467–1470 (2006).
78. Lokhande, C. D., Dubal, D. P. & Joo, O. S. Metal oxide thin film based supercapacitors. *Curr. Appl. Phys.* **11**, 255–270 (2011).
79. Beidaghi, M. & Gogotsi, Y. Capacitive energy storage in micro-scale devices: recent advances in design and fabrication of micro-

- supercapacitors. *Energy Environ. Sci.* **7**, 867–884 (2014).
80. H. M. Jeong, J. W. Lee, W. H. Shin, Y. J. Choi, H. J. Shin, J. K. Kang, and J. W. Choi, Nitrogen-doped graphene for high-performance ultracapacitors and the importance of nitrogen-doped sites at basal planes. *Nano Lett.* **11**, 2472–2477 (2011).
81. L. Yuan, X.-H. Lu, X. Xiao, T. Zhai, J. Dai, F. Zhang, B. Hu, X. Wang, L. Gong, J. Chen, C. Hu, Y. Tong, J. Zhou, and Z. L. Wang, Flexible Solid-State Supercapacitors Based on Carbon Nanoparticles/MnO<sub>2</sub> Nanorods Hybrid Structure. *ACS Nano* **6**, 656–661 (2012).
82. Kim, D., Shin, G., Kang, Y. J., Kim, W. & Ha, J. S. Fabrication of a Stretchable Solid-State Micro-Supercapacitor Array. *ACS Nano* **7**, 7975–7982 (2013).
83. Maeng, J., Kim, Y.-J., Meng, C. & Irazoqui, P. P. Three-Dimensional Microcavity Array Electrodes for High-Capacitance All-Solid-State Flexible Microsupercapacitors. *ACS Appl. Mater. Interfaces* **8**, 13458–13465 (2016).
84. Wei, L., Nitta, N., Yushin, G., Science, M. & States, U. Lithographically Patterned Thin Activated Carbon Films as a New Technology Platform for On-Chip. 6498–6506 (2013).
85. D. Pech, M. Brunet, H. Durou, P. Huang, V. Mochalin, Y. Gogotsi, P.-L. Taberna, and P. Simon, Ultrahigh-power micrometre-sized supercapacitors based on onion-like carbon. *Nat. Nanotechnol.* **5**, 651–654 (2010).
86. Z. Niu, L. Zhang, L. Liu, B. Zhu, H. Dong, and X. Chen, All-solid-state flexible ultrathin micro-supercapacitors based on graphene. *Adv. Mater.* **25**, 4035–4042 (2013).
87. Kim, S. K., Koo, H. J., Lee, A. & Braun, P. V. Selective wetting-induced micro-electrode patterning for flexible micro-supercapacitors. *Adv. Mater.* **26**, 5108–5112 (2014).

88. El-Kady, M. F. & Kaner, R. B. Scalable fabrication of high-power graphene micro-supercapacitors for flexible and on-chip energy storage. *Nat. Commun.* **4**, 1475 (2013).
89. Beidaghi, M. & Wang, C. Micro-Supercapacitors Based on Interdigital Electrodes of Reduced Graphene Oxide and Carbon Nanotube Composites with Ultrahigh Power Handling Performance. *Adv. Funct. Mater.* **22**, 4501–4510 (2012).
90. Yadav, P., Basu, A., Suryawanshi, A., Game, O. & Ogale, S. Highly Stable Laser-Scribed Flexible Planar Microsupercapacitor Using Mushroom Derived Carbon Electrodes. *Adv. Mater. Interfaces* **3**, (2016).
91. Cai, J., Lv, C. & Watanabe, A. Cost-effective fabrication of high-performance flexible all-solid-state carbon micro-supercapacitors by blue-violet laser direct writing and further surface treatment. *J. Mater. Chem. A* **4**, 1671–1679 (2016).
92. Cao, L. *et al.* Direct Laser-Patterned Micro-Supercapacitors from Paintable MoS<sub>2</sub> Films. *Small* **9**, 2905–2910 (2013).
93. El-Kady, M. F., Strong, V., Dubin, S. & Kaner, R. B. Laser Scribing of High-Performance and Flexible Graphene-Based Electrochemical Capacitors. *Science (80-. )*. **335**, 1326–1330 (2012).
94. Lin, J. *et al.* Laser-induced porous graphene films from commercial polymers. *Nat. Commun.* **5**, 1–8 (2014).
95. Gao, W. *et al.* Direct laser writing of micro-supercapacitors on hydrated graphite oxide films. *Nat Nano* **6**, 496–500 (2011).
96. Battery (electricity). *wikipedia* (2016). Available at: [https://en.wikipedia.org/wiki/Battery\\_\(electricity\)](https://en.wikipedia.org/wiki/Battery_(electricity)).
97. Alessandro Volta - Inventor of the Voltaic Pile.
98. Electric Battery History - Invention of the Electric Battery.

99. Scrosati, B. & Garche, J. Lithium batteries: Status, prospects and future. *J. Power Sources* **195**, 2419–2430 (2010).
100. Gwon, H. *et al.* Recent progress on flexible lithium rechargeable batteries. *Energy Environ. Sci.* **7**, 538 (2014).
101. Wang, X. *et al.* Flexible energy-storage devices: Design consideration and recent progress. *Advanced Materials* **26**, 4763–4782 (2014).
102. Zhou, G., Li, F. & Cheng, H.-M. Progress in flexible lithium batteries and future prospects. *Energy Environ. Sci.* **7**, 1307–1338 (2014).
103. Hu, L., Wu, H., La Mantia, F., Yang, Y. & Cui, Y. Thin, flexible secondary Li-ion paper batteries. *ACS Nano* **4**, 5843–5848 (2010).
104. Nishide, H. & Oyaizu, K. Materials science. Toward flexible batteries. *Science (80-. )*. **319**, 737–738 (2008).
105. Pikul, J. H., Gang Zhang, H., Cho, J., Braun, P. V. & King, W. P. High-power lithium ion microbatteries from interdigitated three-dimensional bicontinuous nanoporous electrodes. *Nat. Commun.* **4**, 1732 (2013).
106. Chmiola, J., Largeot, C., Taberna, P.-L. L., Simon, P. & Gogotsi, Y. Monolithic carbide-derived carbon films for micro-supercapacitors. *Science* **328**, 480–483 (2010).
107. Wu, Z., Parvez, K., Feng, X. & Müllen, K. Graphene-based in-plane micro-supercapacitors with high power and energy densities. *Nat. Commun.* **4**, 845–854 (2013).
108. Zhang, L. L. & Zhao, X. S. Carbon-based materials as supercapacitor electrodes. *Chem. Soc. Rev.* **38**, 2520–2531 (2009).
109. Zhu, Y. *et al.* Carbon-based supercapacitors produced by activation of graphene. *Science* **332**, 1537–41 (2011).
110. Bose, S. *et al.* Carbon-based nanostructured materials and their composites as supercapacitor electrodes. *J. Mater. Chem.* **22**, 767–784 (2012).



111. Wang, Y. *et al.* Supercapacitor Devices Based on Graphene Materials. *J. Phys. Chem. C* **113**, 13103–13107 (2009).
112. Zhi, M., Xiang, C., Li, J., Li, M. & Wu, N. Nanostructured carbon–metal oxide composite electrodes for supercapacitors: a review. *Nanoscale* **5**, 72–88 (2013).
113. Wang, G., Zhang, L. & Zhang, J. A review of electrode materials for electrochemical supercapacitors. *Chem. Soc. Rev.* **41**, 797–828 (2012).
114. Simon, P. & Gogotsi, Y. Materials for electrochemical capacitors. *Nat. Mater.* **7**, 845–854 (2008).
115. Bal Sydulu, S., Palaniappan, S. & Srinivas, P. Nano fibre polyaniline containing long chain and small molecule dopants and carbon composites for supercapacitor. *Electrochim. Acta* **95**, 251–259 (2013).
116. Arbizzani, C., Mastragostino, M. & Meneghello, L. Characterization by impedance spectroscopy of a polymer-based supercapacitor. *Electrochim. Acta* **40**, 2223–2228 (1995).
117. Snook, G. A., Kao, P. & Best, A. S. Conducting-polymer-based supercapacitor devices and electrodes. *Journal of Power Sources* **196**, 1–12 (2011).
118. Zhang, Y. *et al.* Progress of electrochemical capacitor electrode materials: A review. *Int. J. Hydrogen Energy* **34**, 4889–4899 (2009).
119. Yadav, P. *et al.* A 3D Hexaporous Carbon Assembled from Single-Layer Graphene as High Performance Supercapacitor. *ChemSusChem* **5**, 2159–2164 (2012).
120. Endo, M. *et al.* Capacitance and Pore-Size Distribution in Aqueous and Nonaqueous Electrolytes Using Various Activated Carbon Electrodes. *J. Electrochem. Soc.* **148**, A910 (2001).
121. Qu, D. & Shi, H. Studies of activated carbons used in double-layer

- capacitors. *J. Power Sources* **74**, 99–107 (1998).
122. Salitra, G., Soffer, A., Eliad, L., Cohen, Y. & Aurbach, D. Carbon Electrodes for Double-Layer Capacitors I. Relations Between Ion and Pore Dimensions. *J. Electrochem. Soc.* **147**, 2486 (2000).
  123. Raymundo-Piñero, E., Kierzek, K., Machnikowski, J. & Béguin, F. Relationship between the nanoporous texture of activated carbons and their capacitance properties in different electrolytes. *Carbon N. Y.* **44**, 2498–2507 (2006).
  124. Kierzek, K., Frackowiak, E., Lota, G., Gryglewicz, G. & Machnikowski, J. Electrochemical capacitors based on highly porous carbons prepared by KOH activation. *Electrochim. Acta* **49**, 515–523 (2004).
  125. Barbieri, O., Hahn, M., Herzog, A. & Kötz, R. Capacitance limits of high surface area activated carbons for double layer capacitors. *Carbon N. Y.* **43**, 1303–1310 (2005).
  126. Zhao, X., Johnston, C. & Grant, P. S. A novel hybrid supercapacitor with a carbon nanotube cathode and an iron oxide/carbon nanotube composite anode. *J. Mater. Chem.* **19**, 8755 (2009).
  127. Pan, H., Li, J. & Feng, Y. P. Carbon nanotubes for supercapacitor. *Nanoscale Research Letters* **5**, 654–668 (2010).
  128. Hu, S., Rajamani, R. & Yu, X. Flexible solid-state paper based carbon nanotube supercapacitor. *Appl. Phys. Lett.* **100**, (2012).
  129. Hahn, M. G. *et al.* Carbon nanotube-nanocup hybrid structures for high power supercapacitor applications. *Nano Lett.* **12**, 5616–5621 (2012).
  130. Du, C. & Pan, N. High power density supercapacitor electrodes of carbon nanotube films by electrophoretic deposition. *Nanotechnology* **17**, 5314–5318 (2006).
  131. Qin, C. L., Lu, X., Yin, G. P., Bai, X. D. & Jin, Z. Activated nitrogen-

- enriched carbon/carbon aerogel nanocomposites for supercapacitor applications. *Trans. Nonferrous Met. Soc. China (English Ed.)* **19**, (2009).
132. Lee, Y. J. *et al.* Preparation and characterization of metal-doped carbon aerogel for supercapacitor. *Curr. Appl. Phys.* **10**, 947–951 (2010).
133. An, H. *et al.* Polypyrrole/carbon aerogel composite materials for supercapacitor. *J. Power Sources* **195**, 6964–6969 (2010).
134. Wang, X. X. *et al.* Preparation and performances of carbon aerogel microspheres for the application of supercapacitor. *Journal of Solid State Electrochemistry* **15**, 643–648 (2011).
135. Kim, S. J., Hwang, S. W. & Hyun, S. H. Preparation of carbon aerogel electrodes for supercapacitor and their electrochemical characteristics. *J. Mater. Sci.* **40**, 725–731 (2005).
136. Xing, W. *et al.* Hierarchical porous carbons with high performance for supercapacitor electrodes. *Carbon N. Y.* **47**, 1715–1722 (2009).
137. Xia, Y., Yang, Z. & Mokaya, R. Templated nanoscale porous carbons. *Nanoscale* **2**, 639–659 (2010).
138. Lai, M. & Riley, D. J. Templated electrosynthesis of nanomaterials and porous structures. *J. Colloid Interface Sci.* **323**, 203–212 (2008).
139. Nelson, P. A. & Owen, J. R. A High-Performance Supercapacitor/Battery Hybrid Incorporating Templated Mesoporous Electrodes. *J. Electrochem. Soc.* **150**, A1313–A1317 (2003).
140. Fuertes, A. B., Lota, G., Centeno, T. A. & Frackowiak, E. Templated mesoporous carbons for supercapacitor application. *Electrochim. Acta* **50**, 2799–2805 (2005).
141. Zhang, L. L., Wei, T., Wang, W. & Zhao, X. S. Manganese oxide-carbon composite as supercapacitor electrode materials. *Microporous Mesoporous Mater.* **123**, 260–267 (2009).

142. Wang, Y. G., Cheng, L. & Xia, Y. Y. Electrochemical profile of nano-particle CoAl double hydroxide/active carbon supercapacitor using KOH electrolyte solution. *J. Power Sources* **153**, 191–196 (2006).
143. Sharma, R. K., Oh, H.-S., Shul, Y.-G. & Kim, H. Carbon-supported, nano-structured, manganese oxide composite electrode for electrochemical supercapacitor. *J. Power Sources* **173**, 1024–1028 (2007).
144. Burke, A. Ultracapacitors: why, how, and where is the technology. *J. Power Sources* **91**, 37–50 (2000).
145. Conway, B. E., Birss, V. & Wojtowicz, J. The role and utilization of pseudocapacitance for energy storage by supercapacitors. *J. Power Sources* **66**, 1–14 (1997).
146. Ferris, A., Garbarino, S., Guay, D. & Pech, D. 3D RuO<sub>2</sub> Microsupercapacitors with Remarkable Areal Energy. *Adv. Mater.* **27**, 6625–6629 (2015).
147. Sakiyama, K. *et al.* Deposition and Properties of Reactively Sputtered Ruthenium Dioxide Films. *J. Electrochem. Soc.* **140**, 834 (1993).
148. Jia, Q. X. *et al.* Epitaxial growth of highly conductive RuO<sub>2</sub> thin films on (100) Si. *Appl. Phys. Lett.* **68**, 1069 (1996).
149. Kim, I.-H. & Kim, K.-B. Electrochemical Characterization of Hydrous Ruthenium Oxide Thin-Film Electrodes for Electrochemical Capacitor Applications. *J. Electrochem. Soc.* **153**, A383 (2006).
150. Chang, J.-K., Lee, M.-T. & Tsai, W.-T. *In situ Mn K-edge X-ray absorption spectroscopic studies of anodically deposited manganese oxide with relevance to supercapacitor applications. Journal of Power Sources* **166**, (2007).
151. Toupin, M., Brousse, T. & Bélanger, D. Charge Storage Mechanism of MnO<sub>2</sub> Electrode Used in Aqueous Electrochemical Capacitor. *Chem. Mater.* **16**, 3184–3190 (2004).

152. Pang, S.-C., Anderson, M. A. & Chapman, T. W. Novel Electrode Materials for Thin-Film Ultracapacitors: Comparison of Electrochemical Properties of Sol-Gel-Derived and Electrodeposited Manganese Dioxide. *J. Electrochem. Soc.* **147**, 444 (2000).
153. Devaraj, S. & Munichandraiah, N. High Capacitance of Electrodeposited MnO<sub>2</sub> by the Effect of a Surface-Active Agent. *Electrochem. Solid-State Lett.* **8**, A373 (2005).
154. Yuan, C. *et al.* Ultrathin Mesoporous NiCo<sub>2</sub>O<sub>4</sub> Nanosheets Supported on Ni Foam as Advanced Electrodes for Supercapacitors. *Adv. Funct. Mater.* **22**, 4592–4597 (2012).
155. Zhang, G. Q., Wu, H. Bin, Hoster, H. E., Chan-Park, M. B. & Lou, X. W. (David). Single-crystalline NiCo<sub>2</sub>O<sub>4</sub> nanoneedle arrays grown on conductive substrates as binder-free electrodes for high-performance supercapacitors. *Energy Environ. Sci.* **5**, 9453 (2012).
156. Bao, L., Zang, J. & Li, X. Flexible Zn<sub>2</sub>SnO<sub>4</sub>/MnO<sub>2</sub> Core/Shell Nanocable–Carbon Microfiber Hybrid Composites for High-Performance Supercapacitor Electrodes. *Nano Lett.* **11**, 1215–1220 (2011).
157. Chen, D., Wang, Q., Wang, R. & Shen, G. Ternary oxide nanostructured materials for supercapacitors: a review. *J. Mater. Chem. A* **3**, 10158–10173 (2015).
158. Liu, X. *et al.* Hierarchical NiCo<sub>2</sub>O<sub>4</sub>@NiCo<sub>2</sub>O<sub>4</sub> Core/Shell Nanoflake Arrays as High-Performance Supercapacitor Materials. *ACS Appl. Mater. Interfaces* **5**, 8790–8795 (2013).
159. Fan, L.-Z. & Maier, J. High-performance polypyrrole electrode materials for redox supercapacitors. *Electrochemistry Communications* **8**, (2006).
160. Gupta, V. & Miura, N. High performance electrochemical supercapacitor from electrochemically synthesized nanostructured polyaniline. *Materials Letters* **60**, (2006).

161. Zhou, Y. *et al.* Electrochemical capacitance of well-coated single-walled carbon nanotube with polyaniline composites. *Electrochim. Acta* **49**, 257–262 (2004).
162. Kalaji, M., Murphy, P. J. & Williams, G. O. The study of conducting polymers for use as redox supercapacitors. *Synth. Met.* **102**, 1360–1361 (1999).
163. Sharma, P. & Bhatti, T. S. A review on electrochemical double-layer capacitors. *Energy Convers. Manag.* **51**, 2901–2912 (2010).
164. Ryu, K. S., Kim, K. M., Park, N.-G., Park, Y. J. & Chang, S. H. *Symmetric redox supercapacitor with conducting polyaniline electrodes. Journal of Power Sources* **103**, (2002).
165. Laforgue, A., Simon, P., Sarrazin, C. & Fauvarque, J.-F. Polythiophene-based supercapacitors. *J. Power Sources* **80**, 142–148 (1999).
166. Gawli, Y. *et al.* 3D Polyaniline Architecture by Concurrent Inorganic and Organic Acid Doping for Superior and Robust High Rate Supercapacitor Performance. *Sci. Rep.* **6**, 21002 (2016).
167. Zhang, H. *et al.* *Tube-covering-tube nanostructured polyaniline/carbon nanotube array composite electrode with high capacitance and superior rate performance as well as good cycling stability. Electrochemistry Communications* **10**, (2008).
168. Wang, S., Hsia, B., Carraro, C. & Maboudian, R. High-performance all solid-state micro-supercapacitor based on patterned photoresist-derived porous carbon electrodes and an ionogel electrolyte. *J. Mater. Chem. A* **2**, 7997–8002 (2014).
169. Sung, J.-H., Kim, S.-J. & Lee, K.-H. Fabrication of all-solid-state electrochemical microcapacitors. *J. Power Sources* **133**, 312–319 (2004).
170. Sung, J.-H., Kim, S.-J. & Lee, K.-H. Fabrication of microcapacitors using conducting polymer microelectrodes. *J. Power Sources* **124**, 343–350

- (2003).
171. Ersoy, D. A., McNallan, M. J. & Gogotsi, Y. Carbon coatings produced by high temperature chlorination of silicon carbide ceramics. *Mater. Res. Innov.* **5**, 55–62 (2001).
  172. Beidaghi, M., Chen, W. & Wang, C. Electrochemically activated carbon micro-electrode arrays for electrochemical micro-capacitors. *J. Power Sources* **196**, 2403–2409 (2011).
  173. Wei Chen *et al.* Integration of Carbon Nanotubes to C-MEMS for On-chip Supercapacitors. *IEEE Trans. Nanotechnol.* **9**, 734–740 (2010).
  174. Hsia, B., Kim, M. S., Vincent, M., Carraro, C. & Maboudian, R. Photoresist-derived porous carbon for on-chip micro-supercapacitors. *Carbon N. Y.* **57**, 395–400 (2013).
  175. Wang, X. *et al.* Manganese oxide micro-supercapacitors with ultra-high areal capacitance. *Nanoscale* **5**, 4119 (2013).
  176. C.-C. Liu, D.-S. Tsai, W.-H. Chung, K.-W. Li, K.-Y. Lee, and Y.-S. Huang, Electrochemical micro-capacitors of patterned electrodes loaded with manganese oxide and carbon nanotubes. *J. Power Sources* **196**, 5761–5768 (2011).
  177. L. Li, J. Zhang, Z. Peng, Y. Li, C. Gao, Y. Ji, R. Ye, N. D. Kim, Q. Zhong, Y. Yang, H. Fei, G. Ruan, and J. M. Tour, High-Performance Pseudocapacitive Microsupercapacitors from Laser-Induced Graphene. *Adv. Mater.* **28**, 838–845 (2016).
  178. Tsumura, A., Koezuka, H. & Ando, T. Macromolecular electronic device: Field-effect transistor with a polythiophene thin film. *Appl. Phys. Lett.* **49**, 1210 (1986).
  179. P. Yadav, C. Chanmal, A. Basu, L. Mandal, J. Jog, and S. Ogale, Catalyst free novel synthesis of graphene and its application in high current OFET and phototransistor based on P3HT/G composite. *RSC Adv.* **3**, (2013).

180. C. Jiang, X. Cheng, X. Wu, X. Yang, B. Yin, Y. Hua, J. Wei, and S. Yin, Effects of P3HT concentration on the performance of organic field effect transistors. *Optoelectron. Lett.* **7**, 30–32 (2011).
181. Liu, B., Xie, G., Du, X., Li, X. & Sun, P. Poly(3-hexylthiophene) based organic field-effect transistor as NO<sub>2</sub> gas sensor. in (eds. Liao, Y., Wang, A., Wang, T. & Ishii, Y.) 750813 (International Society for Optics and Photonics, 2009). doi:10.1117/12.837911
182. S. Tiwari, W. Takashima, S. K. Balasubramanian, S. Miyajima, S. Nagamatsu, S. S. Pandey, and R. Prakash, P3HT-fiber-based field-effect transistor: Effects of nanostructure and annealing temperature. *Jpn. J. Appl. Phys.* **53**, 21601 (2014).
183. Yamashita, Y. Organic semiconductors for organic field-effect transistors. *Sci. Technol. Adv. Mater.* **10**, 24313 (2009).
184. Reese, C., Roberts, M., Ling, M. & Bao, Z. Organic thin film transistors. *Mater. Today* **7**, 20–27 (2004).
185. Klauk, H. Organic thin-film transistors. *Chem. Soc. Rev.* **39**, 2643 (2010).
186. Horowitz, G. Organic Field-Effect Transistors. *Adv. Mater.* **10**, 365–377 (1998).
187. Klauk, H., Gundlach, D. J., Nichols, J. A. & Jackson, T. N. Pentacene organic thin-film transistors for circuit and display applications. *IEEE Trans. Electron Devices* **46**, 1258–1263 (1999).
188. Z. Rang, A. Haraldsson, D. M. Kim, P. P. Ruden, M. I. Nathan, R. J. Chesterfield, and C. D. Frisbie, Hydrostatic-pressure dependence of the photoconductivity of single-crystal pentacene and tetracene. *Appl. Phys. Lett.* **79**, 2731 (2001).
189. H. Klauk, M. Halik, U. Zschieschang, G. Schmid, W. Radlik, and W. Weber, High-mobility polymer gate dielectric pentacene thin film transistors. *J. Appl. Phys.* **92**, 5259 (2002).



190. H. E. Katz, A. J. Lovinger, J. Johnson, C. Kloc, T. Siegrist, W. Li, Y.-Y. Lin, and A. Dodabalapur, A soluble and air-stable organic semiconductor with high electron mobility. *Nature* **404**, 478–481 (2000).
191. Waldauf, C., Schilinsky, P., Perisutti, M., Hauch, J. & Brabec, C. J. Solution-Processed Organic n-Type Thin-Film Transistors. *Adv. Mater.* **15**, 2084–2088 (2003).
192. Sirringhaus, H. Device Physics of Solution-Processed Organic Field-Effect Transistors. *Adv. Mater.* **17**, 2411–2425 (2005).
193. Majewski, L. A., Schroeder, R. & Grell, M. One Volt Organic Transistor. *Adv. Mater.* **17**, 192–196 (2005).
194. Majewski, L. A., Grell, M., Ogier, S. D. & Veres, J. A novel gate insulator for flexible electronics. *Org. Electron.* **4**, 27–32 (2003).
195. Mandal, L. High performance photodetectors and field effect transistors based on low temperature solution processing routes. (2013).
196. Wikipedia. OLED. (2016). Available at: <https://en.wikipedia.org/wiki/OLED>.
197. Thejo Kalyani, N. & Dhoble, S. J. J. Organic light emitting diodes: Energy saving lighting technology - A review. *Renew. Sustain. Energy Rev.* **16**, 2696–2723 (2012).
198. Pope, M., Kallmann, H. P. & Magnante, P. Electroluminescence in Organic Crystals. *J. Chem. Phys.* **38**, 2042 (1963).
199. Stouwdam, J. W. & Janssen, R. A. J. Red, green, and blue quantum dot LEDs with solution processable ZnO nanocrystal electron injection layers. *J. Mater. Chem.* **18**, 1889 (2008).
200. A. H. Mueller, M. A. Petruska, M. Achermann, D. J. Werder, E. A. Akhador, D. D. Koleske, M. A. Hoffbauer, and V. I. Klimov, Multicolor Light-Emitting Diodes Based on Semiconductor Nanocrystals Encapsulated

- in GaN Charge Injection Layers. *Nano Lett.* **5**, 1039–1044 (2005).
201. Coe, S., Woo, W.-K., Bawendi, M. & Bulović, V. Electroluminescence from single monolayers of nanocrystals in molecular organic devices. *Nature* **420**, 800–803 (2002).
  202. Colvin, V. L., Schlamp, M. C. & Alivisatos, A. P. Light-emitting diodes made from cadmium selenide nanocrystals and a semiconducting polymer. *Nature* **370**, 354–357 (1994).
  203. Mirzaei, J., Reznikov, M. & Hegmann, T. Quantum dots as liquid crystal dopants. *J. Mater. Chem.* **22**, 22350 (2012).
  204. Y. Yang, Y. Zheng, W. Cao, A. Titov, J. Hyvonen, J. R. Manders, J. Xue, P. H. Holloway, and L. Qian, High-efficiency light-emitting devices based on quantum dots with tailored nanostructures. *Nat. Photonics* **9**, 259 (2015).
  205. Qian, L., Zheng, Y., Xue, J. & Holloway, P. H. Stable and efficient quantum-dot light-emitting diodes based on solution-processed multilayer structures. *Nat. Photonics* **5**, 543–548 (2011).

## Chapter 2

# Synthesis Methods, Characterization Techniques and Device Fabrication

This chapter presents a brief description of the hot injection method for quantum dot synthesis and Laser pyrolysis process as synthetic methods adopted in this thesis. This follows with the discussion of various experimental tools employed for the characterization of the structural, morphological, optical, electrical and electrochemical properties of the synthesized nanomaterials. The fabrication techniques of different devices are also described in-detail. All the device characterization techniques are also discussed.

## 2.1 Introduction:

This chapter gives the detailed description of the procedures adopted for the synthesis of the materials and the fabrication of devices used for this work. It also describes the characterization techniques used for elucidating the properties of both the materials and devices.

## 2.2 Synthesis of materials:

### 2.2.1 Hot injection method:

Hot injection method is a widely used technique for the synthesis of monodisperse colloidal quantum dots (QDs). QDs synthesis consists of 2 stages, nucleation and gradual growth, these steps are crucial for the size and shape control during synthesis. Hot injection method provides the full control in this regard. In 1993 Murray *et.al.* first described the synthesis of nearly monodisperse colloidal quantum dot using this approach. Since then predominantly this method has been used for the QD synthesis.<sup>1</sup>

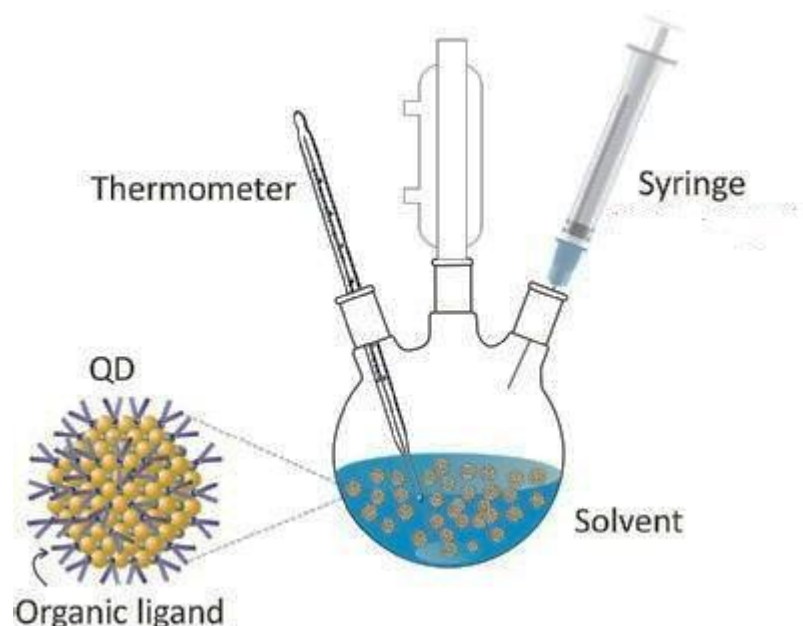


**Figure 2.1:** A schematic of a reaction set-up used in the synthesis of colloidal QDs using hot injection method and representation of organic ligand capped QDs. (ref. <https://www2.warwick.ac.uk/fac/sci/physics/current/postgraduate/regs/mpags/ex5/lds/qd/growth/colloidal/>)

In a typical hot injection method one precursor solution, which is in room temperature, is injected to another precursor solution, which is at elevated temperature (figure 2.1). After the injection, nucleation process starts, as the cold

precursor is added to the hot reaction mixture, overall drop in the reaction temperature occurs; due to this formation of the new nuclei is restricted.<sup>2</sup> When the temperature is further increased, the slow growth in the size of the QD nuclei happens but no new nuclei formation occurs. The nucleation process at higher temperature is very important since it helps to minimize the surface defects of the as formed QDs. After the desired growth, the reaction mixture is suddenly quenched to restrict the further growth. Simultaneously the surfaces of QDs are capped with organic ligands. The capping agents are chosen depending upon the surface charge state of the QDs formed. When the surface of the QDs is cation-rich, ligands with negative end-group (e.g. oleic acid) are used similarly for anion-rich surfaces positive end-group ligands (e.g. oleylamine) are used.

### **2.3 Device fabrication:**

#### **2.3.1 CO<sub>2</sub> Laser based micro patterning:**

CO<sub>2</sub> laser is one of the earliest gas based laser developed and most importantly still it has wide applications in several sectors, such as, medical surgery, industrial cutting and welding, fabrication of micro-fluidic devices using poly (methyl methacrylate) (PMMA) polymer etc. The active laser medium is an air-cooled gas discharge which consists of around 10–20% carbon dioxide (CO<sub>2</sub>), around 10–20% nitrogen (N<sub>2</sub>), a few amount of hydrogen (H<sub>2</sub>) and/or xenon (Xe) (usually used only in a sealed tube), and helium (He). The mechanism of the CO<sub>2</sub> laser generation is quite simple<sup>3</sup>; the N<sub>2</sub> molecules are excited into a metastable vibrational level by discharge process and further transfer their energy to CO<sub>2</sub> molecules by colliding with them. CO<sub>2</sub> molecules relaxes back to the ground state and emit laser energy. Helium (He) serves to depopulate the lower laser level as well as to remove the heat from the system and H<sub>2</sub> helps to convert carbon monoxide to CO<sub>2</sub>. CO<sub>2</sub> laser is basically an infra-red laser (wavelength 10.6 μm) with relatively low energy compared to the other high energy lasers (discussed in the chapter 1). CO<sub>2</sub> laser is a continuous laser with highest power available till date. The basic CO<sub>2</sub> laser system consists of a gas discharge (as mentioned above), a total reflector at one end, and an output coupler (basically a reflecting mirror) at the other (output) end. The mirrors are connected with a X-Y moving stage to move the laser beam. The stage of the laser system, where the substrates are placed, can be moved through the Z-axis to focus the laser beam properly at the substrate. The CO<sub>2</sub> laser systems can be constructed with power ranging from milliwatts (mW) to kilowatts (kW). The operation of a typical laser system is depicted below.

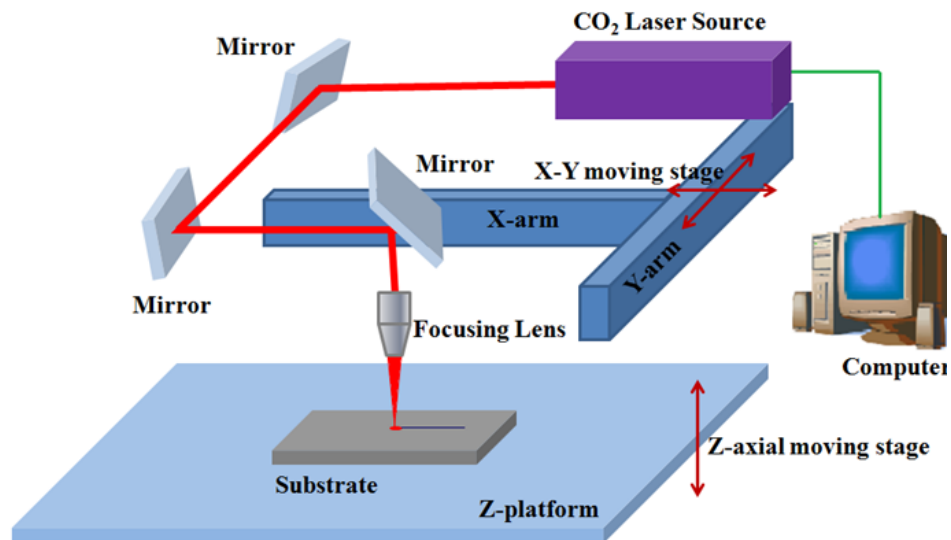


**Figure 2.2:** Construction of a CO<sub>2</sub> laser system (ref. <https://www.linkedin.com/pulse/application-co2-laser-printed-circuit-board-pcb-apple-he>)

In our work we have used the CO<sub>2</sub> laser for the fabrication of micro supercapacitor device in two different methods.

### I. Laser writing:

The CO<sub>2</sub> laser can be used for the pyrolysis of organic molecules. There are few reports in the pyrolysis of aromatic organic molecules into carbon.<sup>4-8</sup> This laser pyrolysis is highly structure specific. Hence not all aromatic compounds can be pyrolysed by this method. Specific mechanism is yet to confirm. The process is believed to occur through high local heating process. On absorption of the laser, causes lattice vibration at the molecules which produces huge local heating (>2500 °C).<sup>4</sup> This heating causes the breaking of the softer bonds like C-O, C=O, C-N etc. present in the organic molecules and results in the formation of gases. The residual aromatic compounds rearrange to form 2D graphitic carbon. The gases liberated during this process cover this irradiating area from the atmosphere to minimize the oxidation of as formed carbon. This method is applied to make carbon electrodes. As the carbonization occurs at the specific area where laser is irradiated, very thin grids (micro-scaled) of carbon can be drawn on the substrates. Hence this is a very useful technique for micro supercapacitor application. Graphene oxides (GO) can also be reduced by CO<sub>2</sub> laser to make electrodes for micro supercapacitors.<sup>6,7</sup>

### I. Laser scribing:

The CO<sub>2</sub> laser can also be used to ablate materials as it forms very high local temperature on irradiation. Using this property, for supercapacitor application micro patterned electrodes can be formed on a substrate where the supercapacitive

material is coated. The laser is applied at the specific area to form interdigitated electrodes by removing the material.

### 2.3.2 Spin Coating

Spin coating is a useful technique for the deposition of thin films of various materials such as polymers, metal oxide suspensions, proteins etc. on to the smooth and flat surface.<sup>9</sup>

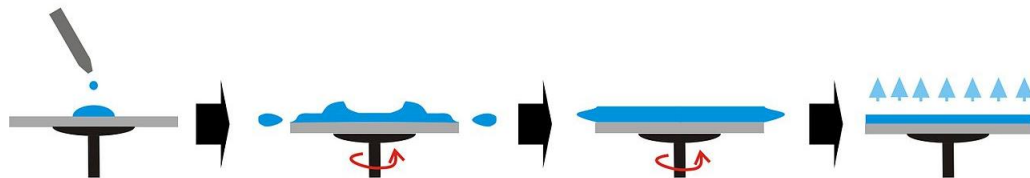


*Figure 2.3: The spin coating process. (ref. <http://www.spincoater.com/what-is-spin-coating.php>)*

In this process a homogenous solution is drop-casted onto the clean substrate which is then rotated at fixed rotations for a given time. Here ‘RPM’ is the abbreviation of the number of rotations in one minute. The RPM can be adjusted depending on the desired film thickness. Due to centrifugal force created during spin coating, the drop casted solution spreads in the outward direction. The excess solution spills out and simultaneously the solvent evaporates which in turn increase the viscosity of material on the substrate. Hence the adhesion of the material with the substrate is improved and a uniform film is formed. Although the uniformity of the film mainly depends on the solution properties such as viscosity, surface tension, solvent evaporation rate etc. The film thickness can also be varied by varying these properties. Multilayered structures can be formed using this technique.

### 2.3.3 Thermal Evaporation

Thermal evaporation is the very simple form of the physical vapour deposition (PVD) technique. Using this technique mainly thin films of metals and some organic molecules are deposited.<sup>10</sup> The metals are chosen with low melting point as compared to tungsten or molybdenum as heating filaments are made of these two elements. The deposition performed inside the vacuum chamber in order to have maximum mean free path for the evaporated to reach the surface and also to avoid any kind of reaction with the constituents from the atmosphere during the film growth. Schematic of a typical thermal evaporation chamber is shown in Fig 2.4.

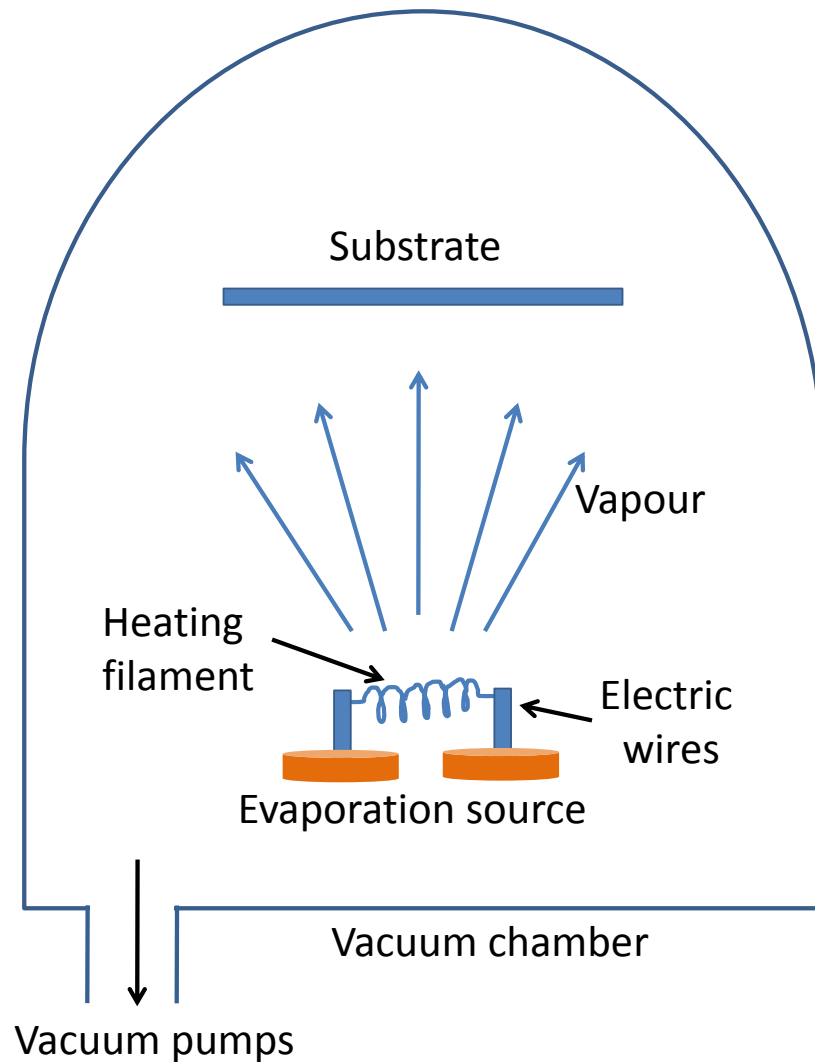


*Figure 2.4: Schematic of the thermal evaporation chamber*

Generally, tungsten is used as boats and filament, while molybdenum is mostly used as a boat. These filaments as well as the boats have an optimum thickness to have a higher resistance. When a huge amount of current is passed through these filaments, ( $\sim 100 - 190$  A) heating occurs across them which results the melting and subsequently evaporating the low temperature metals to be deposited. The vapor of the metals travels upwards and spreads in the entire chamber. Substrates are placed over the filament at an optimum distance on a substrate holder. Keeping them closer to the filament can cause heating up the substrates as well which can damage the soft substrates (thin organic films *etc.*).

#### **2.3.4 Fabrication of OFET Device:**

All the non-flexible and flexible devices were fabricated on the corning glass and PET substrate respectively. The identical device fabrication procedure was followed in both cases. Initially, the base substrates were cleaned by sonicating in soap water and iso-propyl alcohol. Then the substrates were dried under nitrogen flow. Then these were treated with plasma cleaner for better surface adhesion. At



beginning of the device fabrication process, the aluminium gate electrode was deposited through PVD method (thermal evaporation) onto the base substrate. The typical thickness of the electrode was 100 nm. The dielectric layer was then deposited by spin coating of the PVA solutions. For thicker dielectric layer (500 nm) 10 wt.% aqueous PVA solution was taken. While for thinner dielectric layer (300nm) 5 wt.% PVA solution was used. In all the cases the spin rate was set at 2500 rpm and the spinning time was 1 min. The dielectric layer was annealed at 80 °C in vacuum oven for 1 hr. It was then cooled to room temperature before taking out from the vacuum oven. The pentacene (Sigma-Aldrich) channel layer was then deposited at the top of the PVA layer by PVD (thermal evaporation) method at  $10^{-6}$  mbar chamber pressure. The typical thickness of this layer was optimized at 50 nm. Finally 100 nm gold source-drain electrodes were also fabricated by PVD through interdigitated physical mask at the same chamber pressure mentioned above. The channel length (L) and width (W) of the devices was 100  $\mu\text{m}$  and 1000  $\mu\text{m}$  respectively. For inverter the devices were fabricated as stated above. Finally the connections between two or more devices were done using silver paste.

### 2.3.5 Fabrication of QD-LED device fabrication:

The QD-LED devices were fabricated both on the hard substrate (ITO-Glass) and flexible substrate (ITO-PET). In a typical device PEDOT:PSS (~ 50 nm) (Clevios PH-1000, Heraeus) was spin coated at a spin rate of 1500 r.p.m for 60 sec. It was then annealed at 150 °C for 10 min. Then the substrates are coated with PVK or TFB (Sigma-Aldrich). In case of both the layers 8 mg/mL solution in chlorobenzene (CB) was used for spin coating. Two different spin rates of 3000 rpm and 4000 rpm were used for the fabrication. The spin time was fixed at 30 sec. The substrates were baked at 150 °C for 30 min. On top of the HTL QDs were spin coated. Three types of QDs, green, yellow and red-orange QDs emitting, were used for the fabrication of green, yellow and red-orange LEDs. The concentrations of QD solutions in CB were 18 mg ml<sup>-1</sup>, 17 mg ml<sup>-1</sup> and 15 mg ml<sup>-1</sup> respectively. The spin rates were varied for optimization. ZnO nanoparticle (synthesized using synthesis procedure reported in ref. 16) layer (30 mg ml<sup>-1</sup> ZnO solution in ethanol, 3,000 r.p.m. spin speed) was deposited by spin coating. The average thickness of the layer was ~65 nm. The ~100 nm aluminium (Al) top electrode was deposited by vacuum evaporation technique.

## 2.4 Characterization of materials and devices:

### 2.4.1 X-ray Diffraction (XRD):

X-ray diffraction is one of the most essential techniques for the determination of the crystal structure. This is a non-destructive characterization techniques.<sup>11</sup> From this technique precise information about the orientation of the crystal planes and

average crystallite size of various materials can be obtained. This technique is applicable for both the powder as well as thin film materials.<sup>12</sup> The analysis of the XRD is done using Bragg's diffraction law. This law defines the scattering of monochromatic x-rays from a crystalline solid (Fig 2.5).<sup>13,14</sup> The constructive or destructive interference of these scattered x-rays produce a particular intensity profile called as diffraction pattern. If the phases of two adjacent X-ray beams are same after scattering, i.e. their path difference is the integral multiple of  $n\lambda$ , where  $\lambda$  is the incident x-ray wavelength. These scattered x-ray beams undergo constructive interference or destructive interference. The path difference between the two adjacent x-ray beams can be given as  $2d\sin\theta$  where 'd' is the inter-planar distance for a particular set of planes within the crystal and ' $\theta$ ' represents the angle of scattering of x-rays. Hence, the condition for constructive interference can be expressed as,

$$2d\sin\theta = n\lambda$$

This is the expression for Bragg's law.

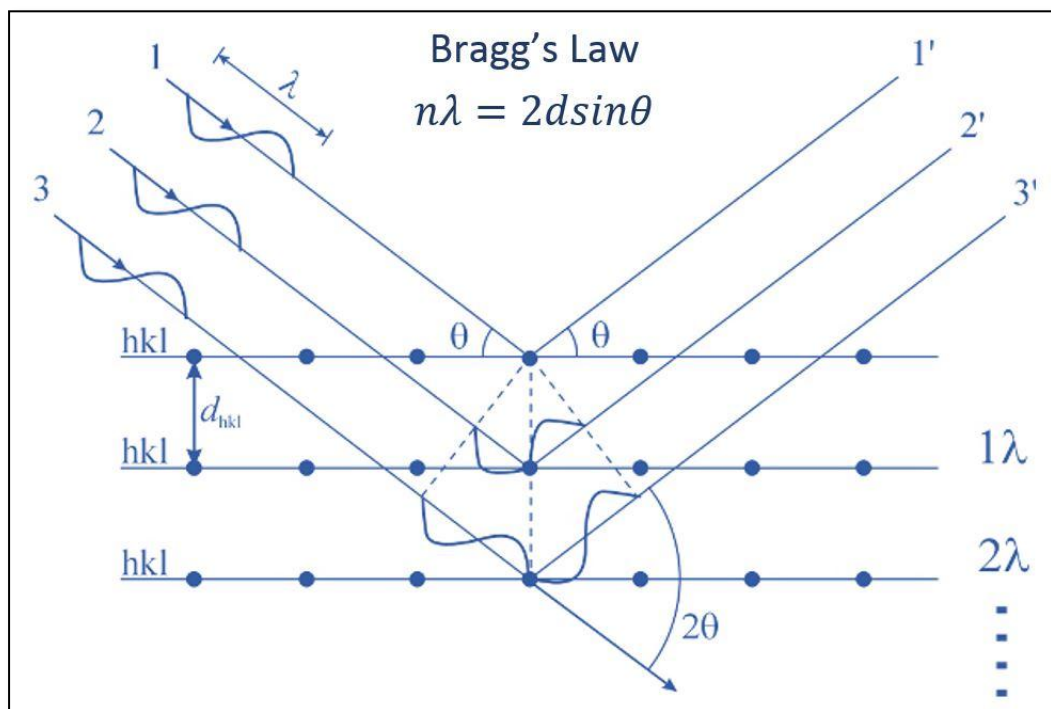


**Figure 2.5:** The working principle of X-ray diffraction.

The scattering of the x-rays depends upon the orientation of a particular plane (h,k,l). In the XRD measurement, the change in X-ray intensity is plotted as a function of  $2\theta$  this is termed as XRD pattern. The crystallite size of the material depends upon the width of the peaks. As the crystallite size increases the peak width decreases. By measuring the peak width at half maxima, a rough estimate of the crystallite size can be obtained using Sherrer Equation given as,

$$t = 0.9\lambda / \beta \cos \theta$$

where,  $t$  represents the crystallite diameter,  $\lambda$  is the incident x-ray wavelength and  $\beta$  denotes the full width at half maxima (FWHM) measured at  $2\theta$ .

## 2.4.2 Raman Spectroscopy

Raman spectroscopy technique is used to observe the low frequency modes, such as vibrational mode, rotational mode etc. in the system. The observation is done on the basis of the inelastic scattering of monochromatic light from a laser ranging from near ultraviolet to near infrared region. The energy of the laser light beam is shifted due to the interaction of the same with the molecular vibrations, phonons or other excitations in the system. This shift in energy gives information about the vibrational modes in the system. Figure 2.6 shows the collection of the Raman spectrum.

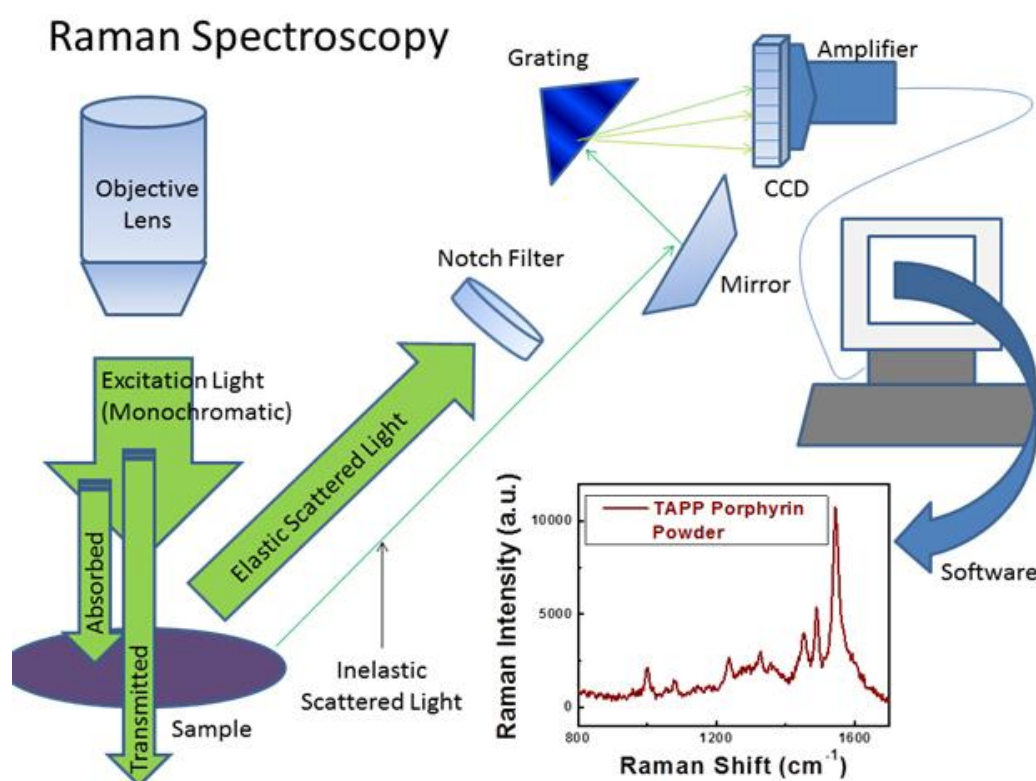


**Figure 2.6:** Schematic showing the process involved in collecting Raman Spectra. (Ref. [https://www3.nd.edu/~kamatlab/facilities\\_spectroscopy.html](https://www3.nd.edu/~kamatlab/facilities_spectroscopy.html))

The Raman Effect occurs when an electromagnetic radiation incidents on molecule and it interacts with the electron density and the bonds of the molecules. This interaction results in in-elastic scattering of the photons. The scattered photons can be of lower (Stokes) or higher (anti-Stokes) energy than the incoming photons (figure 2.7).

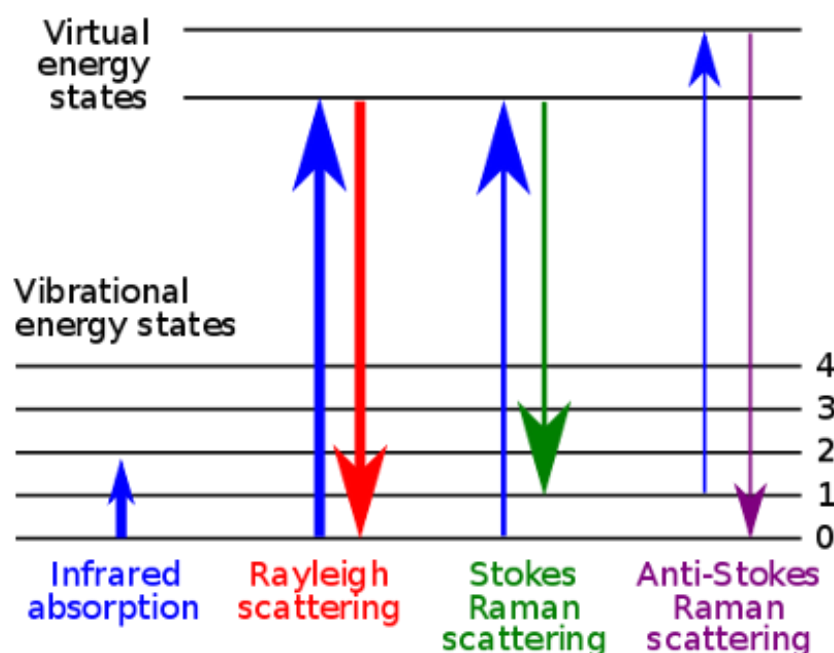


**Figure 2.7:** Energy-level diagram showing the states involved in the Raman signal. (Ref. [https://en.wikipedia.org/wiki/Raman\\_spectroscopy](https://en.wikipedia.org/wiki/Raman_spectroscopy))

The states of a molecule in Raman scattering are different than the rotational and vibrational states of an incoming photon. The energy difference between resulting rovibronic state and original rovibronic state causes the shift in the frequency of emitted photon from the excitation wavelength. This is called as Rayleigh line. For a molecule to show Raman effect, the system should possess a change in the molecular dipole-electric polarizability with respect to vibrational coordinate corresponding to the rovibronic state.

The Raman shift is given by

$$\nabla w (cm^{-1}) = \left( \frac{1}{\lambda_0} - \frac{1}{\lambda_1} \right)$$

Where,  $\nabla w$  represents the Raman shift in wavenumber,  $\lambda_0$  and  $\lambda_1$  denotes the excitation wavelength and the Raman spectrum wavelength respectively.

### 2.4.3 BET surface area analysis

For the analysis of specific surface area of a material, Brunauer-Emmett-Teller (BET) is a very useful technique. The basic principle of this technique is based on physical adsorption of a gas molecule on the solid surface.<sup>15,16</sup> This physical adsorption occurs due to the weak Van der Waals forces between gas molecule (adsorbate) and surface area (adsorbent) of the sample. The measurement is usually carried out at very low temperature using liquid nitrogen. Figure 2.8 shows the basic components of a typical BET instrument.

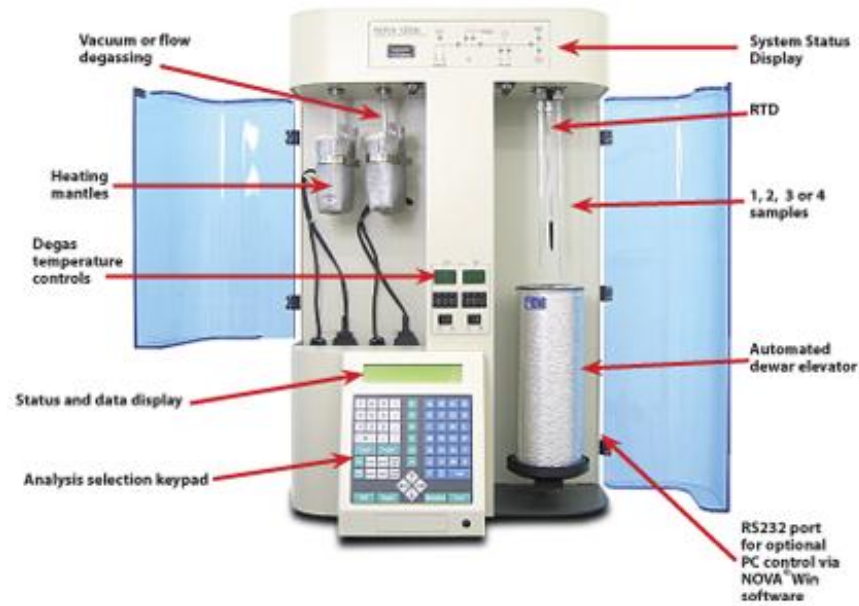


**Figure 2.8:** BET Instrument. (Ref. [http://www.quantachrome.com/gassorption/nova\\_series.html](http://www.quantachrome.com/gassorption/nova_series.html))

The basic principle is an extension of the Langmuir theory, where the both monolayer and multilayer molecular adsorption follows three basic hypotheses, as follows: (a) physical adsorption of gas molecules on a solid in layers is infinite; (b) no interaction occurs between the adsorption layer; and (c) the Langmuir theory can be applied to each layer.

The resulting BET equation is expressed by following equation

$$\frac{1}{v[(P_0/P)-1]} = \frac{c-1}{v_m c} \left(\frac{P}{P_0}\right) + \frac{1}{v_m c} \quad (1)$$

Where,  $P$  and  $P_0$  represent the equilibrium and the saturation pressure of adsorbates at the temperature of adsorption respectively,  $v$  is the quantity of the adsorbed gas,  $v_m$  is the quantity of the monolayer adsorbed gas and  $c$  denotes the BET constant. The  $c$  can be expressed by following equation.

$$c = \exp\left(\frac{E_1 - E_L}{RT}\right) \quad (2)$$

Here,  $E_1$  and  $E_L$  represent the heat of adsorption for the first layer and the second or higher layers respectively.  $E_L$  is equal to the heat of liquefaction. The equation (1) is an adsorption isotherm and can be plotted on the y-axis as a straight line with  $1 / v[(P_0 / P) - 1]$  and on the x-axis with  $\phi = P / P_0$  according to experimental results. This plot is called a BET plot. This linear relationship of the equation is maintained only in the range of  $0.05 < P / P_0 < 0.35$ . The value of the slope ( $A$ ) and the y-intercept ( $I$ ) of the line are used to calculate the monolayer adsorbed gas quantity  $v_m$  and the BET constant  $c$ . The equations 4 and 5 can be used.

$$v_m = \frac{1}{A + I} \quad (3)$$

$$c = 1 + \frac{A}{I} \quad (4)$$

Total surface area  $S_{total}$  and a specific surface area ( $S$ ) are evaluated by the following equations,

$$S_{BET, total} = \frac{(v_m N_s)}{V} \quad (5)$$

$$S_{BET} = \frac{S_{total}}{a} \quad (6)$$

where  $v_m$  is in the units of volume which also represents the units of the molar volume of the adsorbate gas,  $N$  is Avogadro's number,  $s$  represents the adsorption cross section of the adsorbing species,  $V$  denotes the molar volume of adsorbate gas and  $a$  is mass of adsorbent.

#### 2.4.4 X-ray Photoelectron Spectroscopy (XPS)

Since the discovery of the photoelectric effect way back in the year 1887 by Heinrich Hertz the foundation to electron spectroscopy was laid. However, the photoelectron spectroscopy as a technique was established after more than half a century of this discovery. In 1950, Kai Siegbahn successfully reported the first study of photoelectron spectroscopy, later which he received the Nobel Prize in Physics in 1981 for the same.<sup>17</sup> The technique was known as Electron Spectroscopy for Chemical Analysis (ESCA). Later, after few modifications it converted to X-ray photo electron spectroscopy (XPS). XPS is widely used technique for identification of the compositions of the compounds as well as the changes in its chemical structure. For example, the compounds exhibit a different spectrum than a pure element.

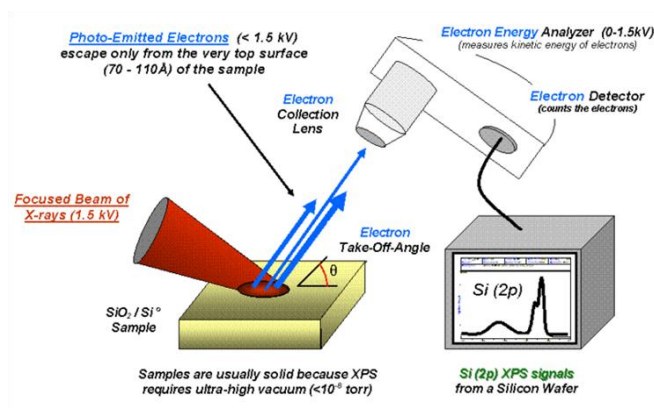


**Figure 2.9:** Basic diagram for XPS ([http://en.wikipedia.org/wiki/X-ray\\_photoelectron\\_spectroscopy](http://en.wikipedia.org/wiki/X-ray_photoelectron_spectroscopy))

Elements in XPS spectroscopy are identified by the peak positions on the spectrum. The concentrations are determined using the heights and areas of the peak with appropriate correction factors. An XPS spectrum is obtained by irradiating a sample with X-ray beams and measuring the resulting kinetic energy as well as the number of the ejected electrons from the surface of the sample during the process. This technique requires ultra-high vacuum (UHV) conditions to minimize any interaction of the electron with the surroundings. XPS also helps to measure the empirical formula, chemical state, elemental composition, and electronic state of the elements exist in a sample. The basic diagram for XPS system is shown in Figure 2.9.

#### 2.4.5 Photoluminescence (PL) Spectroscopy

Photoluminescence (PL) is the spontaneous emission of photons by a material after the absorption of desired amount of energy in the form of light. It is a very important tool for the characterization of the optoelectronic properties of semiconductors since PL spectroscopy can be able to access certain energy level which cannot be detected using the UV-Vis absorbance spectroscopy. The PL is observed in the samples which should possess certain band gap so that the transition from excited state to lower state can lead to luminescence. Typically in a semiconductor sample the electron-hole pairs are created due to the illumination using electromagnetic radiations with energy higher than the band gap of semiconductor. The recombination of the electrons with holes depends upon the lifetime of excited states. This recombination process leads to the emission of photons. The energy of the emitted photons depends upon the absence or presence of non-radiative recombination in the material. Therefore the information regarding the energy levels and defect levels in the sample can be obtained by analyzing the intensity of the PL spectrum as a function of wavelength. Depending on the lifetime of electronic states in the radiative emissions, the PL can be classified as fluorescence or phosphorescence. In fluorescence the sample emits light with longer wavelength than the wavelength of absorbed light. The typical luminescence lifetime range between  $10^{-8}$ - $10^{-5}$  seconds. However in case of phosphorescence, the luminescence lifetime can range from milliseconds to even hours. The peak positions and intensity of the PL spectrum of a sample is observed for the analysis.



*Figure 2.10: shows possible luminescence pathways in semiconductor*

Figure 2.10 shows the different pathways in which the radiative decay can take place in a sample.

### 2.4.6 Field Emission Scanning Electron Microscopy (FESEM)

Field emission scanning electron microscopy (FESEM) is a versatile, non-destructive electron microscopy technique which can provide the information regarding sample's surface topography and composition.<sup>18</sup> In this technique, a focused electron beam, emitted by a field emission source, scans. In case of most common mode, the detection of secondary electrons emitted by the atoms excited by electron beam is observed. The angle and velocity of these secondary electrons depend on surface topography of the sample. An image is generated by the scanning of the sample with focused electrons beam and subsequently collecting secondary electrons with special detector. This image shows the topography of the samples surface. Schematic of a typical SEM is shown in the figure 2.11 a. It consists of a tip with diameter in the order of 100 nm which is made of a field emission material. From this tip a high intensity beam of electrons emanates under an applied field. The emitted electrons are accelerated by an electric field gradient which are deflected and focused by the magnetic lenses to produce narrow beam of electrons.

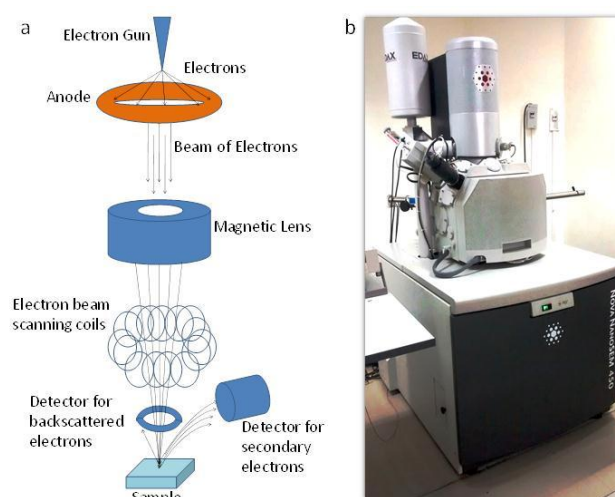


**Figure 2.11:** a) Schematic of FESEM showing main components of the microscope (Ref. <https://www.purdue.edu/ehps/rem/rs/sem.htm>), b) FESEM machine from our lab.

Interaction of beam of electrons produces three types of electrons, secondary, back scattered and characteristic X-rays. The secondary electron imaging (SEI) can produce high resolution images which can reveal details even less than 1nm in size. Very narrow electron beam gives a large depth of field to generate a 3-D appearance which is quite useful for the understanding of the sample surface. Back scattering electrons (BSE) are the electron beam which is reflected from the sample. The intensity of the BSE signal depends upon atomic number of the sample. BSE along with X-rays can be very used for analysis of the distribution of different elements in the sample.



### 2.4.7 Transmission Electron Microscopy (TEM)

Transmission electron microscopy is another form of electron microscopy technique where the transmitted beam of electrons is used for imaging.<sup>19</sup> Since the electrons possess very small de Broglie wavelength, TEM can be capable of imaging at a higher resolution than conventional light microscope. The type of information obtained depends upon the scattering processes experienced by electrons during their passage through the specimen. Elastic scattering is associated with no energy loss and gives rise to diffraction patterns. On the other hand the inelastic scattering causes complex adsorption and scattering effects due to the interactions between the primary electrons and sample electrons at heterogeneities such as grain boundaries, dislocations, second phase particles, defects, density variations, etc. This leads to spatial variation in the intensity of the transmitted electrons.

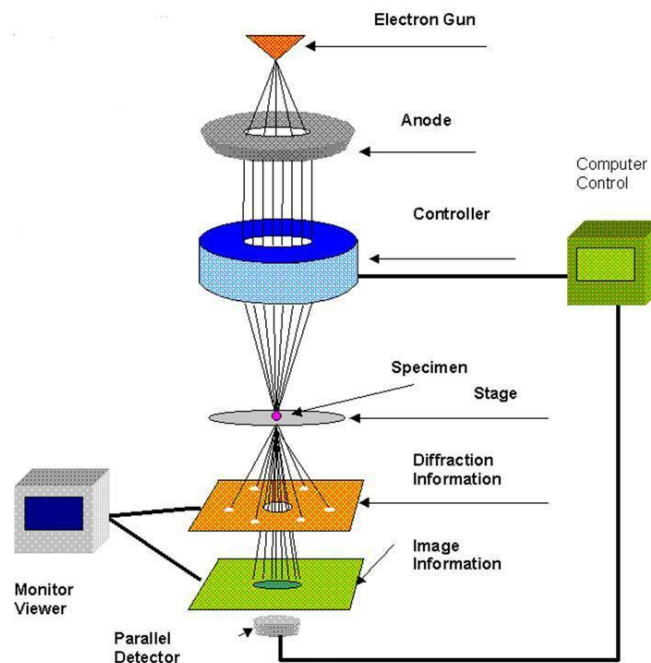


**Figure 2.12:** Schematic of TEM. (Ref. <http://www.rpi.edu/dept/materials/COURSES/NANO/shaw/Page5.html>)

The maximum resolution is related to the wavelength of electrons and the numerical aperture of source with following equation:

$$d = \frac{\lambda}{2n\sin\alpha} \sim \frac{\lambda}{2NA}$$

Where,  $d$  is maximum resolution,  $\lambda$  is wavelength and  $n\sin\alpha$  is numerical aperture of the source. Upon changing the strength of intermediate lens, either imaging of sample or diffraction pattern can be seen by TEM. Figure 2.12 shows schematic of TEM.

In TEM the high magnification ranging from 50 to  $10^6$  can be achieved and also it can provide both image and diffraction information from a single sample.

## 2.4.8 Electrochemical Measurements

### I. Cyclic Voltammetry

Cyclic voltammetry (CV) is a type of electro-chemical measurement which follows the potentiodynamic route. This is used for the study of the both types of capacitive processes, electrical double layer and redox. The CV measurements for double layer capacitor are usually performed in a two electrode system; whereas for redox processes it performs in three electrode system. For three electrode system, the potential of the working electrode is measured against a reference electrode which maintains a constant potential throughout.<sup>20</sup>

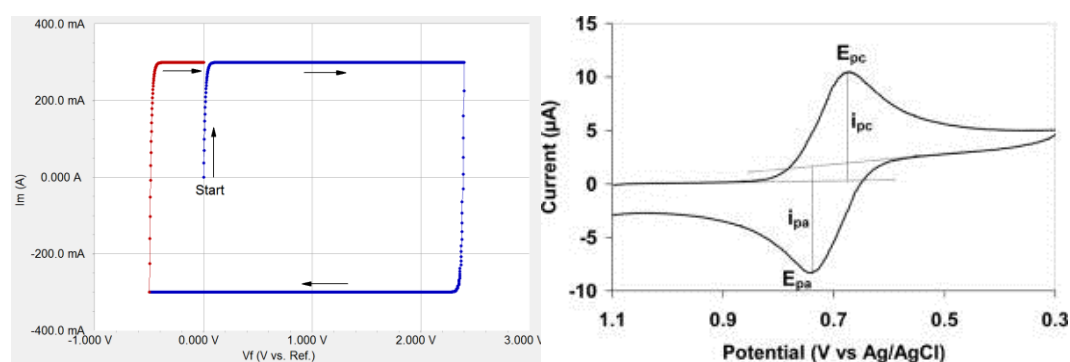


**Figure 2.13:** cyclic voltammetry study of (a) EDLC (ref. <http://www.gamry.com/application-notes/battery-research/testing-electrochemical-capacitors-cyclic-voltammetry-leakage-current/>) and (b) Redox reaction (Ref. [https://en.wikipedia.org/wiki/Cyclic\\_voltammetry](https://en.wikipedia.org/wiki/Cyclic_voltammetry))

When the set potential is reached in a CV experiment, the working electrode's potential is ramped in the opposite direction to return to the initial potential. These cycles of ramps in potential may be repeated as many times as desired. The current thus obtained at the working electrode is plotted against the applied voltage (i.e., the working electrode's potential) to get the cyclic voltammogram trace which is shown in Figure 2.13.

### II. Galvanostatic Charge-Discharge

Galvanostatic charge-discharge is the standard method used to elucidate the electrochemical performance as well as the cycle life of both supercapacitors and batteries.<sup>21</sup> Charge and discharge experiment is conducted at a constant current until a set voltage is reached and change in potential versus capacity is measured in supercapacitors. In charging and discharging two different dynamics is observed. During charging the electrodes involve in absorption of electrolyte ions at its surface while during discharging the dynamics is reversed, desorption of

ions occurs. Typical charge-discharge curve of supercapacitor is shown in figure 2.14

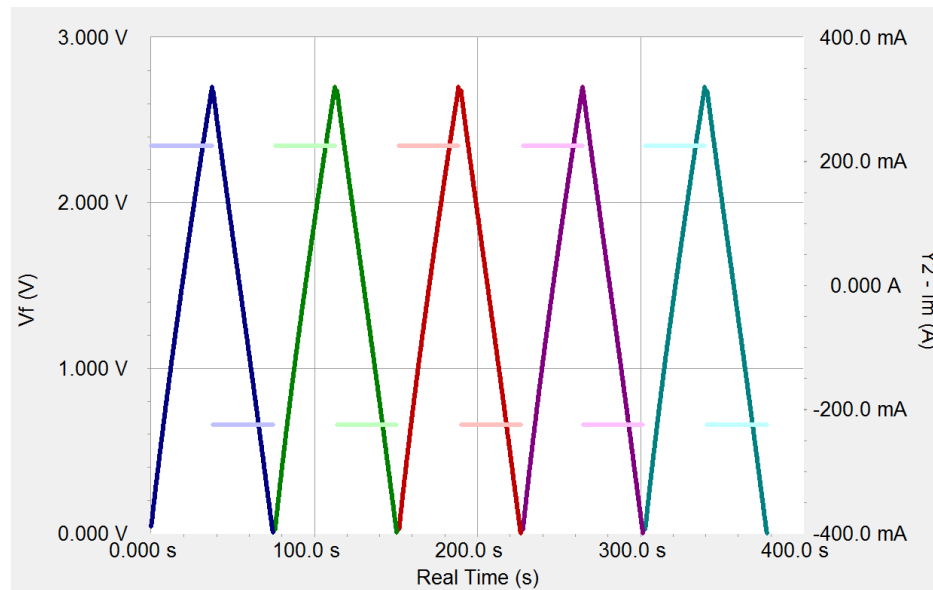


**Figure 2.14:** Charge-discharge curve in supercapacitor. (Ref. <http://www.gamry.com/application-notes/battery-research/electrochemical-capacitors-cyclic-charge-discharge-and-stacks/>)

### III. Electrochemical impedance spectroscopy (EIS)

Electrochemical impedance spectroscopy (EIS) is the most reliable method for the measurement of the equivalent series resistance (ESR) of supercapacitors. It also helps to create the models to describe underlying reaction mechanisms.<sup>22</sup> The capacitor non-idealities can be investigated using these models. Electrochemical impedance is usually measured by applying an AC potential to an electrochemical cell and then measuring the current through the cell. We apply a sinusoidal potential excitation and the response to this potential is an AC current signal. Impedance is represented in the form of Nyquist plot, in which X-axis represents real impedance ( $Z'$ ) the Y-axis represents imaginary part ( $Z''$ ). Nyquist plot gives various types of resistances associated with the electro chemical device such as series resistance, charge transfer resistance, resistance at electrode-electrolyte interfaces etc.<sup>23</sup>

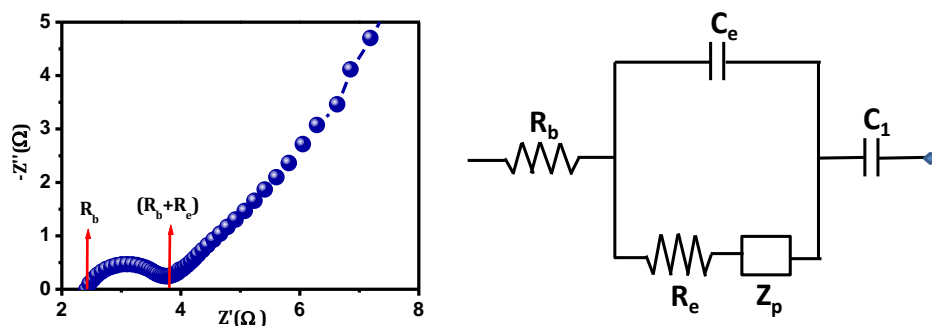


**Figure 2.15:** (a) Nyquist plot (b) equivalent fitted circuit

The Nyquist plot for a carbon based supercapacitor and equivalent circuit diagram are shown in the figure 2.15 a and 2.15 b respectively. The series resistance of the system can be calculated from the X- intercept ( $R_b$ ) which includes the resistance of the electrode, current collector and electrolyte. The diameter of each semicircle ( $R_c$ ) in the Nyquist plot denotes the charge transfer resistance at the interfaces.

#### 2.4.9 Current-Voltage (I-V) study:

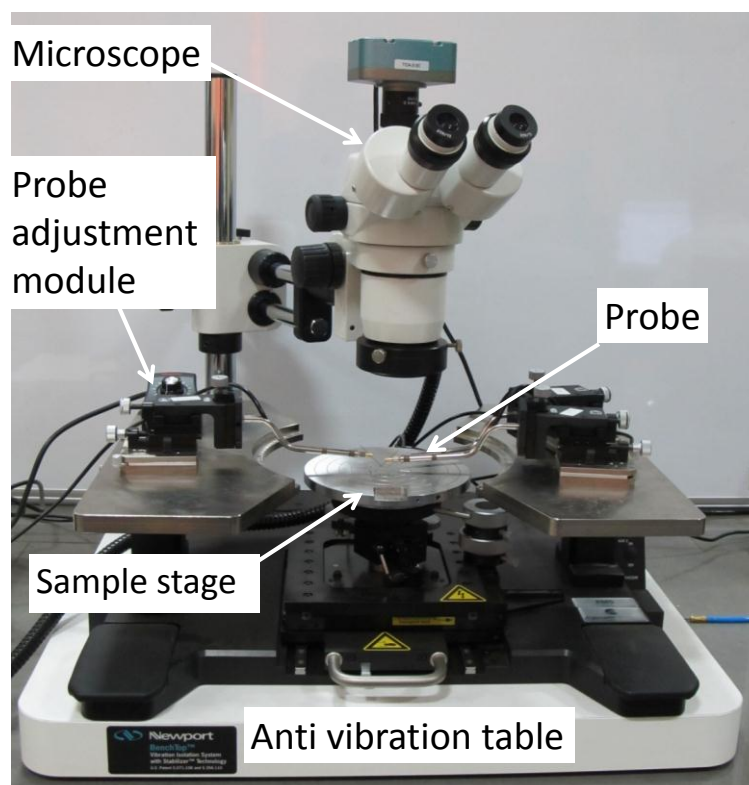


*Figure 2.16: Probe station*

Probe station, is used for several electrical measurements. This instrument consists of microscope and a set of metal probes (figure 2.16). Micrometer screws are used for the precise control of the vertical and X-Y movement of the probe. The microscope is used for observing the micro-electrodes on the sample surface and placing the probes on the respective electrodes. The probe tips are mostly consists of either gold or platinum having various tip diameters ranging from 1 micrometer and higher. The connecting wires for the electrode tips are the tri-axial cables which generate very less noise. The current voltage measurements are done with the Keithly 4200, a semiconductor parameter analyzer, to which these cables are connected. The main advantage of the probe station is the ability to taste the devices having lateral dimensions in the micrometer region. The Keithly 4200 allows measuring of all types of electrical parameters associated with the semiconductors such as 2 probe and 4 probe I-V measurement, capacitance measurements etc.

#### 2.4.10 Chromameter:



*Figure 2.17: Chromameter*

Chromameter is a modified version of the colorimeter which detects the intensity of light along with the purity of its colour. The construction of the Chromameter is quite similar to a camera which consists of a lens and a detector for further processing. It consists of three different aperture size which allows light only from certain area of the source. The light at the detector is further analyzed for light intensity with respect to the reference. As the light is collected from the certain area of the source, it can provide the areal intensity ( $\text{cd m}^{-2}$ ). As mentioned earlier the colour quality can also be determined using the instrument. The collected colour is further processed and correlated with the CIE XYZ colour space<sup>24</sup> to get precise colour quality.

## 2.5 References:

1. Murray, C. B., Norris, D. J. & Bawendi, M. G. Synthesis and characterization of nearly monodisperse CdE (E = sulfur, selenium, tellurium) semiconductor nanocrystallites. *J. Am. Chem. Soc.* **115**, 8706–8715 (1993).
2. de Mello Donegá, C., Liljeroth, P. & Vanmaekelbergh, D. Physicochemical Evaluation of the Hot-Injection Method, a Synthesis Route for Monodisperse Nanocrystals. *Small* **1**, 1152–1162 (2005).
3. Woods, P. T. & Jolliffe, B. W. Stable single-frequency carbon dioxide lasers. *J. Phys. E.* **9**, 395–402 (1976).
4. J. Lin, Z. Peng, Y. Liu, F. Ruiz-Zepeda, R. Ye, E. L. G. Samuel, M. J. Yacaman, B. I. Yakobson, and J. M. Tour, Laser-induced porous graphene films from commercial polymers. *Nat. Commun.* **5**, 1–8 (2014).
5. El-Kady, M. F. & Kaner, R. B. Direct Laser Writing of Graphene Electronics. *ACS Nano* **8**, 8725–8729 (2014).
6. Gao, W. *et al.* Direct laser writing of micro-supercapacitors on hydrated graphite oxide films. *Nat Nano* **6**, 496–500 (2011).
7. El-Kady, M. F., Strong, V., Dubin, S. & Kaner, R. B. Laser Scribing of High-Performance and Flexible Graphene-Based Electrochemical Capacitors. *Science* (80-. ). **335**, 1326–1330 (2012).
8. L. Li, J. Zhang, Z. Peng, Y. Li, C. Gao, Y. Ji, R. Ye, N. D. Kim, Q. Zhong, Y. Yang, H. Fei, G. Ruan, and J. M. Tour, High-Performance Pseudocapacitive Microsupercapacitors from Laser-Induced Graphene. *Adv. Mater.* **28**, 838–845 (2016).
9. Flack, W. W., Soong, D. S., Bell, A. T. & Hess, D. W. A mathematical model for spin coating of polymer resists. *J. Appl. Phys.* **56**, 1199 (1984).
10. Evaporation (deposition). *Wikipedia* (2016). Available at: [https://en.wikipedia.org/wiki/Evaporation\\_%28deposition%29](https://en.wikipedia.org/wiki/Evaporation_%28deposition%29).
11. Drenth, J., Drenth & Jan. in *Encyclopedia of Molecular Biology* (John Wiley & Sons, Inc., 2002). doi:10.1002/047120918X.emb0081
12. Holzwarth, U. & Gibson, N. The Scherrer equation versus the ‘Debye-Scherrer equation’. *Nat. Nanotechnol.* **6**, 534 (2011).
13. Bragg, W. H. & Bragg, W. L. The Reflection of X-rays by Crystals. *Proc. R. Soc. London A Math. Phys. Eng. Sci.* **88**, (1913).
14. Elton, L. R. B. & Jackson, D. F. X-Ray Diffraction and the Bragg Law. *Am. J. Phys.* **34**, 1036 (1966).
15. Brunauer, S., Emmett, P. H. & Teller, E. Adsorption of Gases in Multimolecular Layers. *J. Am. Chem. Soc.* **60**, 309–319 (1938).

16. Sing, K. S. . Adsorption methods for the characterization of porous materials. *Adv. Colloid Interface Sci.* **76**, 3–11 (1998).
17. Chûjô, R., Sato, K. & Nishioka, A. ESCA Spectra of Poly( $\gamma$ -benzyl-L-glutamate). *Polym. J.* **3**, 242–243 (1972).
18. K. C. A. Smith and C. W. Oatley, The scanning electron microscope and its fields of application. *Br. J. Appl. Phys.* **6**, 391–399 (1955).
19. Crewe, A. V., Wall, J. & Welter, L. M. A High-Resolution Scanning Transmission Electron Microscope. *J. Appl. Phys.* **39**, 5861 (1968).
20. Mabbott, G. A. An introduction to cyclic voltammetry. *J. Chem. Educ.* **60**, 697 (1983).
21. Stoller, M. D. & Ruoff, R. S. Best practice methods for determining an electrode material's performance for ultracapacitors. *Energy Environ. Sci.* **3**, 1294 (2010).
22. Taberna, P. L., Simon, P. & Fauvarque, J. F. Electrochemical Characteristics and Impedance Spectroscopy Studies of Carbon-Carbon Supercapacitors. *J. Electrochem. Soc.* **150**, A292 (2003).
23. Toupin, M., Bélanger, D., Hill, I. R. & Quinn, D. Performance of experimental carbon blacks in aqueous supercapacitors. *J. Power Sources* **140**, 203–210 (2005).
24. CIE 1931 color space. *Wikipedia* Available at: [https://en.wikipedia.org/wiki/CIE\\_1931\\_color\\_space](https://en.wikipedia.org/wiki/CIE_1931_color_space).

## Chapter 3

### **CO<sub>2</sub> laser direct written MOF-based metal-decorated and hetero-atom doped porous graphene for flexible micro-supercapacitor with extremely high cycling stability**

Over the past decade flexible and wearable micro-electronic devices and systems are gaining significant importance. Since portable power source is an essential need of such wearable devices, currently there is considerable research emphasis on the development of planar interdigitated micro energy storage devices by employing diverse precursor materials to obtain functional materials (functional carbon, oxides etc.) with the desirable set of properties. Herein we report for the first time the use of metal organic framework (MOF) for high wavelength photothermal laser direct writing of metal-decorated and heteroatom-doped, porous few layer graphene electrodes for micro-supercapacitor application. We argue that the specific attributes of MOF as a precursor and the high wavelength laser writing approach (which creates extremely high localized and transient temperature (>2500°C) due to strong absorption by lattice vibrations) are together responsible for the peculiar interesting properties of the carbon material thus synthesized, thereby rendering extremely high cycling stability to the corresponding micro-supercapacitor device. Our device exhibits near 100% retention after 200,000 cycles and stability under 150° bending.



### 3.1 Introduction:

Over the past decade flexible and wearable micro-electronic devices and systems are gaining significant importance in view of the several novel and interesting emergent applications in the sectors of mobility, biomedical sciences, consumer electronics, sports, clean energy, and environmental sciences.<sup>1,2</sup> Since portable power source is an essential need of wearable devices, micro-scale flexible electrical energy storage devices such as micro-supercapacitors and micro-batteries are concurrently receiving significant attention. Towards this end one major challenge is the integration of the flexible power sources with other functional systems on the electronic motherboards which are mostly planar. Hence the recent research focus is on the development of planar interdigitated micro energy storage devices. Commercially available thin film batteries which are currently being used in microscale power sources have serious limitations such as low cycle life, sudden failure, safety etc. Moreover, these batteries are not convenient to use in the planar electronic circuitry.<sup>1,2</sup>

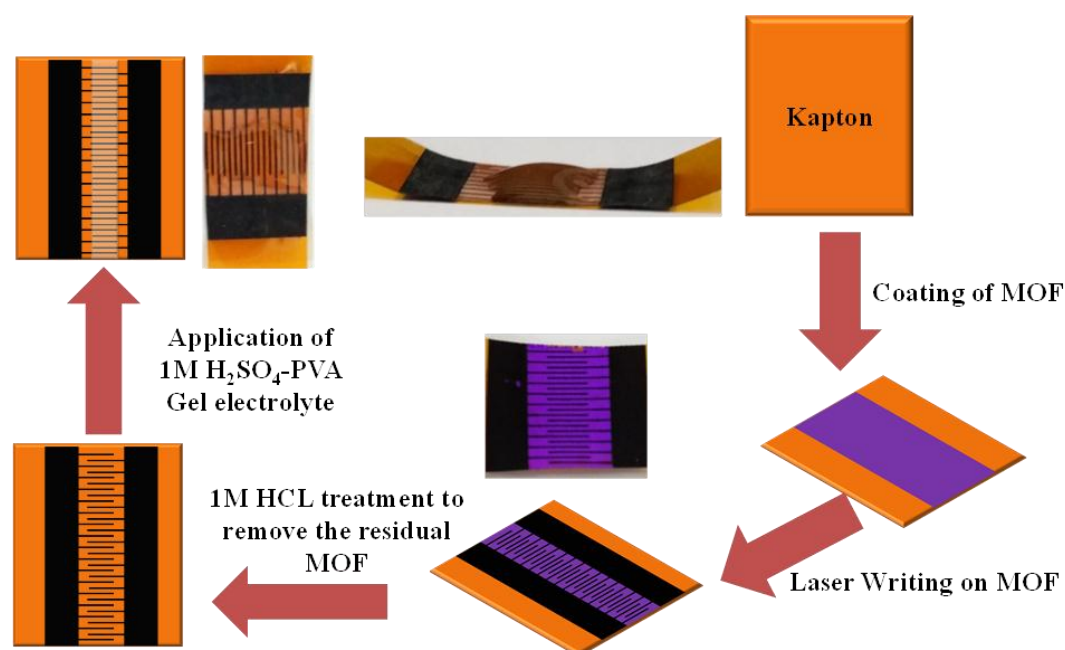
Within the framework of available options, the micro-supercapacitors are catching considerable attention due to their high power density, long cyclic life, fast charge-discharge rate, and most importantly, the ease of their in-plane device fabrication.<sup>1-6</sup> The device performance of supercapacitors mostly depends upon the quality of the electrode materials, amongst other parameters. Microporous carbons are considered to be good candidates for supercapacitor electrode application as they offer high stability as well as low charge transfer resistance between the electrode and the electrolyte. Due to their robust nature, their strain sustainability is also high which enables their use in flexible devices.<sup>7</sup>

Recently several approaches have been employed for the fabrication of carbon based interdigitated micro-supercapacitor devices such as photolithography, physical vapour deposition, direct printing, laser scribing, laser writing etc.<sup>1,2,8-16</sup> Among them, photolithography is the most popular technique because of its precise micro pattern defining ability.<sup>10,17</sup> But the major limitation of this technique is its complicated multi-step device fabrication procedure. Recently therefore, different laser based direct writing techniques are being explored due to

their facile and efficient device processability.<sup>1,2,12,18</sup> In most such cases either laser based reduction of graphene oxide film is used or laser induced graphene formation is realized from a polymer film.<sup>12,16</sup> The carbon thus formed is highly porous as desired for the supercapacitor application.

In this work we report for the first time the use of metal organic framework (MOF) for high wavelength photothermal laser direct writing of metal-decorated and heteroatom-doped, porous conducting few layer graphene electrodes for micro-supercapacitor application. We coin the term laser induced MOF-derived graphene (LIMDG) for this material. We argue that the specific attributes of MOF as a precursor and the high wavelength laser writing approach (which creates extremely high localized and transient temperature (>2500°C) due to strong absorption by lattice vibrations) are together responsible for the peculiar interesting properties of the carbon material thus synthesized, thereby rendering extremely high cycling stability to the corresponding micro-supercapacitor device. Our device exhibits near 100% retention after 200,000 cycles and stability under 150° bending. While carbonization of MOFs by high temperature pyrolysis under reducing or inert atmosphere has been performed previously,<sup>17,19,20</sup> to the best of our knowledge this is the first report of laser carbonization of MOF under ambient for synthesizing carbon for micro-supercapacitor application. Using this protocol we have fabricated interdigitated electrodes of LIMDG on polyimide (Kapton™) substrate. The residual MOF as well as the bare chemically accessible cobalt in the LIMDG matrix are subsequently removed by acid treatment which eventually generates additional porosity. The LIMDG formed by this method is highly interconnected rendering high mechanical stability to the electrodes. Notably, all the device measurements were performed without any metal electrodes and LIMDG itself serves as the electrode.

### 3.2 Experimental Section:



*Scheme 3.1: Schematic of the device fabrication process*

#### 3.2.1 Device fabrication:

Scheme 1 represents the device fabrication process. The micro supercapacitor electrode was fabricated by coating the MOF slurry on kapton substrate which was subsequently laser treated to form LIMDG. The slurry was formed by using 95 wt. % of ZIF 67 as active material and 5 wt. % of polyvinylidene fluoride (PVDF) as binder in N-methyl-2-pyrrolidone (NMP). The slurry was then coated on kapton and kept for drying at 80°C for 24h. The coating was irradiated with CO<sub>2</sub> laser (9-10 watt power, 10.6 μm wavelength, and 1000 pulse per inch line resolution) to make interdigitated electrodes. The width of each electrode was 150 μm and length was 5 mm. The device was treated with 1M HCl to remove residual MOF and the chemically accessible Co to the carbon matrix. It may be noted that any cobalt content that is wrapped with carbon could remain in the material. It was then washed thoroughly with distilled water. The gel electrolyte was applied on the patterned electrodes to make the complete device.

### 3.2.2 Formation of Gel Electrolyte:

1 gm of PVA was dissolved into 10 mL of Deionized (D.I.) water at 90°C. After full dissolution of PVA, the temperature was decreased to 40°C and H<sub>2</sub>SO<sub>4</sub> with adequate molarity was added to it under stirring. After addition, the temperature was again increased to 90°C and was kept constant for a brief period of time to ensure proper mixing of the acid.

### 3.2.3 Characterization technique:

The X-ray diffractometer (XRD) measurements were carried out on a Philips X'Pert PRO diffractometer with nickel-filtered Cu K $\alpha$  radiation ( $\lambda = 1.5405 \text{ \AA}$ ). Raman spectroscopy was performed using LabRAM HR800 from JY Horiba. The Field Emission Scanning Electron Microscopy (FE-SEM) analysis was performed on NOVA NANOSEM 450. Transmission electron microscopy (TEM) was performed using JEM 2200FS TEM microscope operating at an accelerating voltage of 200 kV). The diffractograms were recorded at a scanning rate of  $1^\circ \text{ min}^{-1}$  between  $20^\circ$  to  $80^\circ$ . X-ray photoelectron spectroscopy (XPS) was done on a VG scientific ESCA-3000 spectrometer using non-monochromatized Mg K $\alpha$  radiation (1253.6 eV) at a pressure of about  $1 \times 10^{-9}$  Torr. Laser scribing was done by using Universal Laser Systems® VersaLASER® VLS 2.30. All electrochemical measurements were performed by using BioLogicVMP3 multichannel potentiostat-galvanostat. Cyclic voltammetry measurements were recorded at scan rates from 5 to 100  $\text{mV s}^{-1}$  over the potential range of 0 to 1V. Charge-discharge measurements were performed at current densities from 0.1 to 1 mA in the potential window of 0 to 1V.

### 3.3 Result and Discussion:

The laser pyrolytic carbonization of MOF by the high wavelength ( $\lambda=10.6 \text{ \mu m}$ ) CO<sub>2</sub> laser basically involves a pulsed photothermal process. It can create extremely high localized temperature ( $>2500^\circ\text{C}$ ) due to strong absorption by lattice vibrations over short duration.<sup>[7]</sup> This is significantly higher as compared to the standard tube furnace based pyrolysis of MOF where the pyrolysis temperature used is generally in the range  $700^\circ\text{C}$ - $1200^\circ\text{C}$ .<sup>17,20,21</sup> Moreover, in contrast to the standard pyrolysis done under reducing atmosphere, the laser spot

scanning treatment is done under ambient condition. Due to temporal localization strong oxidation is avoided. Hence, the nature of carbon formed in our case is characteristically different.

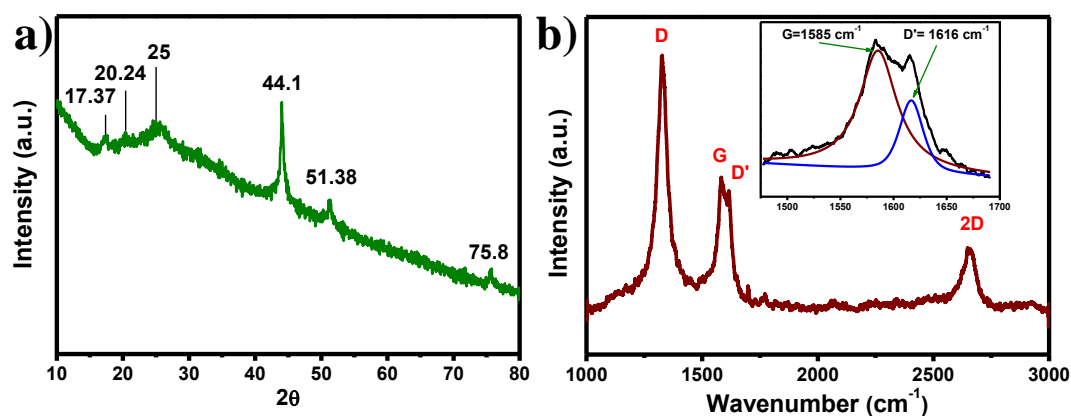


*Figure 3.1: a) X-ray diffraction pattern, and b) Raman Spectrum of the LIMDG material*

In the X-ray diffraction (XRD) pattern of LIMDG (figure 3.1 a), unlike the standard pyrolysed carbon forms, three peaks are noted at  $2\theta$  values of  $17.37^\circ$ ,  $20.24^\circ$  and  $25.5^\circ$ . The (002) peak around  $25.5^\circ$  represents graphitic nature of carbon. On the other hand, the peak at around  $20.24^\circ$  is attributed the  $\gamma$  band of (002) plane by many authors.<sup>22</sup> This  $\gamma$  band denotes the presence of saturated carbon, mainly aliphatic carbon chains, at the edge of the graphitic carbon. The peak around  $17.37^\circ$  signifies the presence of graphene oxide (GO) consisting of –OH and C=O functional groups which are also confirmed from the Fourier transform infrared (FTIR) spectroscopy (Figure 3.2).<sup>23</sup> Additional three sharp peaks around  $44.1^\circ$ ,  $51.38^\circ$  and  $75.8^\circ$  correspond to the (111), (200) and (220) planes of metallic cobalt (Co), respectively (JCPDS no -15-0806). This reveals that although the carbonization is done in air, no discernible metal oxide formation occurs during laser pyrolysis but some part of the carbon is mildly oxidised to form GO.

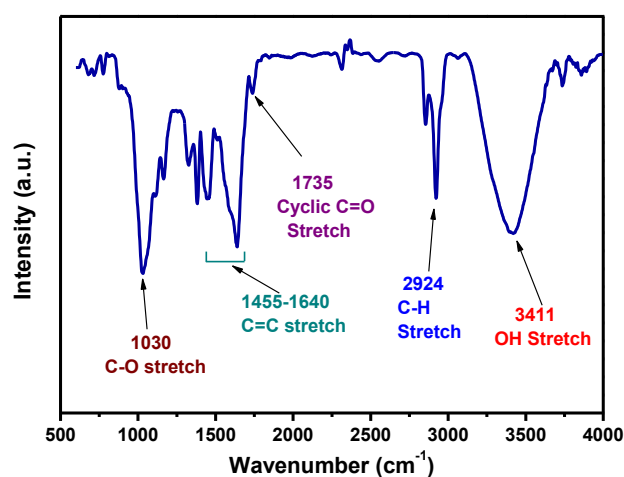


**Figure 3.2:** *Fourier transform infrared (FTIR) spectroscopy*

For more careful evaluation of the true nature of carbon, Raman spectroscopy study was performed (figure 3.1 b). The LIMDG material exhibits three characteristic bands namely D ( $1324\text{ cm}^{-1}$ ), G ( $1585\text{ cm}^{-1}$ ) and 2D ( $2652\text{ cm}^{-1}$ ). The G band arises due to the bond stretching of the  $sp^2$  carbon atom pairs in the ring as well as in the chain, confirming the graphitic nature of the carbon. The D band is responsible for the disorder induced Raman line in defective graphite.<sup>24</sup> In this case the D band appears to be quite sharp which implies the presence of uniform defect types. Also the D and G intensity ratio ( $I_d/I_g = \sim 1.8$ ) indicates a very high defect density which is the unique property of this carbon. Mainly the defects in the graphene arise due to presence of hetero atoms, incomplete graphitization, porosity etc. In this case all the three aforementioned factors are contributing. The XRD study already confirms the presence of Co and from the X-ray photoelectron study (XPS) (figure 3.3 a) doping of nitrogen in the LIMDG is also evident.

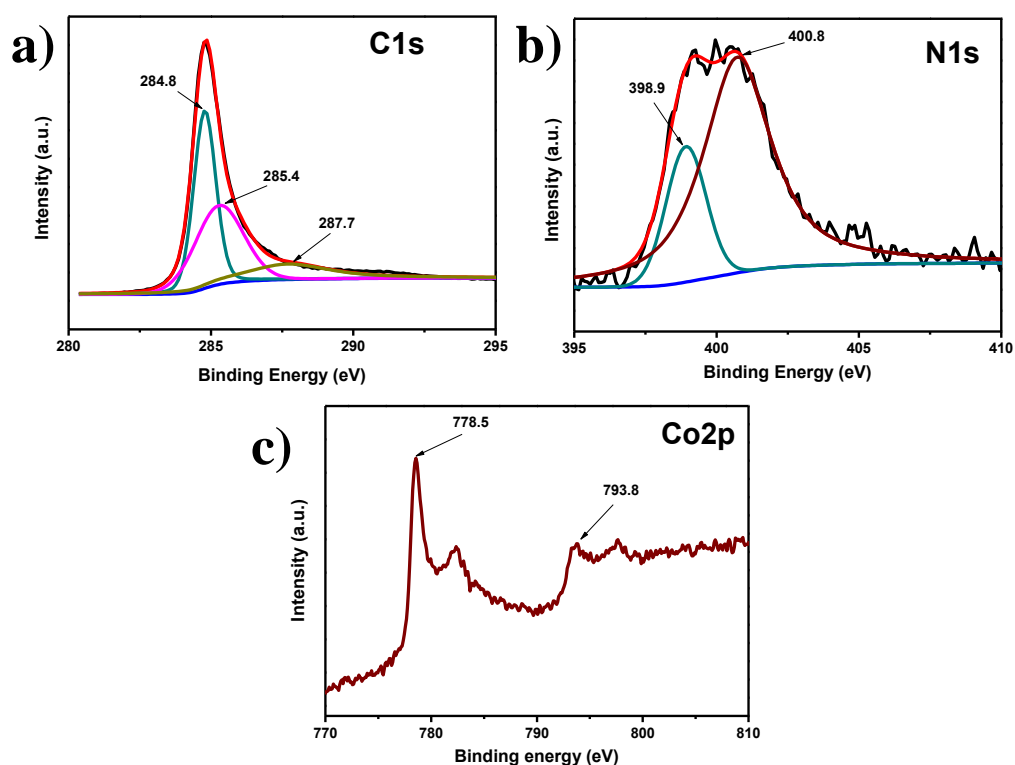


**Figure 3.3:** XPS spectra of LIMDG, a) C1s, b) N1s and c) Co2p contributions.

Moreover the presence of saturated carbon in the LIMDG indicates the incomplete graphitization and the high resolution Field Emission Scanning Electron Microscope (FE-SEM) images (figure 3.4 a and 3.4 b) suggest the existence of a porous network. In Raman spectroscopy the appearance and the intensity of the 2D band are defined by the number of layers of graphene stacked together. Higher 2D intensity denotes lesser number of graphene layers. The nature of the 2D band in LIMDG indicates the presence of a few layer graphene. More interestingly another split band near G (around  $1616\text{ cm}^{-1}$ ) is also observed. This band, denoted by D', also corresponds to the defects in the graphene planes and is generally present in the case of graphitic whiskers and filaments.<sup>25</sup> The transmission electron microscopy (TEM) data on our LIMDG material (Figure 3.4 c and 3.4 d) suggests the presence of carbon filaments rather than graphitic whiskers therein. The presence of cobalt in the MOF and its conversion into cobalt metal during laser pyrolysis can lead to this filament formation because cobalt is quite known for catalysing directional low-D growth.<sup>26,27</sup> The TEM study clearly shows the Co is uniformly embedded throughout 2D graphene sheets. Growth of interconnected tubular network is also clearly visible in the FE-SEM images. The collective observations from the Raman spectroscopy as well as the electronic microscopy

thus reveal the unique nature of carbon generated by laser pyrolysis of MOF and is in the form of a combination of graphitic filaments/curls and few layer graphene units, both supporting high defect density.

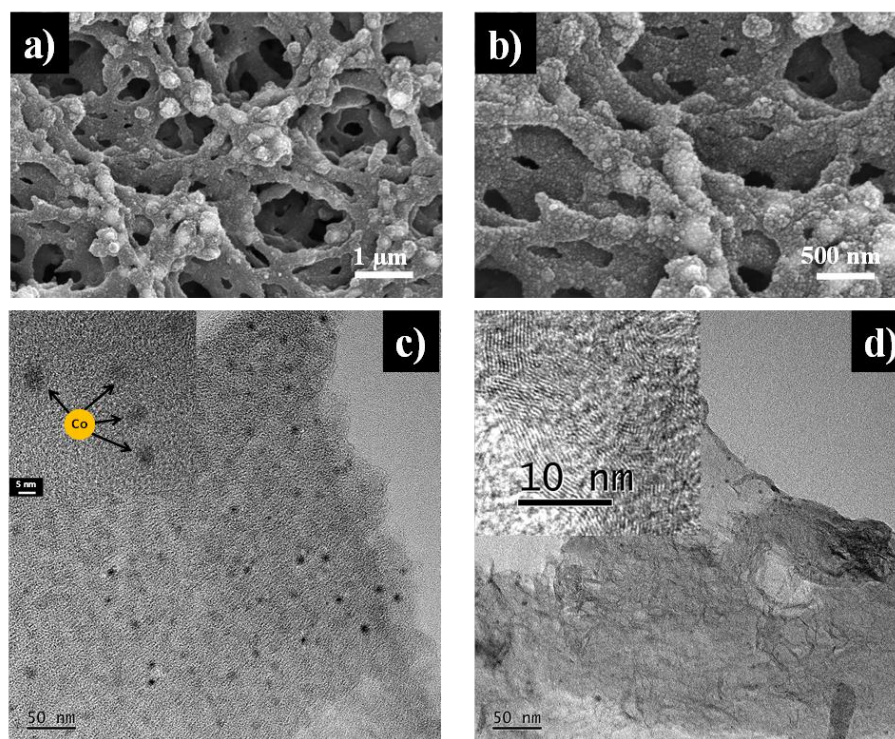


**Figure 3.4:** *a) and b) Field Emission Scanning Electron Microscopy (FESEM) images on 1  $\mu\text{m}$  and 500 nm scales, respectively; and c) and d) Transmission Electron Microscopy (TEM) images on different scales (including insets) revealing uniform decoration of cobalt metal and few layer graphene features. Signatures of the curved graphene catalysed by cobalt are also seen.*

The electrochemical performance of the LIMDG was evaluated by fabricating inter-digitated micro-supercapacitor using PVA/H<sub>2</sub>SO<sub>4</sub> (1M) gel electrolyte as the transport medium. The cyclic voltammetry (CV) study was conducted over the voltage range of 0 to 0.8 V at different scan rates from 5 mV s<sup>-1</sup> to 10,000 mV s<sup>-1</sup> (Figure 3.5 a and 3.5 c). The shape of the CV graph appears nearly rectangular in shape. The device shows an impressive performance even at high scan rate of 10,000 mV s<sup>-1</sup>. As is well known, normally at higher scan rate the electrolytic percolation inside the material gets limited as the ions do not get time to access the whole material which leads to decrease in the performance of the device. However due to the highly porous nature of the LIMDG electrode clear paths for



the ionic movement are provided throughout the electrode matrix which helps in retaining the device performance even at the higher scan rate.

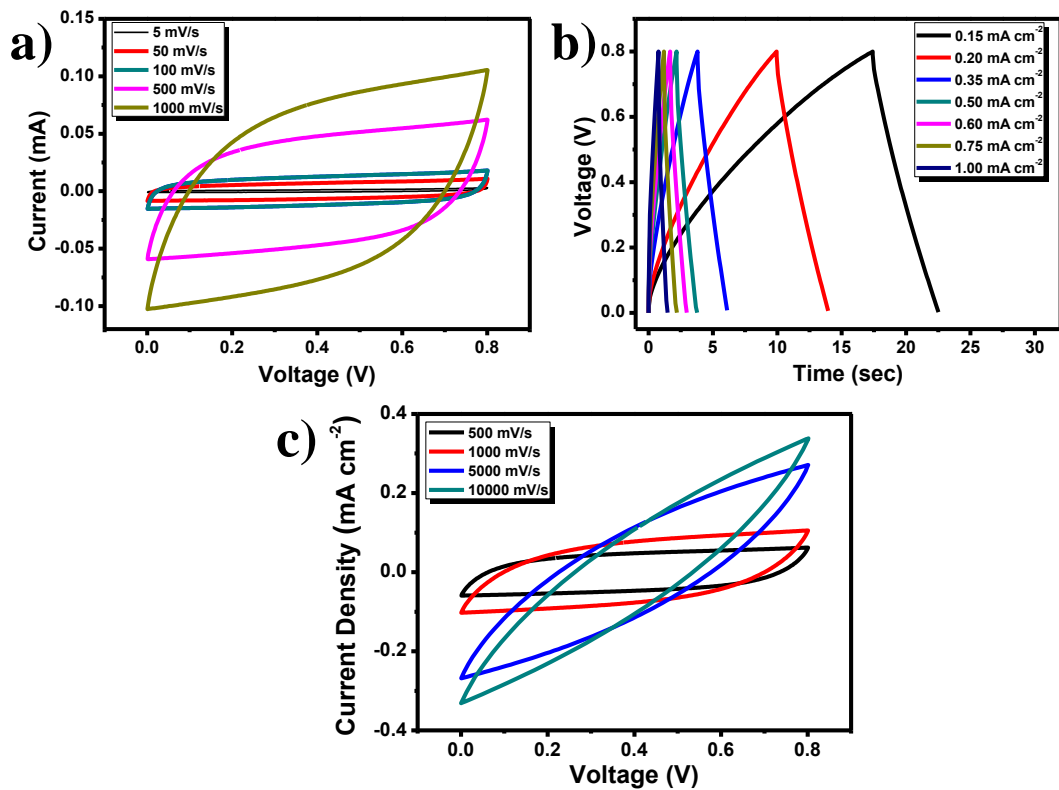


**Figure 3.5:** a) Cyclic Voltammetry data at different scan rates, b) Charge-discharge data at different current densities and c) cyclic voltammetry at higher scan rate

The discharge capacitance value of the device was calculated from the linear part of the discharge curve of the charge-discharge plot (figure 3.5 b) using the following equation

$$C = I_A \times \Delta t \times \Delta V^{-1} \quad (1)$$

where  $I_A$  is the current for the voltage range  $\Delta V$ , and  $\Delta t$  is the time duration for the discharge.

The capacitance value was evaluated for different current densities from  $0.15 \text{ mA cm}^{-2}$  to  $1 \text{ mA cm}^{-2}$ , the highest areal capacitance value obtained being  $1.36 \text{ mF cm}^{-2}$  at a current density  $0.15 \text{ mA cm}^{-2}$ . As noted from the capacitance Vs current density plot (figure 3.6 a), the device shows almost full capacitance retention for all the current densities.

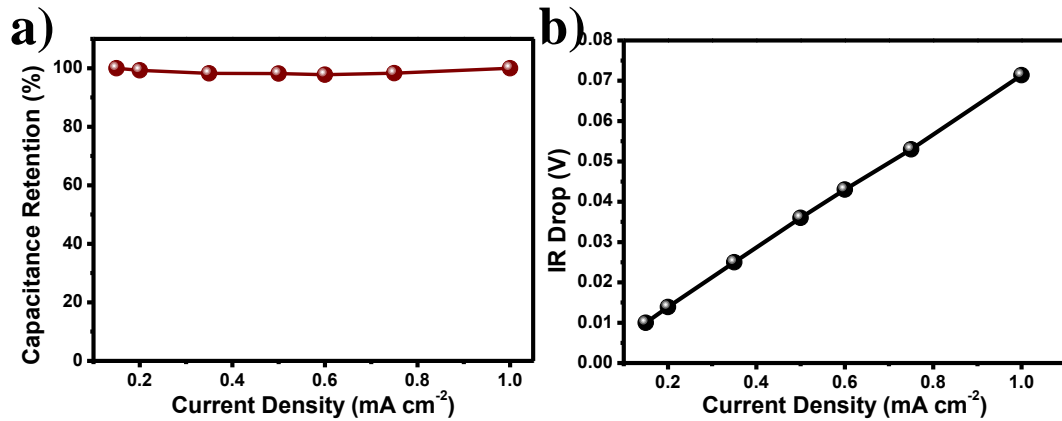


*Figure 3.6: a) percent capacitance retention with current density and b) IR drop vs current density plot of the device.*

The device also exhibited very low IR-drop even at high current density (0.0714 V at 1 mA cm<sup>-2</sup> current density), which signifies overall good device property feature. The IR drop is seen to increase linearly with the increase in the current density (figure 3.6 b) which shows that the device resistance is constant even at higher current density.

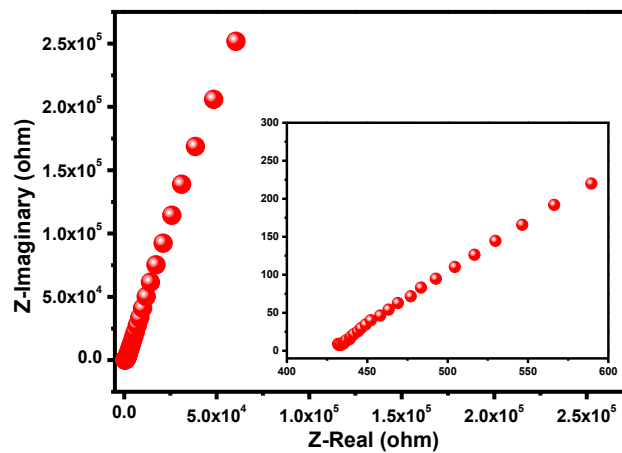


*Figure 3.7: Impedance spectroscopy Data*

Figure 3.7 represents the Nyquist plot for the device as measured by electrochemical impedance spectroscopy (EIS). The intercept on the x-axis of the Nyquist plot represents the equivalent series resistance (ESR) of the device which is 430  $\Omega$  in this case. Notably, the semi-circle in the higher frequency region of the Nyquist plot is absent which indicates the short ion diffusion pathway at the electrode-electrolyte interface. Also the plot is considerably parallel to the imaginary axis which represents the capacitive behaviour of the device.

The energy density and power density of the device were calculated from the following equations:

$$E = \frac{C_v (\Delta V)^2}{2 \times 3600} \quad (2)$$

$$P = \frac{E \times 3600}{\Delta t} \quad (3)$$

Where,  $C_v$  represents the areal capacitance of the device,  $\Delta V$  is the operating voltage window,  $\Delta t$  is the discharge time,  $E$  and  $P$  are the energy density and the power density, respectively. Figure 3.8 shows the energy density vs power density graph (Ragone plot) for the device.

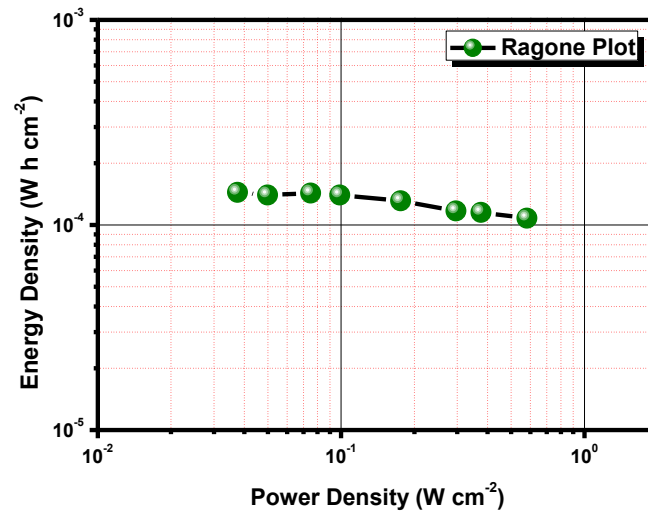


*Figure 3.8: Ragone Plot for the device*

The cyclic stability of the device was measured by charge-discharge experiment at a current density of  $1 \text{ mA cm}^{-2}$  (figure 3.9 a). The capacitance was calculated for each cycle and plotted against the cycle number. The stability study was carried out upto 200,000 cycles and the device showed excellent stability over the full range. The capacitance retention after the experiment was more than 99%. The impedance of the device was measured before and after the stability experiment (figure 3.9 b). It is observed that the charge transfer resistance of the device before and after the experiment was almost the same which also confirms the high cyclic stability of the device. The stability of the device mostly depends upon the structural integrity of the electrode material as well as the stability of the bonding of the material with the substrate. In most of the cases the disruption of the electrode material is found out to be the major cause of the low stability. In our

case, the highly interconnected framework of MOF renders high connectivity of the carbon formed by laser pyrolysis, thereby strengthening the electrode material. Also, we have carefully optimized the laser power such that after carbonization of MOF, the top layer of the kapton substrate is also carbonized to establish strong bonding of LIMDG with the substrate. These factors helped the device sustain even after large number of multiple charge-discharge cycles.

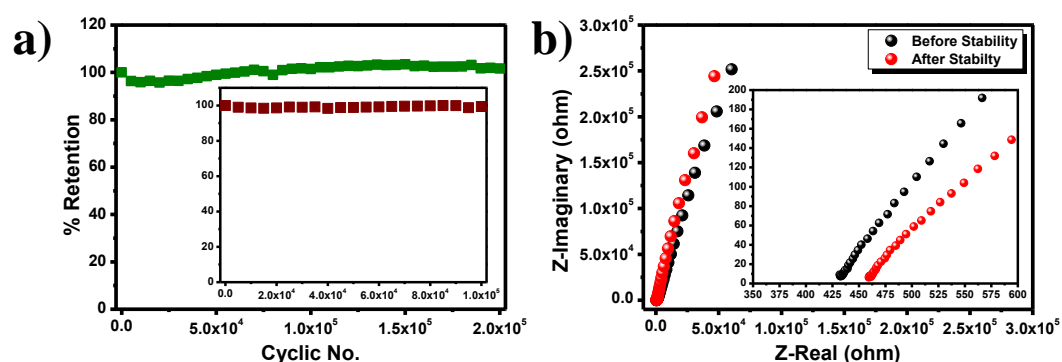


**Figure 3.9:** a) Percent capacitance retention up to 200,000 cycles, the inset shows capacitance retention after 100,000 cycles on another sample after which impedance measurements were performed, b) Impedance comparison of the device before and after cyclic stability measurement up to 100,000 cycles

The flexibility of the micro-supercapacitor device was also observed by performing the CV experiment of the device at  $50 \text{ mV s}^{-1}$  scan rate both under relaxed and bent conditions, where the bending angle is more than  $150^\circ$  (figure 3.10 a). The MSC device under bent condition holds 98% of its performance value of the normal relaxed device. When the device is relaxed to its original state, the performance is almost fully recovered. The high flexibility of the device can again be attributed to the strong carbon network existing in the matrix. We also performed the impedance measurement of the device under the relaxed and bent conditions to observe the resistance change due to bending (figure 3.10 b). In this study also, we did not observe any significant change in the charge transfer resistance from the relaxed device to the bent device.

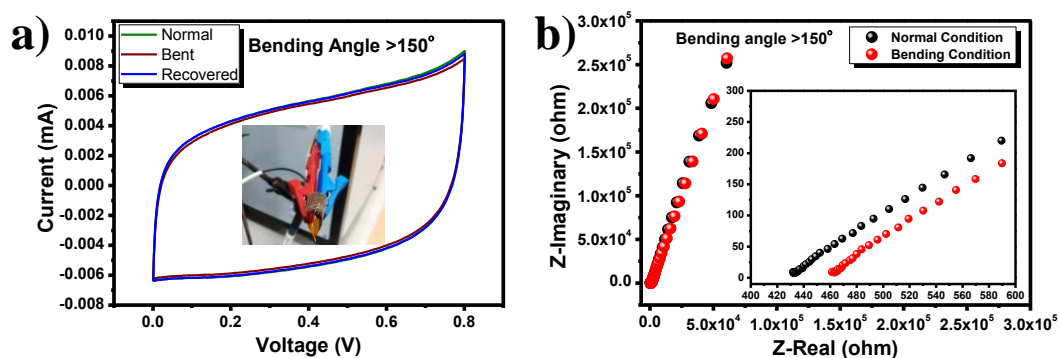


*Figure 3.10. a) Comparison of cyclic voltammetry data for the device under normal, bent and recovered conditions, b) Comparison of the device impedance under normal and bent condition ( $>150^\circ$ ).*

### 3.4 Conclusions:

This is the first report of the fabrication of flexible interdigitated micro supercapacitor by  $\text{CO}_2$  laser direct writing of functional mesoporous carbon (named as LIMDG) by long wavelength photothermal processing of Co-MOF (ZIF-67) on polyimide substrate. The interconnected strong graphitic mesoporous carbon network thus obtained has several unique device-worthy features that are induced by the intrinsic inclusion of the catalytic metal (Co), presence of nitrogen doping, and ambient processing that leads to oxygen surface groups. The device based on this carbon therefore exhibits ultra-high cyclic stability up to 200,000 cycles as well as 98% capacitance retention even at  $150^\circ$  bending angle.

### 3.5 References:

- (1) Majid Beidaghi, Y. G. Capacitive Energy Storage in Micro-Scale Devices: Recent Advances in Design and Fabrication of Micro- Supercapacitors. *Energy Environ. Sci.* **2014**, 7, 867–884.
- (2) Wu, Z. S.; Feng, X.; Cheng, H. M. Recent Advances in Graphene-Based Planar Micro-Supercapacitors for on-Chip Energy Storage. *Natl. Sci. Rev.* **2014**, 1 (2), 277–292.
- (3) Yuan, L.; Lu, X.-H.; Xiao, X.; Zhai, T.; Dai, J.; Zhang, F.; Hu, B.; Wang, X.; Gong, L.; Chen, J.; Hu, C.; Tong, Y.; Zhou, J.; Wang, Z. L. Flexible Solid-State Supercapacitors Based on Carbon Nanoparticles/MnO<sub>2</sub> Nanorods Hybrid Structure. *ACS Nano* **2012**, 6 (1), 656–661.
- (4) Wu, Z.; Parvez, K.; Feng, X.; Müllen, K. Graphene-Based in-Plane Micro-Supercapacitors with High Power and Energy Densities. *Nat. Commun.* **2013**, 4, 845–854.
- (5) Kim, D.; Shin, G.; Kang, Y. J.; Kim, W.; Ha, J. S. Fabrication of a Stretchable Solid-State Micro-Supercapacitor Array. *ACS Nano* **2013**, 7 (9), 7975–7982.
- (6) Maeng, J.; Kim, Y.-J.; Meng, C.; Irazoqui, P. P. Three-Dimensional Microcavity Array Electrodes for High-Capacitance All-Solid-State Flexible Microsupercapacitors. *ACS Appl. Mater. Interfaces* **2016**, 8 (21), 13458–13465.
- (7) Pandolfo, A. G.; Hollenkamp, A. F. Carbon Properties and Their Role in Supercapacitors. *J. Power Sources* **2006**, 157 (1), 11–27.
- (8) Chmiola, J.; Largeot, C.; Taberna, P.-L.; Simon, P.; Gogotsi, Y. Monolithic Carbide-Derived Carbon Films for Micro-Supercapacitors. *Science* **2010**, 328 (5977), 480–483.
- (9) Kim, S. K.; Koo, H. J.; Lee, A.; Braun, P. V. Selective Wetting-Induced Micro-Electrode Patterning for Flexible Micro-Supercapacitors. *Adv. Mater.* **2014**, 26 (30), 5108–5112.

- (10) Niu, Z.; Zhang, L.; Liu, L.; Zhu, B.; Dong, H.; Chen, X. All-Solid-State Flexible Ultrathin Micro-Supercapacitors Based on Graphene. *Adv. Mater.* **2013**, *25* (29), 4035–4042.
- (11) Beidaghi, M.; Wang, C. Micro-Supercapacitors Based on Interdigital Electrodes of Reduced Graphene Oxide and Carbon Nanotube Composites with Ultrahigh Power Handling Performance. *Adv. Funct. Mater.* **2012**, *22* (21), 4501–4510.
- (12) Lin, J.; Peng, Z.; Liu, Y.; Ruiz-Zepeda, F.; Ye, R.; Samuel, E. L. G.; Yacaman, M. J.; Yakobson, B. I.; Tour, J. M. Laser-Induced Porous Graphene Films from Commercial Polymers. *Nat. Commun.* **2014**, *5* (5714), 1–8.
- (13) Lokhande, C. D.; Dubal, D. P.; Joo, O. S. Metal Oxide Thin Film Based Supercapacitors. *Curr. Appl. Phys.* **2011**, *11* (3), 255–270.
- (14) D. Pech, M. Brunet, P. L. Taberna, P. Simon, N. Fabre, F. Mesnilgrente, V. Conedera, and H. Durou, Elaboration of a Microstructured Inkjet-Printed Carbon Electrochemical Capacitor. *J. Power Sources* **2010**, *195* (4), 1266–1269.
- (15) Pech, D.; Brunet, M.; Durou, H.; Huang, P.; Mochalin, V.; Gogotsi, Y.; Taberna, P.-L.; Simon, P. Ultrahigh-Power Micrometre-Sized Supercapacitors Based on Onion-like Carbon. *Nat Nano* **2010**, *5* (9), 651–654.
- (16) El-Kady, M. F.; Kaner, R. B. Scalable Fabrication of High-Power Graphene Micro-Supercapacitors for Flexible and on-Chip Energy Storage. *Nat. Commun.* **2013**, *4*, 1475.
- (17) Xia, B. Y.; Yan, Y.; Li, N.; Wu, H. Bin; Lou, X. W. (David); Wang, X. A Metal–organic Framework-Derived Bifunctional Oxygen Electrocatalyst. *Nat. Energy* **2016**, *1* (1), 15006.
- (18) Cai, J.; Lv, C.; Watanabe, A. Cost-Effective Fabrication of High-Performance Flexible All-Solid-State Carbon Micro-Supercapacitors by Blue-Violet Laser Direct Writing and Further Surface Treatment. *J. Mater. Chem. A* **2016**, *4* (5), 1671–1679.

- (19) Yaghi, O. M.; O’Keeffe, M.; Ockwig, N. W.; Chae, H. K.; Eddaoudi, M.; Kim, J. Reticular Synthesis and the Design of New Materials. *Nature* **2003**, *423* (6941), 705–714.
- (20) Banerjee, A.; Singh, U.; Aravindan, V.; Srinivasan, M.; Ogale, S. Synthesis of CuO Nanostructures from Cu-Based Metal Organic Framework (MOF-199) for Application as Anode for Li-Ion Batteries. *Nano Energy* **2013**, *2* (6), 1158–1163.
- (21) Wang, L.; Han, Y.; Feng, X.; Zhou, J.; Qi, P.; Wang, B. Metal-Organic Frameworks for Energy Storage: Batteries and Supercapacitors. *Coord. Chem. Rev.* **2015**, *307*, 361–381.
- (22) Lu, L.; Sahajwalla, V.; Kong, C.; Harris, D. Quantitative X-Ray Diffraction Analysis and Its Application to Various Coals. *Carbon N. Y.* **2001**, *39* (12), 1821–1833.
- (23) Fang, M.; Wang, K.; Lu, H.; Yang, Y.; Nutt, S. Covalent Polymer Functionalization of Graphene Nanosheets and Mechanical Properties of Composites. *J. Mater. Chem.* **2009**, *19* (38), 7098.
- (24) Al-Jishi, R.; Dresselhaus, G. Lattice-Dynamical Model for Graphite. *Phys. Rev. B* **1982**, *26* (8), 4514–4522.
- (25) Tan, P.; Hu, C.; Dong, J.; Shen, W.; Zhang, B. Polarization Properties, High-Order Raman Spectra, and Frequency Asymmetry between Stokes and Anti-Stokes Scattering of Raman Modes in a Graphite Whisker. *Phys. Rev. B* **2001**, *64*, 214301.
- (26) Bethune, D. S.; Klang, C. H.; de Vries, M. S.; Gorman, G.; Savoy, R.; Vazquez, J.; Beyers, R. Cobalt-Catalysed Growth of Carbon Nanotubes with Single-Atomic-Layer Walls. *Nature* **1993**, *363* (6430), 605–607.
- (27) Eklund, P. C.; M., H. J.; a., J. R. Vibrational Modes of Carbon Nanotubes; Spectroscopy and Theory. *Carbon N. Y.* **1995**, *33* (7), 959–972.



## Chapter 4

### Section A

# Highly stable laser-scribed flexible planar micro-supercapacitor using Mushroom derived carbon electrodes

A report is presented on the fabrication of all solid-state interdigitated flexible micro supercapacitor using ultrafast and highly scalable laser scribing technique, using highly mesoporous carbon synthesized from biomass (mushroom) with hydrothermal pre-processing. The specific protocol used for carbon synthesis renders some unique property features to the material (surface area of  $2604 \text{ m}^2 \text{ g}^{-1}$  with hierarchical pore size distribution) in the context of supercapacitor electrode application. A polyvinyl alcohol (PVA)- $\text{H}_2\text{SO}_4$  gel electrolyte is used for electrochemical measurements. The micro supercapacitor shows high cyclic stability up to 15000 cycles. Moreover it shows nearly 90% stability after 1000 bending cycles at  $60^\circ$  angle. It also retains its performance even under  $120^\circ$  bending condition. This work represents a facile and fast technique for micro-scaled device fabrication that can be easily commercialized. Moreover, the mushroom-derived carbon used to make the electrodes holds great promise in context of the stability and flexibility of flexible supercapacitors.

#### 4A.1 Introduction

Recently flexible or wearable microelectronics has become one of the most exciting fields of research. The development in this field has speeded up considerably over the past decade. To cope up with this current trend flexible and wearable charge storage devices are also being developed with continuously downsized miniaturization and efficient processing protocols. Integration of flexible microscale charge storage devices with electronic circuitry is still challenging because these flexible devices are not well suited with the planar geometry of most electronic devices. Hence planar interdigitated microscale charge storage devices are gaining importance over conventional flip-chip devices.<sup>1-3</sup> Fabrication of such microscale electronic devices is a major challenge because the methods used have to be facile, efficient and compatible with those used in the other flexible device fabrication protocols. Various techniques such as lithography, physical vapour deposition using shadow mask, sputtering, laser writing etc. have been used to fabricate planar interdigitated micro supercapacitors till date.<sup>4-6</sup> Except the laser based methods most other methods are somewhat complicated or time consuming. Of course, they do have specific advantages of concurrent wafer scale processing and scalability which cannot be underplayed. Laser based device fabrication methods are however mostly single step, simple and fast. Most of these have used laser power for the synthesis or direct writing of conducting carbon.<sup>7-9</sup> In this chapter, we report an even simpler and faster method of device fabrication using fast CO<sub>2</sub> laser scribing of a layer of mushroom synthesized conducting carbon to fabricate a planar micro-supercapacitor on a flexible substrate. This approach can be easily extended to other pre-synthesized forms of carbon for EDLCs or metal oxides/sulphides for pseudocapacitors. We also point out that the mushroom synthesized carbon in our case is formed by using a specific hydrothermal pre-processing protocol not used before and naturally renders few layer graphene-graphitic composite that offers the concurrent advantage of flexibility and high conductivity. Mushroom has been used earlier as a precursor for carbon synthesis<sup>10,11</sup> but in these works pre-carbonization at low temperature of 500°C was employed instead of hydrothermal pre-processing (used in the present work) before activation.

Flexible planar micro supercapacitors have some serious issues like low energy density and low stability which limit its practical application. To improve the device performance, quality of the electrode plays a significant role. It has been reported that mesoporous carbon based electrodes in electrochemical double layer capacitors (EDLC) show great promise for micro-supercapacitors both in terms of stability and energy density.<sup>12</sup> This type of material also offers high specific surface area, good electrical conductivity, tailored morphology and low cost.<sup>13</sup> The existence of micropores along with mesopores in porous carbon is desirable for high rate supercapacitor applications, since mesopores can be efficient transport pathways for liquids and gases, thus increasing the accessibility of smaller pores.<sup>[14]</sup> Production of such mesoporous carbon materials from inexpensive and renewable precursors such as biomass has attracted widespread attention in view of their growing application domains.<sup>10,11,15-20</sup> Other precursors such as polymers have also been used to obtain mesoporous carbons with specific architectures for charge storage applications.<sup>21-24</sup> Since carbohydrates have carbon as its primary constituent; carbohydrate containing biomass is a very good inexpensive source of functional carbon. Also the presence of inorganic minerals such as potassium and calcium therein can be advantageous in the creation of porosity in the carbon synthesized using such precursors via pyrolysis. In this work we derived mesoporous carbon (MDC) by controlled pyrolysis of the common form of Mushroom (*Agaricus bisporus*) used as a regular food item. The microstructure of the mushroom appears to be a dense assembly of twisted fibrils. As shown later, these features evolve into a uniformly mesoporous carbon form with desired porosity and conductivity upon controlled pyrolysis. The composition reflected by energy dispersive x-ray analysis (EDAX) indicates the presence of minerals, which serve as porogens for creating porosity, along with the organic part (rich carbon source).

In this report, we have fabricated all solid-state flexible micro-supercapacitor using laser scribed mesoporous carbon based microelectrodes and PVA-H<sub>2</sub>SO<sub>4</sub> gel electrolyte. The supercapacitor grade mushroom derived carbon (MDC) was synthesized from the common form of Mushroom (*Agaricus bisporus*) used as a regular food item. The pattern electrode was fabricated by a simple, scalable and less time consuming method of laser scribing using low energy CO<sub>2</sub> laser. Micro-

supercapacitor thus fabricated showed high volumetric capacitance of  $12.92 \text{ F cm}^{-3}$ . To the best of our knowledge this is the first time that a huge stability up to 15k cycles and high flexibility up to 1000 bending cycles is demonstrated for carbon based micro-supercapacitor.

## 4A.2 Experimental Section

### 4A.2.1 Synthesis of mushroom derived carbon (MDC)

The mushrooms were cleaned with de-ionized water, dried. Then they were put in Teflon lined autoclave in  $0.5 \text{ M H}_2\text{SO}_4$ . The autoclave was heated up to  $190 \text{ }^\circ\text{C}$  and maintained at the target temperature for 24 h. The resulting solid product was recovered by filtration and washed with distilled water and then dried. The carbonaceous precursor thus obtained was chemically activated with KOH. The activating agent/carbonaceous precursor mass ratio,  $A/P$ , was 4:1 and both were mixed by wet impregnation method. The mixture was dried to remove water and then pyrolysed under the following heating program: ramp at  $10 \text{ }^\circ\text{C min}^{-1}$  to  $1000 \text{ }^\circ\text{C}$ , hold for 4 h and then cool down to ambient temperature by natural convection. Further, the samples were washed in  $1\text{M HCl}$  under constant stirring for 24 h, and then with distilled water several times, until neutral pH was reached. Finally, the samples were dried at  $80^\circ\text{C}$  overnight for further studies.

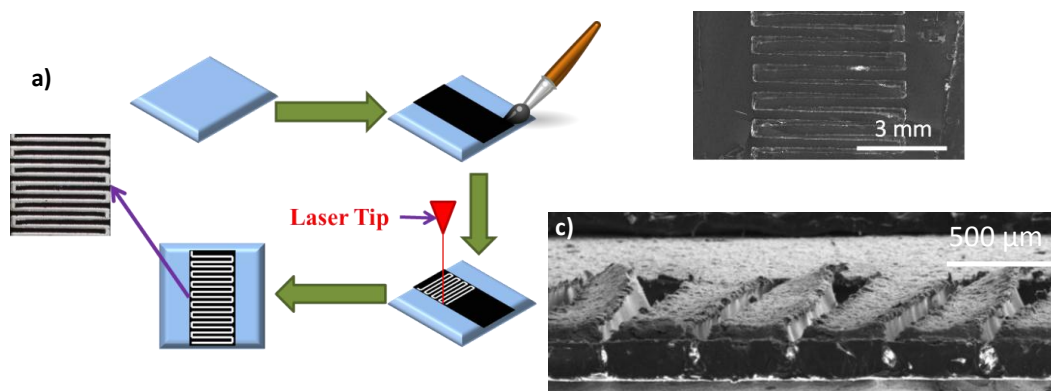


*Figure 4A.1: Device Design: a) Schematic of the device fabrication procedure, b) and c) SEM image of the laser scribed device*

#### 4A.2.2 Fabrication of micro supercapacitor electrodes

Micro-Supercapacitor electrode (EDLC) were fabricated with a mixture of 70wt.% of mushroom derived carbon, 20 wt.% conducting additive (acetylene black) and 10 wt.% Kynar PVDF as binder. To make homogeneous paste with proper viscosity, an optimum amount of N-methyl-2-pyrrolidone (NMP) was added to this mixture. The slurry was then coated on the ITO/PET substrate to make a uniform film and the substrate was dried in vacuum oven at 80°C overnight to remove the solvent (N-methyl-2-pyrrolidone) completely. Then the substrate was scribed using CO<sub>2</sub> laser (4.8-5.2 watt power, 10.6 μm wavelength and 1000 pulse per inch resolution) to form interdigitated pattern. The time consumed to pattern each 1 cm<sup>2</sup> device was just 48-50 sec. The schematic in figure 4A.1 a represents the micro supercapacitor fabrication process.

#### 4A.2.3 Formation of gel electrolyte

1gm of PVA was dissolved into 10 ml of D.I. water under continuous heating at 90°C and stirring. After full dissolution of PVA the temperature was decreased to 40°C and H<sub>2</sub>SO<sub>4</sub> was added under stirring condition according to the required molarity. After addition, the temperature was again increased to 90°C and kept it for brief time to ensure proper mixing of the acid.

#### 4A.2.4 Characterization techniques

The MDC was examined by various techniques such as powder X-ray diffraction measurement using a Philips X'Pert PRO diffractometer with nickel-filtered CuK<sub>α</sub> radiation, Raman spectroscopy using a LabRam HR800 from JY horiba and field emission scanning electron microscopy (FE-SEM) with Hitachi S-4200. Specific surface area value was determined by Brunauer-Emmett-Teller (BET) adsorption/de-sorption method (Quadrasorb automatic volumetric instrument). Laser scribing was done by using Universal Laser Systems® VersaLASER® VLS2.30. All electrochemical measurements were performed by using BioLogicVMP3 multichannel potentio-galvanostat. Cyclic voltammetry measurements were recorded at scan rates from 5 to 100 mVs<sup>-1</sup> at the potential range of 0 to 1V. Charge-discharge measurements were done at current densities from 0.1 to 1 mA in potential window of 0 to 1V. Electrochemical impedance

spectroscopy was carried out in the frequency range 0.01 Hz to 100 kHz. Cyclic stability was tested using chrono charge-discharge at 1mA for 15000 cycles.

#### 4A.2 Results and discussion

The x-ray diffraction (XRD) pattern of the MDC is shown figure 4A.2 a which exhibits two peaks positioned around  $26.1^\circ$  and  $43.8^\circ$  riding on broad hump-like background peaks. The peak centred at  $2\theta = 26.1^\circ$  is fairly sharp and corresponds to the (002) family of planes of graphitic carbon (Interlayer spacing of 0.38-0.39 nm). The contribution at  $43.8^\circ$  corresponds to the (101) planes of graphitic carbon. The size of graphitic crystallites was calculated using Scherrer formula ( $\tau = K\lambda / \beta \cos\theta$ ) and found to be 8.57 nm which corresponds to approximately 22-23 graphitic monolayers ( $8.57/0.38 \sim 22.55$ ). The hump-like contribution below this (002) peak represents turbostratic carbon which is more critical for the application being addressed and leads to high surface area, as discussed later. The graphitic inclusions assist in enhancing conductivity as well as mechanical stability of the material in the electrode configuration.

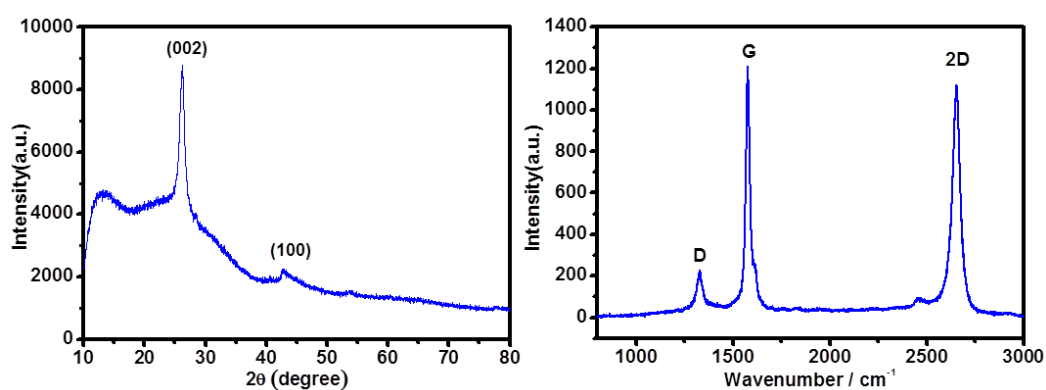


**Figure 4A.2:** Material Characterization: a) XRD pattern, and b) Raman spectrum of MDC

To further evaluate the nature and crystallinity of carbon material, the sample was characterized by using Raman spectroscopy and the results are shown in figure 4A.2 b. The synthesized carbon exhibited three typical bands; namely the G band ( $\sim 1578 \text{ cm}^{-1}$ ), the D band ( $\sim 1329 \text{ cm}^{-1}$ ), and the 2D band ( $2654 \text{ cm}^{-1}$ ). The G band is characteristic of relative vibration of  $sp^2$ -bonded carbon atoms in a 2D hexagonal lattice ( $E_{2g}$  mode).<sup>25</sup> The D band is associated with the vibration of

carbon atoms with dangling bonds for the in-plane terminations of graphitic carbon. The position, intensity (relative to G band) and broadening of D band depend upon the nature and type of the disorder and the functional groups present.<sup>26</sup> The disorder in the system is a result of porosity induced in the graphitic material and incomplete graphitization. The  $I_D/I_G$  ratios of commercial graphite, CVD graphene and MDC are found to be 0.147, 0.137 and 0.149, respectively, which signify the degree of disorder in the system. The D band cannot be seen in highly crystalline graphite.<sup>27</sup> The 2D peak is observed due to second-order Raman vibrations of zone-boundary phonons. The shape of the 2D peak around  $2654\text{ cm}^{-1}$  is indicative of single or a few layer graphene. The 2D or G' contributions are very sensitive to stacking order of graphene sheets and can be used to determine the number of layers of graphene. The 2D peak in single layer graphene is more intense and sharper as compared to multi-layer graphene.<sup>26</sup> In graphite, where  $n=\infty$ , the 2D peak is not sharp and gets broadened. The 2D peak in MDC case is intense and sharper than the 2D peak of commercial graphite. This suggest presence of lesser number of graphene layers in MDC than commercial graphite. The position of 2D peak and  $I_G/I_{2D}$  ratio give an indication of the number of graphene layers in the crystallites. The  $I_G:I_{2D}$  ratios of commercial graphite, MDC and CVD graphene are  $\sim 2.78$ , 1.06 and 0.68, respectively. Lesser value of  $I_G:I_{2D}$  in MDC case signifies lesser number of graphene layers than in graphite but higher number of layers than CVD graphene.<sup>27, 28</sup> Comparison of our  $I_G:I_{2D}$  value with the data of figure 2 of Reference 19 suggests that our sample has about 15-16 layers, fairly consistent with the XRD based rough estimate of 22 layers. Downshift of 2D peak position of MDC as compared to graphite can be assigned to turbostraticity present in MDC. In the case of graphite 2D peak shifts toward higher wave number (upshift) because of interactions between the stacked graphene layers which have tendency to shift the band to higher frequency.<sup>29</sup> Broadening of 2D band of graphite is because more carbon atoms participate in vibrations and electronic bands split into more complex and dispersive configurations. Electron-hole pairs undergo more scattering cycles, so more resonant phonons with different frequencies contribute to wider 2D band.<sup>30</sup>

Further insights into the detailed microstructure of the sample was gained by using FE-SEM and HR-TEM. As shown in the FESEM images of figure 4A.3 a and

4A.3 b the material is formed of curtain-like flakes assembled together. Even in the case of stack like forms seen in figure 4A.3 a, the internal flakes and porosity are apparent. The HR-TEM images further confirm the presence of high degree of porosity. The HR-TEM image of figure 4A.3 c and 4A.3 d further testify to this flake-assembled character of the material and its homogeneity. This specific nature of the material has 3D electrical connectivity compounded with flexibility which is important for the application of interest.

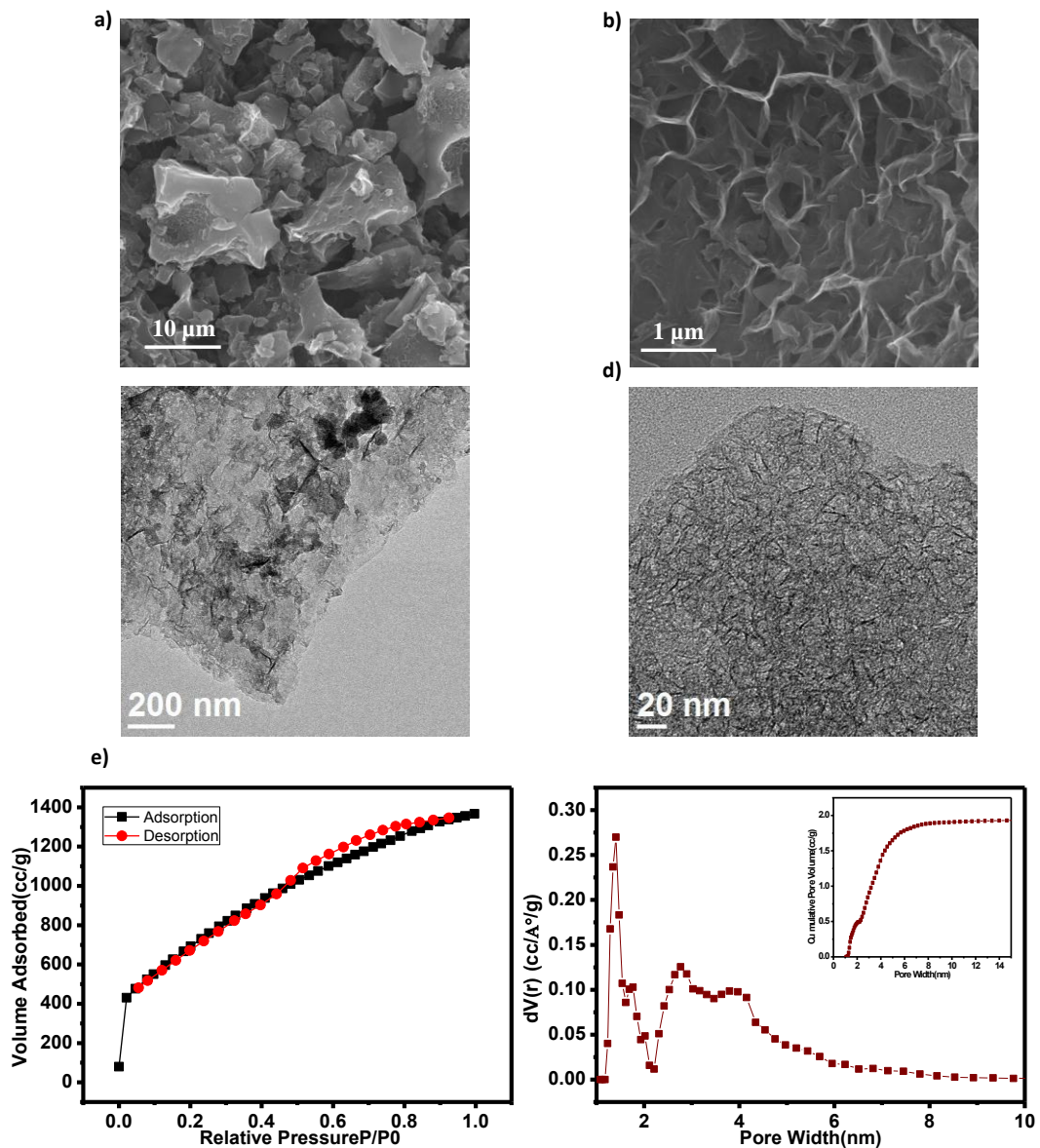


**Figure 4A.3:** Morphological Charecterization: (a)-(b)FESEM Images (c)-(d) HR-TEM images of MDC and (e)  $N_2$  Adsorption/desorption isotherm, and (f) Pore size distribution in  $N_2$  for MDC

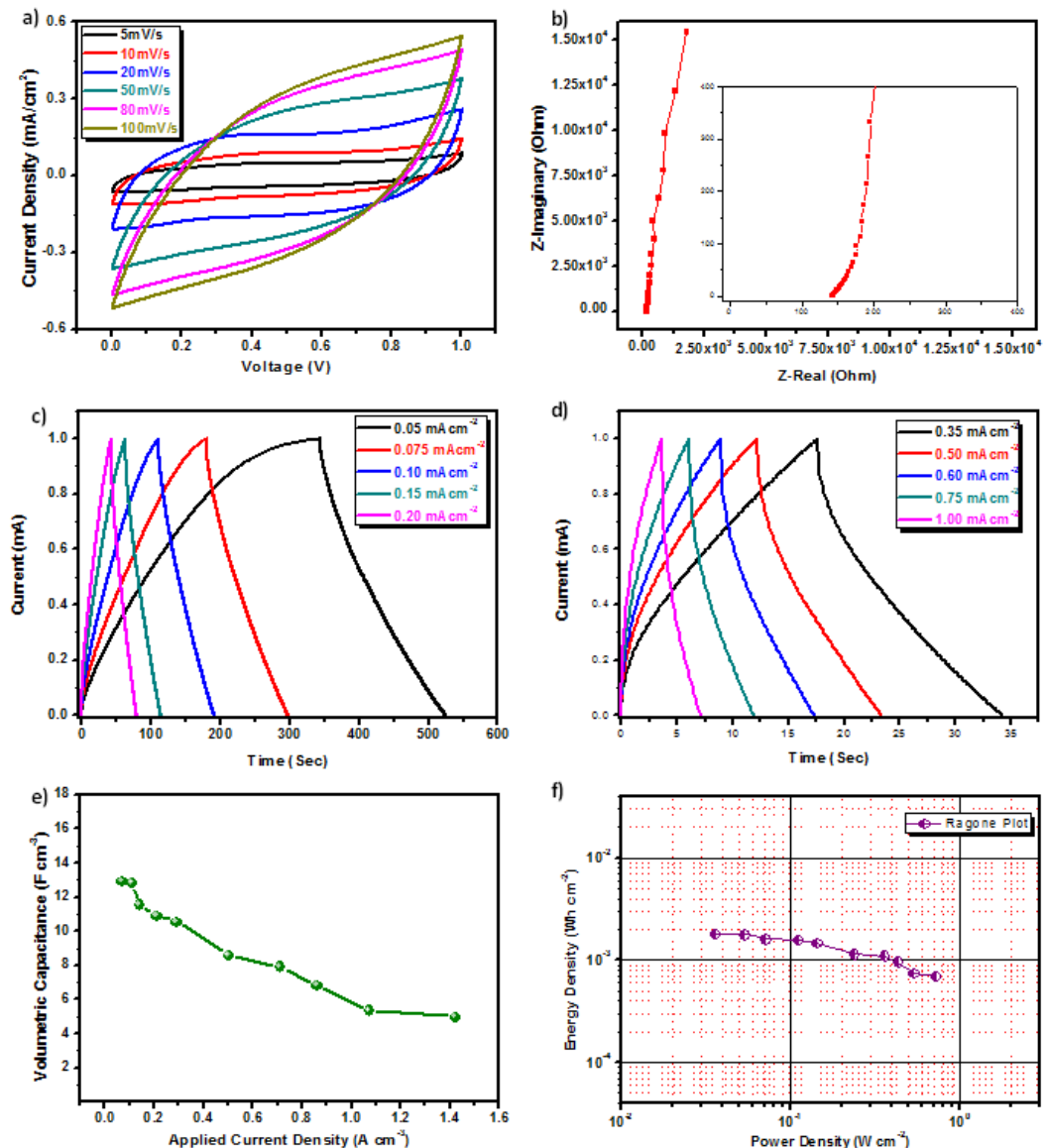


A typical N<sub>2</sub> adsorption-desorption isotherm for mushroom-derived carbon is shown in figure 4A.3 e. This exhibits type IV adsorption isotherm according to IUPAC classification.<sup>31,32</sup> The hysteresis loop arises due to capillary condensation through different mechanisms of adsorption and desorption in micropores. The specific surface area measured using standard BET method is very high 2604 m<sup>2</sup> g<sup>-1</sup>. Figure 4A.3 f shows the pore size distribution by N<sub>2</sub> adsorption. Bimodal distribution of pores is observed having micropores in the range of 1-2 nm and good fraction of mesopores in the range of 2-4 nm. It is interesting that in spite of the presence and contribution of some fraction of the graphitic (stacked) units the specific surface area of the overall material is very high. This can be understood on the basis of the strong 2D band observed in Raman spectrum which reflects almost single layer graphene-like character of the rest of the material, albeit with the desirable distribution of micro and mesopores (induced via activation by minerals and added KOH). The latter considerably enhances the effective N<sub>2</sub> adsorption that defines the specific surface area. High surface area to volume ratio of micropores play an important role in adsorption-desorption of ions via diffusion. Mesopores provide high adsorbate accessibility by giving wider transport channels which is important for fast diffusion of electrolyte ions into micropores.<sup>12</sup> Previous studies have shown that mesopores with pore size comparable or twice the size of electrolyte ions are suitable for electric double layer formation.<sup>10,13</sup>

Figure 4A.1 a shows schematic of device fabrication procedure. An optical image is also shown in the schematic. The SEM micrograph of a typical MDC micro-supercapacitor is shown in the figure 4A.1 b and c. Each device consists of 9 fingers on both sides. Each laser scribed electrode contains identical width of 300 μm, length of 5 mm and thickness of about 7 μm. The gap between every two electrodes is 100 μm. The thickness of the electrode was calculated from the cross-sectional SEM image.

To observe electrochemical performance CV was conducted using PVA-H<sub>2</sub>SO<sub>4</sub> (1M) gel electrolyte over the potential range from 0 to 1 V at different scan rates from 5 mV s<sup>-1</sup> to 100 mV s<sup>-1</sup> [figure 4A.4 a]. The CV of the device shows near rectangular nature and high current density which confirms its high capacitive

behaviour. Absence of any redox peak in the CV confirms the EDLC type behaviour of the device. As scan rate increases the nature of the graph deviates from rectangular shape which is due to fact that the electrolyte cannot get the time to percolate inside the electrode effectively at higher scan rate. Also, the resistance of the device increases with increasing scan rate which limits the performance of the device.



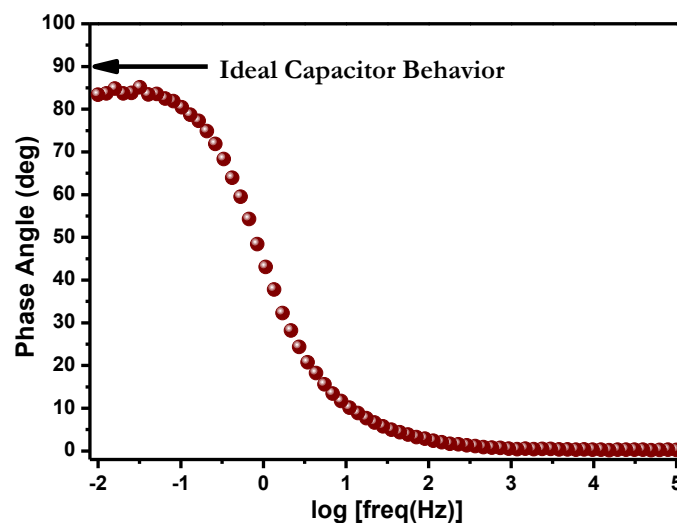
**Figure 4A.4:** Electrochemical characterizations: a) cyclic voltammetry data for different scan rates, b) Nyquist plot, c) and d) charge discharge plots at different current densities, e) volumetric capacitance vs applied current density plot, f) Ragone plot.

Figure 4A.4 c and d show the charge discharge curves for the device at different current densities. The discharge capacitance can be calculated from the equation (1) using linear part of the discharge curve.

$$C = I_A \times \Delta t \times \Delta V^{-1} \quad (1)$$

Where  $I_A$  is the current for voltage range  $\Delta V$   $\Delta t$  is the time duration.

The capacitance values were obtained for different current densities. Highest areal capacitance of  $9.05 \text{ mF cm}^{-2}$  and volumetric capacitance  $12.92 \text{ mF cm}^{-3}$  were obtained for  $0.05 \text{ mA cm}^{-2}$ . The volumetric capacitance was calculated for various current densities ranging from  $0.05 \text{ mA cm}^{-2}$  to  $1 \text{ mA cm}^{-2}$  [figure 4A.4 e]. The slopes of the charge and discharge curves are similar to each other which indicates high columbic efficiency of the device ( $> 95\%$ ). The equivalent series resistance of the device can be calculated from the IR drop in the discharge curve. The resistance value is observed  $\sim 125 \text{ } \Omega \text{ cm}^{-2}$  at different current densities as mentioned above.



*Figure 4A.5: Bode plot of micro-supercapacitor*

Figure 4A.4 b represents AC impedance spectroscopy result for the device. From the intercept at the x-axis of the Nyquist plot [inset of figure 4A.4 b] the equivalent series resistance (ESR) can be calculated. The ESR of the device is found to be  $\sim 140 \text{ } \Omega \text{ cm}^{-2}$ . The ESR value is comparable to the value obtained from the IR drop in the discharge curve. In this plot a high frequency semicircle is observed which is quite common in case of porous electrodes, and is mostly due

to the high resistance to the ionic transport in the smaller pores.<sup>33</sup> The bode phase plot of figure 4A.5 shows that the phase shift is close to 90° in the low frequency region which indicates near ideal electrical double layer charge storage behavior, with negligible contribution of redox or faradaic type charge storage behavior.<sup>34</sup>

The Energy density and power density are very important parameters for practical applications of micro-supercapacitor. These were calculated using the formulae (2) and (3).

$$E = \frac{C_v (\Delta V)^2}{2 \times 3600} \quad (2)$$

$$P = \frac{E \times 3600}{\Delta t} \quad (3)$$

where,  $C_v$  is the volumetric capacitance,  $\Delta V$  is the voltage window, E is the energy density, P is the power density,  $\Delta t$  is the discharge time. Ragone plot of the device is shown in the figure 4A.4 f. The maximum energy density obtained with our device is 1.8 mW h cm<sup>-3</sup> (corresponding power density is 35.8 mW cm<sup>-3</sup>) at 0.05 mA cm<sup>-2</sup> and the maximum power density obtained is 720 mW cm<sup>-3</sup> (corresponding energy density is 0.7 mW h cm<sup>-3</sup>) at 1 mA cm<sup>-2</sup>, respectively.

No.	Materials	Electrolyte	Capacitance	Energy Density	Power Density	Ref no.
1.	Ink-Carbon Fiber	LiCl-PVA	4.3 mF cm <sup>-2</sup>	0.034 mW h cm <sup>-2</sup>	0.38 μW cm <sup>-2</sup>	<sup>36</sup> Flexible thread structure
2.	Ordered Mesoporous Carbon	PVA-KOH	35.67 mF cm <sup>-2</sup> at 0.1 mA	2.16 mW h cm <sup>-2</sup>	7.3 mW cm <sup>-2</sup>	<sup>37</sup> Flexible wire
3.	CNT	Ionogel	430 μF cm <sup>-2</sup> (86 mF cm <sup>-3</sup> )	0.1–0.5 μW h cm <sup>-2</sup>	10 mW cm <sup>-2</sup>	<sup>38</sup> Flexible Micro
4.	Carbon from polyimide	PVA-H <sub>3</sub> PO <sub>4</sub>	800 μF cm <sup>-2</sup> 240 mF cm <sup>-3</sup>	-	-	<sup>39</sup> Flexible Micro
5.	Carbon nanoparticles	PVA-H <sub>3</sub> PO <sub>4</sub>	6.1 mF cm <sup>-2</sup> at 5 mVs <sup>-1</sup> 2.4 mF cm <sup>-2</sup> at 100 mVs <sup>-1</sup>	-	-	<sup>40</sup> Flexible strip
6.	SWNT/rGO fiber	PVA- H <sub>3</sub> PO <sub>4</sub>	300F cm <sup>-3</sup>	6.3 mW h cm <sup>-3</sup>	-	<sup>41</sup> Flexible thread structure
7.	rGO	PVA	<0.4 mF cm <sup>-2</sup>	0.01 μW h cm <sup>-2</sup>	9 μW cm <sup>-2</sup>	<sup>42</sup> Flexible flip-chip

8.	Graphene	0.5M Na <sub>2</sub> SO <sub>4</sub>	0.5 mF cm <sup>-2</sup>	0.07 μW h cm <sup>-2</sup>	7.5 μW cm <sup>-2</sup>	Flexible Micro <sup>43</sup>
9.	OLC	IL mixture	1.1 mF cm <sup>-2</sup>	4.2 μW h cm <sup>-2</sup>	240 mW cm <sup>-2</sup>	Flexible Micro <sup>44</sup>
10.	CDC	1 M Et <sub>4</sub> NBF <sub>4</sub>	1.5 mF cm <sup>-2</sup>	0.8 μW h cm <sup>-2</sup>	84 mW cm <sup>-2</sup>	Hard Substrate Micro <sup>45</sup>
11.	CNT	PVA-based	1.8 mF cm <sup>-2</sup>	0.2 μW h cm <sup>-2</sup>	1.3 W cm <sup>-2</sup>	Hard Substrate Micro <sup>46</sup>
12.	Laser Scribed Graphene (LSG)-MSC	PVA-H <sub>2</sub> SO <sub>4</sub>	3.05 F cm <sup>-3</sup>	0.32 mW cm <sup>-3</sup>	50W cm <sup>-3</sup>	Flexible Micro <sup>5</sup>
13.	Graphene/CNTs	1M Na <sub>2</sub> SO <sub>4</sub> IL	2.16 mF cm <sup>-2</sup> (1.08 F cm <sup>-3</sup> ) 3.93 mF cm <sup>-2</sup> (1.96 F cm <sup>-3</sup> )	0.16 mW h cm <sup>-3</sup> 2.42 mWhcm <sup>-3</sup>	115 W cm <sup>-3</sup> @ 400 V s <sup>-1</sup> 135 W cm <sup>-3</sup> 400 V s <sup>-1</sup>	Micro <sup>47</sup>
14.	Photoresist pyrolysed carbon	Ionogel	600 μF cm <sup>-2</sup>	3 mW h cm <sup>-3</sup>	26 W cm <sup>-3</sup>	Hard Substrate Micro <sup>6</sup>
15.	<b>Mushroom Derived Carbon (MDC)</b>	PVA-H <sub>2</sub> SO <sub>4</sub>	<b>9 mF cm<sup>-2</sup> 12.92 F cm<sup>-3</sup></b>	<b>1.8 mW h cm<sup>-3</sup> at 0.05 mA cm<sup>-2</sup></b>	<b>720 mW cm<sup>-3</sup> at 1 mA cm<sup>-2</sup></b>	<b>Our Work</b>

*T*

*Table 4A.1: Comparison of device performance*

A comparison of the electrochemical performance of our device with other devices reported in the literature is given in the Table 4A.1. The number of these interesting publications with impressive results clearly brings out the current interest in this subject. As may be seen, the performance of our device is either comparable or better than most entries under Nos. 1-10, thanks to the peculiar character of our mushroom derived carbon (MDC). In the devices under entries 11, 13 and 14, the power density is very high but all of them are fabricated on hard substrates. Moreover, for the case of entry no. 14 ionogel (organic electrolyte) is used. In the case of entry no. 13 is very high scan rate of 400 V s<sup>-1</sup> is employed. The laser scribed graphene based flexible micro-supercapacitor device reported in the entry 12 has very high power density (50W cm<sup>-3</sup>), however lower energy density and volumetric capacitance than our report. Also, for this case the scan rate is not given to allow a perfect comparison. These statements reveal that our work conforms to this family of interesting studies reported in the recent literature and will invite further discussion.

The stability of the device was examined by charge-discharge measurement [figure 4A.6 a]. The capacitance was calculated from each cycle and plotted against cycle number. The figure also represents the percent retention of the capacitance. The stability measurement was conducted up to 15000 cycles. The device shows extremely high stability during the course of the measurement. Initially the capacitance value increases till 10000 cycles and after that the capacitance value is seen to stabilize over the next 5000 cycles. This can be explained on the basis of interaction between the electrolyte and the electrode. In the case of gel electrolyte, due to highly dense matrix, the mobility of the ions is low as compared to liquid electrolyte.<sup>35</sup> Thus the percolation of ions inside the porous electrode takes longer time than in the case of liquid electrolyte. Hence with increasing cycle number, deeper pores of the electrode material get accessed by the ions of the electrolyte which in turn gradually increases the capacitance of the device. This is observed in the first 10,000 cycles. After complete percolation access is established for the ions inside the electrode material the capacitance of the device gets stabilised, which is observed over the next 5,000 cycles.

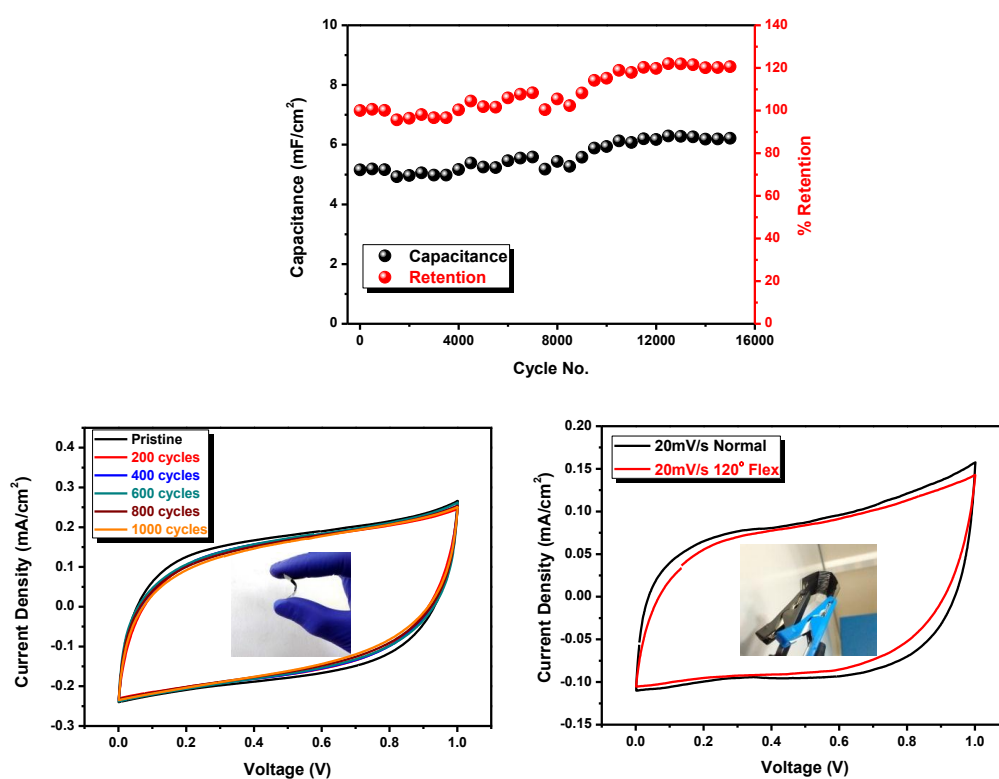


**Figure 4A.6:** Stability and flexibility experiments a) stability of the device upto 15k cycles, b)cyclic voltammetry of the device at 20mV/s with different bending

*cycles, and c) cyclic voltammetry comparison of the device at 20mV/s in normal and 120° bending condition*

Flexibility of the device was also stated in two ways. First, by the cyclic flexibility testing method, where the device is bent at an angle of 60° several times and the CV is measured. Figure 4A.6 b shows the stability under flexibility cycling. After 1000 bending cycles the device almost retains its performance upto 89% as compared to the pristine device. The other way of testing the flexibility was to observe the device performance under the bent condition. Figure 4A.6 c shows the comparative device performance in flat and 120° bent device conditions. In this case also the device retains its performance upto 88% of its original value. We performed comparative impedance analysis of the samples before and after the multi-cycle bending at 60° (figure 4A.7 a) and static bending at 120° (figure 4A.7 b). Negligible change was noted in the impedance values which is commensurate with the results of CV studies.

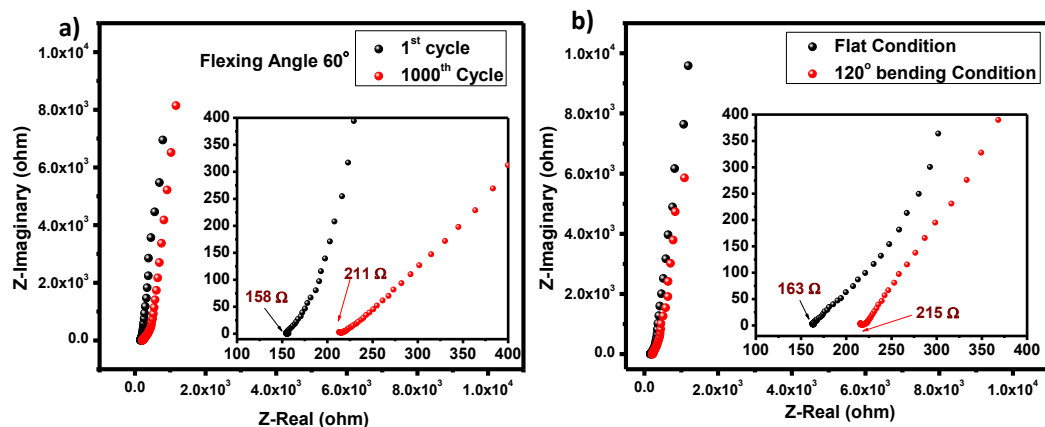


*Figure 4A.7 a) Impedance comparison between pristine device and after 1000 bending cycles (60° bending angle) and b) impedance comparison between flat and 120° bending condition*

### 4A.3 Conclusion

In summary, we have demonstrated highly flexible and extremely stable EDLC micro-supercapacitor device using mushroom derived carbon as the electrode material. The device is fabricated using laser scribing, which is a facile, very fast and highly scalable method. The device shows 89% capacitance retention upto 1000 bending (60°) cycles and 88% performance retention under 120° bent

condition. The device also shows excellent cyclic stability (95% retention) over 15k cycles. The highest volumetric capacitance shown by the device is  $12.92 \text{ F cm}^{-3}$  at  $0.05 \text{ mA cm}^{-2}$ . The device also shows a  $1.8 \text{ mW h cm}^{-3}$  energy density at  $0.05 \text{ mA cm}^{-2}$  and  $720 \text{ mW cm}^{-3}$  power density at  $1 \text{ mA cm}^{-2}$ . These values are quite impressive for a practical flexible micro-supercapacitor, especially given the flexing as well as cyclic stability of the device reported herein. Our electrode material, fabrication scheme, and the device would find good applicability in the domain of flexible microelectronics.

#### 4A.4 References:

1. J. Chmiola, C. Largeot, P.-L. Taberna, P. Simon, Y. Gogotsi, *Science* **2010**, 328, 480.
2. D. Pech, M. Brunet, H. Durou, P. Huang, V. Mochalin, Y. Gogotsi, P.-L. Taberna, P. Simon, *Nat Nano* **2010**, 5, 651.
3. Z. S. Wu, K. Parvez, X. Feng, K. Mullen, *Nat Commun* **2013**, 4.
4. M. Beidaghi, C. Wang, *Advanced Functional Materials* **2012**, 22, 4501.
5. M. F. El-Kady, R. B. Kaner, *Nat Commun* **2013**, 4, 1475.
6. S. Wang, B. Hsia, C. Carraro, R. Maboudian, *Journal of Materials Chemistry A* **2014**, 2, 7997.
7. L. Cao, S. Yang, W. Gao, Z. Liu, Y. Gong, L. Ma, G. Shi, S. Lei, Y. Zhang, S. Zhang, R. Vajtai, P. M. Ajayan, *Small* **2013**, 9, 2905.
8. M. F. El-Kady, R. B. Kaner, *ACS Nano* **2014**, 8, 8725.
9. W. Gao, N. Singh, L. Song, Z. Liu, A. L. M. Reddy, L. Ci, R. Vajtai, Q. Zhang, B. Wei, P. M. Ajayan, *Nat Nano* **2011**, 6, 496.
10. J. Li, Q. Wu, G. Zan, *RSC Advances* **2014**, 4, 35186.
11. P. Cheng, S. Gao, P. Zang, X. Yang, Y. Bai, H. Xu, Z. Liu, Z. Lei, *Carbon* **2015**, 93, 315.



12. P. Simon, Y. Gogotsi, *Nat Mater* **2008**, 7, 845.
13. L. L. Zhang, X. S. Zhao, *Chemical Society Reviews* **2009**, 38, 2520.
14. A. G. Pandolfo, A. F. Hollenkamp, *Journal of Power Sources* **2006**, 157, 11.
15. M. Biswal, A. Banerjee, M. Deo, S. Ogale, *Energy & Environmental Science* **2013**, 6, 1249.
16. M. Wahid, D. Puthusseri, D. Phase, S. Ogale, *Energy & Fuels* **2014**, 28, 4233.
17. H. Wang, Z. Li, J. K. Tak, C. M. B. Holt, X. Tan, Z. Xu, B. S. Amirkhiz, D. Harfield, A. Anyia, T. Stephenson, D. Mitlin, *Carbon* **2013**, 57, 317.
18. H. Wang, Z. Xu, A. Kohandehghan, Z. Li, K. Cui, X. Tan, T. J. Stephenson, C. K. King<sup>TM</sup>ondu, C. M. B. Holt, B. C. Olsen, J. K. Tak, D. Harfield, A. O. Anyia, D. Mitlin, *ACS Nano* **2013**, 7, 5131.
19. Z. Li, Z. Xu, X. Tan, H. Wang, C. M. B. Holt, T. Stephenson, B. C. Olsen, D. Mitlin, *Energy & Environmental Science* **2013**, 6, 871.
20. D. Puthusseri, V. Aravindan, B. Anothumakkool, S. Kurungot, S. Madhavi, S. Ogale, *Small* **2014**, 10, 4395.
21. D. Puthusseri, V. Aravindan, S. Madhavi, S. Ogale, *Energy & Environmental Science* **2014**, 7, 728.
22. P. Yadav, A. Banerjee, S. Unni, J. Jog, S. Kurungot, S. Ogale, *ChemSusChem* **2012**, 5, 2159.
23. L. Qie, W. Chen, H. Xu, X. Xiong, Y. Jiang, F. Zou, X. Hu, Y. Xin, Z. Zhang, Y. Huang, *Energy & Environmental Science* **2013**, 6, 2497.
24. M. Boota, M. P. Paranthaman, A. K. Naskar, Y. Li, K. Akato, Y. Gogotsi, *ChemSusChem* **2015**, 8, 3576.

25. A. C. Ferrari, J. C. Meyer, V. Scardaci, C. Casiraghi, M. Lazzeri, F. Mauri, S. Piscanec, D. Jiang, K. S. Novoselov, S. Roth, A. K. Geim, *Physical Review Letters* **2006**, *97*, 187401.
26. A. Gupta, G. Chen, P. Joshi, S. Tadigadapa, Eklund, *Nano Letters* **2006**, *6*, 2667.
27. C. N. R. Rao, A. K. Sood, K. S. Subrahmanyam, A. Govindaraj, *Angewandte Chemie International Edition* **2009**, *48*, 7752.
28. A. Das, B. Chakraborty, A. K. Sood, *Bulletin of Materials Science* **2008**, *31*, 579.
29. A. C. Ferrari, *Solid State Communications* **2007**, *143*, 47.
30. Y. Hao, Y. Wang, L. Wang, Z. Ni, Z. Wang, R. Wang, C. K. Koo, Z. Shen, J. T. L. Thong, *Small* **2010**, *6*, 195.
31. P. B. Balbuena, K. E. Gubbins, *Langmuir* **1993**, *9*, 1801.
32. J.-S. Lee, S.-I. Kim, J.-C. Yoon, J.-H. Jang, *ACS Nano* **2013**, *7*, 6047.
33. J. Nielsen, J. Hjelm, *Electrochimica Acta* **2013**, *115*, 31.
34. A. Ghosh, Y. H. Lee, *ChemSusChem* **2012**, *5*, 480.
35. J. P. Southall, H. V. S. A. Hubbard, S. F. Johnston, V. Rogers, G. R. Davies, J. E. McIntyre, I. M. Ward, *Solid State Ionics* **1996**, *85*, 51.
36. S. Dai, H. Guo, M. Wang, J. Liu, G. Wang, C. Hu, Y. Xi, *Journal of Materials Chemistry A* **2014**, *2*, 19665.
37. X. Dong, Z. Guo, Y. Song, M. Hou, J. Wang, Y. Wang, Y. Xia, *Advanced Functional Materials* **2014**, *24*, 3405.
38. H. Ben, M. Julian, W. Shuang, I. Jung Bin, C. Carlo, P. Dimos, P. G. Costas, M. Roy, *Nanotechnology* **2014**, *25*, 055401.

39. J. B. In, B. Hsia, J.-H. Yoo, S. Hyun, C. Carraro, R. Maboudian, C. P. Grigoropoulos, *Carbon* **2015**, *83*, 144.
40. L. Yuan, X.-H. Lu, X. Xiao, T. Zhai, J. Dai, F. Zhang, B. Hu, X. Wang, L. Gong, J. Chen, C. Hu, Y. Tong, J. Zhou, Z. L. Wang, *ACS Nano* **2011**, *6*, 656.
41. D. Yu, K. Goh, H. Wang, L. Wei, W. Jiang, Q. Zhang, L. Dai, Y. Chen, *Nat Nano* **2014**, *9*, 555.
42. J. J. Yoo, K. Balakrishnan, J. Huang, V. Meunier, B. G. Sumpter, A. Srivastava, M. Conway, A. L. Mohana Reddy, J. Yu, R. Vajtai, P. M. Ajayan, *Nano Letters* **2011**, *11*, 1423.
43. A. Ferris, S. Garbarino, D. Guay, D. Pech, *Advanced Materials* **2015**, *27*, 6625.
44. P. Huang, D. Pech, R. Lin, J. K. McDonough, M. Brunet, P.-L. Taberna, Y. Gogotsi, P. Simon, *Electrochemistry Communications* **2013**, *36*, 53.
45. P. Huang, M. Heon, D. Pech, M. Brunet, P.-L. Taberna, Y. Gogotsi, S. Lofland, J. D. Hettinger, P. Simon, *Journal of Power Sources* **2013**, *225*, 240.
46. T. M. Dinh, D. Pech, M. Brunet, A. Achour, *Journal of Physics: Conference Series* **2013**, *476*, 012106.
47. J. Lin, C. Zhang, Z. Yan, Y. Zhu, Z. Peng, R. H. Hauge, D. Natelson, J. M. Tour, *Nano Letters* **2012**, *13*, 72.

## Chapter 4

### Section B

# **A Robust Highly Flexible All-solid-state Micro Pseudocapacitor Based on Ternary Oxide $\text{CuCo}_2\text{O}_4$ having Ultrathin Porous Nanowall Type Morphology Blended with CNT**

In this chapter we demonstrate a facile approach to the fabrication of all solid state flexible interdigitated micro pseudocapacitor device using pre-synthesized  $\text{CuCo}_2\text{O}_4$  (CCO) ternary metal oxide as the electrode material. The hydrothermally synthesized CCO exhibits a peculiar 3D interconnected aligned porous nanowall type morphology which is highly desirable for storage as well as charge transfer. The device is fabricated using  $\text{CO}_2$  laser scribing technique and the PVA- $\text{H}_3\text{PO}_4$  gel electrolyte is used as the electrolyte. The as-synthesized CCO as well as its blend with 10 wt.% CNT are examined for the electrochemical performance. CNT blending is shown to reduce the charge transfer resistance dramatically, thereby enhancing the pseudo capacitance. The areal capacitance of  $2.29 \text{ mF cm}^{-2}$  is obtained from the solid state device. Moreover, the CCO-CNT electrode also shows a high stability upto 9000 cycles without a sign of further decay. Importantly, the devices also retain over 65% of their initial capacitance after 1000 large angle ( $60^\circ$ ) bending cycles and 93% of the initial capacitance under  $120^\circ$  bending condition, thanks to the mechanical flexibility afforded by CNTs without disrupting conducting paths.

## 4B.1 Introduction

In recent years, micro-scale flexible electronic devices are at the technological focus. To cope up with this current trend of device development, on-board power sources are also being developed quite rapidly. The foremost amongst these are the flexible supercapacitors and batteries. Integration of these power sources with the flexible device configurations in 3D architectures is a highly challenging task, hence planer micro supercapacitors, which are easier to fabricate and integrate, are gaining importance in this research field. They also offer some technical benefits. Indeed, while the conventional supercapacitors are positioned in between capacitors and batteries in terms of energy density and power density on the Ragone plot, the planer micro supercapacitors offer sufficiently high power density (even higher than conventional supercapacitors and batteries) due to their short ion-diffusion length.<sup>1-5</sup> Several efforts have been employed to improve the performance of the micro supercapacitor devices which include different fabrication techniques as well as the implementation of different new materials as electrodes.

In so far as the fabrication techniques are concerned, various methods like lithography, chemical vapour deposition (CVD), thermal evaporation, laser based techniques etc.<sup>6-11</sup> have been used to make micro patterned devices. In the materials context, typically three types of materials have used as electrodes, namely the functional carbon materials, conducting polymers and transition metal oxides. Carbon materials are found to have low cost with extremely high surface area, good electrical conductivity and chemical stability.<sup>12</sup> Hence, such materials are considered to be ideal for electrical double-layer capacitors, but the problem observed over many years is that they usually suffer from low capacitance.<sup>13</sup> To overcome this limitation, conducting polymers with excellent intrinsic conductivity have been studied and are found to render have higher electrochemical performance than carbon. However, in this case it is seen that during the charging–discharging process, the cycle-life span of the electrode integrity is extremely poor due to its substantial expansion and contraction.<sup>13,14</sup> As compared to these two types of materials, transition metal oxides offer the specific advantage of possessing multiple oxidation states which favour fast redox

reactions and hence results in a much higher electrochemical performance.<sup>13,15</sup> At the same time, these studies have also revealed that most metal oxides are restricted by their poor electrical conductivity and low energy density.<sup>13</sup> Therefore, it is important to explore new and promising electrode candidates that are inexpensive, environmentally friendly and have superior electrochemical performance. Towards this end, binary transition metal oxides or hydroxides such as RuO<sub>2</sub>, MnO<sub>2</sub>, Ni(OH)<sub>2</sub>, VS<sub>2</sub> etc.<sup>16-19</sup> have attracted attention as promising electrode materials for micro supercapacitors (flexible in some cases). However, ternary metal oxides which allow interesting dual cation valence sharing options have not been yet been used in this context. In an isolated interesting recent report a micro-pseudocapacitor based on ternary chalcogenide has been tested wherein the process of electrodeposition combined with photolithography was employed to fabricate the device.<sup>20</sup>

In this present work, we have fabricated all solid state flexible micro pseudocapacitor using the interesting dual mixed-valent CuCo<sub>2</sub>O<sub>4</sub> (CCO) material, which was synthesized using non-templated hydrothermal method. The details of the synthesis and consequences of parametric variations will be reported separately. Briefly, the synthesis involved the use of Cu(NO<sub>3</sub>)<sub>2</sub> and Co(NO<sub>3</sub>)<sub>2</sub> as precursors and Urea as the stabilizing agent. Hydrothermal synthesis led to an appealing morphology in the form of an assembly of ultrathin platelets with a fairly high surface area of 45 m<sup>2</sup> g<sup>-1</sup> for an oxide nanostructure.

For fabrication of interdigitated micro pseudocapacitor we used an ultrafast CO<sub>2</sub> laser scribing technique.<sup>11</sup> The main advantage of this technique is that we can use any type of pre-synthesized material according to the need for the device. This technique also offers the freedom of using both *in-situ* and *ex-situ* composites materials as electrode. Generally metal oxides suffer from high charge transfer resistance, which limits their performance. Therefore, in this work we have used an *ex-situ* composite of CCO and small amount of carbon nanotube (CNT) (10 wt.%) as the electrode material. This was seen to enhance the device performance dramatically by reducing the charge transfer resistance. The stability of the device could be improved from 200 cycles (60% retention) to 5450 cycles (91% retention). Importantly, the devices also showed high degree of flexibility without

performance degradation. The electro-mechanical flexibility afforded by CNT to the functional electrode comprising of an inorganic mixed-valent oxide (hard-soft nanocomposite) is key to this performance.

## **4B.2 Experimental Section**

### **4B.2.1 Materials**

All the chemicals used in the present study were of analytical grade (AR).  $\text{Cu}(\text{NO}_3)_2 \cdot 3\text{H}_2\text{O}$  (>99 %) and  $\text{Co}(\text{NO}_3)_2 \cdot 6\text{H}_2\text{O}$  (>99 %) and were obtained from Merck and labchem, respectively. Urea was procured from Merck, Mumbai, India. Double distilled water was used to prepare the solutions.

### **4B.2.2 Preparation of CCO nanosheets**

The copper cobalt oxide nano-sheets were synthesized by the hydrothermal method. Aqueous solutions of the precursor salts (Cu & Co) with a ratio of 1:2 ( $1 \times 10^{-3}$  M:  $2 \times 10^{-3}$  M) were mixed together initially in a beaker followed by the stirring for 30 min. In this mixture urea was then added and subjected to constant stirring for 30 min under ambient atmosphere. The synthesis was carried out at in a teflon autoclave at  $120^\circ\text{C}$  for 16 hours. The product appeared as a black precipitate which was washed with double distilled water. The clean products were then dried in an oven at  $80^\circ\text{C}$  for 6 h and then annealed at  $350^\circ$  for 2 hours. The characterization was done by using various techniques such as field emission scanning electron microscopy (FESEM), X-ray diffraction etc.

### **4B.2.3 Fabrication of flexible micro-supercapacitor**

The flexible micro-supercapacitors were fabricated in two steps. Initially, (80%) (comprising of CCO and CNT composite 70:10 wt:wt), conducting additive (acetylene black) (15%) and KynarPolyvinylidene fluoride (PVDF) as binder (5%) were mixed together to make a paste using N-methyl-2-pyrrolidone (NMP) as solvent. The pastewas coated on the ITO/PET substrate and dried in vacuum oven at  $80^\circ\text{C}$  overnight to remove the solvent completely. In the second step, the substrate was scribed using  $\text{CO}_2$  laser (14.4-15.6 watt and  $10.6 \mu\text{m}$  wavelength). Prior to testing the PVA- $\text{H}_3\text{PO}_4$  (1M) gel electrolyte was added to the device.

#### 4B.2.4 Preparation of gel electrolyte

1 gm of PVA was put into 10 mL of D.I. water and stirred at 90°C till dissolution was complete. After full dissolution the temperature of the solution was decreased to 40°C and H<sub>3</sub>PO<sub>4</sub> was added under vigorous stirring condition according to the required molarity. After addition, the temperature was increased to 70°C and kept it at the same value for a brief time for proper mixing of the acid with PVA solution.

#### 4B.2.5 Characterization technique

The FESEM analysis was performed on an upgraded field emission scanning electron microscope (Hitachi S-4200). The X-ray diffractometer (XRD) measurements were carried out on a Philips X'Pert PRO diffractometer with nickel-filtered Cu K $\alpha$  radiation ( $\lambda = 1.5405 \text{ \AA}$ ). The diffractograms were recorded at a scanning rate of  $1^\circ \text{ min}^{-1}$  between  $20^\circ$  to  $80^\circ$ . Laser scribing was done by using Universal Laser Systems® VersaLASER® VLS 2.30. All electrochemical measurements were performed by using BioLogicVMP3 multichannel potentiostat-galvanostat. Cyclic voltammetry measurements were recorded at scan rates from 5 to  $100 \text{ mV s}^{-1}$  over the potential range of 0 to 1V. Charge-discharge measurements were performed at current densities from 0.1 to 1 mA in the potential window of 0 to 1V. Transmission electron microscopy (TEM) was performed using JEM 2200FS TEM microscope operating at an accelerating voltage of 200 kV).

### 4B.3 Results and Discussion

#### 4B.3.1 X-ray Diffraction

Figure 4B.1 a depicts the x-ray diffraction pattern of the CuCO<sub>2</sub>O<sub>4</sub> material obtained by the hydrothermal method. The sample was prepared using 1:2 cation ratio of copper and cobalt precursors. The diffraction pattern obtained for this sample shows main peaks at  $2\theta \sim 31.3^\circ$  (220),  $36.3^\circ$  (311),  $\sim 38.95^\circ$  (222),  $\sim 45.0^\circ$  (400),  $\sim 56.02^\circ$  (422),  $\sim 59.5^\circ$  (511) and  $\sim 65.0^\circ$  (440) which are characteristic of the spinel CuCO<sub>2</sub>O<sub>4</sub>, face centred cubic structure with a space group: Fd3m (JCPDS no -01-1155). In Cu-Co-O system, the structure may be viewed as Cu<sup>2+</sup> primarily



substituting for the  $\text{Co}^{2+}$  tetrahedral sites in  $\text{Co}_3\text{O}_4$ , which is represented as  $[(\text{Co}^{2+}(\text{t}) [\text{Co}^{3+}(\text{o})]_2[\text{O}^{2-}]_4$ . Since Co can also acquire 2+ valence, its partial occupancy in the tetrahedral sites cannot be ruled out.

Two additional peaks at  $\sim 35.5^\circ$  (311),  $\sim 49.3^\circ$  (400) can also be noted in the XRD pattern which corresponding to the CuO phase. We have seen that these are always present in differing proportion in the hydrothermally synthesized CCO material which gives us the interesting and desired ultrathin 3D interconnected nanowall morphology. When other synthesis methods are used as reported in the literature, the CuO

contribution can be reduced substantially, but the nanowall morphology is not realized. Since the peculiar morphology is of primary importance for the battery electrode application we decided to live with the presence of the second phase.

Importantly, some concentration of copper coming out from the CCO matrix can also render a defect states with enhanced transport properties. Moreover the specific capacitance of CuO is also quite high<sup>21,22</sup> hence should not affect the overall performance of the device due to its presence.

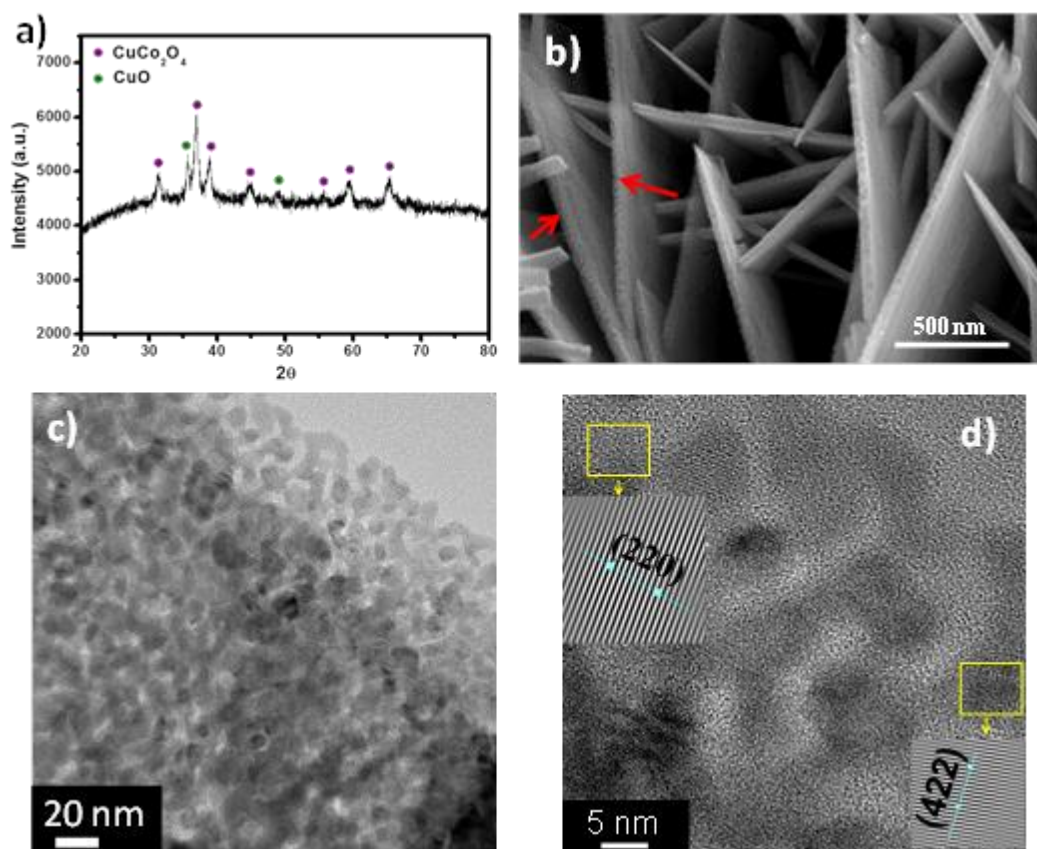


**Figure 4B.1:** a) X-ray diffraction pattern and b) FESEM image of  $\text{CuCo}_2\text{O}_4$  nanowalls (where intra-wall porosity is highlighted by red arrows) for the hydrothermally as-synthesized sample. c) and d) TEM images of  $\text{CuCo}_2\text{O}_4$  showing the crystalline grain and d-spacing respectively.

#### 4B.2.2 Electron Microscopy:

Figure 4B.1 b shows representative FE-SEM image of the synthesized sample which reveals a peculiar 3D interconnected nanowall morphology. Figure 4B.1 b shows that nanowalls are aligned and distributed homogeneously. Interestingly, each nanowall appears to penetrate across another nanowall generating an open configuration. Moreover, as seen in Figure 4B.1 b each nanowall is also in the form of a planar nanoparticulate self-assembly. Such nanoscale porosity combined with the 3D interconnectivity of the nanowalls is highly desirable for storage as well as electron transfer. The average width of the nanowalls is about 70 nm. The elemental mapping of the electrode material is given in the figure 4B.2. Figures 4B.1 c and 1 d present the HRTEM images for the CCO sample. The nanowalls appear to be porous on the nanoscale and are in the form of electronically interconnected crystalline grains (figure 4B.1 c). From the lattice fringes of figure

4B.1 d, the calculated d-value corresponds to the (220) and (422) planes of the cubic  $\text{CuCo}_2\text{O}_4$  phase.

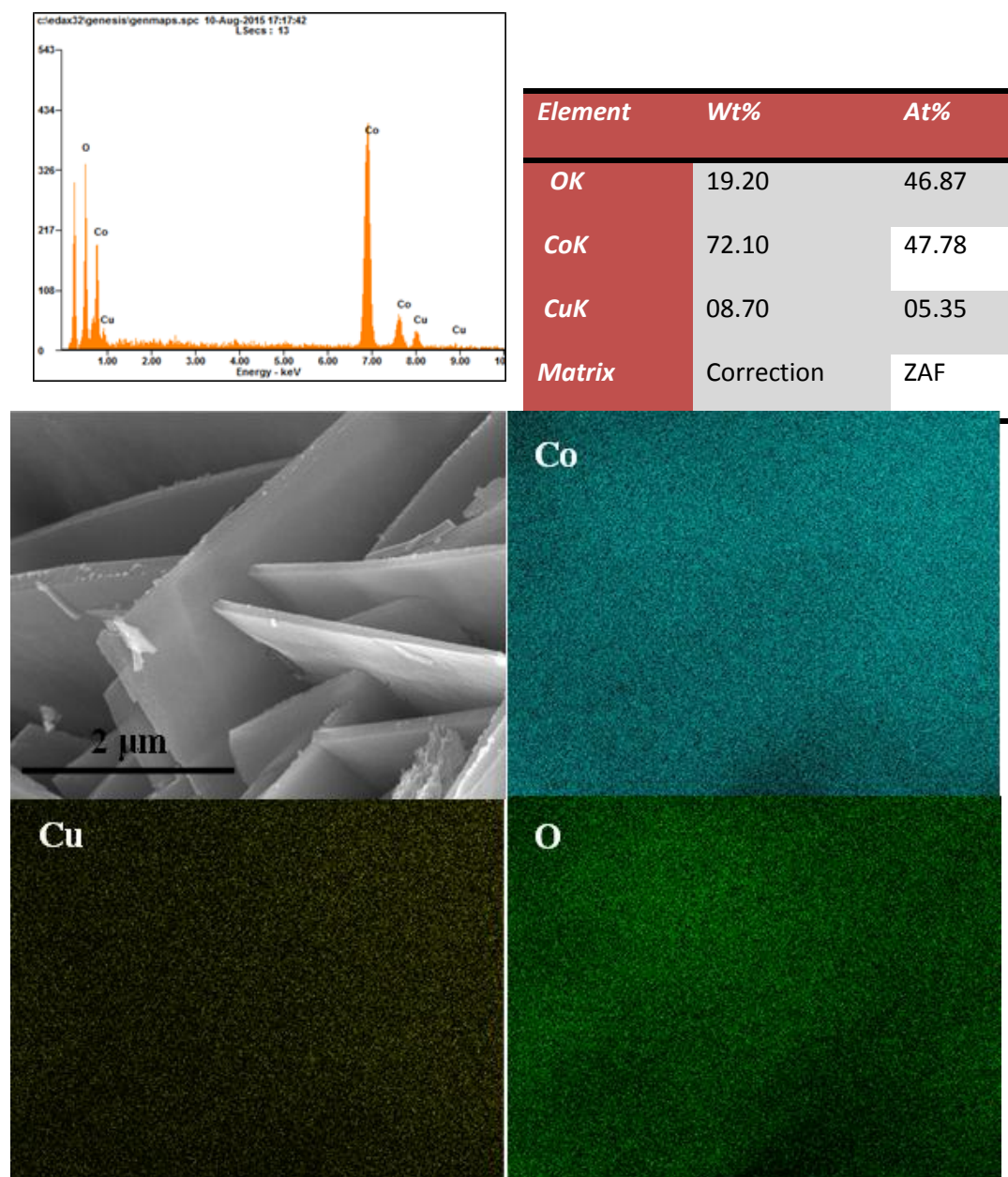


*Figure 4B.2: Elemental analysis of the electrode material. a) EDAX graph, b) elemental analysis and c) elemental mapping.*

### 4B.3.3 Device Fabrication:

Figure 4B.3 a shows the schematic representation of the device fabrication procedure.<sup>11</sup> The width and the length of each electrode are 0.3 mm and 5 mm, respectively. The average thickness of the electrodes is 15  $\mu\text{m}$ . The inter-electrode distance between the two electrodes is 100  $\mu\text{m}$ . The electrode dimensions were calculated from the SEM images. Each device contains a total of 18-20 electrodes (9-10 on each sides). Figure 4B.3 b shows a typical FESEM image of the CCO-CNT electrode which reveals the nanowalls and CNTs mixed across the electrode.

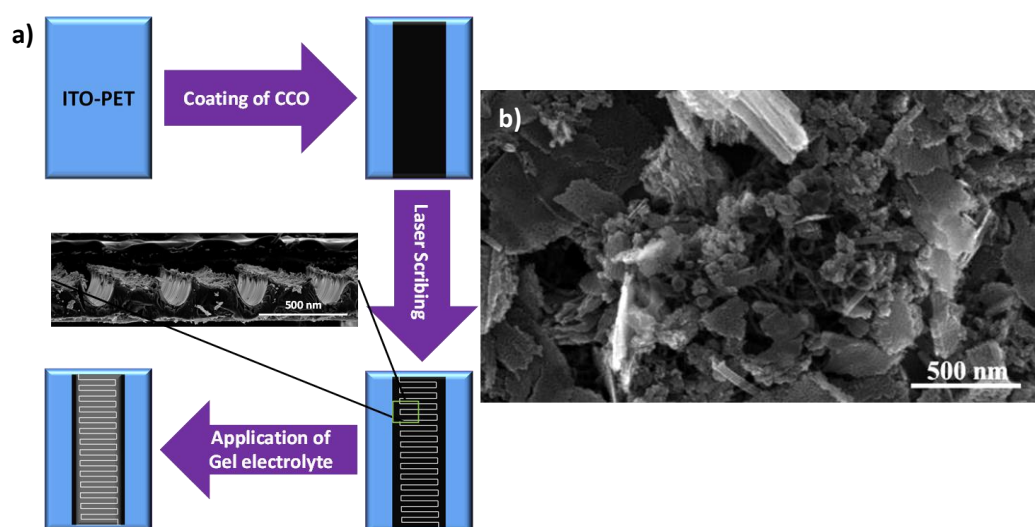
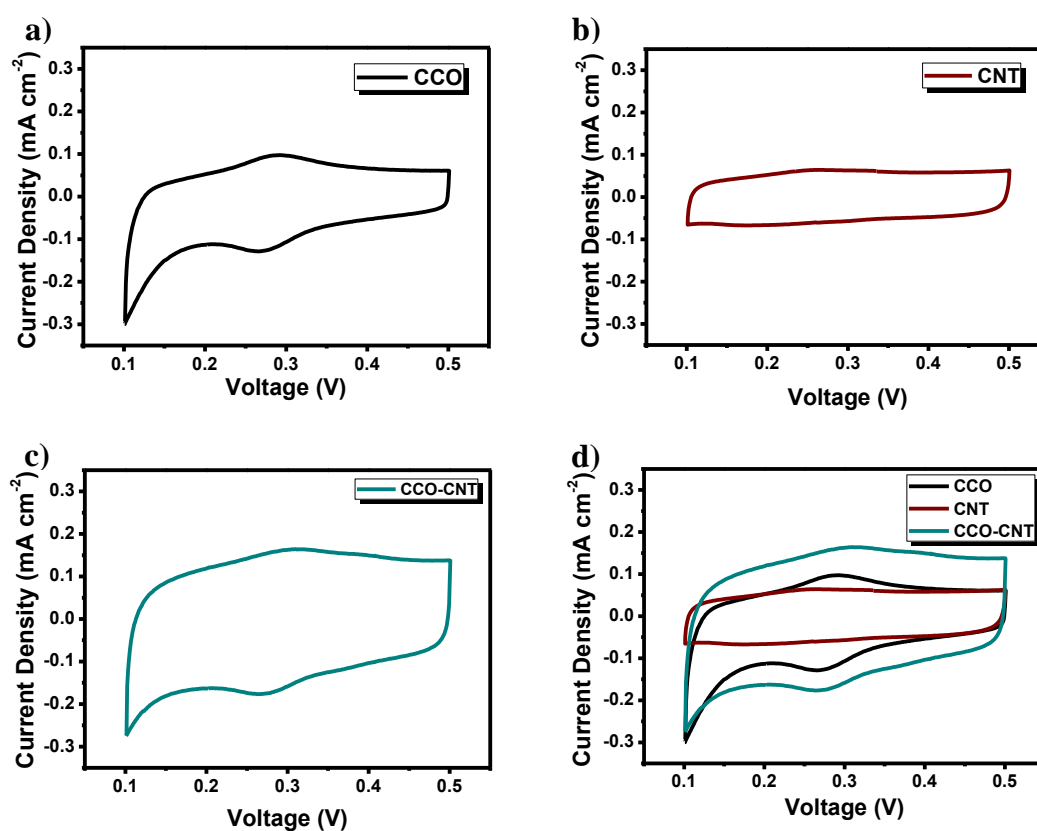


**Figure 4B.3:** a) Schematic of the device fabrication for the study of the CCO-CNT based flexible pseudocapacitor; b) FESEM image of a typical CCO-CNT electrode where CCO nanowalls are interconnected through CNTs (shown by red arrow).

### 4B.3.4 Electrochemical Measurements:

As stated earlier, the electrochemical performance of the devices was measured using PVA (10wt.%)– $\text{H}_3\text{PO}_4$  (1M) gel electrolyte. For all the devices, the cyclic voltammetry (CV) study was done across a voltage range from 0 V to 1 V at different scan rate starting from 5  $\text{mV s}^{-1}$  to 100  $\text{mV s}^{-1}$  (Figure 4B.5). Figure 4B.6 a shows the CV data recorded at 20  $\text{mV s}^{-1}$  for the CCO and CCO+CNT electrode based devices. To confirm the nature of the capacitance we performed the CV in  $\text{H}_3\text{PO}_4$  electrolyte with 3 electrode system where CCO (or CCO+ 10% CNT) was used as the working electrode, graphite paper as the counter electrode and standard  $\text{H}_2$  electrode as the reference electrode (Figure 4B.4). In this experiment

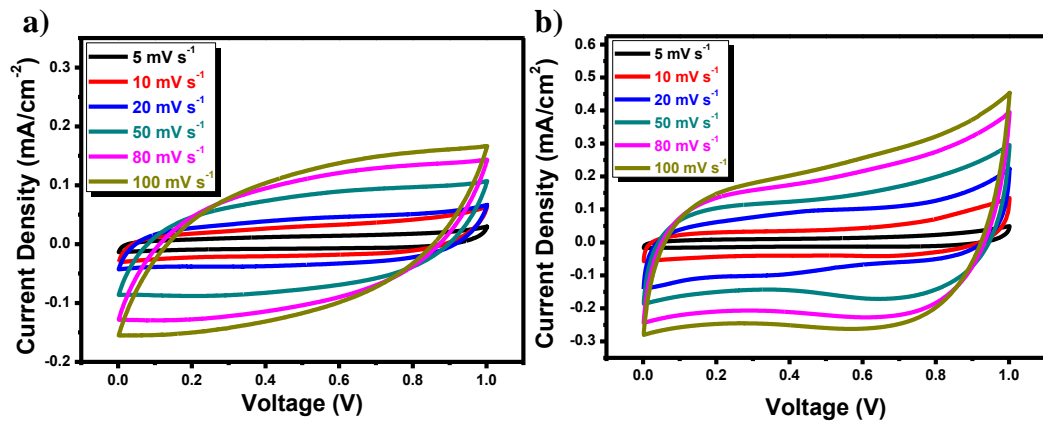
we clearly observed redox peaks, which confirm the faradic nature of charge storage.



**Figure 4B.4:** 3 electrode system measurement: a) CCO, b) CNT, c) CCO+CNT (10%), d) comparative CV graphs of CCO, CNT and CCO-CNT composite at  $20 \text{ mV s}^{-1}$  scan rate vs. Ag/AgCl reference electrode.

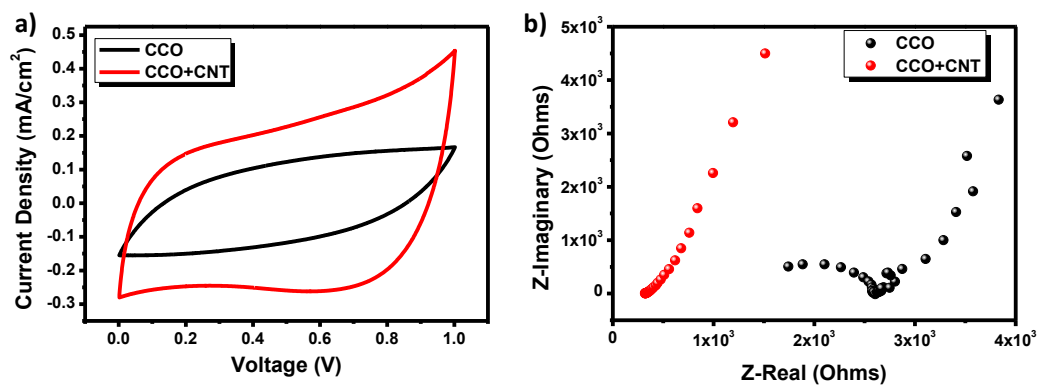
The pristine CCO based micro pseudo-capacitor did not show impressive performance due to quite high charge transfer resistance (as reflected in the electrochemical impedance spectroscopy (EIS) data) which is  $2.6 \times 10^3$  Ohms (figure 4B.6 b). This observation clearly demanded an improvement with respect to the device performance in the context of better charge transport. Thus, we blended a small amount of CNT (10 wt. %) into the CCO material to make an electrode. CNT is known to have very high charge transport character due their 1D nature.<sup>23,24</sup> Hence introduction of CNTs in the CCO electrode, enhances both the interconnectivity between the nanowalls of CCO (figure 4B.1 b) and the charge transport from the electrode to the electrolyte which in turn reduces the

charge transfer resistance drastically. This was also reflected in the performance of the device.



**Figure 4B.5:** Cyclic voltammetry data for solid state device, a) CCO and b) CCO-CNT composite electrode.

The device with CCO-CNT composite as the electrode showed much improved cyclic voltammetry graph (figure 4B.6 a). The impedance of the device was also reduced drastically to 320 Ohms (figure 4B.6 b) which indicates lowering of the charge transfer resistance. Also, the absence of any semi-circle in the EIS plot indicates the short ion diffusion pathway for the interdigitated electrodes.



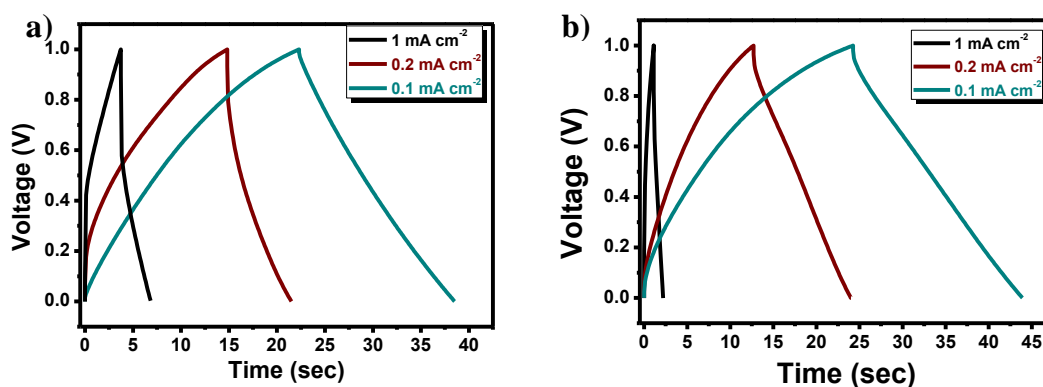
**Figure 4B.6:** Comparison of the a) cyclic voltammetry performance and b) Impedance spectroscopy for pristine CCO and the CCO-CNT composite cases.

Figure 4B.7 a represents the results of the comparative charge discharge studies on the two types of devices (CCO and CCO+CNT). The charge discharge measurement at different current densities was also performed for both CCO and

CCO-CNT composite based devices (Figure 4B.7). The capacitance values were calculated using the linear part of the discharge curve using equation (1)

$$C = I_A \times \Delta t \times \Delta V^{-1} \quad (1)$$

Where  $I_A$  represents the current at the voltage range  $\Delta V$  and  $\Delta t$  is the time duration.



**Figure 4B.7:** Charge-Discharge Measurement of a) CCO and b) CCO+CNT (10%) at different current densities.

The pristine CCO based device showed the areal capacitance of  $1.33 \text{ mF cm}^{-2}$  and gravimetric capacitance of  $0.74 \text{ F g}^{-1}$  at  $0.2 \text{ mA cm}^{-2}$  current density. Addition of a small amount of CNT showed an impressive change in the areal and gravimetric capacitances, which increased to  $2.26 \text{ mF cm}^{-2}$  and  $1.26 \text{ F g}^{-1}$ , respectively, at  $0.2 \text{ mA cm}^{-2}$ . Here in order to calculate the gravimetric capacitance the areal capacitances was divided by the material density on the electrodes which is  $1.8 \text{ mg cm}^{-2}$ .

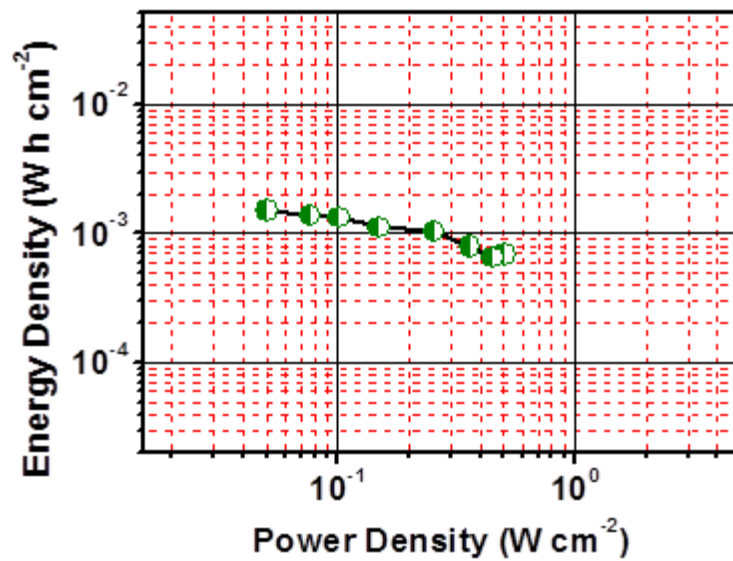


*Figure 4B.8: Ragone plot.*

The energy density (E) and the power density (P) of the devices calculated from the equations,

$$E = (C_v(\Delta V)^2)/(2 \times 3600) \quad (2)$$

$$P = (E \times 3600)/\Delta t \quad (3)$$

Where  $C_v$  represents the volumetric capacitance, and  $\Delta V$  and  $\Delta t$  represent the voltage window and discharge time, respectively. The device with composite electrode showed maximum energy density of  $0.3 \mu\text{W h cm}^{-2}$  at a current density of  $0.2 \text{ mA cm}^{-2}$  where the corresponding power density was  $191.15 \mu\text{W cm}^{-2}$ . The maximum power density of  $490.9 \mu\text{W cm}^{-2}$  was shown by the device at  $1 \text{ mA cm}^{-2}$  where the corresponding energy density was  $0.15 \mu\text{W h cm}^{-2}$ . The energy density and the power density for the liquid state device have also been calculated. The highest energy density of  $1.51 \text{ mWhcm}^{-2}$  was obtained at  $0.1 \text{ mA cm}^{-2}$  current density and the highest power density of  $503 \text{ mW cm}^{-2}$  was obtained at  $1 \text{ mA cm}^{-2}$  current density. Figure 4B.8 represents the corresponding Ragone plot of the device.



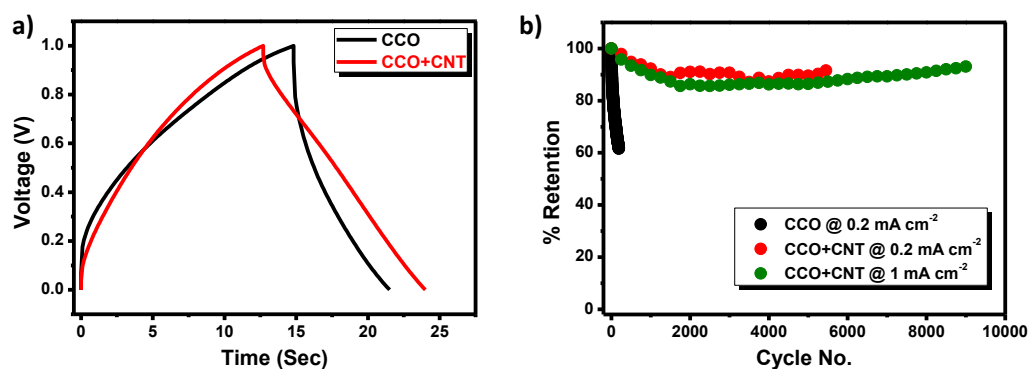


**Figure 4B.9:** Comparison of a) the charge-discharge graphs, and b) capacitance retention values for the pristine CCO and CCO-CNT composite at different current densities.

The cyclic stability performances of both the CCO based and the CNT composite based devices were recorded using charge decrease of its capacitance to 61.7% after 190 cycles. On the other hand, the composite based device shows a dramatic improvement in the stability. Almost 91% of its initial discharge measurement at a current density of  $0.2 \text{ mA cm}^{-2}$  (figure 4B.9 b). Figure 4B.9 b shows that CCO based device exhibits quite a weak performance in terms of cyclic stability and a performance was retained even after 5400 cycles with no sign of further decline. The composite based device was also evaluated at a high current density of  $1 \text{ mA cm}^{-2}$  (figure 4B.9 b) and as seen, the device retained over 93% of its initial capacitance after 9000 cycles which is highest for any micro pseudocapacitor reported till date. Thus, the composite material appears to be the most promising candidate for a flexible micro-supercapacitor.

The mechanical flexibility of the composite was also studied using CV experiment as seen in figure 4B.10. The flexibility test of the device was performed in two ways for the composite material. First, we bent the device at an angle of  $60^\circ$  several times and measured the CV after certain number of bending cycles (figure 4B.10 a). The device was found to retain more than 65% of its capacitance even after 1000 bending cycles. Secondly, we measured the CV under  $120^\circ$  bending condition (figure 4B.10 b) as another test to check the extent of reversible flexibility of the device. It is noted that the device showed over 93% performance retention even at  $120^\circ$  bending condition.

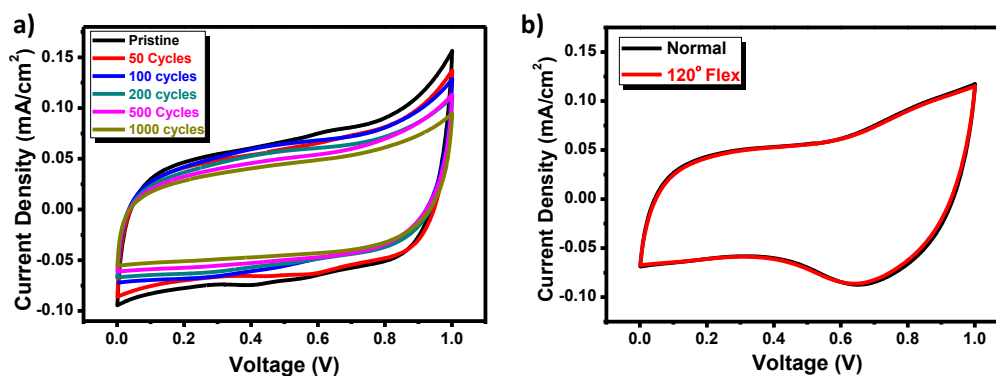


**Figure 4B.10:** Cyclic voltammetry study of the CNT/CCO composite based device: a) after different bending cycles at 60° angle and b) normal and bent (120°) condition.

No	Material	Device	Areal Capacitance	Flexibility	Stability	Substrate	Ref
1	CoNi <sub>2</sub> S <sub>4</sub>	Lithography RGO+Gold+ CoNi <sub>2</sub> S <sub>4</sub> Electrodeposited	11.6 mF cm <sup>-2</sup> (LE) 2.8 mF cm <sup>-2</sup> (SS)	NA	80% till 5000 Cycles (LS)	Hard (Glass)	20
2	Ni(OH) <sub>2</sub>	Lithography Ni/Pt/Ti+ Ni(OH) <sub>2</sub> CBD	16 mF cm <sup>-2</sup> (LE) 2 mF cm <sup>-2</sup> (SS)	NA	80% till 1000 Cycles (SS)	Flexible (PEN)	18
3	MoS <sub>2</sub>	Laser Scribing Silver paste electrode	8 mF cm <sup>-2</sup> (LE) Not reported (SS)	NA	92% till 1000 Cycles (SS)	Hard (Si)	7
5	VS <sub>2</sub>	Lithography Gold+VS <sub>2</sub> Electrophoretic deposition	4.76 mF cm <sup>-2</sup> (SS)	NA	>90% till 1000 Cycles (SS)	Flexible	19
6	CuCo <sub>2</sub> O <sub>4</sub>	Laser Scribing ITO-PET+CCO Brush Coating	10.88 mF cm <sup>-2</sup> (LE) 2.26 mF cm <sup>-2</sup> (SS)	93% @ 120° Bending 65% after 1000 cycles @ 60° bending	>93% till 9000 Cycles (SS)	Flexible (PET)	This Work

**Table 4B.1:** Comparison of interdigitated micro pseudocapacitor devices

In Table 4B.1 we have compared the performance of our device with other micro pseudocapacitor reports till date.<sup>7,18–20</sup> Most of these devices were fabricated using lithographic techniques with incorporation of precious metals like gold, platinum

etc. as electrodes. In our case, we have fabricated the device using laser scribing technique which is quite facile and highly scalable for industrial applications. As may be noted, the areal capacitance of the CCO-CNT blend is quite comparable with the reported devices. We have also shown the performance stability under flexing of the device.

#### **4B.4 Conclusions**

In summary, we have fabricated a robust flexible all solid state interdigitated micro-pseudocapacitor by CO<sub>2</sub> laser scribing of a coating of pre-synthesized dual mixed-valent ternary oxide CuCo<sub>2</sub>O<sub>4</sub> (CCO). The basic electrode material (CCO) showed high charge transfer resistance which was dramatically reduced by blending it with a small quantity (10 wt.%) of CNTs with CCO. The areal capacitance was found to be 2.26 mF cm<sup>-2</sup> at a current density of 0.2 mA cm<sup>-2</sup> for the composite based device which is comparable with the current state of art devices. The CCO-CNT composite based device showed over 93% stability even after 9000 charge-discharge cycles at a current density of 1 mA cm<sup>-2</sup> and no sign of decline. The device also retained more than 93% of its performance even under 120° bending condition and over 65% retention after 1000 cycles of repeated large angle (60°) bending, thanks to the electro-mechanical continuity afforded by CNTs.

**4B.5 References:**

1. Pech, D. *et al.* Ultrahigh-power micrometre-sized supercapacitors based on onion-like carbon. *Nat. Nanotechnol.* **5**, 651–654 (2010).
2. Chmiola, J., Largeot, C., Taberna, P.-L. L., Simon, P. & Gogotsi, Y. Monolithic carbide-derived carbon films for micro-supercapacitors. *Science* **328**, 480–483 (2010).
3. Gao, W. *et al.* Direct laser writing of micro-supercapacitors on hydrated graphite oxide films. *Nat Nano* **6**, 496–500 (2011).
4. Sung, J.-H., Kim, S.-J., Jeong, S.-H., Kim, E.-H. & Lee, K.-H. Flexible micro-supercapacitors. *J. Power Sources* **162**, 1467–1470 (2006).
5. Wu, Z., Parvez, K., Feng, X. & Müllen, K. Graphene-based in-plane micro-supercapacitors with high power and energy densities. *Nat. Commun.* **4**, 845–854 (2013).
6. Beidaghi, M. & Wang, C. Micro-Supercapacitors Based on Interdigital Electrodes of Reduced Graphene Oxide and Carbon Nanotube Composites with Ultrahigh Power Handling Performance. *Adv. Funct. Mater.* **22**, 4501–4510 (2012).
7. Cao, L. *et al.* Direct Laser-Patterned Micro-Supercapacitors from Paintable MoS<sub>2</sub> Films. *Small* **9**, 2905–2910 (2013).
8. El-Kady, M. F. & Kaner, R. B. Scalable fabrication of high-power graphene micro-supercapacitors for flexible and on-chip energy storage. *Nat. Commun.* **4**, 1475 (2013).
9. El-Kady, M. F. & Kaner, R. B. Direct Laser Writing of Graphene Electronics. *ACS Nano* **8**, 8725–8729 (2014).
10. Wang, S., Hsia, B., Carraro, C. & Maboudian, R. High-performance all solid-state micro-supercapacitor based on patterned photoresist-derived porous carbon electrodes and an ionogel electrolyte. *J. Mater. Chem. A* **2**,

- 7997–8002 (2014).
11. Yadav, P., Basu, A., Suryawanshi, A., Game, O. & Ogale, S. Highly Stable Laser-Scribed Flexible Planar Microsupercapacitor Using Mushroom Derived Carbon Electrodes. *Adv. Mater. Interfaces* **3**, (2016).
  12. Zhang, L. L. & Zhao, X. S. Carbon-based materials as supercapacitor electrodes. *Chem. Soc. Rev.* **38**, 2520–2531 (2009).
  13. Wang, G., Zhang, L. & Zhang, J. A review of electrode materials for electrochemical supercapacitors. *Chem. Soc. Rev.* **41**, 797–828 (2012).
  14. Sharma, R. K., Rastogi, A. C. & Desu, S. B. Manganese oxide embedded polypyrrole nanocomposites for electrochemical supercapacitor. *Electrochim. Acta* **53**, 7690–7695 (2008).
  15. Zhao, D.-D., Bao, S.-J., Zhou, W.-J. & Li, H.-L. Preparation of hexagonal nanoporous nickel hydroxide film and its application for electrochemical capacitor. *Electrochem. commun.* **9**, 869–874 (2007).
  16. Si, W. *et al.* On chip, all solid-state and flexible micro-supercapacitors with high performance based on MnOx/Au multilayers. *Energy Environ. Sci.* **6**, 3218–3223 (2013).
  17. Dinh, T. M., Armstrong, K., Guay, D. & Pech, D. High-resolution on-chip supercapacitors with ultra-high scan rate ability. *J. Mater. Chem. A* **2**, 7170–7174 (2014).
  18. Kurra, N., Alhebshi, N. A. & Alshareef, H. N. Microfabricated Pseudocapacitors Using Ni(OH)<sub>2</sub> Electrodes Exhibit Remarkable Volumetric Capacitance and Energy Density. *Adv. Energy Mater.* **5**, n/a-n/a (2015).
  19. J. Feng, X. Sun, C. Wu, L. Peng, C. Lin, S. Hu, J. Yang, and Y. Xie, Metallic Few-Layered VS<sub>2</sub> Ultrathin Nanosheets: High Two-Dimensional Conductivity for In-Plane Supercapacitors. *J. Am. Chem. Soc.* **133**, 17832–17838 (2011).

20. Kurra, N., Xia, C., Hedhili, M. N. & Alshareef, H. N. Ternary chalcogenide micro-pseudocapacitors for on-chip energy storage. *Chem. Commun.* **51**, 10494–10497 (2015).
21. Shinde, S. K., Dubal, D. P., Ghodake, G. S. & Fulari, V. J. Hierarchical 3D-flower-like CuO nanostructure on copper foil for supercapacitors. *RSC Adv.* **5**, 4443–4447 (2015).
22. V. Senthilkumar, Y. S. Kim, S. Chandrasekaran, B. Rajagopalan, E. J. Kim, and J. S. Chung, Comparative supercapacitance performance of CuO nanostructures for energy storage device applications. *RSC Adv.* **5**, 20545–20553 (2015).
23. Coleman, J. N., Khan, U., Blau, W. J. & Gun'ko, Y. K. Small but strong: A review of the mechanical properties of carbon nanotube–polymer composites. *Carbon N. Y.* **44**, 1624–1652 (2006).
24. Wei, B. Q., Vajtai, R. & Ajayan, P. M. Reliability and current carrying capacity of carbon nanotubes. *Appl. Phys. Lett.* **79**, 1172 (2001).

## Chapter 5

# **PVA-Pentacene based high performance all organic flexible field effect transistor for inverter application**

In this chapter we have discussed about flexible organic field effect transistor (OFET) using polyvinyl alcohol based gated dielectric and pentacene based channel. We have optimized the thickness of the gate dielectric on the hard substrate (glass/ITO) and used it to fabricate flexible (ITO/PET) OFET device. The flexible device has shown high on-off ratio of  $5.3 \times 10^4$  with  $0.57 \text{ cm}^2 \text{ V}^{-1} \text{ s}^{-1}$  channel mobility. We have further used this device architecture to fabricate all organic diode-load inverter.

## 5.1 Introduction:

Organic field effect transistors (OFETs) are getting extremely significant for various flexible gadgets such as display devices, smart cards, identification tags etc. because of their some notable advantages such as low cost, facile fabrication method, flexibility, light weight etc.<sup>1-11</sup> The major two components of a field effect transistor (FET) are a semiconductor and a dielectric. In OFETs mostly the semiconductor is organic; dielectrics can be both inorganic and organic materials. Various types of organic semiconductors are used as channel layer in OFET devices. Almost all of them are either polymers or small molecules.<sup>12-18</sup> Since the last decade, pentacene based organic thin film transistors have attracted much attention due to their high field effect mobility, low voltage application, easy processability and low temperature fabrication methods.<sup>19-30</sup> Pentacene is generally deposited through physical vapour deposition (PVD) technique. This yields extremely uniform layer which favors the uniform charge transport throughout the semiconductor layer. The OFET device performance greatly depends upon the quality of the dielectric. Initially, for OFETs inorganic dielectrics such as SiO<sub>2</sub>, Al<sub>2</sub>O<sub>3</sub> etc. have been used. Recently organic dielectric materials are being introduced in the devices to increase the flexibility.<sup>31,12,32-35</sup> Mostly long chained polymers such as polymethylmethacrylate (PMMA), polystyrene (PS), polyvinyl alcohol (PVA), cyanoethylpullulan (CYEPL), polyvinyl chloride (PVC) etc. have been used as dielectric materials.<sup>35-45</sup> Several studies showed that the field effect mobility can be influenced greatly by the dielectric constant ( $k$ ) of the gate dielectric.<sup>35,46</sup> With increase in the  $k$  value of the dielectric the channel mobility of the device will also be increased. Since the high dielectric constant provides the greater polarization in the dielectric on application of voltage, accumulation of more charge carriers in the channel layer occurs. This enhances the channel mobility of the device. Among the organic gate dielectrics PVA possess very high  $k$  value (7.8). Except for the high  $k$  value PVA also possesses several advantages such as solution processability, uniformity in the film *etc.* PVA have been used extensively for fabricating various OFET devices using different organic semiconductors. The major disadvantage of the OFET



devices with organic polymer dielectric is the breakdown of the dielectric layer. To overcome this problem crosslinked-PVA is used.

In this work we have optimized a flexible OFET device using PVA as gate dielectric and pentacene as channel material. Flexible OFET devices with different dielectric layer thickness were fabricated. Crosslinked PVA was also used as dielectric layer. The device with PVA having 300 nm layer thickness showed best performance. The on-off ratio obtained from the device was  $5.3 \times 10^4$  and  $0.57 \text{ cm}^2\text{V}^{-1}\text{s}^{-1}$  channel mobility was observed. Finally we have successfully demonstrated an inverter using the OFET devices. To the best of our knowledge, this is the first demonstration of organic inverter using OFET device having PVA as gate dielectric.

## 5.2 Experimental:

### 5.2.1 PVA solution preparation:

Solid PVA (Sigma-Aldrich) ( $M_w$  89,000-98,000, 99+% hydrolyzed), according to the concentration of the solution, was dissolved in de-ionized (D.I.) water by overnight stirring at 80 °C temperature. After getting the clear solution, it was then cooled to room temperature and filtered using syringe filter before spin coating.

### 5.2.2 Device fabrication:

Figure 5.1 shows the architecture of the device. All the non-flexible and flexible devices were fabricated on the corning glass and PET substrate respectively. The identical device fabrication procedure was followed in both cases. Initially, the base substrates were cleaned by sonicating in soap water and iso-propyl alcohol. Then the substrates were dried under nitrogen flow. Then these were treated with plasma cleaner for better surface adhesion. At beginning of the device fabrication process, the aluminium gate electrode was deposited through PVD method (thermal evaporation) onto the base substrate. The typical thickness of the electrode was 100 nm. The dielectric layer was then deposited by spin coating of the PVA solutions. For thicker dielectric layer (500 nm) 10 wt.% aqueous PVA solution was taken. While for thinner dielectric layer (300nm) 5 wt.% PVA

solution was used. In all the cases the spin rate was set at 2500 rpm and the spinning time was 1 min. The dielectric layer was annealed at 80 °C in vacuum oven for 1 hr. It was then cooled to room temperature before taking out from the vacuum oven. The pentacene (Sigma-Aldrich) channel layer was then deposited at the top of the PVA layer by PVD (thermal evaporation) method at  $10^{-6}$  mbar chamber pressure. The typical thickness of this layer was optimized at 50 nm. Finally 100 nm gold source-drain electrodes were also fabricated by PVD through interdigitated physical mask at the same chamber pressure mentioned above. The channel length (L) and width (W) of the devices was 100  $\mu\text{m}$  and 1000  $\mu\text{m}$  respectively. For inverter the devices were fabricated as stated above. Finally the connections between two or more devices were done using silver paste.

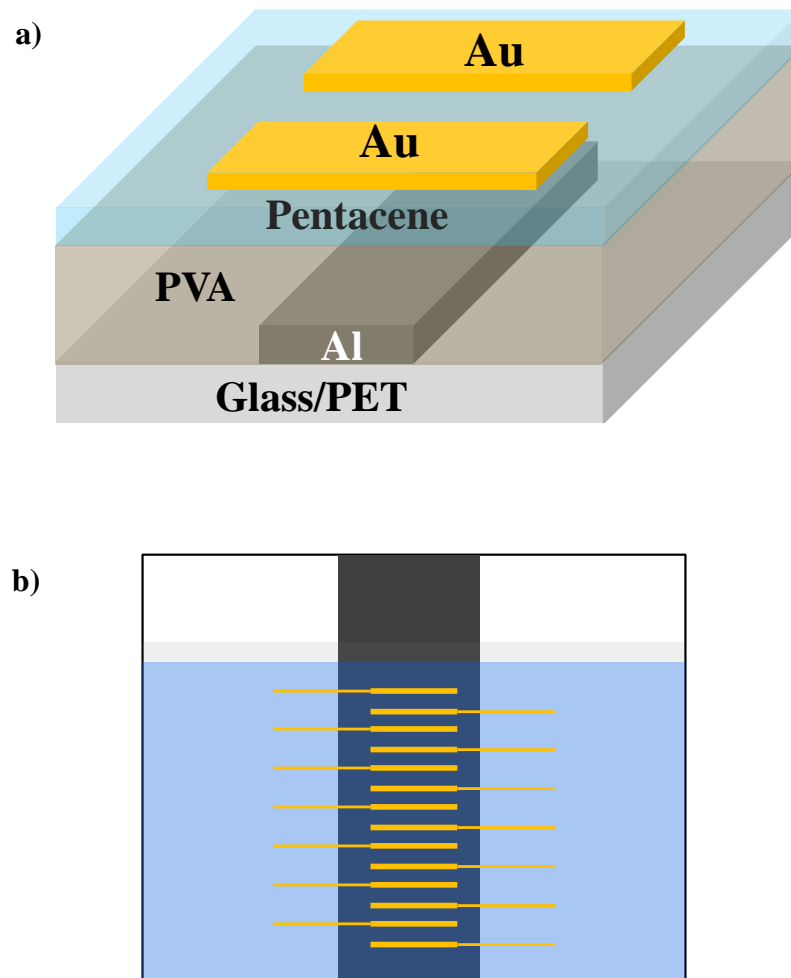


*Figure 5.1: Device architecture of the OFET*

### 5.3 Characterization:

All the current voltage (I-V) measurements and capacitance-voltage (C-V) measurement on the OFETs were performed under ambient conditions using Keithley 4200 semiconductor parameter analyzer unit. For the C-V measurement of the dielectric film, the film was sandwiched between two electrodes; typically aluminium and gold were used as electrodes. The film thickness was measured using Dektak profilometer.

### 5.4 Result and Discussion:

We have tested the device performance of the devices having different dielectric thickness. Mainly the output ( $I_{ds}$ - $V_{ds}$  measurement) and the transfer ( $I_{ds}$ - $V_{gs}$ ) characteristics of the devices were measured. Devices with two different dielectric thicknesses, 500 nm and 300 nm, were fabricated on the corning glass substrates. The areal capacitance ( $C_i$ ) of the device with 500 nm dielectric (Device-1) thickness was  $4.43 \times 10^{-9}$  F  $\text{cm}^{-2}$ . Figure 5.2 represents the device performance of this OFET. The output characteristic (figure 5.2 a) depicted the p-type nature of pentacene. The conductivity of the channel layer has increased systematically after a certain voltage called threshold voltage ( $V_{th}$ ). The detailed mechanism is explained in the first chapter. In the transfer characteristic (figure 5.2 b) the threshold voltage was calculated from the linear region of the  $I_{ds}$ - $V_{gs}$  curve. The device shows very high  $V_{th}$  of  $\sim -47.8$  V. The on-off ratio of the device obtained was  $\sim 5 \times 10^2$  from the  $I_{ds}$ - $V_{gs}$  graph plotted in the log scale. The linear mobility ( $\mu_{lin}$ ) of the device was calculated from this graph using the following equation:

$$\mu_{lin} = \frac{\partial I_{ds}}{\partial V_g} \frac{L}{WV_{ds}C_i} \quad (1)$$

Where  $\frac{\partial I_{ds}}{\partial V_g}$  denotes the slope of the  $I_{ds}$ - $V_{gs}$  curve.

The linear field effect mobility for the device calculated was  $0.016 \text{ cm}^2 \text{ V}^{-1} \text{ s}^{-1}$ . The low performance of this device is attributed to the high thickness of the dielectric layer. The thicker the layer higher voltage is required to polarize the dielectric.

Hence the  $V_{th}$  is substantially high which in turn decreases the effective gate voltage ( $V_g - V_{th}$ ). Thus high  $V_{ds}$  has been required for the device to be working.

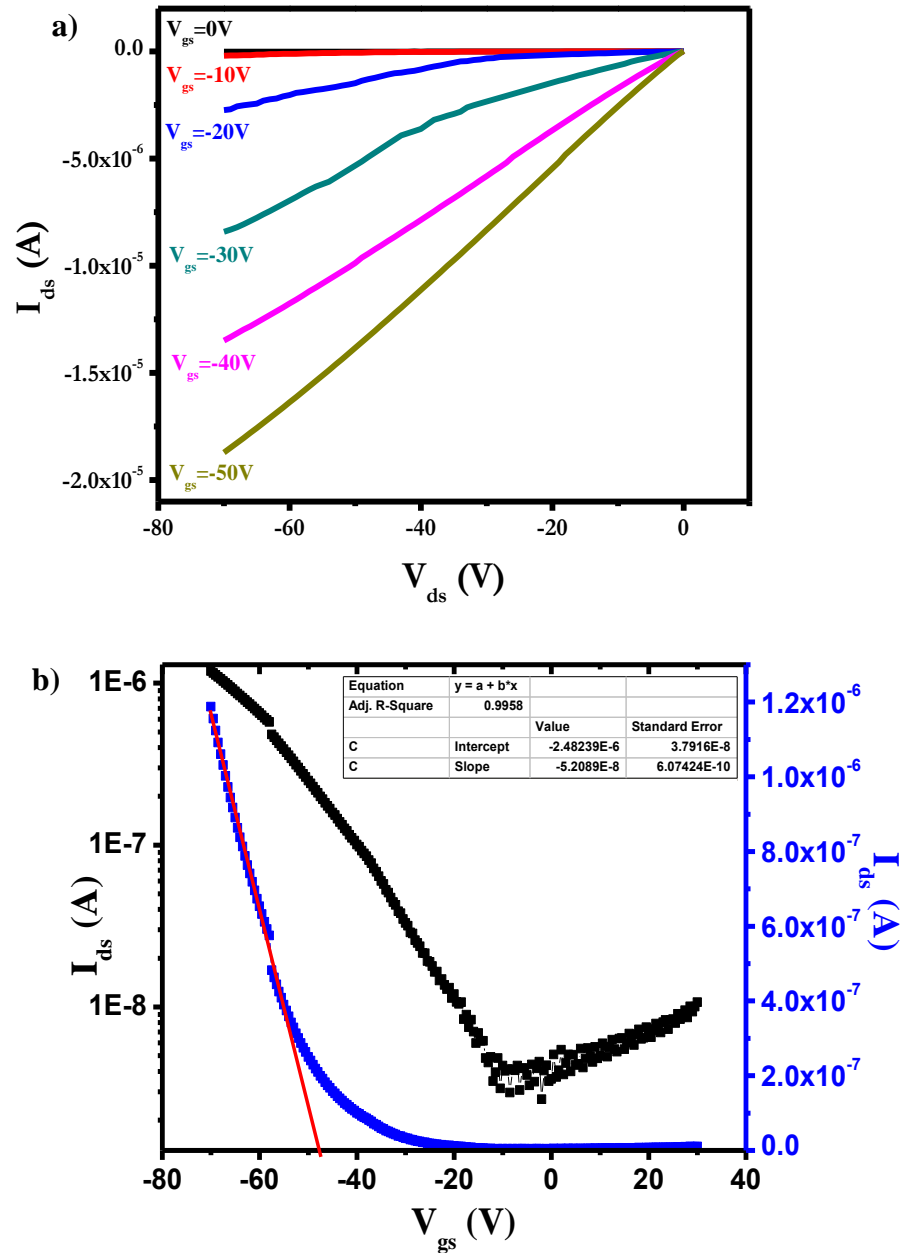


**Figure 5.2:** Device performance measurements. a) Output characteristics and b) transfer characteristics.

In order to reduce the threshold voltage and increase the field effect mobility of the channel layer, thinner dielectric layer (300 nm) was fabricated (Device-2). Figure 5.3 shows the performance of the OFET device with 300 nm dielectric layer. The capacitance obtained for this layer was  $1.58 \times 10^{-8} \text{ F cm}^{-2}$  which is more

than 10 times higher than the thicker dielectric. From the output characteristics (figure 5.3 a) it is quite clear that the operating voltage of the device dropped drastically. The  $V_{th}$  obtained from the transfer characteristics (figure 5.3 b) is -4.3 V which is substantially low. Improvement in the on-off ratio ( $1.4 \times 10^4$ ) of the device was observed. The field effect mobility of the device was also increases to  $0.45 \text{ cm}^2 \text{ V}^{-1} \text{ s}^{-1}$ .

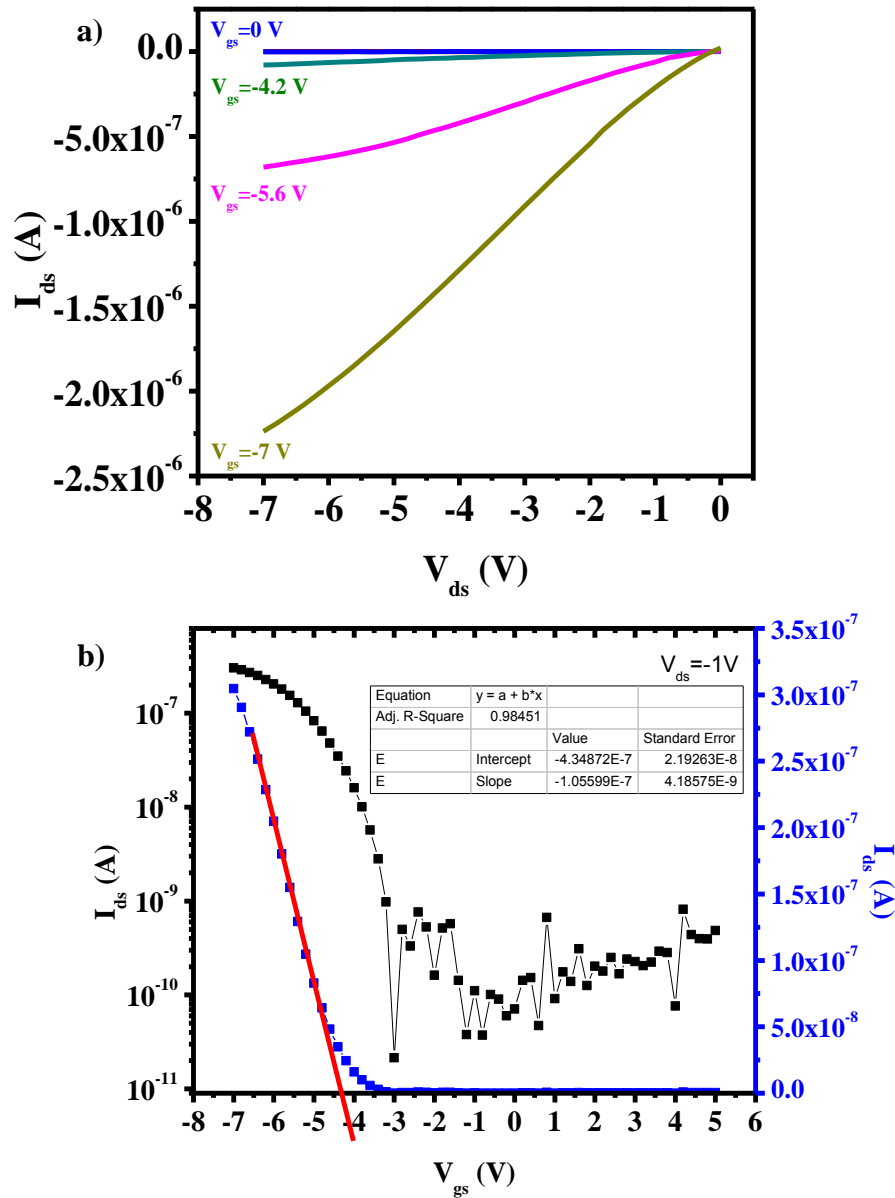


*Figure 5.3: Device performance measurements. a) Output characteristics and b) transfer characteristics.*

Since the thinner dielectric layer showed the better performance, further study of the PVA-pentacene based OFET devices were done using the thinner dielectric layer. Crosslinked PVA layer has also been used as dielectric of the OFET device with same architecture to provide the strength in the dielectric layer (Device-3). Crosslinking of PVA layer was done using potassium dichromate ( $K_2Cr_2O_7$ ) in presence of UV light.<sup>47</sup> The capacitance of the dielectric was obtained  $1.27 \times 10^{-8} \text{ F cm}^{-2}$ , which is comparable to the regular thin PVA layer. Although from the output graph (figure 5.4 a) it is clear that the device was involved considerably high operating voltage. In this case, as the  $I_{ds}$ - $V_{gs}$  graph is non-linear in nature, to get the linear curve we have plotted  $(I_{ds})^{1/2}$  vs  $V_{gs}$  graph. The  $V_{th}$  (-17.9 V) observed from the transfer graph (figure 5.4 b) was also higher than the regular thinner PVA layer. The on-off ratio of the device derived from the  $I_{ds}$ - $V_{ds}$  graph plotted in the log scale was slightly reduced to  $1.3 \times 10^3$  but the field effect mobility went down drastically to  $0.0031 \text{ cm}^2 \text{ V}^{-1} \text{ s}^{-1}$  in compare with the non-crosslinked PVA dielectric.

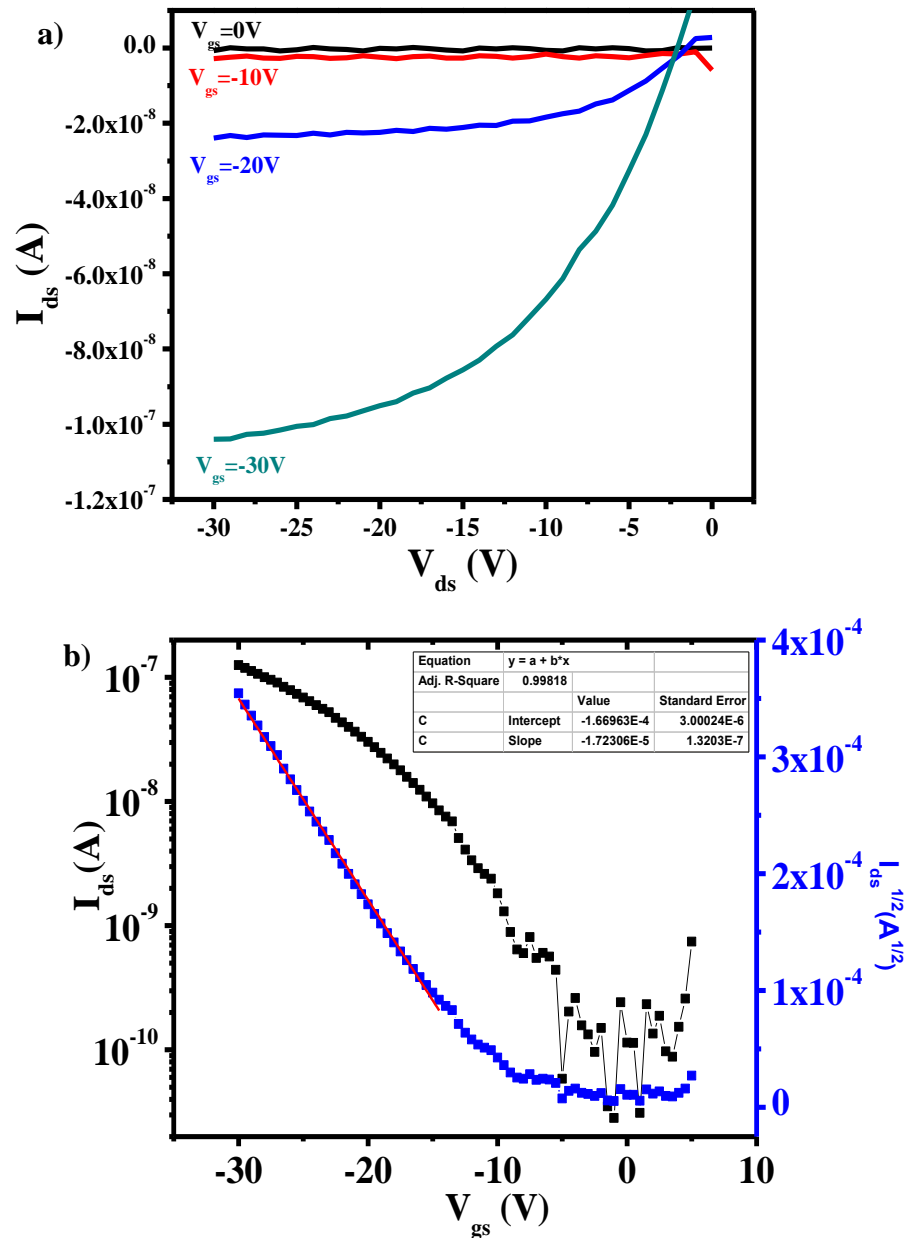


**Figure 5.4:** Device performance measurements. a) Output characteristics and b) transfer characteristics.

Since, among the devices with the dielectric layers deposited at three different conditions, the device with thinner non-crosslinked PVA layer performed best, we fabricated the flexible OFET using that architecture on PET substrate with further optimization (Device-4). The flexible OFET device showed very low operating voltage in the output graph (figure 5.5 a). The areal capacitance ( $C_i$ ) of the dielectric measured was  $1.4 \times 10^{-8} \text{ F cm}^{-2}$ . In the output characteristics the device showed current modulation below  $-3V$ . In this case also the  $I_{ds}$ - $V_{gs}$  curve showed sufficient linearity hence the  $V_{th}$  was calculated from this graph only. The device

exhibited considerably lower  $V_{th}$  of -1.46 V. The on-off ratio of the device obtained from the transfer graph plotted on the log scale was  $5.3 \times 10^4$ . The field effect mobility of the device calculated from the transfer characteristics (figure 5.5 b) is  $0.57 \text{ cm}^2 \text{ V}^{-1} \text{ s}^{-1}$ .

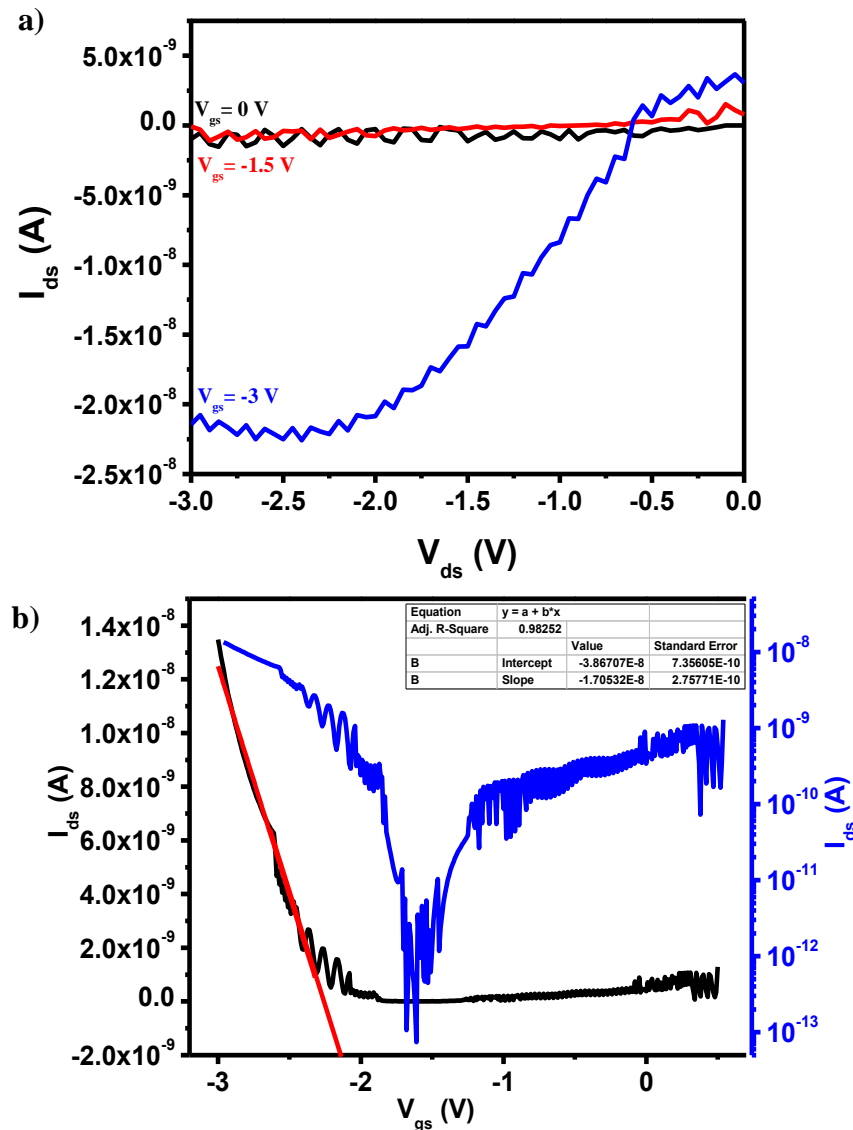


**Figure 5.5:** a) Output characteristics and b) transfer characteristics,

Flexibility of the device was also measured under repeating flexing cycles of  $60^\circ$  bending. The device showed reasonably high flexibility up to 100 bending cycles (figure 5.6). In the figure the source-drain current ( $I_{ds}$ ) at 5V gate voltage is plotted for different bending cycles. It's interesting that, current is actually increasing after a few cycles. A performance summary of all the devices fabricated is given in the table 5.1.



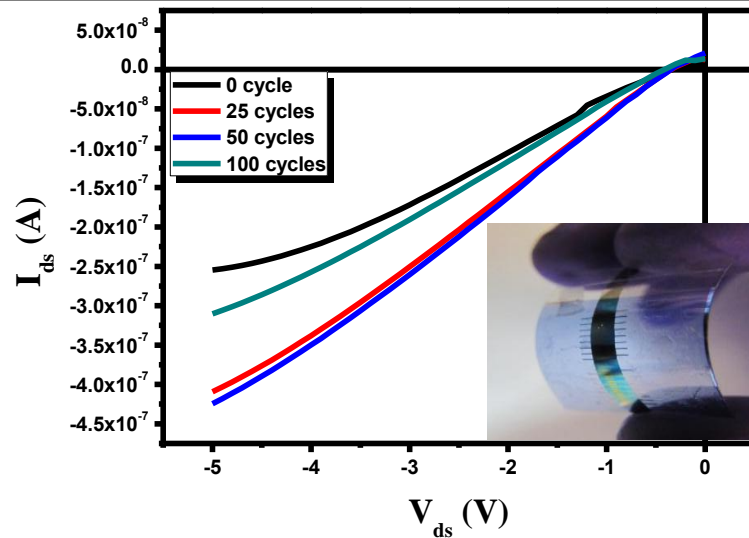


*Figure 5.6: Device performance after several cycles of flexibility of the device and inset photograph of a flexible device fabricated on PET substrate.*

	Substrate	Dielectric Thickness ( $\mu\text{m}$ )	Mobility	Substrate	Dielectric Thickness ( $\mu\text{m}$ )
<b>Device 1</b>	Hard	500	0.016	- 47.8	$5 \times 10^2$
<b>Device 2</b>	Hard	300	0.45	- 4.3	$1.4 \times 10^4$
<b>Device 3</b>	Hard	300 (Cross-linked)	$3.1 \times 10^{-3}$	-17.9	$1.3 \times 10^3$
<b>Device 4</b>	Flexible	300	$\sim 0.57$	$\sim -1.46$	$\sim 5.3 \times 10^4$

*Table 5.1: Device performance summery.*

The inverter was fabricated on glass substrate using the circuit diagram depicted in the figure 5.7 a.<sup>48</sup> This type of inverter is called diode-load transistor. In the circuit, two p-type OFETs were connected such that from the gate electrode of one OFET (OFET-1) served as input ( $V_{in}$ ). The gate electrode of the other OFET (OFET-2) was grounded and source of the OFET-2 was connected with the drain

of the OFET-1. At that point the output voltage of the inverter is measured ( $V_{out}$ ). The drain of OFET-2 was grounded while at the source of the OFET-1 a constant +ve voltage is applied ( $V_{dd}$ ). The OFET-1 is denoted as drive transistor ( $T_D$ ) and the OFET-2 is denoted as load transistor ( $T_L$ ). When  $V_{in}$  is very low (high -ve voltage) the channel of the  $T_D$  is strongly on. Hence the  $V_{out}$  will be equal to  $V_{dd}$ . At above  $V_{th}$  of the  $T_D$  (i.e low -ve voltage) the transistor gets off hence the  $V_{out}$  is reduced to lower voltage. In this case the  $T_D$  has  $V_{th}$  of around -2V. Below this input voltage the output voltage is very high. As we increase the input voltage above the  $V_{th}$  of  $T_D$  the output voltage drops drastically which signifies the working inverter characteristics (figure 5.7 d).

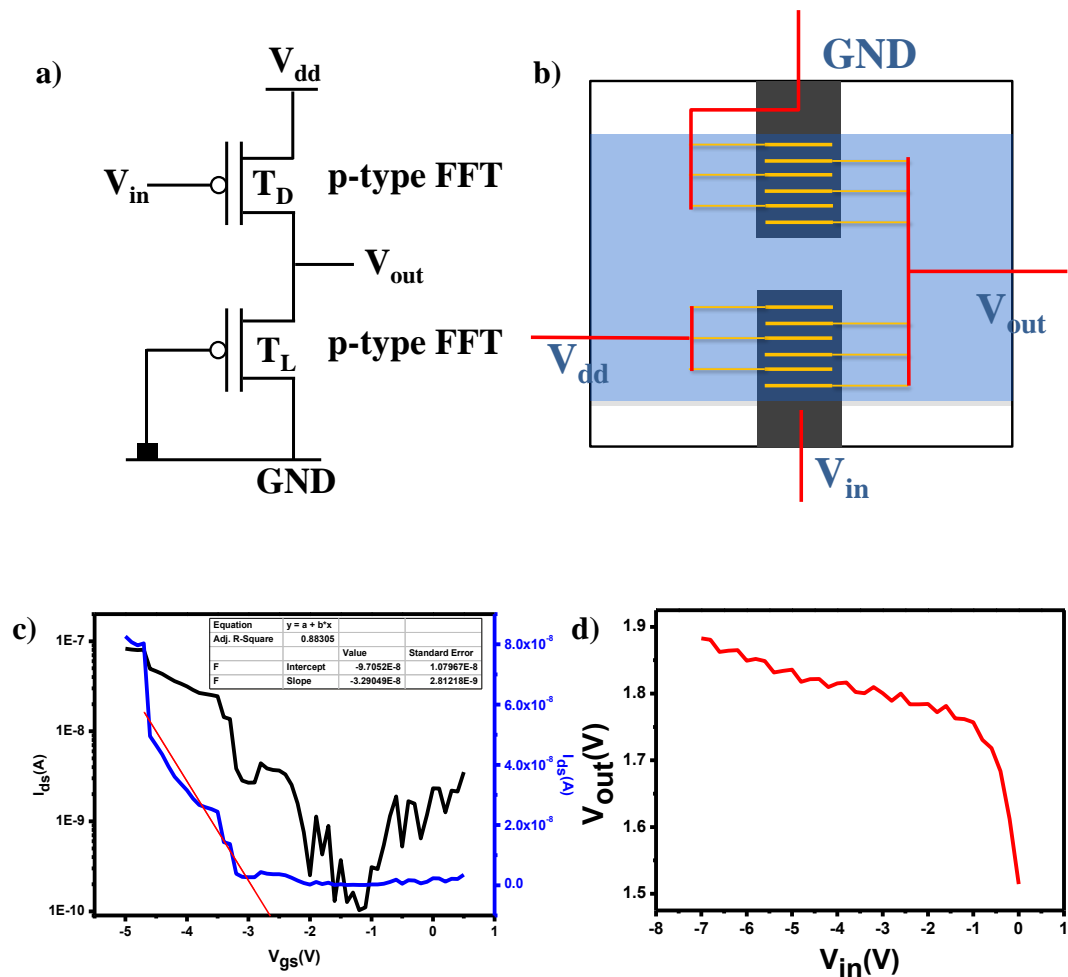


**Figure 5.7:** a) Inverter circuit, b) schematic of the inverter device, c) transfer characteristics for the OFET and d) inverter characteristics.

## 5.5 Conclusion:

In this chapter we have discussed the optimization of the thickness of the PVA dielectric layer for better OFET device performance. The device with thinner dielectric layer (300 nm) on corning glass substrate shows considerably good device performance having  $1.4 \times 10^4$  on-off ratio with high field effect mobility of  $0.45 \text{ cm}^2 \text{ V}^{-1} \text{ s}^{-1}$  and -4.3 V threshold voltage. The same device architecture was used to fabricate the flexible device with further careful optimization of the fabrication conditions. The flexible device showed even more improved performance having  $5.3 \times 10^4$  on-off ratio with  $0.57 \text{ cm}^2 \text{ V}^{-1} \text{ s}^{-1}$  field effect mobility and 1.46 V threshold voltage. Further we have fabricated a diode-load inverter using the OFET on glass substrate. To the best of our knowledge this is the first report of pentacene based all organic OFET based inverter.

## 5.6 References:

1. Reuveny, A., Yokota, T., Sekitani, T. & Someya, T. Ultra-flexible short-channel organic field-effect transistors. *Appl. Phys. Express* **8**, (2015).
2. Pierre, A. *et al.* All-printed flexible organic transistors enabled by surface tension-guided blade coating. *Adv. Mater.* **26**, 5722–5727 (2014).
3. Someya, T. *et al.* A large-area, flexible pressure sensor matrix with organic field-effect transistors for artificial skin applications. *Proc. Natl. Acad. Sci. U. S. A.* **101**, 9966–9970 (2004).
4. Moonen, P. F., Yakimets, I. & Huskens, J. Fabrication of transistors on flexible substrates: From mass-printing to high-resolution alternative lithography strategies. *Adv. Mater.* **24**, 5526–5541 (2012).
5. Yao, Y., Dong, H. & Hu, W. Charge Transport in Organic and Polymeric Semiconductors for Flexible and Stretchable Devices. *Adv. Mater.* n/a-n/a (2015). doi:10.1002/adma.201503007
6. Nakahara, R., Uno, M., Uemura, T., Takimiya, K. & Takeya, J. Flexible three-dimensional organic field-effect transistors fabricated by an

- imprinting technique. *Adv. Mater.* **24**, 5212–5216 (2012).
7. Dumitru, L. M. *et al.* Plain poly(acrylic acid) gated organic field-effect transistors on a flexible substrate. *ACS Appl. Mater. Interfaces* **5**, 10819–10823 (2013).
  8. K. J. Baeg, D. Khim, J. Kim, B. Do Yang, M. Kang, S. W. Jung, I. K. You, D. Y. Kim, and Y. Y. Noh, High-performance top-gated organic field-effect transistor memory using electrets for monolithic printed flexible nand flash memory. *Adv. Funct. Mater.* **22**, 2915–2926 (2012).
  9. Fukuda, K., Takeda, Y., Mizukami, M., Kumaki, D. & Tokito, S. Fully solution-processed flexible organic thin film transistor arrays with high mobility and exceptional uniformity. *Sci. Rep.* **4**, 3947 (2014).
  10. Sekitani, T., Zschieschang, U., Klauk, H. & Someya, T. Flexible organic transistors and circuits with extreme bending stability. *Nat. Mater.* **9**, 1015–1022 (2010).
  11. T. Minami, T. Sato, T. Minamiki, K. Fukuda, D. Kumaki, and S. Tokito, A novel OFET-based biosensor for the selective and sensitive detection of lactate levels. *Biosens. Bioelectron.* **74**, 45–8 (2015).
  12. Allard, S., Forster, M., Souharce, B., Thiem, H. & Scherf, U. Organic Semiconductors for Solution-Processable Field-Effect Transistors (OFETs). *Angew. Chemie Int. Ed.* **47**, 4070–4098 (2008).
  13. E. J. Meijer, D. M. de Leeuw, S. Setayesh, E. van Veenendaal, B. H. Huisman, P. W. M. Blom, J. C. Hummelen, U. Scherf, J. Kadam, and T. M. Klapwijk, Solution-processed ambipolar organic field-effect transistors and inverters. *Nat. Mater.* **2**, 678–682 (2003).
  14. Takimiya, K., Shinamura, S., Osaka, I. & Miyazaki, E. Thienoacene-based organic semiconductors. *Advanced Materials* **23**, 4347–4370 (2011).
  15. Kang, B., Lee, W. H. & Cho, K. Recent advances in organic transistor printing processes. *ACS Applied Materials and Interfaces* **5**, 2302–2315

- (2013).
16. Lee, W. & Park, Y. Organic Semiconductor/Insulator Polymer Blends for High-Performance Organic Transistors. *Polymers (Basel)*. **6**, 1057–1073 (2014).
  17. Z. Wang, J. Zhang, R. Xing, J. Yuan, D. Yan, and Y. Han, Micropatterning of Organic Semiconductor Microcrystalline Materials and OFET Fabrication by ‘Hot Lift Off’. *J. Am. Chem. Soc.* **125**, 15278–15279 (2003).
  18. Wang, C., Dong, H., Hu, W., Liu, Y. & Zhu, D. Semiconducting  $\pi$ -conjugated systems in field-effect transistors: A material odyssey of organic electronics. *Chemical Reviews* **112**, 2208–2267 (2012).
  19. Schmechel, R., Ahles, M. & Von Seggern, H. A pentacene ambipolar transistor: Experiment and theory. *J. Appl. Phys.* **98**, (2005).
  20. Ruiz, R., Papadimitratos, A., Mayer, A. C. & Malliaras, G. G. Thickness dependence of mobility in pentacene thin-film transistors. *Adv. Mater.* **17**, 1795–1798 (2005).
  21. Lin, Y. Y., Gundlach, D. J., Nelson, S. F. & Jackson, T. N. Stacked pentacene layer organic thin-film transistors with improved characteristics. *IEEE Electron Device Lett.* **18**, 606–608 (1997).
  22. H. L. L. Cheng, W. Y. Y. Chou, C. W. W. Kuo, Y. W. W. Wang, Y. S. S. Mai, F. C. C. Tang, and S. W. W. Chu, Influence of Electric Field on Microstructures of Pentacene Thin-Films in Field-Effect Transistors. *Adv. Funct. Mater.* **18**, 285–293 (2008).
  23. Gundlach, D. J., Lin, Y. Y., Jackson, T. N., Nelson, S. F. & Schlom, D. G. Pentacene organic thin-film transistors-molecular ordering and mobility. *IEEE Electron Device Lett.* **18**, 87–89 (1997).
  24. Kitamura, M. & Arakawa, Y. Pentacene-based organic field-effect transistors. *J. Phys. Condens. Matter* **20**, 184011 (2008).

25. Toccoli, T., Pallaoro, A., Tonezzer, M., Coppedè, N. & Iannotta, S. OFET for gas sensing based on SuMBE grown pentacene films. *Solid. State. Electron.* **52**, 417–421 (2008).
26. Yu, J., Yu, X., Zhang, L. & Zeng, H. Ammonia gas sensor based on pentacene organic field-effect transistor. *Sensors Actuators, B Chem.* **173**, 133–138 (2012).
27. Klauk, H., Zschieschang, U., Pflaum, J. & Halik, M. Ultralow-power organic complementary circuits. *Nature* **445**, 745–748 (2007).
28. K. Nomoto, N. Hirai, N. Yoneya, N. Kawashima, M. Noda, M. Wada, and J. Kasahara, A High-Performance Short-Channel Bottom-Contact OTFT and Its Application to AM-TN-LCD. *IEEE Trans. Electron Devices* **52**, 1519–1526 (2005).
29. Rotzoll, R. *et al.* Radio frequency rectifiers based on organic thin-film transistors. *Appl. Phys. Lett.* **88**, 123502 (2006).
30. Choi, J.-M., Kim, J. H. & Im, S. High-gain pentacene-based inverter achieved through high and low energy ultraviolet treatments. *Appl. Phys. Lett.* **91**, 83504 (2007).
31. Yamashita, Y. Organic semiconductors for organic field-effect transistors. *Sci. Technol. Adv. Mater.* **10**, 24313 (2009).
32. Sun, Y., Liu, Y. & Zhu, D. Advances in organic field-effect transistors. *J. Mater. Chem.* **15**, 53 (2005).
33. Vasimalla, S. *et al.* Low voltage, low cost, flexible and balanced ambipolar OFETs based on Br<sub>2</sub> PTCDI-C18/CuPc fabricated on an Al foil gate substrate with good ambient stability. *J. Mater. Chem. C* **4**, 7102–7109 (2016).
34. T. B. Singh, N. Marjanović, P. Stadler, M. Auinger, G. J. Matt, S. Günes, N. S. Sariciftci, R. Schwödiauer, and S. Bauer, Fabrication and characterization of solution-processed methanofullerene-based organic

- field-effect transistors. *J. Appl. Phys.* **97**, 83714 (2005).
35. Ortiz, R. P., Facchetti, A. & Marks, T. J. High-k Organic, Inorganic, and Hybrid Dielectrics for Low-Voltage Organic Field-Effect Transistors. *Chem. Rev.* **110**, 205–239 (2010).
  36. Awadhia, A., Patel, S. K. & Agrawal, S. L. Dielectric investigations in PVA based gel electrolytes. *Prog. Cryst. Growth Charact. Mater.* **52**, 61–68 (2006).
  37. K. Müller, Y. Burkov, D. Mandal, K. Henkel, I. Paloumpa, A. Goryachko, and D. Schmeißer, Microscopic and spectroscopic characterization of interfaces and dielectric layers for OFET devices. *Phys. Status Solidi Appl. Mater. Sci.* **205**, 600–611 (2008).
  38. Saroj, A. L. & Singh, R. K. Thermal, dielectric and conductivity studies on PVA/Ionic liquid [EMIM][EtSO<sub>4</sub>] based polymer electrolytes. *J. Phys. Chem. Solids* **73**, 162–168 (2012).
  39. F. Todescato, R. Capelli, F. Dinelli, M. Murgia, N. Camaioni, M. Yang, R. Bozio, and M. Muccini, Correlation between dielectric/organic interface properties and key electrical parameters in PPV-based OFETs. *J. Phys. Chem. B* **112**, 10130–10136 (2008).
  40. Tsai, T. Da, Chang, J. W., Wen, T. C. & Guo, T. F. Manipulating the hysteresis in poly(vinyl alcohol)-dielectric organic field-effect transistors toward memory elements. *Adv. Funct. Mater.* **23**, 4206–4214 (2013).
  41. Facchetti, A., Yoon, M. H. & Marks, T. J. Gate Dielectrics for Organic Field-Effect Transistors: New Opportunities for Organic Electronics. *Adv. Mater.* **17**, 1705–1725 (2005).
  42. Lu, J., Moon, K.-S. & Wong, C. P. High-k Polymer Nanocomposites as Gate Dielectrics for Organic Electronics Applications. *2007 Proc. 57th Electron. Components Technol. Conf.* 453–457 (2007). doi:10.1109/ECTC.2007.373836

43. A. Klug, M. Denk, T. Bauer, M. Sandholzer, U. Scherf, C. Slugovc, and E. J. W. List, Organic field-effect transistor based sensors with sensitive gate dielectrics used for low-concentration ammonia detection. *Org. Electron. physics, Mater. Appl.* **14**, 500–504 (2013).
44. E. Menard, V. Podzorov, S. H. Hur, A. Gaur, M. E. Gershenson, and J. A. Rogers, High-performance n- And p-type single-crystal organic transistors with free-space gate dielectrics. *Adv. Mater.* **16**, 2097–2101 (2004).
45. Facchetti, A., Yoon, M.-H. & Marks, T. J. Gate Dielectrics for Organic Field-Effect Transistors: New Opportunities for Organic Electronics. *Adv. Mater.* **17**, 1705–1725 (2005).
46. Peng, X., Horowitz, G., Fichou, D. & Garnier, F. All-organic thin-film transistors made of alpha-sexithienyl semiconducting and various polymeric insulating layers. *Appl. Phys. Lett.* **57**, (1990).
47. Miranda, T. M. R., Gonçalves, A. R. & Amorim, M. T. P. Ultraviolet-induced crosslinking of poly(vinyl alcohol) evaluated by principal component analysis of FTIR spectra. *Polym. Int.* **50**, 1068–1072 (2001).
48. K. Myny, S. Member, M. J. Beenhakkers, N. A. J. M. Van Aerle, G. H. Gelinck, J. Genoe, W. Dehaene, S. Member, and P. Heremans, Unipolar Organic Transistor Circuits Made Robust by Dual-Gate Technology. *IEEE J. Solid-State Circuits* **46**, 1223–1230 (2011).



## Chapter 6

### **CdSe-ZnS core-shell quantum dot based solution processed flexible light emitting diodes for flat-panel display application**

In this chapter we report on the synthesis of CdSe-ZnS core-shell colloidal quantum dots using hot injection route. The photoluminescence of synthesized quantum dots is found to depend on the size of core (CdSe) which can be tuned via change in precursor concentration and the injection method. The as synthesized quantum dots are used to fabricate the light emitting diodes (QD-LED) with emission in green, yellow and red region of visible spectrum. Finally, we also demonstrate fabrication of flexible QD-LED on ITO-PET substrate.

## 6.1 Introduction:

Since the inception of the quantum dots (QDs) three decades ago, their properties have been thoroughly investigated by researchers around the globe. The QDs have proved to be excellent materials for optoelectronic applications, especially in the field of light emitting diode (LED) technology. The QDs possess some unique optical properties such as size dependent band gap tuning (quantum confinement effect), narrow emission spectrum with high quantum yield and high luminescence efficiency etc.<sup>1-5</sup> Also QDs can be synthesized using colloidal-based synthesis routes, which are quite facile.<sup>6-17</sup> These characteristics made the colloidal QDs an excellent candidate for the application in the next generation LEDs. QD based LEDs have several advantages over the conventional LEDs and organic LEDs in terms of colour purity, stability and production cost. Although, the efficiencies achieved by the QD-LEDs are significantly lower than the OLEDs however, considering the progress made in the last decade in this field, QD-LEDs should emerge as one of the leading technology in solid state lighting application.<sup>18-33</sup>

The photoluminescence (PL) from colloidal QDs suffer from intrinsic stability issues due to the presence of surface trap states in QDs. Efforts to synthesize highly luminescent stable quantum dots with reduced surface trap states include surface modification using inorganic and organic layers.<sup>34-39</sup> Especially, the core-shell structured QDs (wherein shell of inorganic materials such as CdS, ZnS, ZnSe etc. cover the core of QDs) have shown extremely high quantum yield with less trap states.<sup>40-44</sup> Presence of inorganic shell over over QDs also provide the chemical stability to QDs which is important to improve the longevity of optoelectronic devices. However, the quantum efficiency is observed to decrease after certain optimum shell thickness because of the three mains reasons viz. 1) introduction of defects at the shell due to the lattice mismatch between the core and shell layers, 2) non-uniform shell growth and 3) formation of grain boundaries between the small clusters present in the shell. Hence optimization of the shell thickness is very important to obtain highly luminous QDs.<sup>45</sup>

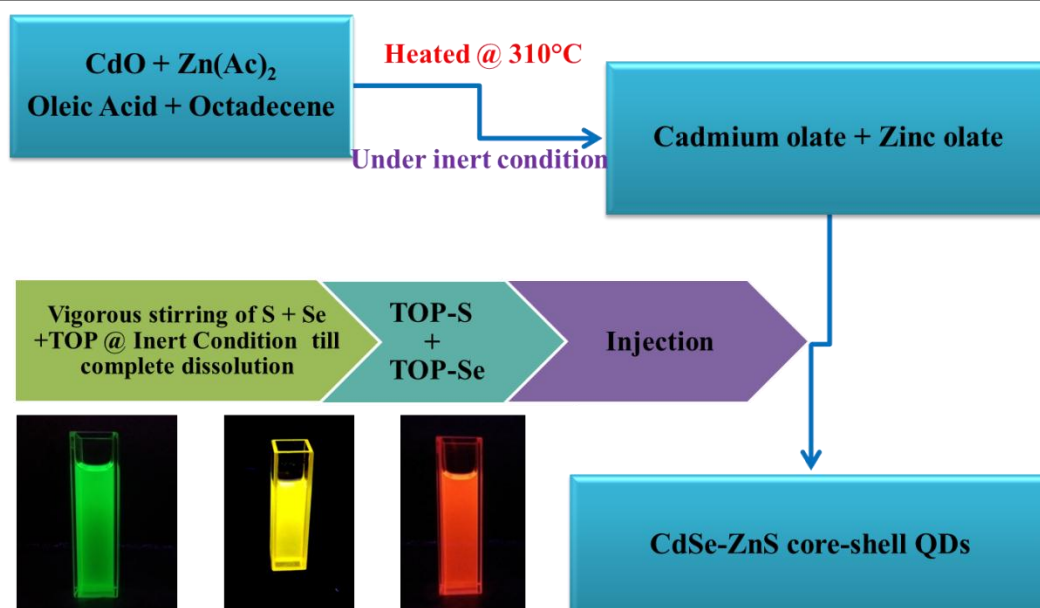
Till date several efforts have been done for the advancement of the LED device. In the conventional device architecture, the emissive layer is sandwiched between a hole transport layer (HTL) and an electron transport layer (ETL). Typically for QD-LEDs poly(N-vinyl carbazole) (PVK) is used as hole transport layer and ZnO serves as electron transport layer. For efficient charge injection to the HTL from the electrode a thin layer of poly (3,4-ethylenedioxythiophene):polystyrene sulphonate (PEDOT:PSS) has also been introduced between the positive electrode and the HTL which is called hole injection layer (HIL). ITO (transparent electrode) and Aluminium serve as bottom and top electrode respectively. Using this device architecture, maximum external quantum efficiency ( $\eta_{EQE}$ ) of 12.6% has been achieved for green QD-LED.<sup>22</sup> Further improvement in the EQE was demonstrated using the inverted architecture in which the HTL and HIL are deposited through PVD method on the top of the QD layer while the ETL remained at the bottom. The red QD-LED fabricated using this technique yields EQE of 18-20% which is quite comparable to state-of-art phosphorescent OLEDs.<sup>24</sup> Recently Yang et.al.<sup>46</sup> have shown that red, green and blue QD-LED can be fabricated using the conventional device architecture. In their device architecture for green and red emitting QD-LED, they used poly(9,9-dioctylfluorene-co-N-(4-(3-methylpropyl))diphenylamine) (TFB) as HTL (instead of PVK) to improve the energy alignment with the QD whereas the blue emitting device were made with the conventional HTL (PVK).<sup>28</sup>

In this work we synthesized CdSe-ZnS core-shell quantum dots by modifying the hot injection method reported by Bae et.al.<sup>45</sup> We have successfully tuned the core size of the core-shell quantum dots by altering the Cd:Zn ratio and the injection method of the sulphur (S) and selenium (Se) precursor. The as synthesized quantum dots were used for the fabrication of flexible QD-LED. In the device fabrication method we followed the protocol reported by Yang et al. Initially the device fabrication method was optimized on the ITO-glass substrates. This optimized method was used to fabricate 0.5 cm<sup>2</sup> orange coloured QD-LED on flexible ITO-PET substrate.

## 6.2 Experimental:

### 6.2.1 Single-Step Synthesis of Quantum Dots:

In a typical synthesis procedure (Scheme 6.1), 0.4 mmol Cadmium oxide (CdO, 99.99%), 4 mmol zinc acetate (99.9%, powder), 17.6 mmol oleic acid (OA, 90%) and 20 mL 1-octadecene (ODE, 90%) were placed in a 250 mL round flask. The mixture was then heated to 150 °C in a heating mantle and the reaction mixture was subsequently degassed under 100 m Torr pressure for 30 min. The flask was then filled with inert gas (argon) and the temperature was further raised to 310 °C to get clear solution. At this temperature a solution of selenium (99.9%, powder) (0.4 mmol) and sulfur (99.9%, powder) (4 mmol) with varying concentration in trioctyl phosphine (TOP, 90%) was quickly injected into the reaction mixture. After the injection the temperature was set at 300 °C for 5 min for the gradual growth of the shell and then it was cooled to room temperature to stop the growth. The QDs were washed with chloroform and excess ethanol (3 times). Finally QDs were re-dispersed in chlorobenzene for device application. Size tuning of the QDs was achieved by varying the Cd-Zn ratio, without altering concentration of other precursors. We also introduced a method of subsequent injection of Se and S into the reaction mixture. For this method two separate solutions of Se and S in TOP were prepared. First, the Se precursor solution was injected to the reaction mixture followed by the S precursor with 5 sec time gap between them.



*Scheme 6.1: Synthesis process of oleic acid capped CdSe-ZnS core-shell quantum dots. Inset is showing green, yellow and orange-red emitting QDs.*

### 6.2.2 Fabrication of QD-LED device fabrication:

The QD-LED devices were fabricated both on the hard substrate (ITO-Glass) and flexible substrate (ITO-PET). In a typical device PEDOT:PSS (~ 50 nm) (Clevios PH-1000, Heraeus) was spin coated at a spin rate of 1500 r.p.m for 60 sec. It was then annealed at 150 °C for 10 min. Then the substrates are coated with PVK or TFB (Sigma-Aldrich). In case of both the layers 8 mg/mL solution in chlorobenzene (CB) was used for spin coating. Two different spin rates of 3000 rpm and 4000 rpm were used for the fabrication. The spin time was fixed at 30 sec. The substrates were baked at 150 °C for 30 min. On top of the HTL QDs were spin coated. Three types of QDs, green, yellow and red-orange QDs emitting, were used for the fabrication of green, yellow and red-orange LEDs. The concentrations of QD solutions in CB were 18 mg ml<sup>-1</sup>, 17 mg ml<sup>-1</sup> and 15 mg ml<sup>-1</sup> respectively. The spin rates were varied for optimization. ZnO nanoparticle (synthesized using synthesis procedure reported in ref. 16) layer (30 mg ml<sup>-1</sup> ZnO solution in ethanol, 3,000 r.p.m. spin speed) was deposited by spin coating. The average thickness of the layer was ~65 nm. The ~100 nm aluminium (Al) top electrode was deposited by vacuum evaporation technique.

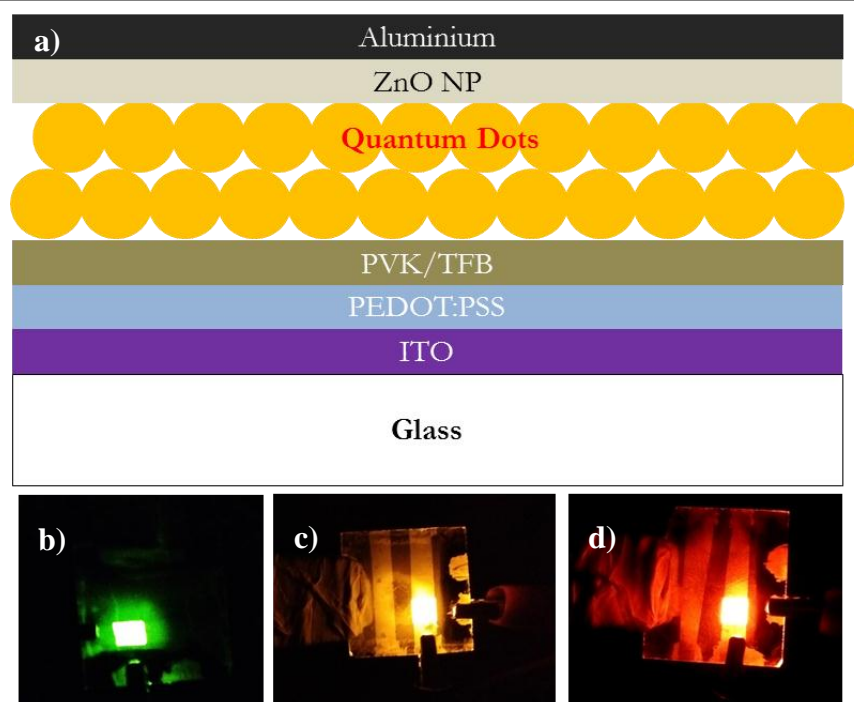


**Figure 6.1:** a) Device architecture of QD-LED, b) green, c) yellow and d) orange-red QD-LED.

### 6.3 Characterization:

Room temperature PL spectra of the QD solutions and films were taken using Fluoromax-4 spectrofluorometer manufactured by Horiba Scientific. The thickness of the layers was measured using Dektak profilometer. Kethley-2400 source meter was used to power the devices and CS-200 chroma meter from Konika-Minolta was used for measuring the light intensity.

### 6.4 Result and Discussion:

#### 6.4.1 Synthesis of core-shell quantum dot:

##### I. Mechanism of core-shell QD formation:

The core-shell QD synthesis procedure reported here is unique because it involves single step processing. The affinity between the ions present in the reaction mixture governs the dynamics of the reaction. Hence understanding of the reaction dynamics is very important for further optimization. The synthesis procedure is very similar to the conventional QD fabrication method where the metal-olate complex is formed at high temperature and it is then reacted with the TOP-halide

complex to form QDs. But in this case two metal-olate complexes (Cd and Zn) and two different TOP-halide complexes (Se and S) are simultaneously present in the reaction mixture. Here Cd-olate and TOP-Se have lower binding energy and thus possess more reactivity than Zn-olate and TOP-S. Hence the nucleation is mainly governed by Cd and Se followed by ZnS shell formation. Although in this method the formation of the side products (ZnSe and CdS) could not be avoided. Since the binding energy of TOP-Se and TOP-S is not very different, always a mixture of CdSe-CdS is formed. Due to the formation of these side products a graduated core-shell QD CdSe-(ZnSe/CdS)-ZnS, formation has been observed. Hence by varying the core diameter the photoluminescence (PL) of the QD can be shifted. In our work we have shown two different ways to shift the PL toward higher wavelength.

## II. Tuning of QD emission by varying Cd:Zn ratio:

We tuned the QD emission by varying the concentration of the Cd precursor (Figure 6.2). Three different precursor ratio (Cd:Zn) viz. 1:10, 1:5.5 and 1:5.17 were used .

It can be clearly seen from the figure, the PL maxima of QD is red shifted from 542 nm to 587 nm as the concentration of the Cd is increased. When the Cd concentration is more than Se, the unreacted Cd-olate remained in the solution after complete CdSe formation. Hence, the remaining Cd reacted with S to form CdS layer at the surface of CdSe. Since the CdS has smaller band gap than ZnS, the PL is observed to shift towards higher wavelength. In 1:10 case the green (542 nm) PL is observed (figure 6.2 a), which shift to yellow (576 nm) in case of 1:5.5 ratio (figure 6.2 b). Further shift to orange (587 nm) was observed in 1:5.17 case (figure 6.2 c).

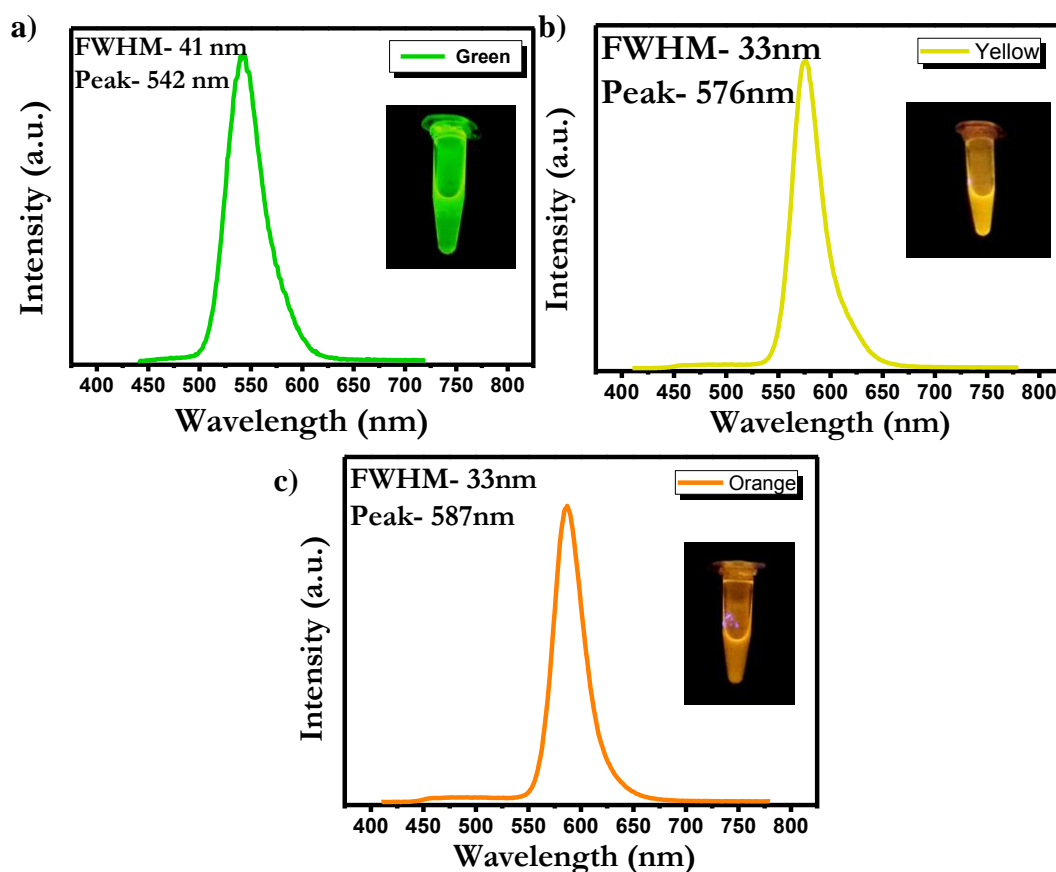


**Figure 6.2:** Photoluminescence (PL) shift by varying Cd concentration, Cd:Zn ratio a) 1:10, b) 1.5:5 and c) 1:5.17.

### III. Tuning of QD emission by varying injection method:

We also modified the injection method of Se and S precursor to red shift the QD PL. In this method, we first injected TOP-Se to the reaction mixture, which minimizes the possibility of CdS formation. The absence of S in the reaction mixture leads to near complete formation of CdSe, which in turn increases the core diameter. Hence, the PL is observed to shift to the higher wavelength.



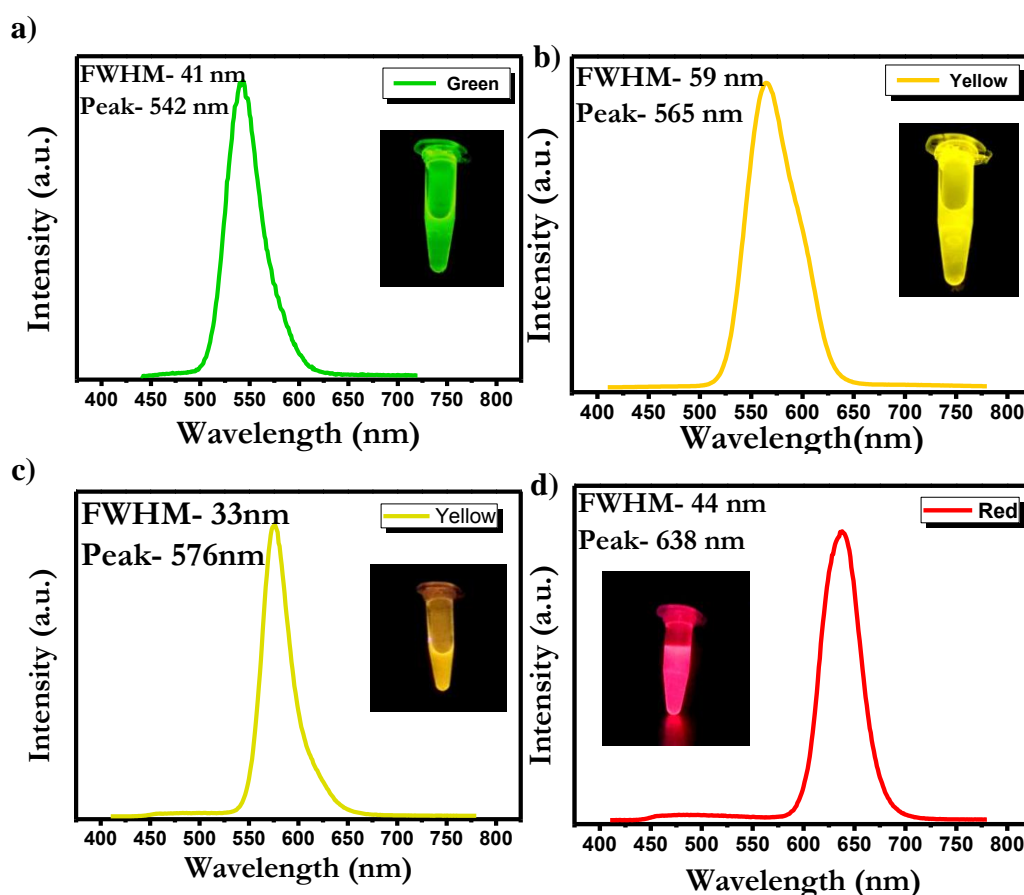


**Figure 6.3:** Photoluminescence (PL) shift by varying injection method with fixed precursor concentration, a) simultaneous injection and b) subsequent injection of Se and S precursor with Cd:Zn concentration 1:10 and c) simultaneous injection and d) subsequent injection of Se and S precursor with Cd:Zn concentration 1:5.5.

It can be noted from the figure 6.3 that the subsequent injection not only lead to shift in PL to higher wavelength, but also results in the increase in full width half maxima (FWHM) of the emission peaks. This is because; the increase of the core size lead to decrease in the shell thickness of the QDs. This leads to inefficient passivation of the QD core resulting in the broader PL spectrum.

#### 6.4.2 Fabrication of QD-LED device:

##### I. Fabrication of Device on the hard substrate:

The QD-LED devices were fabricated on the Glass/ITO substrate using orange-red luminescent quantum dots. The active area for all the devices was  $0.09 \text{ cm}^2$ . Initially, the devices were fabricated by depositing PVK layers with a fixed spin

rate of 3000 rpm. The average thickness of the PVK layer was ~58 nm. Two different thicknesses of the QD layers viz. ~18 nm (1000 rpm) and ~15 nm (2000 rpm) were used. The device with thinner QD layer (~15 nm) showed slightly better performance than the thicker one (~18 nm). Both the devices showed similar turn-on voltages (3V) but the turn-on current of thinner QD layer ( $3.3 \text{ mA/cm}^2$ ) was marginally less than the thicker one ( $5.56 \text{ mA/cm}^2$ ).

S. No.	Device architecture	Turn-on Voltage (V)	Turn-on Current ( $\text{mA cm}^{-2}$ )	Luminosity @ 4V ( $\text{cd m}^{-2}$ )
1	ITO/PEDOT-PSS/PVK/QD(~18nm)/ZnO/Al	3	5.6	NA
2	ITO/PEDOT-PSS/PVK/QD(~15nm)/ZnO/Al	3	3.3	NA
3	ITO/PEDOT-PSS/PVK(~58nm)/QD/ZnO/Al	2	77.8	78
4	ITO/PEDOT-PSS/PVK(~42nm)/QD/ZnO/Al	1.7	18.9	213
5	ITO/PEDOT-PSS/TFB(~40nm)/QD/ZnO/Al	1.8	22.2	341

**Table 6.1:** Comparison of turn-on voltage and turn-on current of the devices.

The next set of devices were fabricated with fixed thickness of QD layer (~15 nm) while the thickness of the PVK layer was varied between 40 – 58 nm. Two different thicknesses were employed, ~50 nm (3000 rpm) and ~42 nm (4000 rpm). In this experiment substantial improvement in the device performance was observed for thinner PVK layer (42 nm). As the thickness of the PVK layer has decreased (from 50 nm to 42 nm), the turn-on voltage and current has also decreased (from 2V and  $77.8 \text{ mA cm}^{-2}$  to 1.7 V and  $18.9 \text{ mA cm}^{-2}$ ). The luminosity of the device at 4 V was also considerably improved from  $78 \text{ cd m}^{-2}$  to  $213 \text{ cd m}^{-2}$ . The table 6.1 shows the comparative device performances.

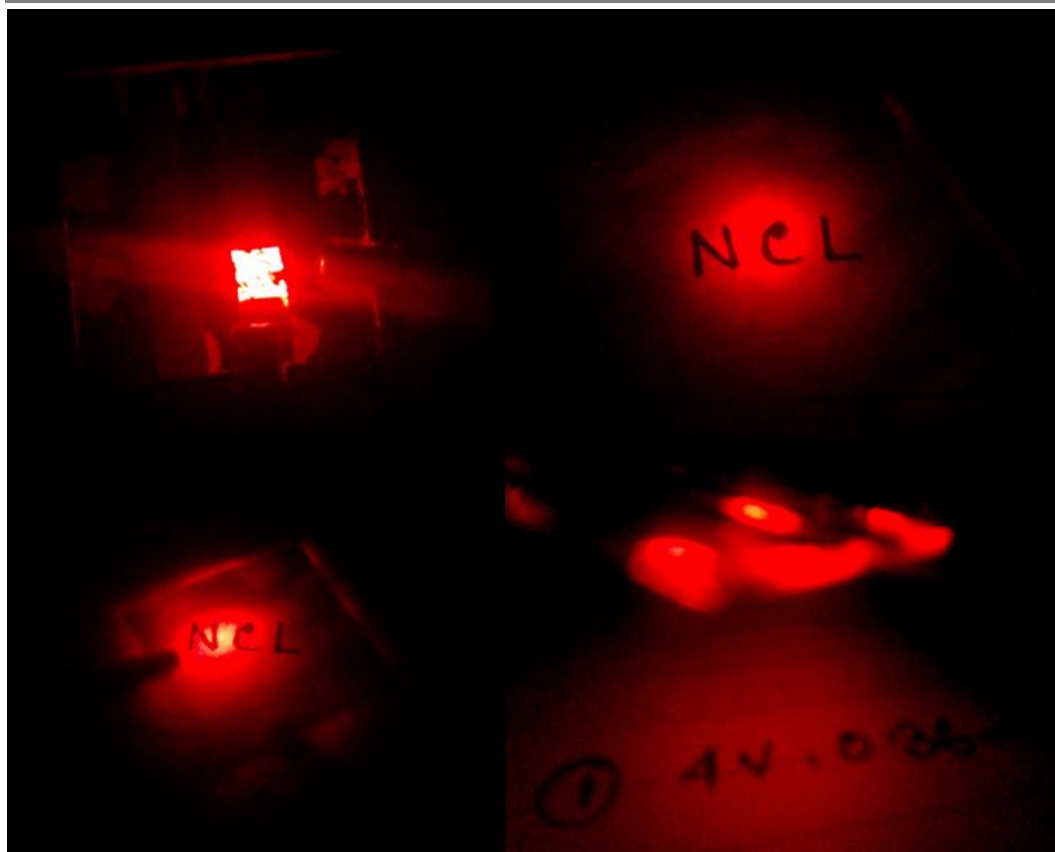


*Figure 6.4: Devices fabricated using TFB as HTL with orange-red emitting QDs.*

In the next set of devices the PVK layer has been replaced by TFB keeping the same spin coating parameters. No major changes were observed in the turn-on voltage (1.8 V) and turn-on current ( $22.22 \text{ mA cm}^{-2}$ ) but the luminosity of the device at 4V substantially improved to  $341 \text{ Cd m}^{-2}$ . The improvement in the device performance can be attributed to the proper charge injection to the QDs from the TFB layer. Since the hole mobility of TFB ( $\sim 10^{-2} \text{ cm}^2 \text{ V}^{-1} \text{ s}^{-1}$ ) is substantially higher than PVK ( $10^{-6} \sim 10^{-5} \text{ cm}^2 \text{ V}^{-1} \text{ s}^{-1}$ ), the effective charge injection from HTL to QD layer improve the device performance. Using the same device architecture we fabricated green and yellow QD-LEDs. The green LED device showed the luminosity of  $227 \text{ cd m}^{-2}$  while the yellow LED device exhibited the highest luminosity of  $319 \text{ cd m}^{-2}$ . Figure 6.4 demonstrates the devices glowed at 4V using this device architecture. The average luminosity of the devices in the figure was  $\sim 250 \text{ cd m}^{-2}$ .

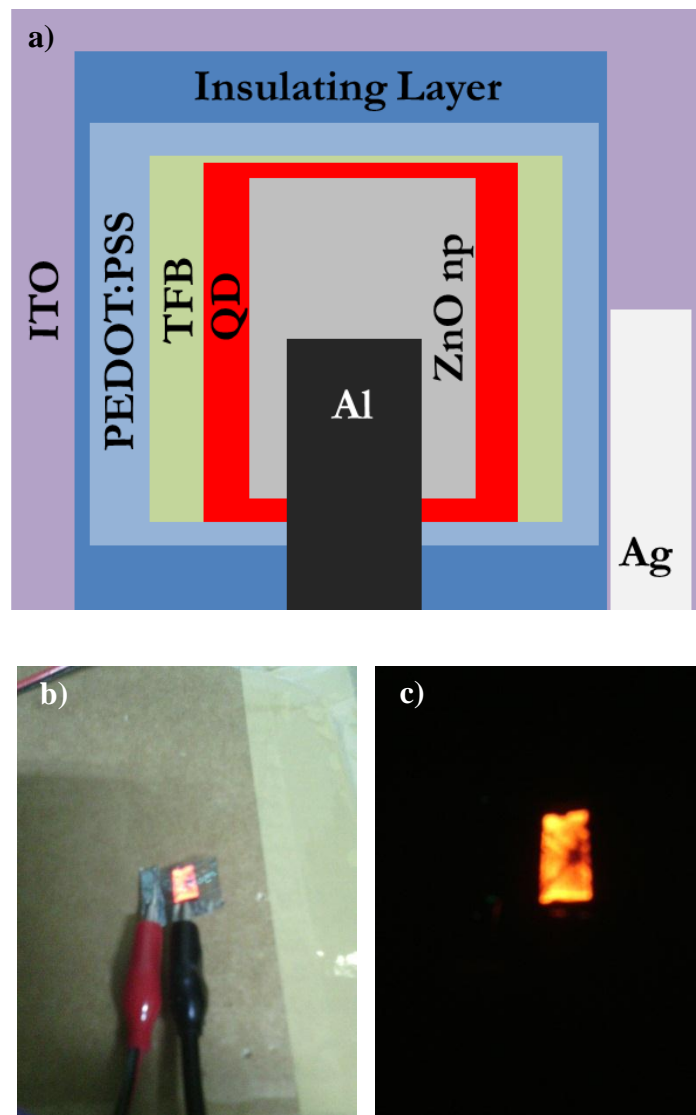


*Figure 6.4: a) Device architecture of flexible QD-LED and b) & c) shows the working devices.*

## II. Fabrication of Device on the flexible substrate:

Further, we fabricated flexible QD-LED using orange-red emitting QDs in collaboration with Keetronics (flexible electronics company). In the flexible devices an insulating layer, polyvinyl alcohol (PVA), was introduced at one side of the ITO to separate the Al and ITO to get electrically shorted. The PVA and PEDOT:PSS layers have been deposited using screen printing technique by Keetronics. The Rest of the device was fabricated using the previously mentioned technique. The flexible device had an active area of  $0.5 \text{ cm}^2$ . The device showed turn-on voltage of 2V and turn-on current of  $80 \text{ mA cm}^{-2}$  with the luminosity of  $\sim 156 \text{ cd m}^{-2}$  at 4V.

## 6.5 Conclusion:

In this work we synthesized green, yellow and orange-red emitting CdSe-ZnS core-shell quantum dots using single step hot injection method. We varied the Cd:Zn ratio to tune the core-shell structure of the QDs, which resulted in its tuned emission. We employed different injection techniques to understand the reaction dynamics of the formation of QDs. Subsequent injection of TOP-Se and TOP-S in the hot reaction mixture, instead of simultaneous injection, increases the core size of the QDs, which shifts the PL towards higher wavelength. Subsequently we optimized the QD based LED devices on the glass-ITO substrate. The highest luminosity achieved was  $341 \text{ cd-m}^{-2}$  using orange-red QDs. Finally, we could successfully demonstrate flexible QD-LED on ITO-PET substrate using orange-red QDs. The device showed  $\sim 156 \text{ cd m}^{-2}$  luminosity.

## 6.6 References:

1. Shirasaki, Y., Supran, G. J., Bawendi, M. G. & Bulovic, V. Emergence of colloidal quantum-dot light-emitting technologies. *Nat Phot.* **7**, 13–23 (2013).
2. J. Lim, W. K. Bae, J. Kwak, S. Lee, C. Lee, and K. Char, Perspective on synthesis, device structures, and printing processes for quantum dot displays. *Opt. Mater. Express* **2**, 594 (2012).
3. Alivisatos, A. P. Semiconductor Clusters, Nanocrystals, and Quantum Dots. *Science (80-. )*. **271**, (1996).
4. Shirasaki, Y., Supran, G. J., Bawendi, M. G. & Bulović, V. Emergence of colloidal quantum-dot light-emitting technologies. *Nat. Photonics* **7**, 933–933 (2013).
5. Reineke, S. Complementary LED technologies. *Nat Mater* **14**, 459–462 (2015).
6. Bao, J. & Bawendi, M. G. A colloidal quantum dot spectrometer. *Nature* **523**, 67–70 (2013).
7. Red, green and blue lasing enabled by single-exciton gain in colloidal quantum dot films. Red, green and blue lasing enabled by single-exciton gain in colloidal quantum dot films. *Nat. Nanotechnol.* **7**, 335–339 (2012).
8. Debnath, R., Bakr, O. & Sargent, E. H. Solution-processed colloidal quantum dot photovoltaics: A perspective. *Energy Environ. Sci.* **4**, 4870 (2011).
9. A. H. Ip, S. M. Thon, S. Hoogland, O. Voznyy, D. Zhitomirsky, R. Debnath, L. Levina, L. R. Rollny, G. H. Carey, A. Fischer, K. W. Kemp, I. J. Kramer, Z. Ning, A. J. Labelle, K. W. Chou, A. Amassian, and E. H. Sargent, Hybrid passivated colloidal quantum dot solids. *Nat. Nanotechnol.* **7**, 577–582 (2012).

10. Kim, J. Y., Voznyy, O., Zhitomirsky, D. & Sargent, E. H. 25th anniversary article: Colloidal quantum dot materials and devices: A quarter-century of advances. *Advanced Materials* **25**, 4986–5010 (2013).
11. Rajh, T., Micic', O. I. & Nozik, A. J. Synthesis and Characterization of Surface-Modified Colloidal CdTe Quantum Dots. *J. Phys. Chem* **97**, 11999–12003 (1993).
12. D. K. Harris, P. M. Allen, H. S. Han, B. J. Walker, J. Lee, and M. G. Bawendi, Synthesis of cadmium arsenide quantum dots luminescent in the infrared. *J. Am. Chem. Soc.* **133**, 4676–4679 (2011).
13. Keuleyan, S., Lhuillier, E. & Guyot-Sionnest, P. Synthesis of colloidal HgTe quantum dots for narrow mid-IR emission and detection. *J. Am. Chem. Soc.* **133**, 16422–16424 (2011).
14. Tang, J. & Sargent, E. H. Infrared colloidal quantum dots for photovoltaics: Fundamentals and recent progress. *Adv. Mater.* **23**, 12–29 (2011).
15. Guzelian, A. A., Banin, U., Kadavanich, A. V, Peng, X. & Alivisatos, A. P. Colloidal chemical synthesis and characterization of InAs nanocrystal quantum dots. *Appl. Phys. Lett.* **69**, 1432–1434 (1996).
16. Teitelboim, A., Meir, N., Kazes, M. & Oron, D. Colloidal Double Quantum Dots. *Acc. Chem. Res.* **49**, 902–910 (2016).
17. Guyot-Sionnest, P. Colloidal quantum dots. *Comptes Rendus Physique* **9**, 777–787 (2008).
18. T.-H. Kim, K.-S. Cho, E. K. Lee, S. J. Lee, J. Chae, J. W. Kim, D. H. Kim, J.-Y. Kwon, G. Amaratunga, S. Y. Lee, B. L. Choi, Y. Kuk, J. M. Kim, and K. Kim, Full-colour quantum dot displays fabricated by transfer printing. *Nat Phot.* **5**, 176–182 (2011).
19. Caruge, J. M., Halpert, J. E., Wood, V., Bulović, V. & Bawendi, M. G. Colloidal quantum-dot light-emitting diodes with metal-oxide charge transport layers. *Nat. Photonics* **2**, 247–250 (2008).

20. K.-S. Cho, E. K. Lee, W.-J. Joo, E. Jang, T.-H. Kim, S. J. Lee, S.-J. Kwon, J. Y. Han, B.-K. Kim, B. L. Choi, and J. M. Kim, High-performance crosslinked colloidal quantum-dot light-emitting diodes. *Nat. Photonics* **3**, 341–345 (2009).
21. J. Kwak, W. K. Bae, D. Lee, I. Park, J. Lim, M. Park, H. Cho, H. Woo, D. Y. Yoon, K. Char, S. Lee, and C. Lee, Bright and efficient full-color colloidal quantum dot light-emitting diodes using an inverted device structure. *Nano Lett.* **12**, 2362–2366 (2012).
22. K. H. Lee, J. H. Lee, H. D. Kang, B. Park, Y. Kwon, H. Ko, C. Lee, J. Lee, and H. Yang, Over 40 cd/A efficient green quantum dot electroluminescent device comprising uniquely large-sized quantum dots. *ACS Nano* **8**, 4893–4901 (2014).
23. K. H. Lee, J. H. Lee, W. S. Song, H. Ko, C. Lee, J. H. Lee, and H. Yang, Highly efficient, color-pure, color-stable blue quantum dot light-emitting devices. *ACS Nano* **7**, 7295–7302 (2013).
24. Mashford, B., Stevenson, M. & Popovic, Z. High-efficiency quantum-dot light-emitting devices with enhanced charge injection. *Nat. ...* **7**, 407–412 (2013).
25. Qian, L., Zheng, Y., Xue, J. & Holloway, P. H. Stable and efficient quantum-dot light-emitting diodes based on solution-processed multilayer structures. *Nat. Photonics* **5**, 543–548 (2011).
26. A. H. Mueller, M. A. Petruska, M. Achermann, D. J. Werder, E. A. Akhador, D. D. Koleske, M. A. Hoffbauer, and V. I. Klimov, Multicolor Light-Emitting Diodes Based on Semiconductor Nanocrystals Encapsulated in GaN Charge Injection Layers. *Nano Lett.* **5**, 1039–1044 (2005).
27. Coe, S., Woo, W.-K., Bawendi, M. & Bulović, V. Electroluminescence from single monolayers of nanocrystals in molecular organic devices. *Nature* **420**, 800–803 (2002).



28. Y. Yang, Y. Zheng, W. Cao, A. Titov, J. Hyvonen, J. R. Manders, J. Xue, P. H. Holloway, and L. Qian, High-efficiency light-emitting devices based on quantum dots with tailored nanostructures. *Nat. Photonics* **9**, 1–9 (2015).
29. Xin, Y., Nishio, K. & Saitow, K. White-blue electroluminescence from a Si quantum dot hybrid light-emitting diode. *Appl. Phys. Lett.* **106**, 201102 (2015).
30. Z. Tan, J. Xu, C. Zhang, T. Zhu, F. Zhang, B. Hedrick, S. Pickering, J. Wu, H. Su, S. Gao, A. Y. Wang, B. Kimball, J. Ruzyllo, N. S. Dellas, and S. E. Mohney, Colloidal nanocrystal-based light-emitting diodes fabricated on plastic toward flexible quantum dot optoelectronics. *J. Appl. Phys.* **105**, 34312 (2009).
31. X. Yang, E. Mutlugun, C. Dang, K. Dev, Y. Gao, S. T. Tan, X. W. Sun, and H. V. Demir, Highly Flexible, Electrically Driven, Top-Emitting, Quantum Dot Light-Emitting Stickers. *ACS Nano* **8**, 8224–8231 (2014).
32. Jo, J.-H. *et al.* High-efficiency red electroluminescent device based on multishelled InP quantum dots. *Opt. Lett.* **41**, 3984 (2016).
33. J. Pan, J. Chen, Q. Huang, Q. Khan, X. Liu, Z. Tao, W. Lei, F. Xu, and Z. Zhang, Flexible quantum dot light emitting diodes based on ZnO nanoparticles. *RSC Adv.* **5**, 82192–82198 (2015).
34. Xie, R., Kolb, U., Li, J., Basché, T. & Mews, A. Synthesis and Characterization of Highly Luminescent CdSe–Core CdS/Zn<sub>0.5</sub>Cd<sub>0.5</sub>S/ZnS Multishell Nanocrystals. *J. Am. Chem. Soc.* **127**, 7480–7488 (2005).
35. Talapin, D. V. *et al.* CdSe/CdS/ZnS and CdSe/ZnSe/ZnS Core–Shell–Shell Nanocrystals. *J. Phys. Chem. B* **108**, 18826–18831 (2004).
36. Peter, R., Bleuse, J. & Pron, A. Highly Luminescent CdSe/ZnSe Core/Shell Nanocrystals of Low Size Dispersion. *Nano Lett.* **2**, 781–784 (2002).
37. J. J. Li, Y. A. Wang, W. Guo, J. C. Keay, T. D. Mishima, M. B. Johnson,

- and X. Peng, Large-Scale Synthesis of Nearly Monodisperse CdSe/CdS Core/Shell Nanocrystals Using Air-Stable Reagents via Successive Ion Layer Adsorption and Reaction. *J. Am. Chem. Soc.* **125**, 12567–75 (2003).
38. B. O. Dabbousi, J. Rodriguez-Viejo, F. V. Mikulec, J. R. Heine, H. Mattoussi, R. Ober, K. F. Jensen, and M. G. Bawendi, (CdSe)ZnS Core–Shell Quantum Dots: Synthesis and Characterization of a Size Series of Highly Luminescent Nanocrystallites. *J. Phys. Chem. B* **101**, 9463–9475 (1997).
39. Bae, W. K., Char, K., Hur, H. & Lee, S. Single-step synthesis of quantum dots with chemical composition gradients. *Chem. Mater.* **20**, 531–539 (2008).

# Chapter 7

## Summary and Future work

**In this chapter we present closing comments on the work presented in this thesis. Towards the end, new approaches for future work in this exciting field of research are discussed.**

## 7.1 Summary:

The thesis primarily deals with the fabrication of electronic devices on flexible substrates. It broadly covers three types of devices namely flexible micro supercapacitor, flexible field effect transistor and inverter, and flexible quantum dot based light emitting diode. In our work we have mainly concentrated on the fabrication of flexible devices using organic molecules and nano particles. We have also emphasized on the development of microscale device fabrication techniques. In the micro supercapacitor work we have primarily used CO<sub>2</sub> laser for both laser writing and laser scribing purpose. In the case of laser writing work we have synthesized graphitic carbon from metal organic framework (MOF) using CO<sub>2</sub> laser for micro supercapacitor. In the laser scribing work we have developed a protocol to fabricate micro supercapacitor using pre-synthesized materials. In the field effect transistor topic, we have optimized the dielectric thickness for best device performance on a flexible substrate. We have been able to construct an inverter using the optimized transistors. In the final segment, we have demonstrated the fabrication of different coloured flexible light emitting diode display using CdSe/ZnS core/shell quantum dots as emitting layer. The optimization of both the quantum dots and the LED device are discussed in the thesis.

The first and second chapters of the thesis deal with the Introduction and Experimental aspects. This is followed by the working chapters 3-6.

### Summary of each topic

Chapter 3 reports, for the first time, the fabrication of flexible interdigitated micro supercapacitor by CO<sub>2</sub> laser direct writing of functional mesoporous carbon (named as LIMDG) by long wavelength photothermal processing of Co-MOF (ZIF-67) on polyimide substrate. The interconnected strong graphitic mesoporous carbon network thus obtained has several unique device-worthy features that are induced by the intrinsic inclusion of the catalytic metal (Co), presence of nitrogen doping, and ambient processing that leads to oxygen surface groups. The device

based on this carbon therefore exhibits ultra-high cyclic stability up to 200,000 cycles as well as 98% capacitance retention even at 150° bending angle.

In chapter 4A, we have demonstrated highly flexible and extremely stable EDLC micro-supercapacitor device using mushroom derived carbon as the electrode material. The device is fabricated using laser scribing, which is a facile, very fast and highly scalable method. The device shows 89% capacitance retention upto 1000 bending (60°) cycles and 88% performance retention under 120° bent condition. The device also shows excellent cyclic stability (95% retention) over 15k cycles. The highest volumetric capacitance shown by the device is 12.92 F cm<sup>-3</sup> at 0.05 mA cm<sup>-2</sup>. The device also shows a 1.8 mW h cm<sup>-3</sup> energy density at 0.05 mA cm<sup>-2</sup> and 720 mW cm<sup>-3</sup> power density at 1 mA cm<sup>-2</sup>. These values are quite impressive for a practical flexible micro-supercapacitor, especially given the flexing as well as cyclic stability of the device reported herein. Our electrode material, fabrication scheme, and the device would find good applicability in the domain of flexible microelectronics.

In chapter 4B, we have presented work on the fabrication of a robust flexible all solid state interdigitated micro-pseudocapacitor by CO<sub>2</sub> laser scribing of a coating of pre-synthesized dual mixed-valent ternary oxide CuCo<sub>2</sub>O<sub>4</sub> (CCO). The basic electrode material (CCO) showed high charge transfer resistance which was dramatically reduced by blending it with a small quantity (10 wt.%) of CNTs with CCO. The areal capacitance was found to be 2.26 mF cm<sup>-2</sup> at a current density of 0.2 mA cm<sup>-2</sup> for the composite based device which is comparable with the current state of art devices. The CCO-CNT composite based device showed over 93% stability even after 9000 charge-discharge cycles at a current density of 1 mA cm<sup>-2</sup> and no sign of decline. The device also retained more than 93% of its performance even under 120° bending condition and over 65% retention after 1000 cycles of repeated large angle (60°) bending, thanks to the electro-mechanical continuity afforded by CNTs.

In the chapter 5, we have discussed the optimization of the thickness of the PVA dielectric layer for better OFET device performance. The device with thinner dielectric layer (300 nm) on corning glass substrate shows considerably good

device performance having  $1.4 \times 10^4$  on-off ratio with high field effect mobility of  $0.45 \text{ cm}^2 \text{ V}^{-1} \text{ s}^{-1}$  and  $-4.3 \text{ V}$  threshold voltage. The same device architecture was used to fabricate the flexible device with further careful optimization of the fabrication conditions. The flexible device showed even more improved performance having  $5.3 \times 10^4$  on-off ratio with  $0.57 \text{ cm}^2 \text{ V}^{-1} \text{ s}^{-1}$  field effect mobility and  $1.46 \text{ V}$  threshold voltage. Further we have fabricated a diode-load inverter using the OFET on glass substrate. To the best of our knowledge this is the first report of pentacene based all organic OFET based inverter.

In the final chapter 6 we have reported synthesis of green, yellow and orange-red emitting CdSe-ZnS core-shell quantum dots using single step hot injection method. We varied the Cd:Zn ratio to tune the core-shell structure of the QDs, which resulted in its tuned emission. We employed different injection techniques to understand the reaction dynamics of the formation of QDs. Subsequent injection of TOP-Se and TOP-S in the hot reaction mixture, instead of simultaneous injection, increases the core size of the QDs, which shifts the PL towards higher wavelength. Subsequently we optimized the QD based LED devices on the glass-ITO substrate. The highest luminosity achieved was  $341 \text{ cd} \cdot \text{m}^{-2}$  using orange-red QDs. Finally, we could successfully demonstrate flexible QD-LED on ITO-PET substrate using orange-red QDs. The device showed  $\sim 156 \text{ cd} \cdot \text{m}^{-2}$  luminosity.

## 7.2 Future work:

In the field of flexible electronic devices several interesting research directions are being pursued internationally. Recently flexible microelectronics along with light emitting diodes is one of the booming fields of research. Based on the current scenario, the following points appear important for further research in this field.

1. Currently flexible room temperature gas sensing is one of the hottest fields of research. For gas sensing metal oxides such as  $\text{Fe}_3\text{O}_4$ ,  $\text{CuO}$ ,  $\text{Co}_2\text{O}_3$  etc. are one of the useful materials. Recently ternary metal oxides are also gaining importance. The major drawback of these metal oxides is their poor conductivity. Embedding these metal oxides into porous conducting material, such as carbon, solves the issue. Using  $\text{CO}_2$  laser pyrolysis both metal oxide

and carbon can be synthesized along with the simultaneously micro device fabrication. Hence this method can be extremely useful for the synthesis of metal oxide embedded highly porous carbon. This type material can also be useful for other catalytic reactions like electrochemical water splitting, CO<sub>2</sub> reduction reaction etc. This method can be further extended to the synthesis of ternary metal oxide. Careful optimization will be needed in the case of the synthesis of ternary metal oxide since this pyrolysis reaction occurs in air under drastic conditions (temperature can go over 2500 °C).

2. Recently both organic and inorganic perovskites are gaining importance in the field of light emitting diodes (LEDs). The basic advantages of these materials are their ease of fabrication, pure colour quality and low cost. However these suffer from low quantum yields which in turn decrease the quantum efficiency of the LEDs made using them. To improve their quantum yield confining the excited electrons and holes, and recombining them efficiently is very important. Quantum dots core shell nanostructures are made to improve the quantum yield where the core possessing smaller band gap than the shell. Hence in this band configuration the shell forms a electronic barrier around the core which restricts the excited electron hole pair at the core to disperse. Thus, almost all the excitons (excited electron and hole pair) can be recombined which in turn increases the quantum yield. The same concept can be employed in the synthesis of hybrid perovskites. The selection of the core and shell materials along with the proper reaction condition would be extremely important since the reaction dynamics will be quite different for the quantum dots.

## List of Publications

1. “CO<sub>2</sub> laser direct written MOF-based metal-decorated and hetero-atom doped porous graphene for flexible all-solid-state micro-supercapacitor with extremely high cycling stability”, **Aniruddha Basu**, Kingshuk Roy, Neha Sharma, Sunit Rane, Chandrashekhar Rode and Satishchandra Ogale, *ACS Appl. Mater. Interfaces*, vol. 8, issue 46, 31841–31848 (2016) DOI: 10.1021/acsami.6b10193
2. “Highly Stable Laser-Scribed Flexible Planar Microsupercapacitor Using Mushroom Derived Carbon Electrodes”, Poonam Yadav<sup>†</sup>, **Aniruddha Basu**<sup>†</sup>, Anil Suryawanshi, Onkar Game and Satishchandra Ogale, *Advanced Materials Interfaces*, vol. 3, issue 11, (2016), DOI: 10.1002/admi.201600057  
<sup>†</sup> equal contribution
3. “A robust highly flexible micro-pseudocapacitor based on ternary oxide CuCo<sub>2</sub>O<sub>4</sub> having ultrathin porous nanowall type morphology blended with CNT”, **Aniruddha Basu**,<sup>†</sup> Monika Bhardwaj,<sup>†</sup> Yogesh Gawli,<sup>ab</sup> Chandrasekhar Rodea and Satishchandra Ogale, *ChemistrySelect* Vol. 1, issue 16, 5159–5164 (2016). DOI: 10.1002/slct.201601348.  
<sup>†</sup> equal contribution
4. “Starch (Tapioca) to carbon dots: an efficient green approach to an on–off–on photoluminescence probe for fluoride ion sensing”, **Aniruddha Basu**, Anil Suryawanshi, Begraj Kumawat, Anshu Dandia, Debanjan Guin, Satishchandra Ogale, *The Analyst*, Vol. 140, Issue 6, 1837-1841, (2015) DOI: 10.1039/C4AN02340D
5. “Evaluation of n-type ternary metal oxide NiMn<sub>2</sub>O<sub>4</sub> nanomaterial for humidity sensing”, Yogesh Gawli, Satish Badadhe, **Aniruddha Basu**, Debanjan Guin, Manjusha V Shelke, Satishchandra Ogale, *Sensors and Actuators B: Chemical*, Vol. 191, 837–843 (2014), DOI: 10.1016/j.snb.2013.10.071



6. *“Catalyst free novel synthesis of graphene and its application in high current OFET and phototransistor based on P3HT/G composite”*, Prasad Yadav, Chetan Chanmal, **Aniruddha Basu**, Lily Mandal, Jyoti Jog, Satishchandra Ogale, **RSC Advances**, Vol. 3, Issue 39, 18049-18054 (2013)